



HAL
open science

High frequency thermomechanical study of heterogeneous materials with interfaces

Haoming Luo

► **To cite this version:**

Haoming Luo. High frequency thermomechanical study of heterogeneous materials with interfaces. Mechanics [physics.med-ph]. Université de Lyon, 2020. English. NNT : 2020LYSEI130 . tel-03210615

HAL Id: tel-03210615

<https://theses.hal.science/tel-03210615v1>

Submitted on 28 Apr 2021

HAL is a multi-disciplinary open access archive for the deposit and dissemination of scientific research documents, whether they are published or not. The documents may come from teaching and research institutions in France or abroad, or from public or private research centers.

L'archive ouverte pluridisciplinaire **HAL**, est destinée au dépôt et à la diffusion de documents scientifiques de niveau recherche, publiés ou non, émanant des établissements d'enseignement et de recherche français ou étrangers, des laboratoires publics ou privés.



N°d'ordre NNT : 2020LYSEI130

THESE de DOCTORAT **DE L'UNIVERSITE DE LYON**
opérée au sein de
I'Institut National des Sciences Appliquées de Lyon

Ecole Doctorale N° ED162
MECANIQUE, ENERGETIQUE, GENIE CIVIL, ACOUSTIQUE

Spécialité/ discipline de doctorat :
Génie Mécanique

Soutenue publiquement le 18/12/2020, par :
Haoming LUO

High frequency thermomechanical
study of heterogeneous materials with
interfaces

Devant le jury composé de :

RUFFLE Benoît	Professeur, Université de Montpellier	Rapporteur
VASSEUR Jérôme	Professeur, Université de Lille	Rapporteur
JACQUET-RICHARDET Georges	Professeur, INSA Lyon	Examinateur
LIU Haozhe	Professeur/Chercheur, HPSTAR	Examinateur
TANGUY Anne	Professeur, INSA Lyon	Directrice de thèse
GIORDANO Valentina	Chargé de Recherche CNRS	Co-directrice
LUND Fernando	Professeur, University of Chile	Invité
GRAVOUIL Anthony	Professeur, INSA Lyon	Invité

Département FEDORA – INSA Lyon - Ecoles Doctorales – Quinquennal 2016-2020

SIGLE	ECOLE DOCTORALE	NOM ET COORDONNEES DU RESPONSABLE
CHIMIE	<p><u>CHIMIE DE LYON</u> http://www.edchimie-lyon.fr Sec. : Renée EL MELHEM Bât. Blaise PASCAL, 3e étage secretariat@edchimie-lyon.fr INSA : R. GOURDON</p>	<p>M. Stéphane DANIELE Institut de recherches sur la catalyse et l'environnement de Lyon IRCELYON-UMR 5256 Équipe CDFA 2 Avenue Albert EINSTEIN 69 626 Villeurbanne CEDEX directeur@edchimie-lyon.fr</p>
E.E.A.	<p><u>ÉLECTRONIQUE, ÉLECTROTECHNIQUE, AUTOMATIQUE</u> http://edeea.ec-lyon.fr Sec. : M.C. HAVGOUDOUKIAN ecole-doctorale.eea@ec-lyon.fr</p>	<p>M. Gérard SCORLETTI École Centrale de Lyon 36 Avenue Guy DE COLLONGUE 69 134 Écully Tél : 04.72.18.60.97 Fax 04.78.43.37.17 gerard.scorletti@ec-lyon.fr</p>
E2M2	<p><u>ÉVOLUTION, ÉCOSYSTÈME, MICROBIOLOGIE, MODÉLISATION</u> http://e2m2.universite-lyon.fr Sec. : Sylvie ROBERJOT Bât. Atrium, UCB Lyon 1 Tél : 04.72.44.83.62 INSA : H. CHARLES secretariat.e2m2@univ-lyon1.fr</p>	<p>M. Philippe NORMAND UMR 5557 Lab. d'Ecologie Microbienne Université Claude Bernard Lyon 1 Bâtiment Mendel 43, boulevard du 11 Novembre 1918 69 622 Villeurbanne CEDEX philippe.normand@univ-lyon1.fr</p>
EDISS	<p><u>INTERDISCIPLINAIRE SCIENCES-SANTÉ</u> http://www.ediss-lyon.fr Sec. : Sylvie ROBERJOT Bât. Atrium, UCB Lyon 1 Tél : 04.72.44.83.62 INSA : M. LAGARDE secretariat.ediss@univ-lyon1.fr</p>	<p>Mme Emmanuelle CANET-SOULAS INSERM U1060, CarMeN lab, Univ. Lyon 1 Bâtiment IMBL 11 Avenue Jean CAPELLE INSA de Lyon 69 621 Villeurbanne Tél : 04.72.68.49.09 Fax : 04.72.68.49.16 emmanuelle.canet@univ-lyon1.fr</p>
INFOMATHS	<p><u>INFORMATIQUE ET MATHÉMATIQUES</u> http://edinfomaths.universite-lyon.fr Sec. : Renée EL MELHEM Bât. Blaise PASCAL, 3e étage Tél : 04.72.43.80.46 infomaths@univ-lyon1.fr</p>	<p>M. Luca ZAMBONI Bât. Braconnier 43 Boulevard du 11 novembre 1918 69 622 Villeurbanne CEDEX Tél : 04.26.23.45.52 zamboni@maths.univ-lyon1.fr</p>
Matériaux	<p><u>MATÉRIAUX DE LYON</u> http://ed34.universite-lyon.fr Sec. : Stéphanie CAUVIN Tél : 04.72.43.71.70 Bât. Direction ed.materiaux@insa-lyon.fr</p>	<p>M. Jean-Yves BUFFIÈRE INSA de Lyon MATEIS - Bât. Saint-Exupéry 7 Avenue Jean CAPELLE 69 621 Villeurbanne CEDEX Tél : 04.72.43.71.70 Fax : 04.72.43.85.28 jean-yves.buffiere@insa-lyon.fr</p>
MEGA	<p><u>MÉCANIQUE, ÉNERGÉTIQUE, GÉNIE CIVIL, ACOUSTIQUE</u> http://edmega.universite-lyon.fr Sec. : Stéphanie CAUVIN Tél : 04.72.43.71.70 Bât. Direction mega@insa-lyon.fr</p>	<p>M. Jocelyn BONJOUR INSA de Lyon Laboratoire CETHIL Bâtiment Sadi-Carnot 9, rue de la Physique 69 621 Villeurbanne CEDEX jocelyn.bonjour@insa-lyon.fr</p>
ScSo	<p><u>ScSo*</u> http://ed483.univ-lyon2.fr Sec. : Véronique GUICHARD INSA : J.Y. TOUSSAINT Tél : 04.78.69.72.76 veronique.cervantes@univ-lyon2.fr</p>	<p>M. Christian MONTES Université Lyon 2 86 Rue Pasteur 69 365 Lyon CEDEX 07 christian.montes@univ-lyon2.fr</p>

少年游·里昂

匆匆七月，雍园恰似，英气正当年。
雁过几回，富耶山上，我辈岂由天。

低声问，梦留何地？何地唤凉城。
莫问前程，但行何怕，理想即人生。

(07/2017)

蝶恋花·伦敦

感君赠我双红豆，踏碎长云闲看风雨骤。
雨去风休人不瘦，日暖碧空云如旧。

云如旧，垂杨柳，极目西洋鸿雁朝天走。
忽忆长安慈恩有，太白盛名太白酒。

(08/2018)

青玉案·铁一

寻香四月长安路，柳絮舞，春不住。
且放青龙逐日暮。

乐游花见，粉樱红院，汉阙犹真晤。

十年喜报无重数，意返窗前望一幕。
换了人间三两度。

案台依旧，那时应是，少年凝眉处。

(04/2020)

Acknowledges

My heartfelt thanks to my supervisor, Prof. Anne Tanguy for her continuous support and constant encouragement, both scientific and otherwise that make me successfully complete this thesis. Then, I want to extend my sincere gratitude to my co-supervisors, Dr. Valentina Giordano and Prof. Anthony Gravouil. They have walked me through all the stages of work and redaction of this thesis. Their conscientious academic spirit and modest, open-minded personality inspire me both in academic study and daily life.

Many thanks for Prof. Fernando Lund for his grant Eco-Chili that provided me the opportunity to visit Santiago, Chile for one month in 2019.

Also, I would like to express my heartfelt gratitude to all of my committee members : Prof. Benoît Rufflé, Prof. Jérôme Vasseur, Prof. Haozhe Liu, Prof. Georges Jacquet-Richardet and Prof. Fernando Lund for generously offering their time, support, guidance, and goodwill throughout the review of this document. Thanks for letting my defense be an enjoyable moment, and for their brilliant comments and suggestions.

Many thanks to my fantastic labmates : Alexis Bonetto, Bo Chen, Efoe Wallace, Florian Meray, Marie Gibert, Mederic Chaudey, Nicolas Jacquet, Quanshangze Du, Jin Huang, Paul Desmarchelier, Renzi Bai, Shuai Chen, Thomas Jailin, Tristan Djourachkovitch, Tristan Maquart, Thibaut Hirschler, Ye Lu, Zhaofeng Han, Zikang Low. They made the lab a friendly place to work in and taught me much about science and life. Special thanks to all the professors of the MIMESIS. Each at some point agreed to hear my questions and suggest helpful advice. My thanks go also to all the people of LaMCoS who without exception always responded to my questions and requests with a smile.

And, of course, this is also an opportunity to thank my families who helped me greatly in this period of my life, each in their own way.

Acknowledges

Abstract

Heat transfer is actually intimately related to the sound propagation (acoustic transfer) in materials, as in insulators and semi-conductors the main heat carriers are acoustic phonons. The concept of the presence of interfaces has been largely exploited for efficiently manipulating phonons from long-wavelength to nanometric wavelengths, *i.e.*, frequencies in THz regime, responsible for thermal transport at room temperature.

In this thesis, the finite element method is used to perform transient analysis of wave-packet propagation in different mediums. I started with a parametric study of attenuation of acoustic wave-packets in a 2D semi-infinite elastic system with periodic circular interfaces. Three key parameters are investigated, including rigidity contrast, interface density and phonon wavelength. Different energy transfer regimes (propagative, diffusive, and localized) are identified allowing to understand the phonon contribution to thermal transport. Besides the circular interfaces, mechanical response and acoustic attenuation for different types of interfaces are also investigated, such as Eshelby's inclusion, dendritic shape inclusion and porous materials with ordered/disordered holes. In order to extend the study to amorphous materials, I also considered a heterogeneous medium with random rigidities distributed in space according to a Gaussian distribution based on the theory of heterogeneous shear elasticity of glasses. Finally yet importantly, viscoelastic constitutive laws are proposed to take into account the frequency-dependent intrinsic phonon attenuation in glasses, with the aim of reproducing such intrinsic attenuation using a homogeneous viscous medium. Finite element simulation confirms that a continuum model may strictly follow the atomistic attenuation (Γ) for a well-calibrated macroscopic linear viscoelastic constitutive law. Compared with the experimental data in a-SiO₂, our second constitutive law reproduces qualitatively and quantitatively the three regimes of acoustic attenuation versus frequency : successively $\Gamma \propto \omega^2, \omega^4, \omega^2$.

KEYWORDS : Nanocomposite material ; Nanophononic material ; Amorphous material ; Acoustic and thermal transfer ; Acoustic attenuation ; Numerical simulations.

Résumé

Le transfert de chaleur est intimement lié à la propagation du son (transfert acoustique) dans les matériaux, par exemple dans les isolants et les semi-conducteurs, les principaux vecteurs d'énergie sont des phonons acoustiques. Le concept de présence d'interfaces a été largement exploité pour manipuler efficacement les phonons des longueurs d'onde macroscopiques aux longueurs d'onde nanométriques. Les derniers correspondent aux fréquences en régime THz, qui sont responsables du transport thermique à température ambiante.

Dans cette thèse, la méthode des éléments finis est utilisée pour effectuer des analyses transitoires de la propagation des paquets d'ondes dans différents milieux à 2D. Elle est commencée par une étude paramétrique de l'atténuation des paquets d'ondes dans un système élastique semi-infini avec des interfaces circulaires périodiques. Trois paramètres clés sont étudiés, notamment le contraste de rigidité, la densité d'interface et la longueur d'onde des phonons. Différents régimes de transfert (propagatif, diffusif et localisé) sont identifiés, qui permettent d'identifier la contribution des phonons à la conductivité thermique. Outre les interfaces circulaires, la réponse mécanique et l'atténuation acoustique pour différents types d'interfaces sont également étudiées, telles que l'inclusion de forme dendritique, l'inclusion d'Eshelby, et les matériaux poreux avec des pores ordonnés / désordonnés. Afin d'étendre l'étude aux matériaux amorphes, j'ai également considéré un milieu hétérogène avec des rigidités aléatoires réparties dans l'espace selon une distribution gaussienne basée sur la théorie de l'élasticité de cisaillement hétérogène des verres. Enfin et surtout, deux versions de lois de comportement viscoélastiques sont proposées pour prendre en compte l'atténuation intrinsèque des phonons dépendant de la fréquence dans les verres, dans le but qu'un milieu visqueux homogène puisse reproduire cette atténuation intrinsèque. La simulation par éléments finis confirme qu'un modèle continu peut suivre strictement l'atténuation atomistique (Γ) avec une loi de comportement viscoélastique linéaire macroscopique bien calibrée. Par rapport aux données expérimentales de a-SiO₂, notre deuxième loi de comportement reproduit qualitativement et quantitativement les trois régimes d'atténuation acoustique en fonction de la fréquence : successivement $\Gamma \propto \omega^2, \omega^4, \omega^2$.

KEYWORDS : Matériau anocomposite ; Matériau nanophononique ; Matériau amorphe ; Transfert acoustique et thermique ; Atténuation acoustique ; Simulation numérique.

Contents

Acknowledges	vii
Abstract	ix
Résumé	xi
Contents	i
List of Figures	v
General introduction	1
1 Numerical & theoretical methods	5
1 Finite Element code	7
1.1 General introduction to finite element method	7
1.2 Mesh : spatial discretization	11
1.3 Dynamic problem : temporal discretization	13
1.4 Boundary conditions	15
2 Constitutive models	17
2.1 Elasticity	18
2.2 Linear visco-elasticity	19
2.3 Generalized visco-elasticity	21
3 Wave propagation in a homogeneous elastic medium	21
3.1 Formulation	21
3.2 Wave speed in a homogeneous elastic medium	22
4 Heterogeneous materials with interfaces	24
4.1 Elastic inclusion	24
4.2 Eshelby's inclusion	25
4.3 Random elasticity	26
2 Acoustic attenuation in the presence of elastic inclusions	27
1 Model of bi-phasic materials : circular inclusions	29
1.1 Geometry	30
1.2 Materials properties	30

1.3	Boundary conditions	30
1.4	Perfect connection between the matrix and the inclusions	32
1.5	Spatial and temporal discretization	32
2	Equilibrium Vibrational Properties	32
2.1	Vibrational Density of States	33
2.2	Representative normal modes	34
3	Wave-Packet Propagation : Different Regimes	36
3.1	Envelope of the kinetic energy	36
3.2	Different propagation regimes	37
3.3	Phase diagram of propagation regimes	40
3.4	Meaningful quantities for describing different dynamical regimes	42
4	Penetration Length	44
4.1	Definition of the Penetration length	44
4.2	Penetration length vs $\frac{E_i}{E_m}$ & R for $\omega = 5$ THz	45
4.3	Penetration length vs $\frac{E_i}{E_m}$ & ω for $R=25$ Å	45
5	Discussion and conclusion	48
3	Mechanical response and acoustic attenuation for different types of interfaces	51
1	Dendritic inclusion	53
1.1	Dendrite phase in metallic glass	53
1.2	Reconstruction of the dendritic shape inclusion	55
1.3	Finite element simulation	57
1.4	Acoustic transport in an isotropic homogeneous material with dendritic inclusions	57
1.5	Measurement of the sound speed	61
1.6	Discussion	68
1.7	Conclusion and perspectives	69
2	Eshelby's inclusion	70
2.1	Ellipsoidal Eshelby's Inclusion	70
2.2	Implementation in the FE code	71
2.3	FE simulation by varying the ratio b/a	74
2.4	Wave propagation in a medium with an Eshelby's inclusion	81
2.5	Conclusion and perspectives	81
3	Nano-porous materials : from perfectly periodic to disordered holes arrangement	84
3.1	Porous structure	84
3.2	The optic-like approach to phonon scattering from periodic interfaces	84
3.3	Model of nano-porous structure : ordered and disordered	89
3.4	Estimation of the coherence length	91
3.5	Results : Envelopes of the kinetic energy	92
3.6	Discussion	94
3.7	Conclusion and perspectives	96

4	Acoustic attenuation in a medium with heterogeneous elasticity	97
4.1	Introduction of the vibrational anomalies in glasses in the tera- hertz range	97
4.2	Introduction of the theory of heterogeneous elasticity	98
4.3	Wave propagation in a medium with heterogeneous elasticity . . .	102
4.4	Discussion	106
4.5	Conclusion	108
4	Effective constitutive laws for an amorphous material (with acoustic attenua- tion)	109
1	Acoustic attenuation and apparent visco-elasticity	111
1.1	Introduction on acoustic attenuation in amorphous materials . . .	111
1.2	Three regimes of acoustic attenuation vs frequency	112
1.3	Acoustic attenuation in a viscous medium	112
2	A simple Constitutive model for longitudinal and transverse attenuation in glasses	115
2.1	Description of the model	115
2.2	Calibration of the model	118
2.3	Finite element simulation	119
2.4	Results compared to MD simulation	121
3	Taking into account the different attenuation regimes (ω^2 & ω^4)	124
3.1	Description of the new model	125
3.2	Calibration of the model	126
3.3	Influence of the parameters on the Q^{-1}	127
3.4	Crossover frequencies	129
3.5	Discussion	130
4	Conclusion	132
	General conclusions and prospects	135
A	Supplementary materials for the Chap.2	137
1	Contribution of phonons to thermal conductivity	137
2	1 alignment vs 10 alignments : verification of the periodic boundary condi- tion	138
B	Data of disorder holes	141
C	Complex constitutive tensor & implementation of the viscoelastic constitutive law in FE code	143
1	3D complex constitutive tensor	143
2	Finite Elements Simulations details	144

D	Existence of $\omega - \omega^3 - \omega$ behavior	147
1	$\alpha < 1$	147
1.1	Numerator	147
1.2	Denominator	150
1.3	Combination of the numerator and the denominator	150
1.4	Existence of $\omega - \omega^3 - \omega$ behavior	151
2	$\alpha > 1$	152
3	Conclusion	152
	Bibliography	153

List of Figures

1.1	Finite element mesh : discrete representation of the domain in the computations. (a) Left : TEM image of a Zr-Cu-Al-Ti-Ni metallic glass with nano-crystalline inclusions [TLI 17] Right : 2D mesh with triangle and quadrangle elements . (b) Left : SEM of the as-cast $\text{Ti}_{45}\text{Zr}_{25}\text{Nb}_6\text{Cu}_5\text{Be}_{17}\text{Sn}_2$, the dendrite-phase (light gray) distributes homogeneously in the glass-matrix (dark gray). Right : 2D mesh with triangle elements.	8
1.2	Example of shape function : (a) the shape function over entire domain. (b) the shape function inside an element.	10
1.3	Influence of mesh size : Finite element method computed displacement fields when wave passing through the model. Left panel : from top to bottom : 4 levels of element size are shown from coarse to fine. Right panel : snapshots of displacement fields. For the matrix, the Young's modulus is 92.25 GPa. For the inclusion, the Young's modulus is 46.125 GPa.	12
1.4	Illustration of time discretization : Δt (dt) is a time step and the indices n and $n + 1$ are successive time steps. N_{dt} is total number of time steps.	13
1.5	(a) Illustration of boundary conditions for a mechanical problem. (b) semi-infinite solid can be represented by only modeling the rectangle with Periodic Boundary Conditions (PBC) and Perfect Matched Layers (PML) as drawn (Ω represents simulation domain, $\partial\Omega$ indicates boundary conditions).	15
1.6	Hooke's model	19
1.7	Kelvin-Voigt model	19
1.8	Maxwell model	20
1.9	Generalized Maxwell model	21
1.10	Fundamental deformation patterns generated by Longitudinal (P), Shear (S), Rayleigh and Love (SH) waves [MIC 15].	23
1.11	Different interfaces in a heterogeneous medium	25
2.1	Transmission Electron Microscope image of a Zr-Cu-Al-Ti-Ni metallic glass with nano- crystalline inclusions, taken from [TLI 17]	29

2.2	2D simulation model of a solid with circular inclusions : this semi-infinite solid can be represented by only modeling only the part inside the red rectangle with Periodic Boundary Conditions (PBC) and Perfect Matched Layers (PML) as drawn; Grey disks represent the inclusions.(Ω represents simulation domain, $\partial\Omega$ indicates boundary conditions)	29
2.3	Schematic illustration of the central part of the sample for $L=60 \text{ \AA}$ and $\Phi = 2R = 20 \text{ \AA}$: in yellow represents the matrix material, in red the inclusions. Periodic reproduction of this sample along the vertical direction is assured by periodic boundary conditions.	30
2.4	Wave packet imposed as the displacement of the left side of the sample, for two different frequencies : 2 THz, 5 THz	31
2.5	From top to bottom : (a) The VDOS for $R = 25 \text{ \AA}$ and $\frac{E_i}{E_m} = 0.2, 0.4, 1.2, 10.0$ at discrete frequencies ν with width $\Delta\nu = 1 \text{ THz}$. Inset : VDOS vs ν for $\frac{E_i}{E_m} = 0.2$ and $R = 25 \text{ \AA}$. The red line corresponds to $\Delta\nu = 1 \text{ THz}$, while the shaded region to a $\Delta\nu$ varying between 0.4 and 1 THz (b) VDOS (blue) and partial DOS of inclusions (red) for $R = 25 \text{ \AA}$ and $\frac{E_i}{E_m} = 0.2$ (c) Fraction of VDOS supported by the matrix for $R = 25 \text{ \AA}$ and different values of $\frac{E_i}{E_m}$, at discrete frequencies ν with $\Delta\nu = 1 \text{ THz}$ (Triangle, square, diamond and pentagram symbol are used to indicate $\frac{E_i}{E_m} = 0.2, 0.4, 1.2$ and 10.0 respectively).	35
2.6	(a) Visualization of the normal modes obtained in the system with $\frac{E_i}{E_m} = 0.2$ and $R = 25 \text{ \AA}$. The frequencies of the characteristic normal modes (from top to bottom) are : $\nu = 0.325195 \text{ THz}$ ($\omega = 2\pi\nu = 2.04 \text{ THz}$); $\nu = 0.790191 \text{ THz}$ ($\omega = 4.96 \text{ THz}$); $\nu = 2.000000 \text{ THz}$ ($\omega = 12.57 \text{ THz}$); $\nu = 3.999998 \text{ THz}$ ($\omega = 25.13 \text{ THz}$); $\nu = 6.00019 \text{ THz}$ ($\omega = 37.70 \text{ THz}$); $\nu = 14.22239 \text{ THz}$ ($\omega = 89.36 \text{ THz}$). (b) Visualization of one normal mode obtained in the system with $\frac{E_i}{E_m} = 10$ and $R = 25 \text{ \AA}$. The frequency of the mode is : $\nu = 2.00281$ ($\omega = 12.58 \text{ THz}$).	36
2.7	The envelope of kinetic energy for different rigidity contrasts for $\omega = 5 \text{ THz}$, $R = 25 \text{ \AA}$ is reported as a red line, while the instantaneous distribution of kinetic energy is given at $t=7.9463 \text{ ps}$ (green dotted line) and at $t=12.7174 \text{ ps}$ (blue line). Gray areas delimited by dotted lines indicate the positions of the circular inclusions.	38
2.8	Snapshots of 5 cases at the same time ($t = 1.27171 \times 10^{-11} \text{ s}$) with $\omega = 5 \text{ THz}$ and $R = 25 \text{ \AA}$ (dashed circles indicate the positions of the inclusions) (a) $E_i/E_m = 0.2$ (b) $E_i/E_m = 0.4$ (c) $E_i/E_m = 0.6$ (d) $E_i/E_m = 1.0$ (e) $E_i/E_m = 2.0$	39
2.9	(a) Time dependence of the wave packet center position for different rigidity contrasts. We report as well the expected behaviors for propagative regime $\langle x \rangle(t) \propto Vt$ (green line), diffusive regime $\langle x \rangle(t) \propto (2Dt)^{\frac{1}{2}}$ (yellow line) and localized regime $\langle x \rangle(t) \propto cst$ (red line). (b) Standard deviation versus time calculated by Eq.2.13.	41

2.10	Visualization of the different dynamical regimes of the Wave Packets (propagative, diffusive, localized), as a function of the radius R of the inclusions and of the relative rigidity E_i/E_m for frequencies ω ranging from 2 to 7 THz.	42
2.11	Diffusivity obtained from Eq. (2.16), for different values of the rigidity contrast E_i/E_m	43
2.12	Penetration length $l_p(\frac{E_i}{E_m}, R)$, with $\frac{E_i}{E_m}$ the stiffness ratio and R the radius of inclusion for the frequency of wave packets $\omega=5\text{THz}$.(Top : 3D Bottom : 2D)	46
2.13	(a) Penetration length $l_p(\omega)$ for $\frac{E_i}{E_m} = 0.2, 0.4$ and 10.0 , with $R = 25\text{\AA}$. Inset : mean free paths Λ vs ω for $\frac{E_i}{E_m} = 1.2$ and $R = 25\text{\AA}$. (b) Frequency, which corresponds to the minimum l_p for each $\frac{E_i}{E_m}$ for $R = 25$. (c) Color representation of the penetration length in the parametric space $(E_i/E_m, \omega)$ for $R = 25$ (d) Idem in a 3D plot.	47
3.1	Cross sectional SEM images of the as-cast $\text{Ti}_{45}\text{Zr}_{25}\text{Nb}_6\text{Cu}_5\text{Be}_{17}\text{Sn}_2$, the dendrite-phase (light gray) distributes homogeneously in the glass-matrix (dark gray).	53
3.2	Flowchart from SEM to the finite element model : (1) Region of interest extracted from SEM image ; (2) Pixel-level labeling using Matlab toolbox Image Labeler ; (3) Binary image ; (4) Contour detection ; (5) Independent zone detection ; (6) Mesh generation.	55
3.3	2D simulation model of a solid with dendritic inclusion : this semi-infinite solid can be represented by only modeling only the part inside the red rectangle with Periodic Boundary Conditions (PBC) and Perfect Matched Layers (PML) as drawn ; Black patterns represent the inclusions. (Ω represents simulation domain, $\partial\Omega$ indicates boundary conditions)	57
3.4	Comparisons of envelopes between circular and dendritic inclusions with $\frac{E_i}{E_m} = 0.2$ for different normalized frequencies ω/ω_0 (where $\omega_0 = 2\pi v_L/L$) : total simulation time steps $8400dt$	58
3.5	Fig.3.5 on a log-log scale. Black line indicates a $1/x$ decay.	59
3.6	Snapshots of 3 case at $4200 \times dt$ and $8400 \times dt$ with $\frac{E_i}{E_m} = 0.2$ for circular and dendritic inclusion : (a) $\omega/\omega_0 = 0.6$ (b) $\omega/\omega_0 = 1.2$ (c) $\omega/\omega_0 = 4.8$. (see Supplementary Materials for the corresponding videos).	60
3.7	Comparisons of the penetration length between the circular and dendritic shape with $E_i/E_m = 0.2$ and 10.0 for longitudinal waves	62
3.8	Comparisons of the diffusivity between the circular and dendritic shape with $E_i/E_m = 0.2$ and 10.0 for random longitudinal waves.	63
3.9	Stiffness of long fiber composites : (a) Matrix with cylinder fibers (b) Axial loading : Voigt model (c) Transverse loading : Reuss model. Subscript f and m indicate fiber and matrix respectively. σ_1 is the the load parallel to the fiber direction and σ_2 is the load perpendicular to the fiber direction. f is the volume fraction for the fiber and $1 - f$ the for the matrix.	64

3.10	Average position (left) and instantaneous speed (right) for dendritic inclusion with $E_i/E_m = 0.2$ and $\frac{\omega}{\omega_0} = 0.6$ for longitudinal waves. Yellow lines : unsmoothed data; Blue lines : Nearest neighbors smoother; Red lines : Bezier interpolation.	66
3.11	Instantaneous wave speed for dendritic and circular inclusion with $\frac{E_i}{E_m} = 0.2$ ($\langle x \rangle$ is smoothed by the Bezier interpolation). Red line indicates the dendritic inclusion and blue line indicates the circular inclusion. . . .	67
3.12	Model of a square matrix with an elliptic inclusion in the center.	71
3.13	(a) Mesh for a circular inclusion. (b) Mesh for an elliptic inclusion with $b/a = 0.25$	72
3.14	Average strain vs time $\bar{\epsilon}_{ij}^I(t)$ for different damping. The shadow region is ϵ_{ij}^n range, and the middle lines are average values $\bar{\epsilon}_{ij}^I$. In all three cases, the strains in equilibrium state are identical respectively with a negligible error (<1%). Left : $\alpha=1e-17$ and $\beta=1e-17$; Middle : $\alpha=1e-16$ and $\beta=1e-16$; Right : $\alpha=1e-16$ and $\beta=1e-15$	74
3.15	Strains field inside the inclusion : In stead of a uniform field, dispersion of the strains is attributed to the size effect for $L=60 \text{ \AA}$, $a= 20 \text{ \AA}$, $b/a = 0.25$. Along the x direction, a dispersion of the shear strains inside the inclusion up to 10% is found in equilibrium state (lower left plot).	76
3.16	Contour of displacement inside and outside of the inclusion. Semi-major axis $a = 5 \text{ \AA}$, $b/a=1$ and $L = 240 \text{ \AA}$	79
3.17	(a) Comparison between the numerical and the analytic results. Red circles are the numerical results and colored surface is the analytic results from Ref.[JIN 17]. $L=240 \text{ \AA}$, $a=5 \text{ \AA}$ and $b/a = 1$. (b) Only the points outside of the inclusion (black points) are used to reproduce analytic results outside of the inclusion. As such, the details on the interface (green line) cannot be given.	80
3.18	Effect of model length on the displacement field : $\ u\ (x,y)$ for $L=120$ (yellow circles), 180 (green circles) or 240 \AA (red circles). $a=5 \text{ \AA}$ and $b/a = 0.9$	80
3.19	(a) Coordinated system : origin is in lower left corner of $L=240 \text{ \AA}$. $X = \sqrt{2}x$ with $x \in [0, L]$. (b) Displacement amplitude along the diagonal line $\ u\ (X)$ for $L=120, 180, 240$ or 300 \AA . $a=5 \text{ \AA}$ and $b/a = 0.9$	81
3.20	Before the wave packet touches the inclusion, comparison of displacement fields for three different inclusions with $R = 10 \text{ \AA}$ and $\omega = 5 \text{ THz}$: Top : an Eshelby's inclusion with an eigenstrain = ϵ^* (Eq.3.7). Middle : an Eshelby's inclusion with an eigenstrain = $0.1 \times \epsilon^*$. Bottom : an elastic inclusion with $E_i/E_m = 0.2$	82
3.21	Idem. Near the inclusion.	82

3.22	2D porous material : SEM images of 2D porous phononic crystals (PnC) (A) Sin_x PnC with surface roughness $\eta_{wall} = 2.25$ nm, with position distribution $\eta_{eff,p} = 11.6$ nm and with size distribution $\eta_{eff,s} = 10.3$ nm. Left : top view; Right : Side view of the profile of the holes. (B) Ordered and disordered in position PnC used to tune heat conduction at low temperature in the work of J. Maire[MAI 17].	85
3.23	Reflection from a rough surface and three reflection regimes : diffuse, specular and intermediate regime [ZIM 62].	88
3.24	Illustration of effective roughness ascribed to the two types of disorder. The grey region is the material and the white regions are the holes. Left : center aligned circular with random radii; Right : center non-aligned circular with identical radii.	89
3.25	(a) Example of specular parameter as a function of wavelength λ for different values of the roughness η . (b)Phase diagram of the coherence regime as a function of the disorder parameter and of the wavelength. Coherent and non-coherent regime is identified. White circles are the data points for the FE simulations.	92
3.26	Envelope of the kinetic energy $P(x)$ for the ordered and the disordered PnC with wavelength $\lambda = 54, 84, 104, 163$ and 402 nm. Exponential decay is illustrated as the black lines. Crossover from the first exponential decay regime to the second exponential regime is clearly shown for the periodic cases and the envelope in fact turns to a $1/x$ decay.	94
3.27	Some results based on the heterogeneous shear modulus in the literature (a)From MD simulation : Resonance frequencies $\Omega_{L,T}(k)$ (straight lines) and Brillouin line widths $\Gamma_{L,T}(k)$, multiplied with π . The dashed line indicates the BP position, which is near the transverse Ioffe-Regel crossing. (Insert : Reduced density of states $g(\omega)/\omega^2$ as obtained from the velocity autocorrelation function) [MAR 13] (b) From the CPA : Reduced density of states $g(\omega)/g_D(\omega)$ as a function of reduced frequency ω/ω_D for different values of the parameter G_{min}/G_0 . (c) Comparison of results of MD simulations (symbols) with the predictions of heterogeneous-elasticity theory in SCBA. Real (imaginary) part of G is shown in upper (lower) panel as a function of frequency. The SCBA parameters are $\gamma - \gamma_c = 0.08$ and $K/G_0 = 3.166$ [MAR 13, SCH 15b].	103
3.28	Illustration of the disordered elasticity model with height L and correlation length ξ . The gray level indicates the random elasticity. Wave-packets are imposed at the left side boundary. PBCs are applied on the top and bottom boundaries. PMLs are applied on the right side boundary.	103
3.29	Demonstration of the average envelope of the kinetic energy. The black dots are the envelopes from nine different configurations with random elasticity and the red line is the average.	106

3.30	Average envelopes of the kinetic energy as a function a position x and frequency ω . $L = 90$ nm for $\omega = 0.3$ THz and $L = 60$ nm for other frequencies. (The envelopes are vertically shifted with respect to each other to be visually clear)	107
3.31	Comparison of the mean-free path (nm) as a function of frequency ω (THz) from our FE simulations (yellow), MD simulations (blue) and the prediction of the SCBA theory (gray). Data from Refs. [SCH 15b, MAR 13].	107
4.1	Illustration of the viscoelastic models : the Kelvin-Voigt model for the hydrostatic part and the standard linear model (one type of the generalized Maxwell model with N=1) for the deviatoric part	116
4.2	Identification of parameters τ_a and τ_b by fitting $Q_{L,T}^{-1}$ against Γ/ω (data from Beltukov et al, 2016) [BEL 16] : (a) Evolution of $Q_T^{-1}(\omega)$ for transverse modes with $\tau_a = 9.3e - 15$. (b) Evolution of $Q_L^{-1}(\omega)$ for longitudinal modes with $\tau_a = 9.3e - 15$ s and $\tau_b = 3.3e - 15$ s.	120
4.3	2D simulation model of solid : A semi-infinite solid can be represented by only modeling a single layer (green zone) with Periodic Boundary Conditions (PBCs) on the top and bottom and Perfectly Matched Layers (PMLs) on the right edge.	121
4.4	Envelope of the normalized kinetic energy $P_\omega(x)/P_\omega(0)$ for different frequencies in a semi-log graph. Top : longitudinal polarization; bottom : transverse polarization. Numbers near curves represent angular frequencies ω in THz.	122
4.5	Result obtained from finite element (FE) simulation compared to atomistic analysis for longitudinal waves (blue or red) and transverse waves (green or black). For FE simulation, solid lines with open symbols (blue or green) show the mean free path Λ_{FE} obtained by the exponential fit of the envelope. For DM simulation (Y. Beltukov [BEL 18]), points show the results from the DHO fit of the DSF, Λ_{DSF} ; Solid lines show the mean free path Λ_{BL} ; Dashed lines show the penetraion length l_{pen} . (The Ioffe-Regel frequencies for longitudinal and transverse waves are shown by red and black arrow respectively.)	124
4.6	Illustration of the viscoelastic model : two Maxwell-like models are in parallel.	125

4.7	(a) Extracted from Ref. [AYR 11] : acoustic linewidth $\Gamma/2\pi$ of the sample in Ref. [AYR 11] (named "this work" in the figure) at 300K compared to visible BLS result (Ref. [MAS 97]) and UV-BLS ones (Refs. [MAS 04] and [BEN 05]). The point above the Ioffe-Regel frequency is from Ref. [MAS 97]. (b) Extracted from [BAL 10] : sound attenuation, $\Gamma/2\pi$, of v -SiO ₂ as a function of frequency in log-log scale. The points at high frequency (red circles) are from the work in Ref. [BAL 10] at T=1620K. Lower frequencies data are from : picosecond optical technique (POT)[DEV 08], BUVS[MAS 06, BEN 05], BLS [VAC 80], and a tunneling junction (TJ) technique [DIE 79].	126
4.8	Comparison between Γ/ω and Q^{-1} with $\tau_1 = 3e39s^{-3}$, $\tau_2 = 2.7e13s^{-1}$ and $\alpha = 1.4$ (red line) or $\alpha = 0.05$ (green line) . The red (green) line is the Q^{-1} of the present viscoelastic model. Experimental data are from : IXS [BAL 10], POT [AYR 11], BUVS [MAS 06, BEN 05], BLS [VAC 80] and TJ [DIE 79]. The blue dashed lines are two power law fits representing $\Gamma/\omega \propto \omega$ and $\Gamma/\omega \propto \omega^3$, respectively.	128
4.9	Evolution of Q^{-1} as a function of τ_2 , τ_1 and α , respectively. The red arrow indicates the growth direction of the parameter.	131
A.1	Snapshots of displacement field at the same time with $\omega = 5$ THz, $\frac{E_i}{E_m} = 1.2$ and $R = 25 \text{ \AA}$ (a) 1 alignment with PBCs on the top and bottom (b) 10 parallel alignments of inclusions on the top and bottom	138
A.2	Snapshots of displacement field at the same time with $\omega = 5$ THz, $\frac{E_i}{E_m} = 0.2$ and $R = 25 \text{ \AA}$ (a) 1 alignment on the top and bottom (b) 10 parallel alignments of inclusions on the top and bottom	139
A.3	Snapshots of displacement field at the same time with $\omega = 9$ THz, $\frac{E_i}{E_m} = 0.2$ and $R = 25 \text{ \AA}$ (a) 1 alignment on the top and bottom (b) 10 parallel alignments of inclusions on the top and bottom	140

General introduction

In September 2020, Apple officially released its new iPad Air equipped with the world first mass-produced 5 nm chip manufactured by TSMC. The limits of chip manufacturing are constantly being explored and the next milestone will be 3 nm. Despite this, technological developments of semiconductor device fabrication have known an important slowing down, mainly due to the need of dealing with the heat problem [WAL 16] : for example, the extreme miniaturization of electronic devices inevitably leads to a local overheating and dissipation which is detrimental to the device performance and lifetime. As such, controlling, converting and recycling the heat is the core of the current research in thermal science as well as microtechnology [PRA 09, TER 09, MER 12, ZEN 14, FRA 14, MOO 16, ANU 16, YAN 17, VER 18].

In light of the vigorous push of the energy harvesting technology based on thermoelectricity, the ubiquitous heat found an efficient way of recycling it and converting it into a usable source of energy. Thermoelectric efficiency depends on the capability of materials of keeping a temperature gradient constant, and thus on its good thermal insulation. To reduce the thermal conductivity, it is traditionally achieved by adding impurities, nanoparticles, void, etc., which enhance the scattering of the energy carrying quanta in materials, electrons and phonons. As the acoustic phonons are the main heat carriers in insulators and semi-conductors, a lot of research has focused on the reduction of phonon contribution to the thermal conductivity using nanoscale structuring of materials. On the other hand, with the help of periodic phononic crystal structures, novel coherent effects arise due to, for example, Bragg's interference. Strategies come up by engineering the phonon dispersion relation, leading to the aperture of forbidden gaps in the phonon dispersion [LIU 00, KHE 06].

In fact, acoustic metamaterials, including phononic crystals, have been initially investigated for applications in acoustics, where sonic or ultrasonic waves in sub-MHz frequency range play a major role. They can be shaped to realize acoustic guides, filters, lenses, with a macrostructure in millimeter lengthscale [LIU 00, KHE 06, ZHA 09, CUM 16]. More recently, they have been introduced also in thermal science with the similar concept for manipulating phonons but with nanometric and sub-nanometric wavelengths in THz frequencies range, which are the dominant heat carriers at room temperature, for realizing tunable multi-functional thermal metamaterials [LEE 16, PAR 17], thermal cloaks and camouflage [SKL 18], etc. In both applications, it is matter of guiding, filtering, hindering, the propagation of acoustic waves (phonons), responsible for the sound propagation when their wavelength is macroscopic, and for thermal transport at

room temperature when it is nanometric.

Amorphous materials such as glasses are natural poor conductors of heat compared to crystalline materials. Lattice contribution to the thermal conductivity in crystalline solids has been widely studied in the frame of the phonon gas model. However, in amorphous solids the lack of a periodic atomic structure leads to very different scenarios for vibrational energy transport. Depending on the transport behavior, Allen and Feldman classified the harmonic normal modes of vibration in amorphous solids as propagons, diffusons and locons [ALL 99, FEL 99]. Propagons are phonon-like plane waves, typically having long wavelength, that can travel at the sound velocity over long distance before scattering from disorder. This distance of ballistic propagation is the mean-free path. Diffusons are modes that scatter over a distance less than their wavelength and moves diffusively. Locons are localized modes and cannot transport heat [BEL 18]. Therefore, specific dynamics of phonons will directly affect thermal transport, with two different contributions : a propagative one, which depends on phonon mean-free path, heat capacity, velocity and vibrational density of states [KIT 04], and a diffusive one, involving the phonon diffusivity rather than the mean-free path and velocity [LAR 14, ALL 90, ALL 99]. Due to the wave-particle duality, phonons are nothing but acoustic vibrations with well defined frequencies. In crystals, normal modes are phonons with infinite coherence time, but in amorphous solids like glasses, the normal modes are not plane waves [TAN 02]. As such, using a wavepacket with finite coherence time allows a description of the vibrations preventing the permanent mixing with other plane waves. Wavepackets are thus a good representation for phononic excitations in amorphous materials, and - with a proper choice of their coherence time - in crystals [SCH 02].

Besides the thermal transport property, the mechanical properties of amorphous materials also exhibit their unique charm. Many amorphous materials, such as metallic glasses, polymers and oxide glasses, show a significant degree of universality. First of all, it is now widely accepted that these materials possess heterogeneous elasticity at the nanoscale [BOV 05, TSA 09, MON 09b, CAP 09] and this has been used to explain numerous vibrational anomalies in atomistically disordered materials, like glasses, in the THz frequency range [TAN 10, MAR 13, SCH 15b]. Secondly, they share a common elementary mechanism of plastic deformation that consists in local irreversible rearrangements involving few tens of particles in response to a homogeneous structure loading. The elastic response of the surrounding medium to such a local shear transformation zone (STZ) exhibits quadrupolar symmetric displacement field, which is well described by the Eshelby inclusion with a shear eigenstrain [BUL 94, BAR 02, MAL 04, ALB 16, NIC 18], allowing mesoscopic models as the elementary bricks of plasticity [BUL 94, MAL 04, ALB 16]. In addition, in-situ introducing a second crystalline phase into the bulk metallic glasses has been reported to improve the global ductility and plasticity of the original brittle materials [ALB 13]. In-situ formed dendrite-phase not only displays a reinforced ductility and a more homogeneous plastic response [HAY 00, GEN 20], but also has potentially good sound attenuation performance due to the phonon-interface scattering, however, there is still a lack of research on this latter.

The title of this thesis clearly describes our main work using three keywords : high fre-

quency, thermo-mechanics and heterogeneous materials with interfaces. *High frequency* indicates that we are interested in the acoustic waves at high frequencies, more specifically, in the THz frequency ranges which are, as introduced, the main heat carriers at room temperatures in semiconductors and insulators. Some *heterogeneous materials with interfaces* are numerically prepared based on which simulations will be investigated, including elastic homogeneous media with periodic elastic inclusions, dendritic inclusions, Eshelby inclusions and disordered holes as well as heterogeneous media with random elasticity. Considering the high frequency of the phonons, all these heterogeneities in the structures are at the nanoscale. Finally, based on the theory of Allen and Feldman[FEL 99, ALL 93, ALL 90], *thermo-mechanics* is thus treated as to get a better understanding of the mechanical response and transport properties of the high-frequency acoustic waves inside the heterogeneous nanostructures above, the strong scattering of acoustic waves giving rise to diffusive transport similar to heat.

To study the acoustic wave propagation and attenuation in such complex structured materials, it is necessary to model phonon propagation on large scale systems, more apt at representing real materials, where the effect of heterogeneities and interfaces can be properly investigated. Such large systems are out of reach for atomistic simulations and can be realistically modeled only through finite-element simulations, to catch the effect of the interfaces and elastic heterogeneities on acoustic properties and thermal transport. Its computing time depends on spatial discretization [GER 14, BEL 13, BON 14, ACH 12], making thus affordable longer simulations on larger systems. More importantly, rich literature and relative research on the finite element method (FEM) help us implement easily various types of loading and boundary conditions with specific functions, such as the periodic boundary conditions and absorbing boundary conditions. In addition, the use of the wave packets makes the spectrum of the external excitations smooth enough and centered on well defined frequencies which thus avoid the numerical instability problem in calculations caused by the extreme high-frequency excitations such as shocks. Last but not least, to correctly describe for example highly dissipative glassy materials, the macroscopic elastic model is unable to reproduce the frequency-dependent acoustic attenuation which has an atomistic origin. As such, continuum viscoelastic constitutive laws will be developed to encode their specific frequency dependent phononic attenuation.

In the first chapter, the theoretical basis of the finite element method is presented as well as the simple mechanical constitutive models that will be used, and a reminder about the definitions of wave speeds. Different types of interfaces are available to construct various heterogeneous media that will be presented there.

In the second chapter, we present a FE numerical simulation of the transient propagation of an acoustic Wave-Packet in a 2D nanophononic material (with periodic elastic inclusions), which allows to identify the effect of the elastic inclusions on the acoustic attenuation length and thus on the transport regime for the vibrational energy. Three parameters are studied : the rigidity contrast between the inclusion and the matrix, the size of the inclusions and the frequency of the incident wave-packet, the constant distance between inclusions being used as reference length.

In the third chapter, mechanical response and acoustic attenuation for four types of

interfaces will be investigated. Starting with the dendritic inclusion, we will consider the same problem as in the last chapter but only changing the shape of the inclusions. Then, the Eshelby's inclusion will be embedded, which can be used to represent local plasticity events in amorphous materials. Next, spatial disorder will be introduced in our models including disordered porous and finally random elastic media.

In the fourth chapter, we propose to develop a model to homogenize the effective attenuation triggered by multiple atomistic mechanisms, and characterized by a given non-trivial frequency dependence. We will show that our models are able to bridge atomic and macroscopic scales in amorphous materials and reproduce well the phonon attenuation with a ω^2 or $\omega^2 - \omega^4 - \omega^2$ dependency.

Finally, we draw general conclusions and some prospects.

Chapter 1

Numerical & theoretical methods

How to use the finite element method to perform transient analysis of wave-packet propagation in the heterogeneous medium? In this first chapter, the theoretical basis of the finite element method is presented as well as the simple mechanical constitutive models that will be used, and a reminder about the definitions of wave speeds. Different types of interfaces are available to construct various heterogeneous media that will be presented here.

Contents

1	Finite Element code	7
1.1	General introduction to finite element method	7
1.2	Mesh : spatial discretization	11
1.3	Dynamic problem : temporal discretization	13
1.4	Boundary conditions	15
2	Constitutive models	17
2.1	Elasticity	18
2.2	Linear visco-elasticity	19
2.3	Generalized visco-elasticity	21
3	Wave propagation in a homogeneous elastic medium	21
3.1	Formulation	21
3.2	Wave speed in a homogeneous elastic medium	22
4	Heterogeneous materials with interfaces	24
4.1	Elastic inclusion	24
4.2	Eshelby's inclusion	25
4.3	Random elasticity	26

1 Finite Element code

1.1 General introduction to finite element method

In this thesis, the *finite element method* (FEM) is the most important numerical tool used to perform the study of mechanical wave propagation in a solid medium. Development of the finite element can be traced back to 1940s. With both the improvement of theory and the leaps of calculation ability, FEM has become a reliably tool in scientific research and engineering application [ZIE 00a, HUG 12, MIC 15, BEL 13]. In our work, the numerical simulations are preformed using the finite element code Cast3m which is a numerical simulation software dedicated to structural mechanics, and developed by the French Alternative Energies and Atomic Energy Commission (CEA). It is a free code based on the FORTRAN language, and the user language is GIBIANE. Every year, a stable new version will be released and can be downloaded from [Cast3m website](#).

The finite element method consists of subdividing the structure into a finite number of elements of simple geometry and looking for approximate resolution of equations on an appropriate basis of functions. The geometrical elements can be the following :

- One dimension : line segment
- Two dimensions : triangle or quadrangle
- Three dimensions : tetrahedron or hexahedron

As shown in Fig.1.1, we used 2D triangle and quadrangle elements to generate numerical meshes to approximate the geometries given for example by the Transmission Electron Microscope (TEM) or Scanning Electron Microscope (SEM) images. These meshes can be then used in the computation. Inside each element, the interpolation functions of the internal displacement field are chosen as to be simple but representative of the element's structural behavior as will be detailed later.

Multiphysics problems described by partial differential equations (PDEs), including heat transfer, mass transport, fluid flow and electromagnetic potential, can be solved by FEM in *weak* form. Compared to the initial PDE (*strong* form) which seeks an exact solution at each point over a domain, *weak form* relaxes solution requirements and expects an approximation of the solution.

In the following example, the case of 1D wave equation will be shown to quickly present the derivation from the governing equation (*strong* form) to *weak* form as well as the application of the finite element method on the weak form (known as *spatial discretization*).

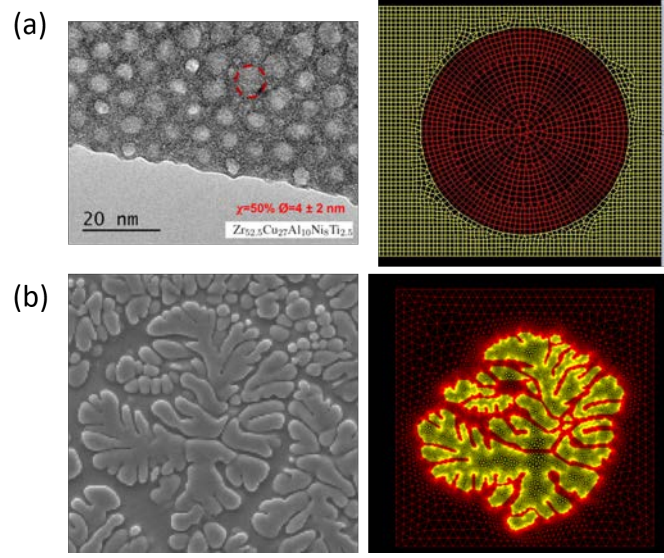


FIGURE 1.1: Finite element mesh : discrete representation of the domain in the computations. (a) Left : TEM image of a Zr-Cu-Al-Ti-Ni metallic glass with nano-crystalline inclusions [TLI 17] Right : 2D mesh with triangle and quadrangle elements . (b) Left : SEM of the as-cast $\text{Ti}_{45}\text{Zr}_{25}\text{Nb}_6\text{Cu}_5\text{Be}_{17}\text{Sn}_2$, the dendrite-phase (light gray) distributes homogeneously in the glass-matrix (dark gray). Right : 2D mesh with triangle elements.

1.1.1 Strong form

The governing equation of 1D wave equation in an elastic bar $x \in [0, L]$ with Young's modulus E and mass density ρ reads :

$$\begin{aligned} \text{1-D wave equation :} \quad & \frac{\partial^2 u(x, t)}{\partial t^2} = c^2 \frac{\partial^2 u(x, t)}{\partial x^2} \\ \text{Wave speed :} \quad & c = \frac{E}{\rho} \end{aligned}$$

where u is the unknown displacement.

1.1.2 Weak form

Now, multiplying the governing differential equation with an arbitrary scalar function or a so called *test function* $v(x)$ and then integrating over the entire domain, the corresponding weak form for 1D wave equation reads :

$$\int_0^L \rho \frac{\partial^2 u(x, t)}{\partial t^2} v(x) dx = \int_0^L E \frac{\partial^2 u(x, t)}{\partial x^2} v(x) dx, \quad \forall v \in u \quad (1.1)$$

where the functional space $u = \{v \text{ with good properties of regularity}\}$ [ZIE 00b] . Next, integration by parts gives

$$\int_0^L \rho \frac{\partial^2 u}{\partial t^2} v(x) dx = E \left[\frac{\partial u(L, t)}{\partial x} v(x) - \frac{\partial u(0, t)}{\partial x} v(x) - \int_0^L \frac{\partial u}{\partial x} \frac{\partial v}{\partial x} dx \right] \quad (1.2)$$

In the right side of equation, one can specify Neumann type boundary condition, (*i.e.*, derivative of the solution u) at the borders. Here, we suppose that free boundary condition ($\frac{\partial f}{\partial n} = 0$, *i.e.*, $\frac{\partial u}{\partial x} = 0$) is imposed at $x = 0$ and $x = L$ and the weak form for the wave equation is thus :

$$\int_0^L \rho \frac{\partial^2 u}{\partial t^2} v + E \frac{\partial u}{\partial x} \frac{\partial v}{\partial x} dx = 0 \quad (1.3)$$

This is the so called *weak formulation* of the wave equation. It is noticed that the core idea of weak formulation is to transform a derivative equation to an integral equation, as such, the assumption is that any possible displacement field must have first derivatives which may be integrated. Thus, the derivatives $\frac{\partial u}{\partial x}$ and $\frac{\partial v}{\partial x}$ are not necessarily continuous, however, u and v must be continuous, meaning that only C^0 continuity and L^2 is required. Instead in its strong form, C^2 continuity is required for the displacement. In addition, instead of satisfying the wave equation at any point, the weak form only requires an equality over the integral domain.

1.1.3 Finite element method

For most boundary value problems the geometry and loading are too complex to find a displacement that satisfies the governing PDE and all the boundary conditions. With the FEM, the domain V is divided into subdomains V_h and make sure continuity exists over subdomain boundaries. With this approach, the FEM is expected to find a set of $u_h \in V_h$ to approximates the exact solution. Displacement assumption is made for each one single element :

$$u(x, t) = \sum_{i=1}^n u_i(t) N_i(x) \quad (1.4)$$

$$v(x) = \sum_{i=1}^n v_i N_i(x) \quad (1.5)$$

where $N_i(x)$ is the *element shape function* which is a piecewise differentiable linear function whose value is 1 at the node i and 0 at the other nodes, and u_i is nodal value of u . An example of a shape function is shown in Fig.1.2.

Each point $x = 0, h, 2h, \dots$ is called *node* and the interval $x \in [x_i, x_{i+1}]$ is called *finite element*. Here, each element has two nodes and the internal kinematic relation is imposed by the shape function as shown in Fig.1.2(b) for example where :

$$N_1(x) = \frac{x_2 - x}{h}$$

$$N_2(x) = \frac{x - x_1}{h}$$

Therefore, the shape function Eq.1.4 for a 1-D linear element reads :

$$u(x, t) = \sum_{i=1}^2 u_i(t) N_i(x) = \frac{x_2 - x}{h} u_1(t) + \frac{x - x_1}{h} u_2(t) \quad (1.6)$$

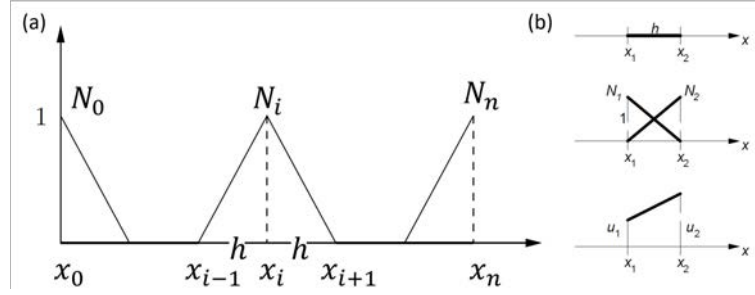


FIGURE 1.2: Example of shape function : (a) the shape function over entire domain. (b) the shape function inside an element.

and the derivative reads :

$$\frac{\partial u(x,t)}{\partial x} = \sum_{i=1}^2 u_i(t) \frac{dN_i(x)}{dx} = -\frac{1}{h}u_1(t) + \frac{1}{h}u_2(t) \quad (1.7)$$

Numerous types of elements have been developed depending on the space dimension of the problem (1-D, 2-D or 3-D), the geometry of the structure and the loading (beam, shell, etc) as well as on the specific materials properties (*e.g.* anisotropy in carbon fiber composites). The shape functions are well-defined for the standard elements, and in practices, one can use them directly without having to derive them from the beginning.

Let's come back to the weak form of the wave equation. Substituting the Eqs.1.4 and 1.5 , Eq.1.3 yields

$$\int_0^L \rho \sum_{i=1}^n N_i \ddot{u}_i \sum_{j=1}^n N_j v_j + E \sum_{i=1}^n \frac{dN_i}{dx} u_i \sum_{j=1}^n \frac{dN_j}{dx} v_j dx = 0 \quad (1.8)$$

$$\text{that is } \sum_{j=1}^n \int_0^L (\rho \sum_{i=1}^n N_i \ddot{u}_i N_j + E \sum_{i=1}^n \frac{dN_i}{dx} u_i \frac{dN_j}{dx}) dx \cdot v_j = 0 \quad (1.9)$$

which must be valid for an arbitrary function v , thus for every j :

$$\sum_{i=1}^n \int_0^L (\rho N_i N_j dx \cdot \ddot{u}_i + \int_0^L E \frac{dN_i}{dx} \frac{dN_j}{dx} dx \cdot u_i) = 0 \quad (1.10)$$

This is equal to write

$$\sum_{i=1}^n [M_{ji} \ddot{u}_i(t) + K_{ji} u_i(t)] = 0 \text{ or in matrix form } \mathbb{M} \ddot{\mathbf{U}}(t) + \mathbb{K} \mathbf{U}(t) = 0 \quad (1.11)$$

where \mathbf{U} is the displacement vector, \mathbb{M} is the mass matrix whose components read

$$M_{ij} = M_{ji} = \int_0^L \rho N_i N_j dx \quad (1.12)$$

and \mathbb{K} is the stiffness matrix, which is a sparse diagonal matrix, whose components read

$$K_{ij} = K_{ji} = \int_0^L E \frac{dN_i}{dx} \frac{dN_j}{dx} dx \quad (1.13)$$

It can be noticed that the mass information is encoded in \mathbb{M} and the rigidity is encoded in \mathbb{K} . Solving the original PDE is equivalent to perform matrix operations. In addition, as said the entire domain is subdivided into a finite number of elements, as such the integral over $x \in [0, L]$ equals to the sum of the integrals over each element :

$$\int_0^L dx = \sum_{elem} \int_{x_i}^{x_{i+1}} dx \text{ in 1D} \quad (1.14)$$

Furthermore, the integral over each element is numerically solved by *Gaussian quadrature rules* in which the values at the Gauss points $x(\xi_i)$ are determined, of course, by the shape function and the nodal values, e.g., $u(x(\xi_i), t) = \sum_{j=1}^n N_j[x(\xi_i)] u_j(t)$.

This procedure can be generalized to 2D and 3D problems. Various boundary conditions as well as the first temporal derivative of the displacement vector can also be taken into account. To conclude, for a wave propagation problem, we can get the space semi-discrete form [MIC 15] :

$$\mathbb{M}\dot{\mathbf{U}}(t) + \mathbb{C}\dot{\mathbf{U}}(t) + \mathbb{K}\mathbf{U}(t) = \mathbf{F}(t) \quad (1.15)$$

where \mathbb{C} is an additional damping matrix and \mathbf{F} is the external force vector.

1.2 Mesh : spatial discretization

In the finite element method, the domain Ω is subdivided into a mesh, *i.e.*, a collection of geometrically simple elements. On each element, piecewise polynomial functions (shape function) are supposed which are usually of low degree. Hence, in order to get a better approximation of PDE solution, one can refine the subdivision or increase the order of the polynomial functions.

As shown in Fig.1.3, a set of simulations has been done based on different levels of element size from coarse to fine. The wave propagates in a homogeneous medium with a soft circular *inclusion* inside, it is clear that, in order to improve the simulation result, mesh refinement is a good choice. However, mesh refinement increases the computational cost by increasing the number of elements. Besides, for example, the 3rd mesh in Fig.1.3 gives a enough precision compared with the 4th one. Therefore, before starting the simulation, the mesh density needs to be carefully considered, especially when computing power is limited.

It is clear that the element size in element-based acoustic computations should be related to the wavelength. A common rule is that at least six linear elements should be used per wavelength [MAR 08]. Since the wavelength depends on the material as $\lambda = \frac{2\pi c}{\omega}$, where the $c \propto \sqrt{E/\rho}$ is wave speed, the mesh should be adapted depending on the rigidity and wave frequency. As such, a special attention should be payed in the case when the medium becomes soft (low E) or the frequency becomes high (high ω). For example, in the above case (Fig.1.3), a soft inclusion often needs a finer mesh than the rigid matrix.

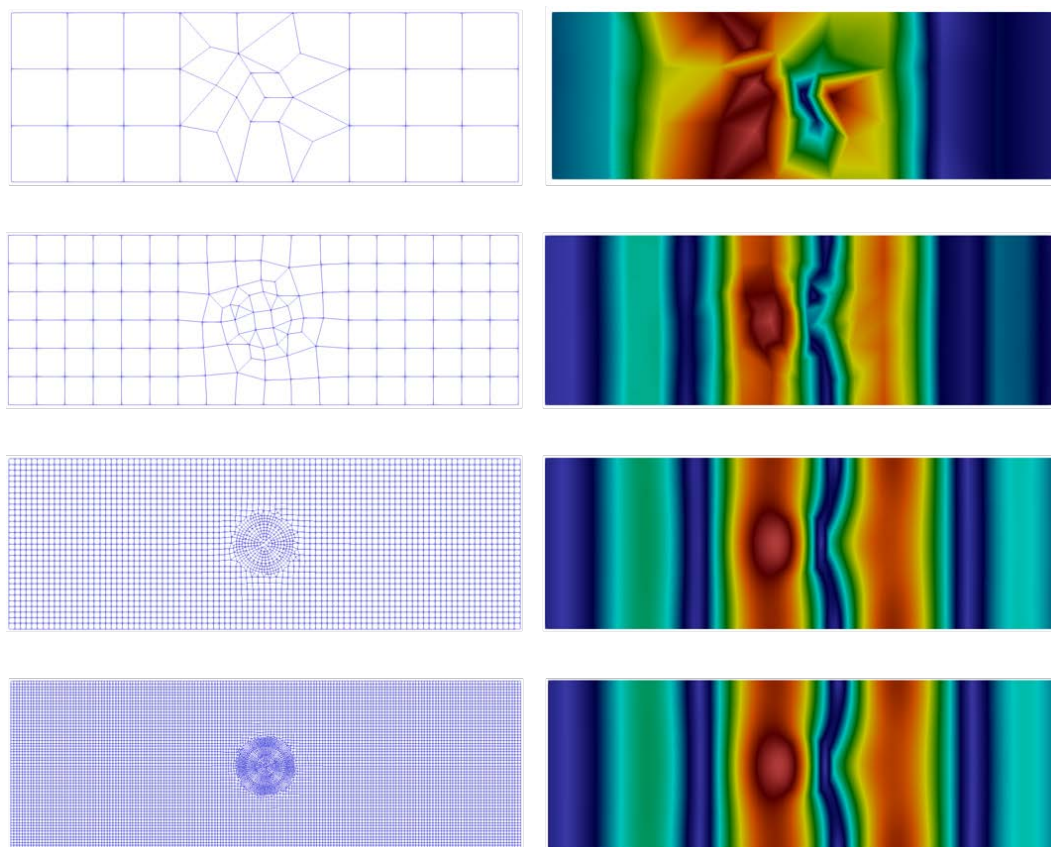


FIGURE 1.3: Influence of mesh size : Finite element method computed displacement fields when wave passing through the model. Left panel : from top to bottom : 4 levels of element size are shown from coarse to fine. Right panel : snapshots of displacement fields. For the matrix, the Young's modulus is 92.25 GPa. For the inclusion, the Young's modulus is 46.125 GPa.

1.3 Dynamic problem : temporal discretization

1.3.1 Time discretization

Eq.1.15 gives a semi-discrete form in space. For transient analysis, the governing equations must be discretized in both space and time. Temporal discretization involves the integration of every term in the differential equations over a time step Δt as shown in Fig.1.4. The choice of the time step will be explained later.

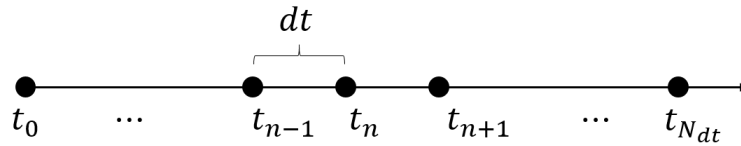


FIGURE 1.4: Illustration of time discretization : Δt (dt) is a time step and the indices n and $n + 1$ are successive time steps. N_{dt} is total number of time steps.

1.3.2 Time integration

Among all the FEM time integration schemes, Newmark scheme [NEW 59] is the most common solution for a dynamic structure. We have selected the symplectic central-difference algorithm from the Newmark scheme family, with the parameters $\gamma = \frac{1}{2}$ and $\beta = 0$. We start from the space-time discretized form (combined with the central-difference time integrator) :

$$\mathbb{K}U_n^p + \mathbb{C}\dot{U}_{n+\frac{1}{2}} + \mathbb{M}\ddot{U}_{n+1} = F_{n+1} \quad (1.16)$$

where \mathbb{M} is the lumped mass matrix and \mathbb{C} is a possible damping matrix either related to the domain (*e.g.*, viscous medium in Chap.4) or to the boundaries (*e.g.*, perfect matched layer in Sec.1.4). Tab.1.1 gives an algorithm to explicit the related central difference integration.

These chosen values of γ and β make sure that once a good time step is determined for a set of meshing values, our calculation will always be converge. Moreover, the choice of this Newark scheme ensures a good precision to the discrete balance equations (linear momentum, angular momentum and energy preservation)[STA 19]. We can thus chose automatically the initial time step for different inclusions sizes, and rigidity ratios (the ratio of Young's modulus between inclusions and amorphous matrix in this study), thus facilitating a systematic parametric study. Hughes, Geradin, and Rixen [GER 14] have done a detailed stability analysis of the Newmark scheme family. It shows that in order to ensure the convergence, the time step Δt :

$$\Delta t < \Delta t_{cr} = \frac{\Delta l}{2c} \quad (1.17)$$

in the case of central-difference scheme, where the wave celerity c is a parameter depending on the propagating medium and Δl is linked to mesh size. Therefore, when the mesh

Algorithm Central difference Newmark algorithm ($\gamma = 1/2$ & $\beta = 0$)

1. Initialisation of U_0, \dot{U}_0 and

$$\ddot{U}_0 = \mathbb{M}^{-1}(\mathbf{F}_0 - \mathbb{K}U_0 - \tilde{\mathbb{C}}\dot{U}_0)$$

with \dot{U}_0 being and velocity at the absorbing boundary.

2. **for** $n=0$ **to** N_{dt}

3. Prediction of the displacement and the velocity

$$\begin{aligned} U_n^p &= U_n + \Delta t \dot{U}_n + \frac{\Delta t^2}{2} \ddot{U}_n \\ \dot{U}_n^p &= \dot{U}_n + \frac{\Delta t}{2} \ddot{U}_n \end{aligned}$$

4. Calculation of the internal force

$$\mathbf{F}_{n+1}^{int} = \mathbb{K}U_{n+1} + \tilde{\mathbb{C}}\dot{U}_{n+\frac{1}{2}}$$

where

$$\begin{aligned} U_{n+1} &= U_n^p \\ \dot{U}_{n+\frac{1}{2}} &= \frac{1}{\Delta t}(\tilde{U}_{n+1} - \tilde{U}_n) \end{aligned}$$

with the \tilde{U}_n values being the U_n restricted to the absorbing boundary.

5. Evaluation of the updated acceleration

$$\ddot{U}_{n+1} = \mathbb{M}^{-1}(\mathbf{F}_{n+1} - \mathbf{F}_{n+1}^{int})$$

where \mathbf{F}_{n+1} is the external force at step (n+1), being 0 in our case.

6. Correction of the updated velocity

$$\dot{U}_{n+1} = \dot{U}_n^p + \frac{\Delta t}{2} \ddot{U}_{n+1}$$

7. **end**

TABLE 1.1: Flowchart for explicit central difference time integration for a case with the perfect matched layer (PML) boundary condition in Sec.1.4.1.

needs to be refined (Δl decreases) or when the medium becomes rigid (high E), one needs to reduce accordingly the time step Δt .

1.4 Boundary conditions

Illustration of boundary conditions for a mechanical problem is given in Fig. 1.5(a), where two types of boundary conditions can be classified :

$$\begin{cases} \mathbf{u}(\mathbf{X}, t) & = \mathbf{u}_d(\mathbf{X}, t), \text{ on } \partial\Omega_u \\ \boldsymbol{\sigma}(\mathbf{X}, t) \cdot \mathbf{n}(\mathbf{X}, t) & = \mathbf{F}(\mathbf{X}, t), \text{ on } \partial\Omega_f \end{cases}$$

The first boundary condition is Dirichlet boundary condition as it specifies the values of the solution \mathbf{u} , and the second type is Neumann boundary condition because it is related to the derivative of a solution \mathbf{u} through the constitutive law relating the stress tensor $\boldsymbol{\sigma}$ to the local strains. The default configuration involves free boundary conditions ($\boldsymbol{\sigma} \cdot \mathbf{n} = 0$), meaning that there is no external loading.

We mainly applied three explicit boundary conditions in our finite element calculations. As shown in Fig. 1.5(b), the first one is the wave packet implantation at $\partial\Omega_u$, and the second one is periodic boundary condition (PBC) at $\partial\Omega_p$. Both are Dirichlet boundary conditions. The last one is absorbing boundary conditions, or Perfect Matched Layers (PML) at $\partial\Omega_a$ which is a Neumann boundary conditions.

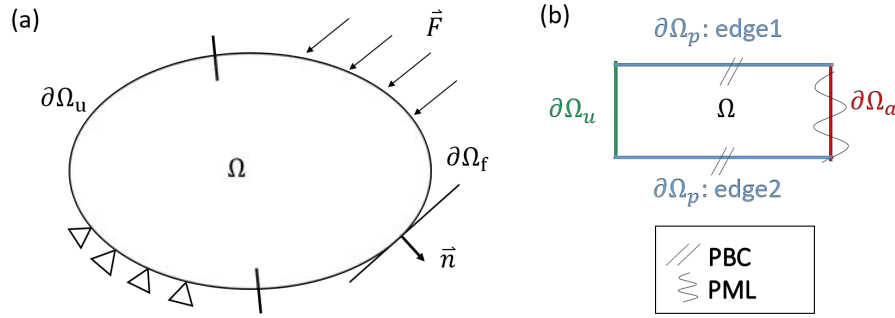


FIGURE 1.5: (a) Illustration of boundary conditions for a mechanical problem. (b) semi-infinite solid can be represented by only modeling the rectangle with Periodic Boundary Conditions (PBC) and Perfect Matched Layers (PML) as drawn (Ω represents simulation domain, $\partial\Omega$ indicates boundary conditions).

1.4.1 Periodic boundary conditions (PBC)

The periodic boundary condition reads :

$$u_\eta|_{edge1} = u_\eta|_{edge2}, \quad \eta = x, y \quad (1.18)$$

with \mathbf{u} is the nodal displacement. To link the above condition to the displacement vector \mathbf{u} , we build a matrix \mathbb{L} such that

$$\mathbb{L}\mathbf{u} = 0 \quad (1.19)$$

where \mathbb{L} only has non-zero components at the positions corresponding to PBC (1 for $u_{\eta}|_{edge1}$ and -1 for $u_{\eta}|_{edge2}$). The PBC is then imposed in the equilibrium equation by adding the Lagrange multiplier Λ in the functional from which the equilibrium equation derives. For a static problem $\mathbb{K}\mathbf{u} = \mathbf{F}$, the functional containing the Lagrange multiplier to minimize is $E(\mathbf{u}, \Lambda) = \frac{1}{2}\mathbf{u}^T \mathbb{K}\mathbf{u} - \mathbf{F}\mathbf{u} + \Lambda^T (\mathbb{L}\mathbf{u} - 0)$. To find the stationary point, let the first partial derivatives of $E(\mathbf{u}, \Lambda)$ be zero

$$\begin{cases} \frac{\partial E}{\partial \mathbf{u}} = 0 \rightarrow \mathbb{K}\mathbf{u} + \mathbb{L}^T \Lambda = \mathbf{F} \\ \frac{\partial E}{\partial \Lambda} = 0 \rightarrow \mathbb{L}\mathbf{u} = 0 \end{cases} \quad (1.20)$$

where the solution of the Lagrange multipliers Λ are the force connecting edge1 and edge2. Notice that the second equation is the original constraint.

In the dynamic case, the equations to solve are

$$\begin{cases} \mathbb{K}\mathbf{u} + M\ddot{\mathbf{u}} + \mathbb{L}^T \Lambda = \mathbf{F} \\ \mathbb{L}\mathbf{u} = 0 \end{cases} \quad (1.21)$$

In Cast3m, the matrix \mathbb{L} and the Langrange multipliers can be constructed by using the operator **RELA**.

1.4.2 Perfect Matched Layers (PML)

The PML detailed in [LYS 69, BET 77, KIM 14, BON 14] results from the creation of a viscous boundary that can absorb the incident wave and prevent the reflected wave. With this method, only a finite number of nodal points need to be considered; thus, an infinite system may be approximated by a finite system with a special viscous boundary condition. On this viscous boundary, the normal stress ζ and the shear stress τ are related to the perpendicular velocity and the tangential velocity of the incident wave respectively. It can be written as :

$$\zeta = a\rho V_p \dot{u}_x \quad (1.22)$$

$$\tau = b\rho V_s \dot{u}_y \quad (1.23)$$

with $V_s = \sqrt{\frac{G}{\rho}}$ is the S-wave celerity and $V_p = \sqrt{\frac{E}{\rho}}$ is the P-wave celerity, ν is Poisson ratio, E and G are elastic moduli, u_x and u_y represent the displacement caused by the P-wave and S-wave respectively. Lysmer and Kulemeyer [LYS 69] have proposed to use $a = b = 1$, which has been verified as having nice performance [KIM 14] to absorb quasi-perfectly elastic harmonic waves : it can perfectly absorb waves perpendicular to the boundary, and if the wave attacks the absorbing boundary with an inclined incident angle, the absorption ratio may be as low as 50 % .

For example, for a 1D problem $u(x, t)$, only Eq.1.22 is considered. Replacing $\zeta = E \frac{\partial u}{\partial x}$ and $a = 1$, the PML reads :

$$\frac{\partial u}{\partial x} = \frac{1}{V_p} \frac{\partial u}{\partial t} \quad (1.24)$$

The corresponding weak form for 1D wave equation (Eq.1.2) together with the PML at $x = L$ (Eq.1.24) reads[BON 14] :

$$\int_0^L (E \frac{\partial u}{\partial x} \frac{\partial v}{\partial x} + \rho \frac{\partial^2 u}{\partial t^2} v) dx = \frac{E}{V_p} \frac{\partial u}{\partial t}(L, t) v(L) \quad (1.25)$$

$$, \forall x \in [0, L]$$

where v is a test function. The first term is the virtual internal work and the second term is the virtual kinetic work. Notice that there is an additional term $\frac{E}{V_p} \frac{\partial u}{\partial t}(L, t) v(L)$ in the RHS, which is brought by the PML and can be thought as a local damping, denoted as \tilde{C} . Similar to the Eq.1.13, its components read $\tilde{C}_{ij} = -\frac{E}{V_p} N_i N_j|_{x=L}$ in 1D case. In Cast3m, the damping matrix for the absorbing boundary can be constructed using the operator AMOR.

1.4.3 Wave packet

We will study the vibrational properties of a model system (with interfaces). To study the propagation of the vibrational energy, we excite a quasi-monochromatic wave packet on one side of the sample around $x = 0$ in a small time interval around $t = 0$ [BEL 16, LUO 19]. To excite the vibrations in the sample we used the excitation displacement at $\partial\Omega_u$

$$U(\omega, t) = U_0 \exp\left(-\frac{(t - 3t_0)^2}{2t_0^2}\right) \sin(\omega t) \quad (1.26)$$

with U_0 being a constant value, ω is the frequency of this quasi-monochromatic excitation. The coherent time t_0 should be chosen carefully, the width of the wave packet increases with the increasing t_0 and a wide wave packet needs more time to enter the sample compared to a narrow one. On the other hand, we require a wave packet with a well-defined frequency, thus t_0 should not be too small which leads to a broad frequency spectrum.

A wave packet is imposed into the model as Dirichlet boundary conditions :

$$\mathbf{u}_\eta(t)|_{\partial\Omega_u} = U(\omega, t) \mathbf{n}_\eta, \quad \eta = x \text{ or } y \quad (1.27)$$

Specifically, when $\eta = x$, it is longitudinal waves. When $\eta = y$, it is transverse waves.

2 Constitutive models

Constitutive equations shows how a solid deforms as a response to stresses, to loading rate, to changes of temperature and to many other factors. This description of the intrinsic behavior of the solid is needed to close the system of equations of motion relating

time dependent strains and stresses in continuum elasticity [SAL 12]. How to choose a constitutive equation depends on the material properties and the specific situation. In this section, I will introduce two fundamental stress-strain constitutive relationships used in this thesis : linear elasticity and visco-elasticity. Elasticity will be used in the Chap. 2-4 to model elastic media, whether homogeneous or heterogeneous, without intrinsic dissipation. Visco-elasticity will be used in the Chap. 5 to model a viscous medium where energy looks dissipated during the wave propagation.

Let's start from defining the 2nd order strains tensor ϵ_{ij} with respect to displacement vector u_i [KIT 04, FRA 12, LAN 86] :

$$\epsilon_{ij} = \frac{1}{2} \left(\frac{\partial u_i}{\partial x_j} + \frac{\partial u_j}{\partial x_i} + \frac{\partial u_m}{\partial x_i} \frac{\partial u_m}{\partial x_j} \right) \quad (1.28)$$

$$= \epsilon_{ij}^{(1)} + \epsilon_{ij}^{(2)} \quad (1.29)$$

by defining :

$$\epsilon_{ij}^{(1)} = \frac{1}{2} \left(\frac{\partial u_i}{\partial x_j} + \frac{\partial u_j}{\partial x_i} \right) : \text{the terms linear in the displacements}$$

$$\epsilon_{ij}^{(2)} = \frac{1}{2} \frac{\partial u_m}{\partial x_i} \frac{\partial u_m}{\partial x_j} : \text{the terms quadratic in the displacements}$$

For strains much less than unity (case of *geometric linearity*), higher order terms are negligible , so :

$$\epsilon_{ij} \approx \epsilon_{ij}^{(1)} = \frac{1}{2} \left(\frac{\partial u_i}{\partial x_j} + \frac{\partial u_j}{\partial x_i} \right) \quad (1.30)$$

This strain tensor is referred to as the small strain tensor, or the linearized strain tensor. This form of the strain tensor is very convenient because it allows for a linear relationship between strain and displacements. Since we focus on the harmonic vibrational properties of structures which naturally means small strains, thus the linearized strain will be used in all further discussions.

2.1 Elasticity

In mechanics and materials science, elasticity is the ability of a body to resist a force and to return to its original size and shape when that force is removed. Depending on the strain magnitude, elasticity can be classified as linear elasticity or finite elasticity. As the name suggests, linear elasticity represents the linear relationship between stress and strain, which is the simplest constitutive law, known as Hooke's law. Linear elasticity is appropriate for traditional materials undergoing small deformations. In the limit of small strains and at room temperature, linear elasticity is enough to model glassy materials [WAN 12].

Hooke's law :

In 1D, Hooke's law can be illustrated as a single spring in Fig. 1.6 with a constant rigidity :

$$\sigma = E \epsilon \quad (1.31)$$

where E is the Young's modulus.

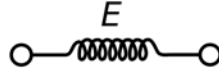


FIGURE 1.6: Hooke's model

In 3D, Hooke's law can be written in tensor form as : $\boldsymbol{\sigma} = \boldsymbol{C} : \boldsymbol{\epsilon}$, where \boldsymbol{C} is the elastic tensor. For isotropic materials, the most general form of Hooke's law is written as :

$$\sigma_{ij} = 3K\left(\frac{1}{3}\epsilon_{kk}\delta_{ij}\right) + 2G\left(\epsilon_{ij} - \frac{1}{3}\epsilon_{kk}\delta_{ij}\right) \quad (1.32)$$

where K is the bulk modulus and G is the shear modulus. The hydrostatic (or spherical) part of strain is given by $\epsilon_{ij}^{sph} = \frac{1}{3}\delta_{ij}\epsilon_{kk}$ and the deviatoric part, which is isochoric, is $\epsilon_{ij}^{dev} = \epsilon_{ij} - \frac{1}{3}\delta_{ij}\epsilon_{kk}$, where δ_{ij} is Dirac function and repeated indices indicate summation as in Einstein's notations.

2.2 Linear visco-elasticity

Linear visco-elasticity is related to Newton's law for fluids that assumes a linear relation between stress and strain rate. This model implies a dissipative (viscous) behavior. There are different ways to combine linear viscosity and linear elasticity in solids, depending on their combined effect, either on the stress (force relaxation) or on the strain (creep flow) components [BRI 08, MAR 14, CHR 12].

2.2.1 Kelvin-Voigt model :

Kelvin-Voigt model is represented in Fig.1.7. It consists of an elastic spring and a viscous dashpot in parallel. Applying an axial stress on this Kelvin-Voigt model, σ_{total} and ϵ_{total} can be defined as follows :

$$\begin{aligned} \sigma_{total} &= \sigma_{spring} + \sigma_{damping} \\ \epsilon_{total} &= \epsilon_{spring} = \epsilon_{damping} \end{aligned} \quad (1.33)$$

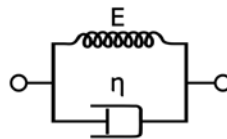


FIGURE 1.7: Kelvin-Voigt model

Kelvin-Voigt stress-strain constitutive relation can be expressed as below :

$$\begin{aligned}\sigma &= \sigma^{ela} + \sigma^{vis} \\ &= E\epsilon^{ela} + \eta\dot{\epsilon}^{vis}\end{aligned}\quad (1.34)$$

Where η is the viscosity. In 1D, it gives rise to the time dependent strain $\epsilon(t) = \frac{\sigma}{E}(1 - \exp(\frac{-Et}{\eta}))$. It is used for example to model rubber [MAR 14].

2.2.2 Maxwell model :

The Maxwell model can be represented by a purely viscous damper and a purely elastic spring connected in series as shown in Fig.1.8. Applying an axial stress on this Maxwell model, σ_{total} and ϵ_{total} can be defined as follows :

$$\begin{aligned}\sigma_{total} &= \sigma_{spring} = \sigma_{damping} \\ \epsilon_{total} &= \epsilon_{spring} + \epsilon_{damping}\end{aligned}\quad (1.35)$$

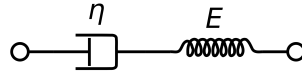


FIGURE 1.8: Maxwell model

Maxwell stress-strain constitutive relation can be expressed as below :

$$\begin{aligned}\dot{\epsilon} &= \dot{\epsilon}^{ela} + \dot{\epsilon}^{vis} \\ &= \dot{\sigma}^{ela}/E + \sigma^{vis}/\eta \\ &= \dot{\sigma}/E + \sigma/\eta\end{aligned}\quad (1.36)$$

Such a material tends exponentially to thermal equilibrium after an external stress perturbation with a *relaxation time* τ :

$$\tau = \eta/E \quad (1.37)$$

Solution of the initial inhomogeneous differential equation Eq.1.36 is :

$$\sigma(t) = E \int_0^t dt' \gamma(t-t') \dot{\epsilon}(t') \quad \text{fo a one-dimensional system} \quad (1.38)$$

with

$$\gamma(t) = e^{-t/\tau} \quad (1.39)$$

It is used for example to model glasses near their melting temperature [MAR 14].

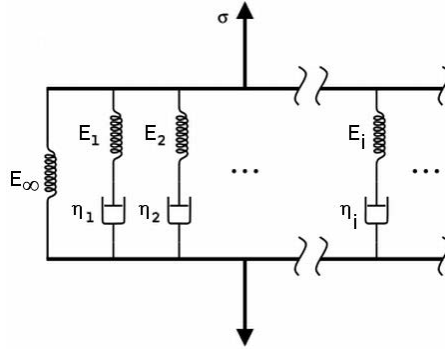


FIGURE 1.9: Generalized Maxwell model

2.3 Generalized visco-elasticity

2.3.1 Generalized-Maxwell model :

Fig.1.9 shows us a generalized Maxwell model[BRI 08, ROY 01] which consists of one conservation branch (with only one spring) and N dissipation branches (with one spring and one dashpot). As detailed later, it is simple to write the strain-stress relation in the complex domain :

$$E^*(s) = E_\infty + \sum_{j=1}^N E_j \frac{\tau_j s}{1 + \tau_j s} \quad (1.40)$$

with $s = i\omega + \xi$ the Laplace frequency parameter (with $\xi \rightarrow 0$). Temporal expression of the generalized-Maxwell model has the same form as Eq.1.38 but the $\gamma(t)$ is :

$$\gamma(t) = 1 + \sum_{j=1}^N \frac{E_j}{E_\infty} e^{-t/\tau_j} \quad (1.41)$$

3 Wave propagation in a homogeneous elastic medium

3.1 Formulation

Let's start from clarifying some notations. $x_i (i = 1, 2, \dots, n)$ denote coordinates where n is space dimension. All our works are investigated in Euclidean space, so there exists the relation that $x_1 = x$, $x_2 = y$ and $x_3 = z$. For displacement field : $u_1 = u$, $u_2 = v$ and $u_3 = w$ are respectively the displacement parallel to the axis x , y and z .

Combining Hooke's law (Eq. 1.32) and the expression for linear strains (Eq. 1.30) and supposing that the medium is isotropic, stresses can be expressed as a function of the displacements u_i as :

$$\sigma_{ij} = \lambda \left(\frac{\partial u_k}{\partial x_k} \right) \delta_{ij} + G \left(\frac{\partial u_i}{\partial x_j} + \frac{\partial u_j}{\partial x_i} \right) \quad (1.42)$$

where the elastic constants λ and G are also called the lamé constants. The conversion between the elastic moduli can be found in the [Conversion formula](#).

Supposing now that the medium is homogeneous, that the medium is homogeneous and isotropic, the elastodynamic equilibrium equation ($\nabla \cdot \sigma_{ij} = \rho \ddot{u}_i$) can be given by [\[MIC 15\]](#) :

$$G\nabla^2 u_i + (\lambda + G)\nabla(\nabla \cdot u_i) = \rho \ddot{u}_i \quad (1.43)$$

where $\nabla^2 = \frac{\partial^2}{\partial x^2} + \frac{\partial^2}{\partial y^2} + \frac{\partial^2}{\partial z^2}$ is the Laplacian operator. The above equation is also called *Navier's equation* which expresses the propagation of free waves in an homogeneous, isotropic and elastic medium.

We only consider waves propagating in the x-y plane indicating that the displacement field remains invariant with respect to x_3 , *i.e.*, $\frac{\partial u_i}{\partial z} = 0$.

Eq. 1.43 yields the set of equations :

$$G\left(\frac{\partial^2}{\partial x^2} + \frac{\partial^2}{\partial y^2}\right)u + (\lambda + G)\left(\frac{\partial^2 u}{\partial x^2} + \frac{\partial^2 v}{\partial x \partial y}\right) = \rho \frac{\partial^2 u}{\partial t^2} \quad (1.44)$$

$$G\left(\frac{\partial^2}{\partial x^2} + \frac{\partial^2}{\partial y^2}\right)v + (\lambda + G)\left(\frac{\partial^2 u}{\partial x \partial y} + \frac{\partial^2 v}{\partial y^2}\right) = \rho \frac{\partial^2 v}{\partial t^2} \quad (1.45)$$

$$G\left(\frac{\partial^2}{\partial x^2} + \frac{\partial^2}{\partial y^2}\right)w = \rho \frac{\partial^2 w}{\partial t^2} \quad (1.46)$$

It is observed that Equations (1.44-1.46) split in two groups. Eq.1.44-1.45 are coupled equations for u and v . They will describe wave motion in the *propagation plane*. Eq. 1.46 describes wave motion in the direction perpendicular to the plan x-y. Assuming a wave propagating in the x direction. Fig. 3.1(a) and (b) show the *longitudinal* and *transverse* waves. Such waves are named P and S waves. Fig. 3.1 (c) and (d) show the spacial waves appearing at surface of a half-space with free boundary conditions : *Rayleigh* and *Love* surface waves. Our work only focuses on volumic waves and not on surface waves.

3.2 Wave speed in a homogeneous elastic medium

In the above cases (a) and (b) shown in Fig.3.1, the waves propagate in the x direction and no deformation exists in plane y-z ($\frac{\partial u_i}{\partial y} = 0$). As given in Ref. [\[MIC 15\]](#), the displacement field depends only on x and time t :

$$u(x,t) = u(x \pm ct), \quad v(x,t) = v(x \pm ct), \quad w(x,t) = w(x \pm ct) \quad (1.47)$$

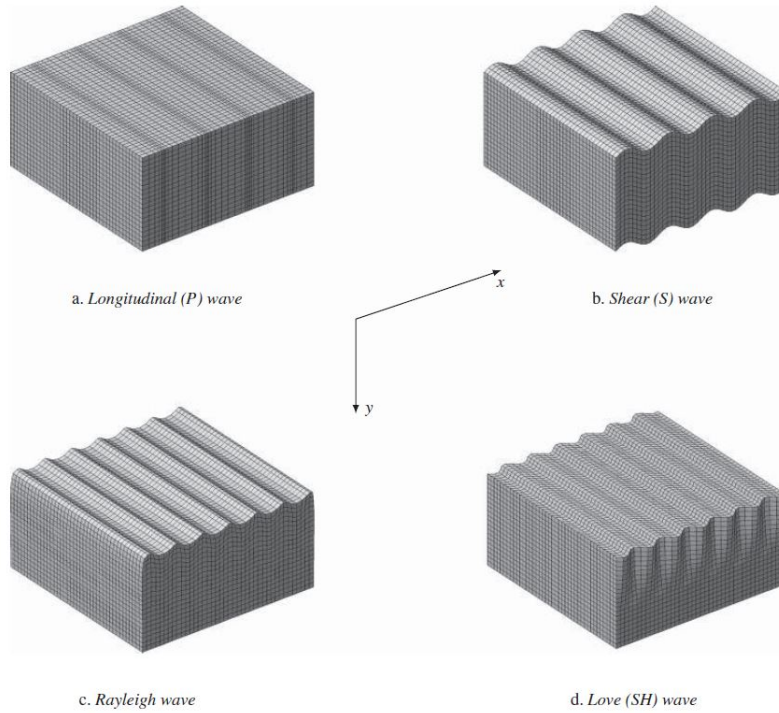


FIGURE 1.10: Fundamental deformation patterns generated by Longitudinal (P), Shear (S), Rayleigh and Love (SH) waves [MIC 15].

where c is the propagation speed of the wave. Combining $\frac{\partial}{\partial y} = 0$ with Eq. 1.47, Eqs. 1.44-1.46 can be rewritten as :

$$(\lambda + 2G) \frac{\partial^2 u}{\partial x^2} = c^2 \rho \frac{\partial^2 u}{\partial x^2} \quad (1.48)$$

$$G \frac{\partial^2 v}{\partial x^2} = c^2 \rho \frac{\partial^2 v}{\partial x^2} \quad (1.49)$$

$$G \frac{\partial^2 w}{\partial x^2} = c^2 \rho \frac{\partial^2 w}{\partial x^2} \quad (1.50)$$

Equations 1.48-1.50 are uncoupled equations for the three components of the displacement field and show the existence of two different waves speed c .

3.2.1 Longitudinal waves

Longitudinal waves correspond to the case where the displacements are parallel to the direction of propagation as shown in Fig.3.1(a). The solution of c from the Eq. 1.48 is characterized by the longitudinal wave speed c_L :

$$c_L = \sqrt{\frac{\lambda + 2G}{\rho}} = \sqrt{\frac{K + \frac{4}{3}G}{\rho}} = \sqrt{\frac{E(1-\nu)}{\rho(1+\nu)(1-2\nu)}} \quad (1.51)$$

3.2.2 Transverse waves

Transverse waves correspond to the waves where the displacements are orthogonal to the propagation direction. There exist two transverse waves vibrating respectively in the x-z and y-z plane (Eqs. 1.49 and 1.50) with a transverse wave speed c_T :

$$c_T = \sqrt{\frac{G}{\rho}} = \sqrt{\frac{E}{2(1+\nu)\rho}} \quad (1.52)$$

In 3D case, there are one longitudinal wave and two transverse waves. In 2D case, shear wave in y-z plane exists no longer. In fact, since we will deal with two-dimensional problems with *plane strain* assumption, we also ignore the displacement in the z direction.

3.2.3 Phase velocity and group velocity

Wave speeds can be derived in many ways, the above being probably the simplest one. They can also be defined through the dispersion relation (or phonon band structure), which represents frequency ω as a function of wavevector k . In the band structure, the branches starting from the (k, ω) point $(0, 0)$, three for 3D and two for 2D, are the acoustic branches corresponding to the longitudinal and transverse modes. The ratio $\frac{\omega}{k}$ defines the *phase velocity* at a given frequency. For a quasi-monochromatic wave-packet, energy propagates not at the phase velocity but rather at the *group velocity* $\frac{d\omega}{dk}$. In a homogeneous medium, acoustic branches are straight lines, so that the *phase velocity* equals to the *group velocity* ($\frac{\omega}{k} = \frac{d\omega}{dk}$) and both are frequency-independent constants given by the Eqs. 1.51 or 1.52. However, in a heterogeneous medium with interfaces, the situation becomes more complicated, not only the two speeds may be different, but also the speeds will depend on the frequency. In the next section, I will give a brief introduction about the different types of interfaces used in my thesis.

4 Heterogeneous materials with interfaces

Interface is a surface for 3D (or curve for 2D) with different materials properties on both sides. In this thesis, I concentrate on the wave propagation in a heterogeneous medium derived from the different interfaces. Specifically, I have a uniform homogeneous matrix material in which inclusions with different mechanical properties to the matrix are embedded. As shown in Fig.1.11, I illustrate three types of 2D interfaces : (a) elastic inclusion, (b) Eshelby's inclusion and (c) random elasticity.

4.1 Elastic inclusion

Consider a homogeneous linear elastic solid M with elastic tensor C^M as shown in Fig.1.11(a), let a sub-domain I with an interface Γ is also a homogeneous linear elastic solid with elastic constant C^I . In the case of elastic inclusions, inclusions have different

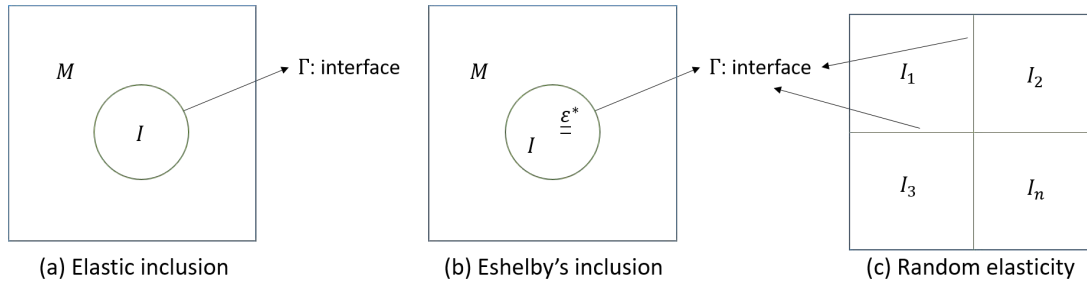


FIGURE 1.11: Different interfaces in a heterogeneous medium

stiffnesses compared with matrix. The mismatch ratio of the stiffness will be denoted as $\frac{E_i}{E_m}$ where E_i (E_m) is the Young's modulus of the inclusions (matrix). This interface is established due to the stiffness mismatch. Except that, the initial conditions and constitutive relation are the same in both phases.

In this case, it is important to clarify the connection across the interface and the continuity conditions. Each inclusion in the composite assumed to be *perfectly connected* with the matrix. There is no intermediate phase between them. In this context, the displacements are continuous across the interface. Let us define $[f]$ as the jump of field f from the inclusion to the matrix. For a **perfect connection** :

$$[u]_{\Gamma} = 0 \quad (1.53)$$

the perfect connection is ensured as long as we perform a nodal equivalence operation so that at the interface the matrix and inclusion share the same nodes.

Stress tensor in the matrix :

$$\sigma^M = C^M : \epsilon^M \quad (1.54)$$

Stress tensor inside the inclusion :

$$\sigma^I = C^I : \epsilon^I \quad (1.55)$$

The stiffness ratio and the length of the interface are two factors contributing to the heterogeneity.

4.2 Eshelby's inclusion

Consider now a homogeneous linear elastic solid M with elastic tensor C^M as shown in Fig.1.11(b), let a sub-domain I with an interface Γ undergo a uniform permanent (inelastic) deformation, prescribed as "stress-free strain" or "eigenstrain" ϵ^* , which could be due, for example, to a phase change, plasticity, or to thermal effects. The elastic tensor of the inclusion C^I can be identical to the matrix or not. In either, an interface is established due to the mismatch of the strain across the interface in the stress-free state. The Eq.1.53 still holds true in the case of Eshelby's inclusion[WEI 05, FRA 12].

Stress tensor in the matrix :

$$\boldsymbol{\sigma}^M = \mathbf{C}^M : \boldsymbol{\epsilon}^M \quad (1.56)$$

Stress tensor inside the inclusion :

$$\boldsymbol{\sigma}^I = \mathbf{C}^I : (\boldsymbol{\epsilon}^I - \boldsymbol{\epsilon}^*) \quad (1.57)$$

with now $\boldsymbol{\epsilon}^I = \boldsymbol{\epsilon}^M$ at the interface[FRA 12]. The eigenstrain causes in fact a surface force at the interface between the inclusion and the matrix. In our case, we only consider the homogeneous Eshelby's inclusion ($\mathbf{C}^I = \mathbf{C}^M$), resulting in a surface force $\mathbf{F}_s = (\mathbf{C}^I : \boldsymbol{\epsilon}^*) \cdot \mathbf{n}$ with \mathbf{n} is the normal vector at the interface.

Especially, for an ellipsoidal Eshelby's inclusion, the relation between $\boldsymbol{\epsilon}^I$ and $\boldsymbol{\epsilon}^*$ can be expressed through a constant tensor as :

$$\boldsymbol{\epsilon}^I = \mathbf{S} : \boldsymbol{\epsilon}^* \quad (1.58)$$

where the Eshelby tensor \mathbf{S} only depends on the moduli \mathbf{C} , the shape (aspect ratio) and orientation of the ellipsoidal inclusion. It can be shown that Eshelby inclusion is equivalent to an elastic inclusions ($\boldsymbol{\sigma}$ and $\boldsymbol{\epsilon}$ must be the same in the two ellipsoids) :

$$\boldsymbol{\sigma}^I = \boldsymbol{\sigma}^H \quad (1.59)$$

$$\mathbf{C}^I : (\boldsymbol{\epsilon}^I - \boldsymbol{\epsilon}^*) = \mathbf{C}^H : \boldsymbol{\epsilon}^I \quad (1.60)$$

$$\mathbf{C}^I : (\mathbf{S} - \mathbf{I}) : \boldsymbol{\epsilon}^* = \mathbf{C}^H : \mathbf{S} : \boldsymbol{\epsilon}^* \quad (1.61)$$

where \mathbf{I} the identity tensor. To ensure the equation holds, the moduli of the equivalent elastic inclusion is thus

$$\mathbf{C}^H = \mathbf{C}^I : (\mathbf{S} - \mathbf{I}) : \mathbf{S}^{-1} \quad (1.62)$$

4.2 Random elasticity

Random elasticity is a generalized case of the elastic inclusion, as shown in Fig.1.11(c), each zone being an independent elastic solid with a random stiffness. Each zone is *perfectly connected* to the neighbor zones. In this thesis, we tune the Young's modulus of each zone following a Gaussian distribution and the Poisson's ratio of the entire heterogeneous medium will be supposed to be the same.

Stress tensor inside each elastic zone :

$$\boldsymbol{\sigma}_n = \mathbf{C}_n : \boldsymbol{\epsilon}_n, \quad n = 1, 2, \dots \quad (1.63)$$

The spatial statistic fluctuations of the Young's modulus are assumed according to a Gaussian distribution, which is the basis of heterogeneous-elasticity theory to model glasses[MAR 13, SCH 15b].

After having presented the different tools used in the numerical calculations performed in this thesis, we will now turn to formally talk about my work in the following chapters.

Chapter 2

Acoustic attenuation in the presence of elastic inclusions

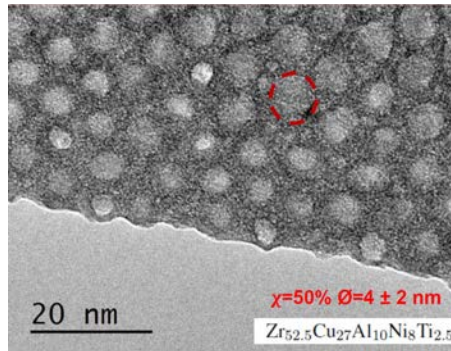
Assuming elastic behavior in the matrix and in the inclusions and perfect connection conditions, we present a FE numerical simulation of the transient propagation of an acoustic Wave-Packet in a 2D nanophononic material, which allows to identify the effect of the elastic inclusions on the acoustic attenuation length and thus on the transport regime for the vibrational energy. Three parameters are studied : the rigidity contrast between the inclusion and the matrix, the size of the inclusions and the frequency of the incident wave-packet.

Contents

1	Model of bi-phasic materials : circular inclusions	29
1.1	Geometry	30
1.2	Materials properties	30
1.3	Boundary conditions	30
1.4	Perfect connection between the matrix and the inclusions	32
1.5	Spatial and temporal discretization	32
2	Equilibrium Vibrational Properties	32
2.1	Vibrational Density of States	33
2.2	Representative normal modes	34
3	Wave-Packet Propagation : Different Regimes	36
3.1	Envelope of the kinetic energy	36
3.2	Different propagation regimes	37
3.3	Phase diagram of propagation regimes	40
3.4	Meaningful quantities for describing different dynamical regimes	42
4	Penetration Length	44
4.1	Definition of the Penetration length	44
4.2	Penetration length vs $\frac{E_i}{E_m}$ & R for $\omega = 5$ THz	45
4.3	Penetration length vs $\frac{E_i}{E_m}$ & ω for $R=25$ Å	45
5	Discussion and conclusion	48

1 Model of bi-phasic materials : circular inclusions

In this section, inspired by Fig. 2.1 corresponding to a nanostructuration, we used Finite Element numerical calculations to study the vibrational properties of a 2D semi-infinite elastic system with circular inclusions positioned along a cubic lattice. A parametric study of the acoustic attenuation of wave packets is performed in the nanocomposite : the roles of the rigidity contrast between the inclusion and the matrix, the size of the inclusions, and the frequency of the wave-packet are studied. In fact, similar phononic structures have been investigated by J. Vasseur et al. [VAS 08, PEN 08, DEY 17], which demonstrated the band gap in a phononic crystal constituted by cylindrical dots on a homogeneous plate and the possibility of tailoring phonon band structures by shaping spatiotemporal modulations of stiffness.



F1

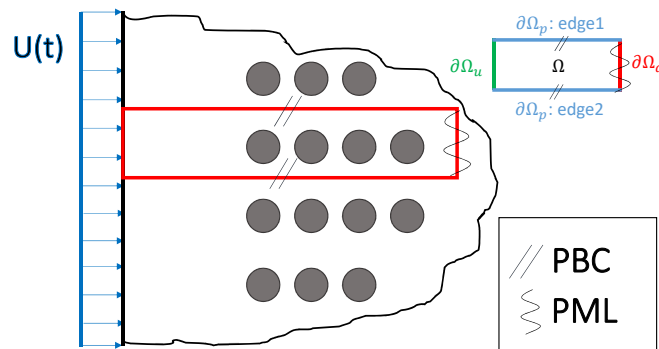


FIGURE 2.2: 2D simulation model of a solid with circular inclusions : this semi-infinite solid can be represented by only modeling only the part inside the red rectangle with Periodic Boundary Conditions (PBC) and Perfect Matched Layers (PML) as drawn ; Grey disks represent the inclusions. (Ω represents simulation domain, $\partial\Omega$ indicates boundary conditions)

1.1 Geometry

The computational model consists of 28 square blocs, aligned in the horizontal direction (as shown in Fig. 2.2 and Fig. 2.3) : the first two with only the matrix phase, then 25 containing each a single circular inclusion, and finally another one without inclusion. The large number of squares is necessary for establishing the wave-packet and studying the transient behavior during its propagation from left to right. The size of each square is $L=60 \text{ \AA}$, thus determining the distance between inclusions. In the meantime, the radius of the inclusions will be considered as a control variable.

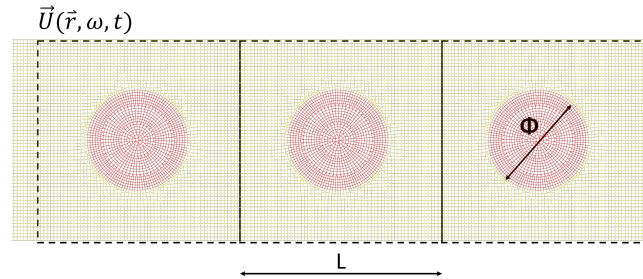


FIGURE 2.3: Schematic illustration of the central part of the sample for $L=60 \text{ \AA}$ and $\Phi = 2R = 20 \text{ \AA}$: in yellow represents the matrix material, in red the inclusions. Periodic reproduction of this sample along the vertical direction is assured by periodic boundary conditions.

1.2 Materials properties

In order to be consistent with previous MD works of Beltukov et al [BEL 16, BEL 18], we choose for the matrix material the amorphous silicon investigated there, assigning to the matrix the elastic properties identified in those works. The matrix material is a model amorphous silicon, linearly elastic with isotropic homogeneous elastic behavior characterized by the Young's modulus $E_m = 92.25 \text{ GPa}$, the mass density $\rho = 2303 \text{ kg/m}^3$ and the Poisson ratio $\nu = 0.34$. For the inclusions, the Poisson's ratio is supposed to be the same, while the Young's modulus E_i is taken as another control variable and defined as $E_i = E_m \times \frac{E_i}{E_m}$, this latter being the stiffness ratio. We used also an isotropic, homogeneous and linear elastic model for the inclusion here. For information, as given by Eqs.1.51 and 1.52, the speed of longitudinal wave in the matrix is $c_L = 7966 \text{ m/s}$, and the transverse one is $c_T = 3856 \text{ m/s}$.

1.3 Boundary conditions

1.3.1 Load : wave-packets

The wave-packet is generated imposing a displacement on the left side of the first square, and it is established in the first 2 squares before touching the first inclusions. The

following 25 squares with circular inclusions constitute the useful area for the analysis, while the last empty square allows for the implementation of the absorbing boundary conditions. To produce the quasi-monochromatic propagating wave-packet (Fig. 2.4) at the origin of the excitation energy, we impose the displacement on the left side of the sample around $x = 0$ in a small time interval around $t = 0$:

$$\underline{U}(\omega, t) = \underline{U}_0 \exp\left(-\frac{(t - 3t_0)^2}{2t_0^2}\right) \sin(\omega t) \quad (2.1)$$

where \underline{U}_0 is a constant vector, ω is the frequency of this quasi-monochromatic excitation, and $t_0 = \frac{\pi}{\omega}$ is the half period of the excitation. A displacement \underline{U}_0 parallel to the boundary corresponds to a transverse excitation, while the one perpendicular to the boundary to a longitudinal excitation. For the sake of simplicity, we will consider here only longitudinal excitations. The amplitude U_0 has been chosen as $U_0 = 4.9 \times 10^{-3} \text{ \AA}$ similarly to what was done in the previous molecular dynamics simulations of propagating wave-packets [BEL 18], small enough for preventing anharmonic effects. This choice will allow for further comparisons of the results. In addition, it should be mentioned here that a linear constitutive behavior is employed in the Finite Element simulation, no anharmonicity existing, as a results, the choice of U_0 should not modify wave propagation phenomena but only the amplitude of wave-packet.

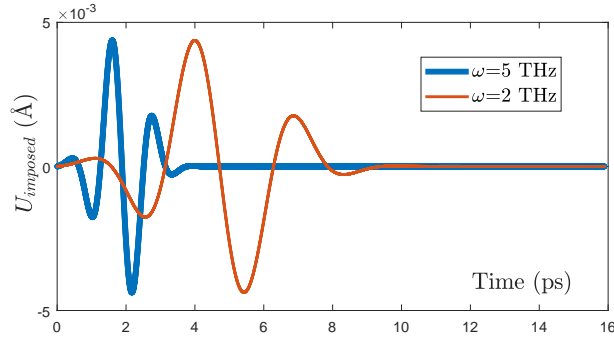


FIGURE 2.4: Wave packet imposed as the displacement of the left side of the sample, for two different frequencies : 2 THz, 5 THz

Note : In the works of future chapters, we will use $t_0 = \frac{3\pi}{\omega}$, which gives a narrower frequency band, therefore being more representative as a quasi-monochromatic wave packet. However, we checked that no significant disparity was observed for the quantitative results such as the penetration length in the current chapter between whether $t_0 = \frac{3\pi}{\omega}$ or $t_0 = \frac{\pi}{\omega}$.

1.3.2 PBCs & PMLs

We focused our study on a single alignment of inclusions :

- Periodic boundary conditions (PBCs) are imposed at the top and bottom of the sample shown in Fig. 2.2; Lagrangian multipliers are used to realize the PBCs as detailed in Sec.1.4.1.

- Absorbing boundary conditions, or PML (Perfect Matched Layers) are imposed on the right side, to avoid waves reflection. (cf. Sec.1.4.2)

1.4 Perfect connection between the matrix and the inclusions

Each inclusion of the composite is perfectly connected with the matrix. There is no intermediate interface between them. In this context, the displacements are continuous across the interface between the matrix and the inclusions as shown in Eq.1.53.

1.5 Spatial and temporal discretization

In this work, we use the P-1 element which has quadrangle shape and has 4 nodes on the corners. The pre-defined side length of quadrangle element has been chosen 1 Å for a wave packet frequency $\omega = 5$ THz, which means that the wave has approximately 90 elements per wavelength in the matrix medium. As the frequency increases and the wavelength becomes shorter, we have refined the mesh size accordingly. Attention should be paid in the case of $E_i/E_m > 1$, where the increasing sound speed leads to a shorter wavelength inside the inclusion, for a given frequency. Especially for the extreme case $E_i/E_m = 10$, wavelength in the inclusions decreases scaling as $1/\sqrt{E_i/E_m} = 1/\sqrt{10} \approx 1/3.2$, as such the wave has approximate 30 elements per wavelength at 5 THz. If, unfortunately, not enough elements are given, as a result, numerical errors will accumulate and eventually lead to erroneous simulations.

We can get the space-time discretized form for a 2D plain strain problem (combined with the central-difference time integrator) :

$$\mathbb{M}\ddot{\mathbf{U}}_{n+1} = \mathbf{F}_{n+1} - \mathbb{K}\mathbf{U}_n^p - \tilde{\mathbb{C}}\dot{\mathbf{U}}_{n+\frac{1}{2}} \quad (2.2)$$

Here, \mathbb{K} is stiffness matrix, \mathbb{M} is lumped mass matrix, $\tilde{\mathbb{C}}$ and $\dot{\mathbf{U}}$ are the damping matrix and the velocity vector of the PML, respectively. \mathbf{F} is a possible nonzero external force vector. The indices n and $n + 1$ are successive time steps, and the superscript p means predictor. Time integration follows the Newmark central difference schema as presented in Sec.1.3.2 Tab.1.1. The chosen time step is 1.59 fs and the simulations ends at 15.59 ps.

2 Equilibrium Vibrational Properties

We first characterize the vibrational response of our systems at equilibrium, before applying a traveling wave packet. We can compute the vibrational density of states (VDOS) of the system and its vibrational modes by performing a spectral analysis, consisting in diagonalizing the dynamical matrix. The dynamical matrix is defined as $\mathbb{D} = \mathbb{K}^{-1}\mathbb{M}$ [MIC 15].

2.1 Vibrational Density of States

The vibrational density of states (VDOS) corresponds to the model distribution. It is defined as :

$$VDOS(\omega) = \frac{1}{N} \sum_{i=1}^N \delta(\omega - \omega_i) \quad (2.3)$$

with ω_i spanning the spectrum of eigenfrequencies of the system.

The eigenvectors of the dynamical matrix are the vibrational eigenmodes (also called normal modes), and the eigenvalues are the squared frequencies ω_i^2 of the related vibrations [KIT 04]. This is done automatically using the command *VIBR* in Cast3M on successive finite ranges of frequencies. The VDOS is then obtained by counting the number of eigenfrequencies in the intervals with width $\Delta\nu$ around each frequency ω .

$$VDOS(\omega) = \frac{1}{N} \sum_{i=1}^N H(\Delta\nu - |\omega - \omega_i|) \quad (2.4)$$

where $H(n)$ is Heaviside function whose value is zero for negative arguments and one for positive arguments, such as :

$$H(n) = \begin{cases} 0, & n < 0 \\ 1, & n \geq 0 \end{cases}$$

In Fig. 2.5 (a) we report the DOS for several rigidity contrasts ranging from 0.2 to 10, calculated with $\Delta\nu = 1$ THz. In order to estimate the resolution of our calculation on the basis of the chosen frequency interval width, we have calculated the DOS for different $\Delta\nu$, going from 0.4 to 1 THz, as reported in the inset. It can be seen that the choice $\Delta\nu = 1$ THz is reasonable and does not deteriorate too much the resolution. As usual in 2D systems dominated by plane waves, the VDOS shows an initial $\propto \omega$ dependence, but, due to the presence of inclusions in our systems and finite dimension, it is then a non-monotonous function of the frequency. It is interesting to spatially solve the VDOS and separate the contribution of the matrix from the one of the inclusions. For that, we give the definition of the partial VDOS (PDOS) :

$$PDOS_M(\omega) = \frac{1}{N} \sum_{i=1}^N \delta(\omega - \omega_i) \left(\sum_{n \in M} \|\mathbf{u}_i(n)\|^2 \right) \quad (2.5)$$

and

$$PDOS_I(\omega) = \frac{1}{N} \sum_{i=1}^N \delta(\omega - \omega_i) \left(\sum_{n \in I} \|\mathbf{u}_i(n)\|^2 \right) \quad (2.6)$$

where $\mathbf{u}_i(n)$ is normalized normal vector for node n , with $\sum_{n \in M} \|\mathbf{u}_i(n)\|^2 + \sum_{n \in I} \|\mathbf{u}_i(n)\|^2 = 1$. Node n may belong to I (the inclusion), to M (the matrix) or to the both (on the interface). The fraction of the PDOS, $f(\omega)$, indicates the percentage of the PDOS in the total VDOS :

$$f_M(\omega) = \frac{PDOS_M(\omega)}{PDOS_M(\omega) + PDOS_I(\omega)} = \frac{\sum_{n \in M} \|\mathbf{u}_i(n)\|^2}{\sum_{n \in M} \|\mathbf{u}_i(n)\|^2 + \sum_{n \in I} \|\mathbf{u}_i(n)\|^2} \quad (2.7)$$

and

$$f_I(\omega) = 1 - PDOS_M(\omega) \quad (2.8)$$

This is shown in Fig. 2.5 (b), for $\frac{E_i}{E_m} = 0.2$ and $R = 25 \text{ \AA}$. Since the inclusion is much softer, its vibrational modes are softer than the ones of the matrix, and indeed its contribution to the VDOS is limited to frequencies smaller than $\approx 6 \text{ THz}$. The relative ratio of the matrix to the inclusion contribution to the VDOS is reported in Fig. 2.5 (c) for $R = 25 \text{ \AA}$ and different values of $\frac{E_i}{E_m}$. It is clear that the frequencies corresponding to a specific response of the inclusions progressively increase with the inclusion rigidity. In the most rigid case, when $\frac{E_i}{E_m} = 10$, the high frequency modes are mainly supported by the inclusions, while in softer cases, the response of the inclusions is mainly located below 6 THz. Only for a very weak rigidity contrast, such as $\frac{E_i}{E_m} = 1.2$, it is not possible to clearly identify a specific range for a dominating contribution from the inclusions. From this, we can conclude that by exploring rigidity contrasts ranging from 0.2 to 10, we are able to observe a phenomenology corresponding to all possible situations : from the case where the low frequency modes are mainly supported by the inclusions (low $\frac{E_i}{E_m}$) up to the case where the the inclusions resonate at frequencies higher than the response of the matrix ($\frac{E_i}{E_m} = 10$).

2.2 Representative normal modes

Fig. 2.6 allows to visualize the spatial extent of the eigenmodes for different frequencies and rigidity contrasts. The low frequency vibrations for $\frac{E_i}{E_m} = 0.2$ are clearly supported by the inclusions, that appear to become mute at high frequency, while the matrix dominates the response at low frequency in the most rigid system with $\frac{E_i}{E_m} = 10$. If the effect is stronger for stronger rigidity contrasts (0.2 and 10), in all cases the presence of the inclusions affects the eigenmodes, giving rise to a very inhomogeneous spatial distribution, in some frequency ranges. Sometimes, it becomes difficult to locate the interfaces in the complex shape of the vibration modes (see for example $E_i/E_m=0.2$ and $\nu = 0.790191 \text{ THz}$ in Fig. 2.6-a) The question thus arises how such complex spatial vibrational heterogeneity can affect the transient propagation of traveling wave-packets in our systems.

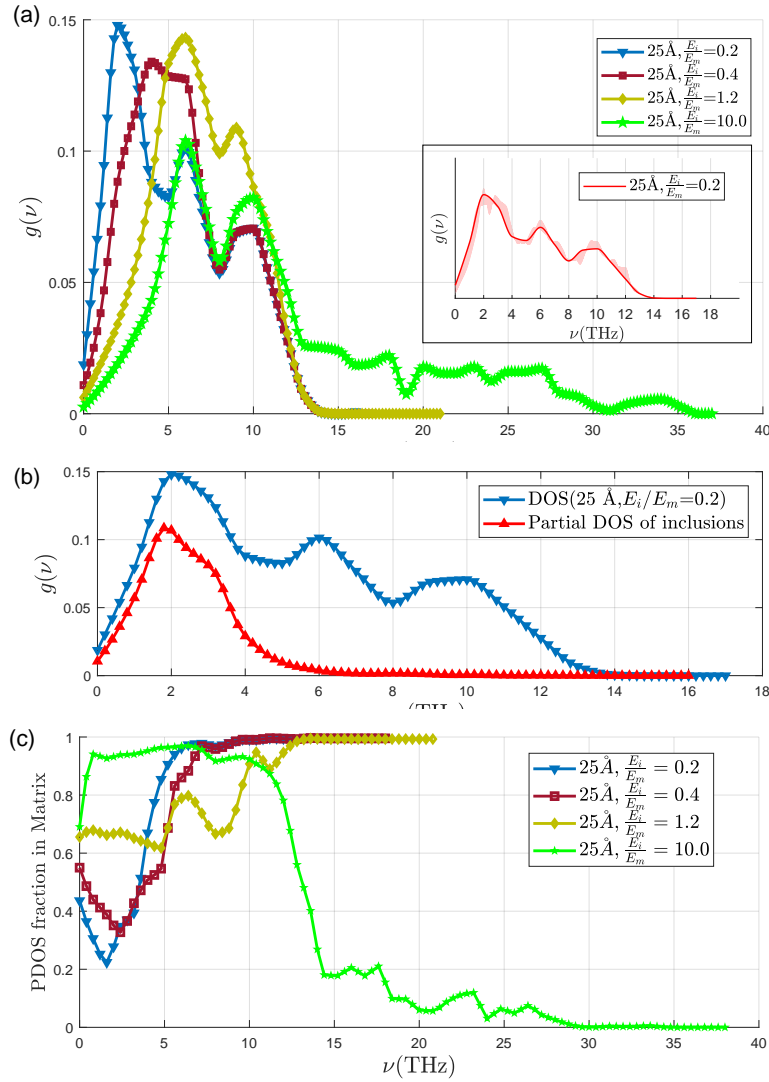


FIGURE 2.5: From top to bottom : (a) The VDOS for $R = 25 \text{ \AA}$ and $\frac{E_i}{E_m} = 0.2, 0.4, 1.2, 10.0$ at discrete frequencies ν with width $\Delta\nu = 1 \text{ THz}$. Inset : VDOS vs ν for $\frac{E_i}{E_m} = 0.2$ and $R = 25 \text{ \AA}$. The red line corresponds to $\Delta\nu = 1 \text{ THz}$, while the shaded region to a $\Delta\nu$ varying between 0.4 and 1 THz (b) VDOS (blue) and partial DOS of inclusions (red) for $R = 25 \text{ \AA}$ and $\frac{E_i}{E_m} = 0.2$ (c) Fraction of VDOS supported by the matrix for $R = 25 \text{ \AA}$ and different values of $\frac{E_i}{E_m}$, at discrete frequencies ν with $\Delta\nu = 1 \text{ THz}$ (Triangle, square, diamond and pentagram symbol are used to indicate $\frac{E_i}{E_m} = 0.2, 0.4, 1.2$ and 10.0 respectively).

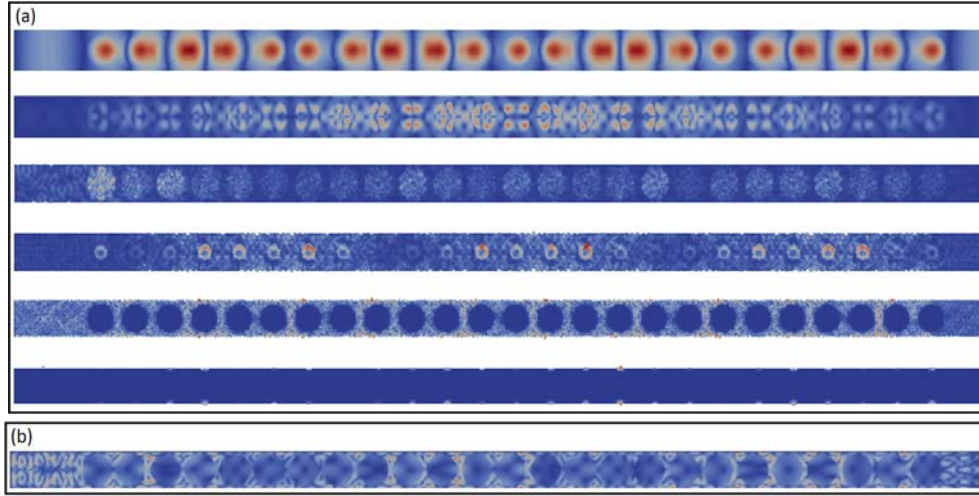


FIGURE 2.6: (a) Visualization of the normal modes obtained in the system with $\frac{E_i}{E_m} = 0.2$ and $R = 25 \text{ \AA}$. The frequencies of the characteristic normal modes (from top to bottom) are : $\nu = 0.325195 \text{ THz}$ ($\omega = 2\pi\nu = 2.04 \text{ THz}$); $\nu = 0.790191 \text{ THz}$ ($\omega = 4.96 \text{ THz}$); $\nu = 2.00000 \text{ THz}$ ($\omega = 12.57 \text{ THz}$); $\nu = 3.99998 \text{ THz}$ ($\omega = 25.13 \text{ THz}$); $\nu = 6.00019 \text{ THz}$ ($\omega = 37.70 \text{ THz}$); $\nu = 14.22239 \text{ THz}$ ($\omega = 89.36 \text{ THz}$). (b) Visualization of one normal mode obtained in the system with $\frac{E_i}{E_m} = 10$ and $R = 25 \text{ \AA}$. The frequency of the mode is : $\nu = 2.00281$ ($\omega = 12.58 \text{ THz}$).

3 Wave-Packet Propagation : Different Regimes

In this section, I will focus on wave propagation in a nanocomposite material. I will show evidence of three different regimes : propagative, diffusive and localized, induced by the presence of interfaces. Firstly, I present the envelope of the kinetic energy which shows the maximum amplitude of the kinetic energy at each location, as the wave-packet goes through the sample. At the same time, visualization of the results (snapshot of wave propagation) are given to have more intuitive pictures about them. Then, mean-free path and diffusivity are computed for the propagative and diffusive regime, respectively. Finally, a parametric study of the different regimes of acoustic transfer is performed as a function of the frequency (2, 5 and 7 THz) versus the relative rigidity E_i/E_m and the size of the inclusions R . The result is displayed on a phase diagram where the three aboved mentioned regimes appear, as well as mixed regimes dicussed in the text.

3.1 Envelope of the kinetic energy

The wave-packet created on the left side of the sample, propagates along the sample, in the x direction. Due to the presence of interfaces, and related spatial inhomogeneities, the wave-packet wave-vector k does not remain constant, the wave-packet being scattered by the inclusions. To understand how such scattering affects the energy transfer, we measure the envelope of the kinetic energy induced in the system by the propagation of the wave-

packet, averaged over the y-direction. The energy envelope is defined for each excitation frequency ω as

$$P_\omega(x) = \max_t E_k(x, t) \quad (2.9)$$

where $E_k(x, t)$ is the instantaneous kinetic energy supported by the frame located in x with width $\Delta x = 2 \text{ \AA}$.

As an example, we report in Fig. 4.4 the kinetic energy envelope (red curve) for longitudinal excitations with inclusions radius $R = 25 \text{ \AA}$ at a wave-packet frequency of $\omega = 5 \text{ THz}$, for different rigidity contrasts. Note that the wavelength for transverse plane waves in the matrix at this frequency is $2\pi c_T/\omega = 48 \text{ \AA}$, and the wavelength for longitudinal plane waves in the matrix is $2\pi c_L/\omega = 100 \text{ \AA}$. Instantaneous wave-packets (green and blue curves) are shown for clarity. The positions of the inclusions are indicated by the gray area delimited by dotted lines. It is clear that the envelope presents oscillations correlated with the presence of interfaces. Moreover, the inclusions cause a more or less efficient attenuation of the kinetic energy along the main direction of propagation. Since the simulations are performed at constant energy (no damping term in the numerical scheme), the observed attenuation is not related to a global dissipation of energy, but it is due to a redistribution of the kinetic energy in directions different from the one of propagation, so that, when averaging this effect along the transverse y-direction, an effective attenuation along the x-direction appears.

To confirm our interpretation of the energy envelope behavior, we report in Fig. 2.8 the displacement field at $t=7.9463 \text{ s}$ for $\omega = 5 \text{ THz}$ and different rigidity contrasts. Here we can see that at this frequency for a soft inclusion (Fig. 2.8 (a)) the wave-packet looks pinned inside the inclusions, while for no rigidity contrast ($E_i = E_m$) it is insensitive to their presence and propagates without any perturbation (Fig. 2.8 (d)). It is worth underlying that all snapshots have been taken at the same time, which clearly shows that the effective velocity of the wave-packet increases with the inclusion rigidity, so that when inclusions are more rigid than the matrix the wave-packet is accelerated (Fig. 2.8(e)). Moreover, except for the case of no contrast, the wave-packet is always spread, and thus attenuated, along the x-direction.

3.2 Different propagation regimes

In order to understand the energy transfer along the x-direction in the different cases, we calculate the average position of the wave-packet by the weighted arithmetic average

$$\langle x \rangle(t) = \frac{\sum_i x_i E_k(i, t)}{\sum_i E_k(i, t)} \quad (2.10)$$

Considering this average position, three propagation behaviors can be identified :

1. Propagative regime $\langle x \rangle(t) \propto Vt$
2. Diffusive regime $\langle x \rangle(t) \propto (2Dt)^{\frac{1}{2}}$

2. Acoustic attenuation in the presence of elastic inclusions

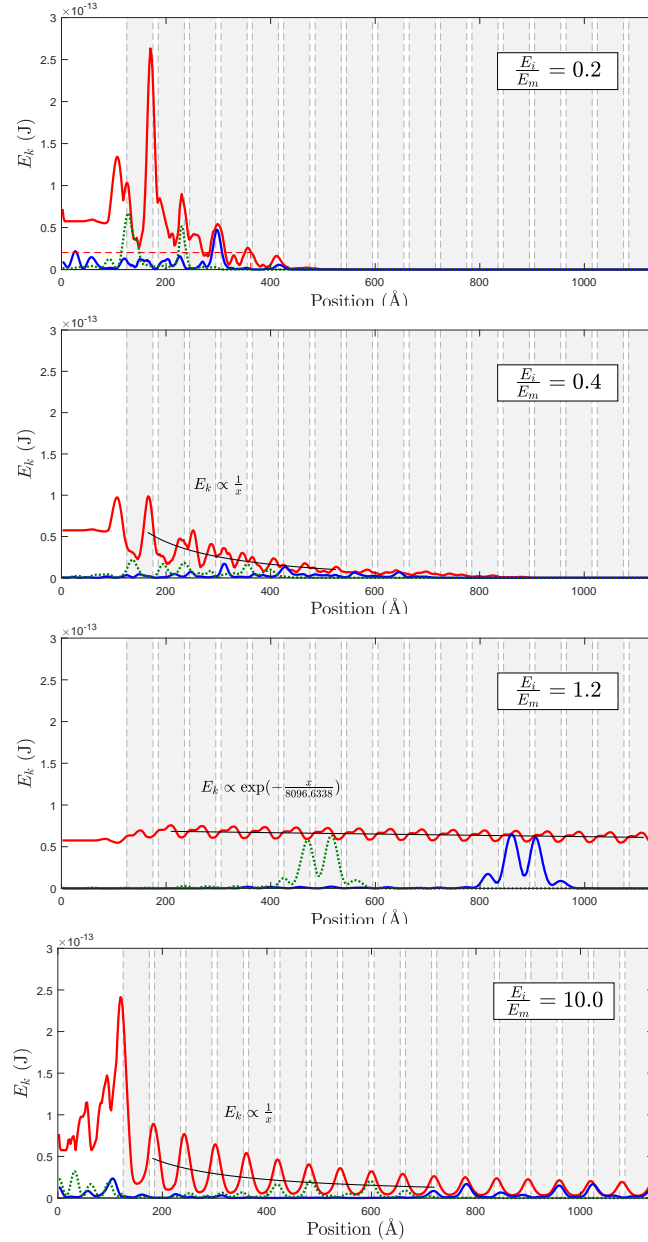


FIGURE 2.7: The envelope of kinetic energy for different rigidity contrasts for $\omega = 5$ THz, $R = 25 \text{\AA}$ is reported as a red line, while the instantaneous distribution of kinetic energy is given at $t=7.9463$ ps (green dotted line) and at $t=12.7174$ ps (blue line).

Gray areas delimited by dotted lines indicate the positions of the circular inclusions.

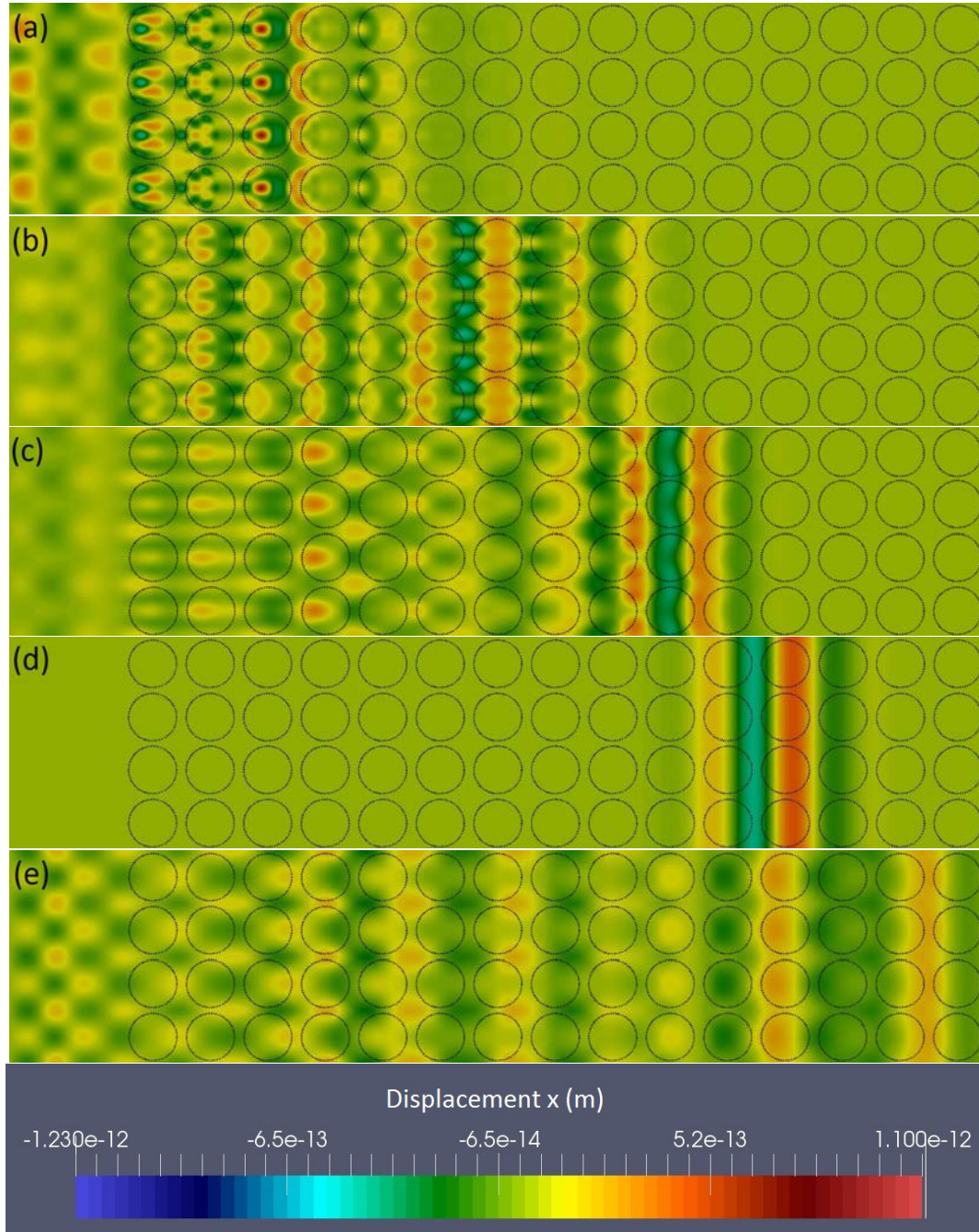


FIGURE 2.8: Snapshots of 5 cases at the same time ($t = 1.27171 \times 10^{-11}$ s) with $\omega = 5$ THz and $R = 25 \text{ \AA}$ (dashed circles indicate the positions of the inclusions) (a) $E_i/E_m = 0.2$ (b) $E_i/E_m = 0.4$ (c) $E_i/E_m = 0.6$ (d) $E_i/E_m = 1.0$ (e) $E_i/E_m = 2.0$.

3. Localized regime $\langle x \rangle(t) \propto cst$

The *propagative* regime is also called *ballistic* regime in literature, from which an evident speed of the propagating wave can be observed. In this regime, interfacial effects being weak, wave-packet can still maintains its general shape and the major parts moves forward with few parts being scattered from their original propagation direction. In the *diffusive* regime, wave-packet encounters strong scattering, being dispersed, stretched and separated. Some parts move forward, but more is left behind. No longer a single speed can be attributed for this wave-packet, and its propagation behavior is analogous to a diffusive thermal transport, *i.e.* the Fourier's Law, from which a diffusivity is defined. The last regime is the *localized* one, for which the average position oscillates around a constant value for a long time.

For example, fig. 2.9(a) shows a representative set of different regimes of energy transfer at $\omega = 5$ Thz :

- The case $\frac{E_i}{E_m}=0.4$ (green dots) is a clear example of *diffusive* regime where $\langle x \rangle \propto \sqrt{t}$;
- The case $\frac{E_i}{E_m}=1.2$ (yellow dots) yields to a propagative regime $\langle x \rangle = v_L \cdot t$.

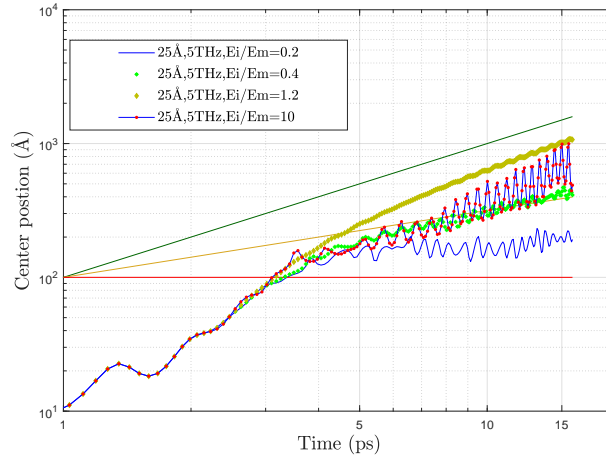
The other cases shown in this figure are more complex :

- The most rigid case $\frac{E_i}{E_m}=10$ (red dots with blue line) is initially similar to a diffusive regime, but becomes progressively propagative,
- In the very soft case $\frac{E_i}{E_m}=0.2$ (blue line) the wave-packet is initially pinned ($\langle x \rangle = cst$) and progressively gets unpinned following a diffusive motion.

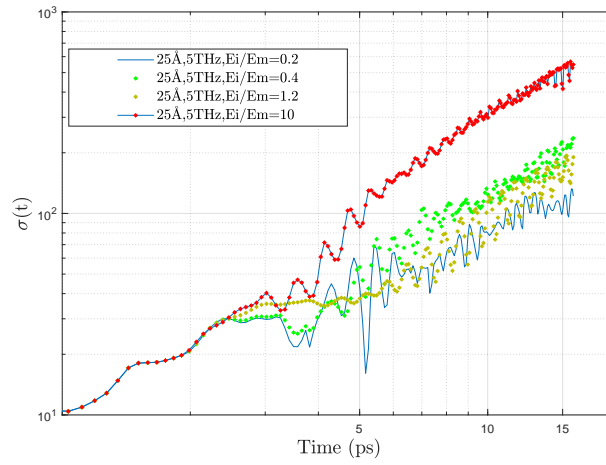
For $\frac{E_i}{E_m}=0.2$, as shown in Fig. 4.4 (a), the attenuation is extremely efficient and the energy seems pinned at the interface between the first inclusion and the matrix, on the inclusion's side. Even if its energy is not strictly localized, the pinning induces a small delay in the energy transfer.

3.3 Phase diagram of propagation regimes

We have build a frequency dependent phase diagram for different dynamical regimes based on the effective time dependence of energy transportation : propagative, diffusive, localized or mixed. The different regimes of energy transfer and their dependence on the parameters are summarized in Fig. 2.10 : here it can be seen that when increasing rigidity contrast and frequency, an increasingly complex behaviour arises. Softer inclusions induce the most complex behaviour over large frequency ranges. The departure from the propagative regime is more pronounced for large rigidity contrasts (especially for softer inclusions) and for high frequencies (when the incident wavelength becomes comparable to the inclusions size). This effective behaviour results from various phenomena : scattering at matrix/inclusion interfaces, waves interference[XIE 18, TIA 10, MAI 17], waves reflexion on curved surfaces inducing billiard motion[SCH 98], gallery modes along the



(a) Center position



(b) Standard deviation

FIGURE 2.9: (a) Time dependence of the wave packet center position for different rigidity contrasts. We report as well the expected behaviors for propagative regime $\langle x \rangle(t) \propto Vt$ (green line), diffusive regime $\langle x \rangle(t) \propto (2Dt)^{\frac{1}{2}}$ (yellow line) and localized regime $\langle x \rangle(t) \propto cst$ (red line). (b) Standard deviation versus time calculated by Eq. 2.13.

interfaces[MCC 92, VER 06], or acoustic resonances of the inclusions. In any case, the

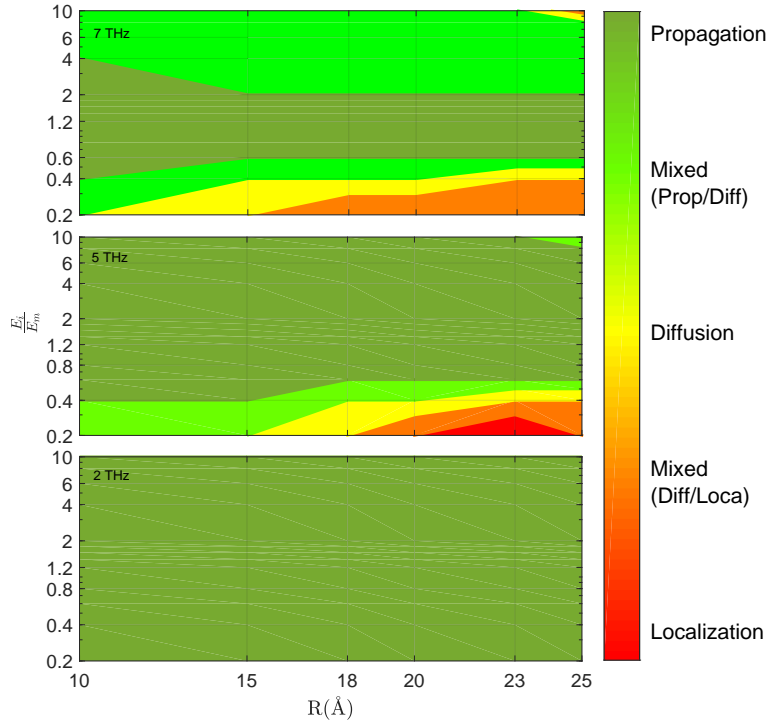


FIGURE 2.10: Visualization of the different dynamical regimes of the Wave Packets (propagative, diffusive, localized), as a function of the radius R of the inclusions and of the relative rigidity E_i/E_m for frequencies ω ranging from 2 to 7 THz.

3.4 Meaningful quantities for describing different dynamical regimes

Different dynamical regimes lead to very different behaviors of the envelope of kinetic energy as a function of the wave-packet path. As such, we can identify different physical quantities for characterizing the propagation of the wave-packet in the different regimes. For example, in case of a weak rigidity contrast (Fig. 4.4 (c)) a global exponential attenuation similar to a Beer-Lambert law is observed[SWI 62, BEL 18]

$$P_\omega(x) \propto \exp(-x/\Lambda(\omega)) \quad (2.11)$$

while for larger rigidity contrasts (Fig. 4.4 (b) and (d)), the algebraic attenuation of the envelope

$$P_\omega(x) \propto 1/x \quad (2.12)$$

is the signature of a diffusive process [BEL 18]. The spreading of the envelope can be quantified by the standard deviation :

$$\begin{aligned}\sigma(x, t) &= \sqrt{\langle (x - \langle x \rangle)^2 \rangle} \\ &= \sqrt{\frac{\sum_i (E_k(i, t) \times x_i^2)}{\sum_i E_k(i, t)} - \langle x \rangle^2}\end{aligned}\quad (2.13)$$

where x_i is the position of the i^{th} frame with width Δx in the x -direction, and $E_k(i, t)$ is the instantaneous total kinetic energy supported by that frame. The spreading $\sigma(x, t)$ can also be rewritten

$$\sigma(x, t) = \sqrt{R^2(t) - \langle x \rangle^2} \quad (2.14)$$

by introducing R^2 , the squared width [BEL 16] defined as

$$R^2(t) = \frac{\int_{-\infty}^{\infty} x^2 E(\omega, x, t) dx}{\int_{-\infty}^{\infty} E(\omega, x, t) dx} \quad (2.15)$$

In case of a diffusive process, $\sigma^2(t)$ is proportional to the time t , with a slope related to the one-dimensional diffusivity.

$$\sigma^2(t) = 2D(\omega)t. \quad (2.16)$$

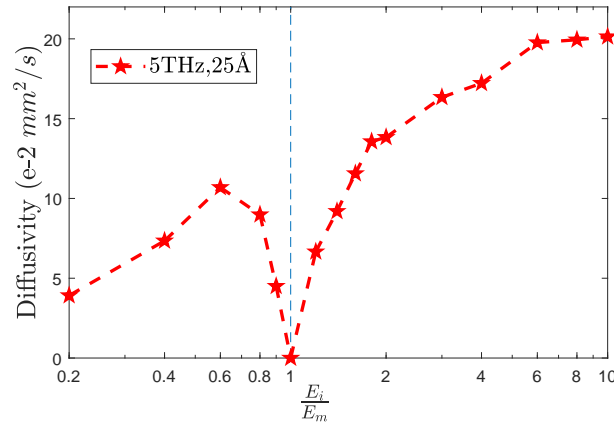


FIGURE 2.11: Diffusivity obtained from Eq. (2.16), for different values of the rigidity contrast E_i/E_m .

The diffusive spreading of the wave packet can thus be quantified by the diffusivity parameter D (Eq. 2.16). The dependence of D on the rigidity contrast is shown in Fig. 2.11 for $\omega = 5$ THz. It is globally increasing with ω but exhibits a deep minimum for $E_i/E_m \approx 1$. The most interesting range for reducing energy transfer thus appears to be the low- E_i/E_m range, where the low diffusivity is not counterbalanced by an important

propagative contribution, as it is the case for $E_i/E_m \approx 1$, whose dominant contribution to energy transfer is the propagative one. Note that the largest spreading of the wave-packet takes place in the highest rigidity contrast case, $E_i/E_m = 10$ (Fig. 2.9(b)), due to the wave-packet acceleration within the inclusions.

In order to get a quantitative insight on the energy transfers, comparing the different dynamical regimes, in presence of inclusions with rigidity contrast, we can define a parameter describing the spatial penetration of the energy envelope beyond the effective shape of this latter. This is illustrated in the next section, where we extend the study mainly reported here for $\omega = 5$ THz and $R = 25$ Å, to a large range of inclusions volume fractions and excitation frequencies and perform an extensive parametric study of this spatial attenuation.

4 Penetration Length

Depending on the dynamical regime, the characteristic length that describes energy transfer is not unique, which makes it difficult to compare different regimes. For example, in the propagative regime the characteristic length is the mean free path $\Lambda(\omega)$ which can be fitted by the Beer-Lambert law as mentioned above. In the diffusive regime, the energy envelope follows an $1/x$ decay without any intrinsic lengthscale, which depends only on the initial energy [BEL 18]. The ability for heat transfer is then better quantified by the diffusivity (see previous section), which directly enters in the computation of the thermal conductivity, although absent from the attenuation behavior of the envelope. Finally, in the case of an energy envelope pinned over a small length l_{pin} , this latter will be the characteristic length. In order to quantify the ability of a system for energy transfer, independently on the dynamical regime, we look at the long-time penetration length. In the following, the penetration length will be presented and be used to compare the attenuation ability in the different regimes.

4.1 Definition of the Penetration length

The penetration length is defined as the traveled length above which the energy per unit length remains always smaller than the maximum excitation energy per unit length divided by e :

$$P_\omega(x \geq l_p) \leq \frac{1}{e} P_\omega(x = 0) \quad (2.17)$$

This definition allows us to take into account the presence of oscillations in the energy envelope, which would mine the standard definition of penetration length. Concerning the three regimes cited above, this length will correspond to the mean free path in the propagative case, be very close to l_{pin} for a pinned energy envelope, and be representative of the energy spread in the sample in the diffusive case. We have measured the penetration length l_p as a function of the inclusion radius, ranging from 10 to 25 Å (corresponding to

volume fractions from 8.7% to 54.5% in 2D), of the rigidity contrast, ranging from 0.2 to 10, and of the excitation frequency, ranging from 2 THz to 14 THz.

Note : In this work, we only measured the penetration length on the original envelopes. Due to the large oscillations causing local maximum energy ('peak'), multiple measurements on smoothed envelopes (with different smoothing levels) would be more convenient. We have made these modification in our analysis in other works, which has shown us that only few cases are affected by this local peaks. As such, the current measurements are still convincing.

4.2 Penetration length vs $\frac{E_i}{E_m}$ & R for $\omega = 5$ THz

In Fig. 2.12 we report the radius and rigidity contrast dependence for a wave-packet of frequency 5 THz, as representative for all frequencies. First, it can be seen that the penetration length decays with the radius R of the inclusion, that is, with the size $2\pi R$ of the interface. The penetration length reaches a minimum close to $R = 25 \text{ \AA}$. For larger radii, the inclusions will be separated by less than a few angstroms, almost touching each other, thus opening a continuous path for the acoustic energy transfer and consequently increasing the attenuation length l_p .

Second, the penetration length strongly decreases also with the rigidity contrast, but there is a clear asymmetry between the case $E_i > E_m$ and the case $E_i < E_m$. Indeed, the more rigid inclusions induce an acceleration of the acoustic waves (larger sound velocity as shown in Fig. 2.8) together with a marked broadening of the wave-packet (Fig. 2.9(b)), and these two effects result in an increased penetration length. It can be concluded that for the same rigidity contrast (same ratio of acoustic impedances), the softer inclusions will more efficiently limit the penetration of the wave-packet inside the sample. However, the penetration length is not strictly a monotonous function of the rigidity contrast, but goes through a minimum, whose value depends on the excitation frequency. For $\omega = 5$ THz and $R = 25 \text{ \AA}$ for example, two minima can be found, close to $E_i/E_m = 4$ and $E_i/E_m = 0.4$. Note that in all cases, the attenuation length remains larger than the inclusions size, approaching the distance between three inclusions at its minimum value.

4.3 Penetration length vs $\frac{E_i}{E_m}$ & ω for $R=25 \text{ \AA}$

In Fig. 2.13 we report the frequency and rigidity contrast dependence for a wave-packet of radius 25 \AA , as representative for all radii. At 5THz, the penetration length for a more rigid inclusion is always longer than for soft inclusions, it is however possible to reverse the situation and get a more efficient sound attenuation with rigid inclusions if another excitation frequency is used. Indeed, as shown in Fig. 2.13 (a), the penetration length depends on the frequency and, for rigid inclusions, displays a clear minimum at 7 THz. This effect is due to a resonance of the inclusions that will keep the acoustic energy. Indeed, as seen in Fig. 2.13(b), the frequency of the minimum in the penetration length evolves linearly with the sound velocity within the inclusion, meaning that inclusions specific vibrations play a key role in determining the frequency dependence of l_p . This

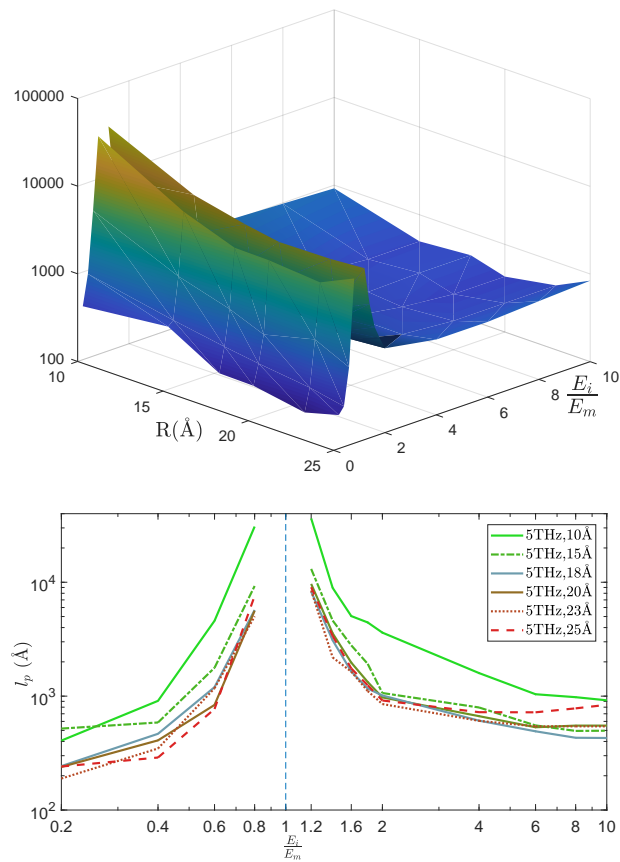


FIGURE 2.12: Penetration length $l_p(\frac{E_i}{E_m}, R)$, with $\frac{E_i}{E_m}$ the stiffness ratio and R the radius of inclusion for the frequency of wave packets $\omega=5\text{THz}$.(Top : 3D Bottom : 2D)

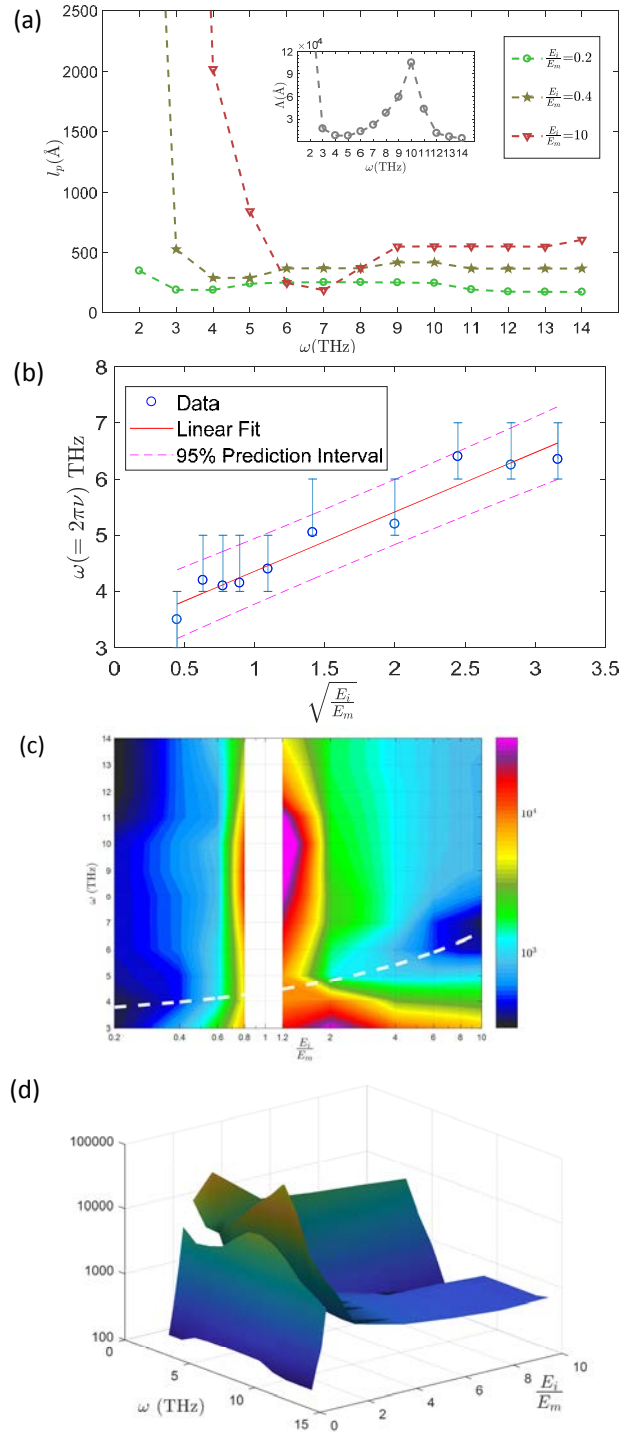


FIGURE 2.13: (a) Penetration length $l_p(\omega)$ for $\frac{E_i}{E_m} = 0.2, 0.4$ and 10.0 , with $R = 25 \text{ \AA}$. Inset : mean free paths Λ vs ω for $\frac{E_i}{E_m} = 1.2$ and $R = 25 \text{ \AA}$. (b) Frequency, which corresponds to the minimum l_p for each $\frac{E_i}{E_m}$ for $R = 25$. (c) Color representation of the penetration length in the parametric space $(E_i/E_m, \omega)$ for $R = 25$ (d) Idem in a 3D plot.

resonant effect is reported in the Fig. 2.13 (c) with white long-dashed line showing the proportionality in the minimum frequency with the sound velocity (in log-linear scale). A 3d plot (Fig. 2.13 (d)) underlines this non-monotonous dependence of the penetration length on the frequency, especially in the high rigidity case that appears to be the most selective with the frequency.

To conclude this part, our numerical measurements have allowed us to definitely assess the following : i) far from a resonance of the inclusions, the penetration length will decrease with the interface size, provided that there is no inclusions percolation, ii) the attenuation is globally more efficient for softer inclusions, apart from specific excitation frequencies. The dependence of the penetration length on the three investigated parameters (interface size, rigidity contrast and excitation frequency) is however complex and not monotonous, although it exhibits a sufficiently smooth behavior. It should thus exist a continuous trajectory in the three-parameter space relating local minima of the penetration length, and suggesting an efficient optimization of the acoustic attenuation.

5 Discussion and conclusion

In the previous parts, we have shown that wavepackets dynamics results from a complex mixture of scattering, resonances and propagation. The deviation from the initial direction of propagation leads to an effective attenuation of the energy in the direction of propagation, also described as an apparent dissipation in the transient regime. The goal of our study was to perform a systematic parametric study of this apparent attenuation, using modelisation tools related to continuum mechanics approaches. Our numerous finite element calculations have revealed that the dependence of the attenuation length on the different parameters is far from simple, and exhibits the following non monotonous behaviours : 1) with respect to the volume fraction, and thus the interface area, suggesting the existence of optimal inclusions radius and interface area, allowing for an efficient scattering without leading to any percolation between the inclusions; 2) with respect to the rigidity contrast. Softer inclusions clearly appear as more efficient for energy attenuation, but the rigid inclusions are also able to pin the vibrational energy, and thus suddenly decrease the attenuation length, at specific frequencies ; 3) with respect to the excitation frequency, as due for example to the previously mentioned inclusions resonances, which contribute to pin the energy at a given frequency or also to the reduction of the wavelength which becomes comparable with the nanostructure characteristic length (radius and inter-inclusions distance).

It is shown here that systems with softer inclusions have more effect on a global attenuation averaged over all frequencies, thus contributing clearly to decrease the thermal conductivity. The same conclusion holds for the diffusivity that increases with the inclusions rigidity when the diffusive regime matters.

The continuum mechanics description of nano-composite materials used here is clearly a simplified description of real systems, both perfectly periodic nanophononic materials and nanocomposites with randomly distributed inclusions such as the one in

Fig. 2.1, since only interfacial effects on the acoustic attenuation and thermal diffusivity are here taken into account with model interfaces. Other scattering sources such as anharmonicity, thermal activation, or disorder are all neglected, as well as the acoustic dispersion due to atomic discretization. Despite such well-circumscribed simplifications, our parametric study uses continuum calculations to catch the physics behind energy transport in nanophononic materials and can serve as a guide for materials design and optimization. The model can be used as a basis that could be improved to take progressively into account additional effects. Looking at Fig. 2.13 for example, it is clear that our material can be optimized for energy transport enhancement or inhibition, by choosing the parameters in order to enhance or reduce the acoustic attenuation (the same for the diffusivity) at a given wave-packet frequency. Interestingly, the figure suggests also that such a system could be used as acoustical spectrometer : the attenuation length shows a marked decrease at a characteristic frequency depending on the rigidity ratio, especially in the case of tougher inclusions. A systematic backup of the results for given sets of parameters could now be used to perform real time simulations [LU 18a, LU 18b].

The generalisation of our results to amorphous-based nanophononic or nanocomposite materials, such as the one reported in Fig. 2.1, is however not so trivial, as a strong energy dissipation due to structural disorder is already present even in the absence of interfaces [BEL 18, DAM 15]. Such materials being today at the focus of an intense research for technological applications, it will be of interest to extend the present parametric study to amorphous/nano-crystalline composites, in order to assess the thermal transport regime in presence of a strong intrinsic energy dissipation together with the artificially introduced (through the nanostructuring) dissipation channel. This will likely require a continuum description of the materials mechanical properties using a frequency dependent visco-elastic constitutive law [SCH 15a, LUO 20].

Finally, it is worth noticing that these results could have direct applications for high frequency nanophononic materials as acoustic filters for example. Such an approach is also useful to identify the general trends affecting the phononic contribution to thermal conductivity. It gives however an overestimation of the thermal conductivity, since more quantitative calculation needs to take into account the atomic scale dispersive contribution to the vibrational density of states, together with atomic scale scattering processes controlling the diffusivities in the strong diffusive regime at THz frequencies in glasses. Within this clearly identified limitation, this parametric study on attenuation can be used to optimize different properties : for example the acoustic attenuation at a given frequency, but also the diffusivity of kinetic energy, and thus the thermal conductivity.

Chapter 3

Mechanical response and acoustic attenuation for different types of interfaces

Four additional types of interfaces are implanted in our FE codes : the elastic inclusion with dendritic interface, the Eshelby's inclusion, the disorder porous medium and random elasticity. Different studies on the mechanical response and/or acoustic attenuation have been carried out assuming elastic behavior in the matrix. The four themes are independent, but they are intimately related : they all allow exploring how to simulate different interfacial effects on acoustic resonance, wave packets propagation and apparent attenuation. Depending on the application scenarios, these studies provide a wider range of ideas for the subsequent research.

Contents

1	Dendritic inclusion	53
1.1	Dendrite phase in metallic glass	53
1.2	Reconstruction of the dendritic shape inclusion	55
1.3	Finite element simulation	57
1.4	Acoustic transport in an isotropic homogeneous material with dendritic inclusions	57
1.5	Measurement of the sound speed	61
1.6	Discussion	68
1.7	Conclusion and perspectives	69
2	Eshelby's inclusion	70
2.1	Ellipsoidal Eshelby's Inclusion	70
2.2	Implementation in the FE code	71
2.3	FE simulation by varying the ratio b/a	74
2.4	Wave propagation in a medium with an Eshelby's inclusion	81
2.5	Conclusion and perspectives	81
3	Nano-porous materials : from perfectly periodic to disordered holes arrangement	84
3.1	Porous structure	84
3.2	The optic-like approach to phonon scattering from periodic interfaces	84
3.3	Model of nano-porous structure : ordered and disordered	89
3.4	Estimation of the coherence length	91
3.5	Results : Envelopes of the kinetic energy	92
3.6	Discussion	94
3.7	Conclusion and perspectives	96
4	Acoustic attenuation in a medium with heterogeneous elasticity	97
4.1	Introduction of the vibrational anomalies in glasses in the terahertz range	97
4.2	Introduction of the theory of heterogeneous elasticity	98
4.3	Wave propagation in a medium with heterogeneous elasticity	102
4.4	Discussion	106
4.5	Conclusion	108

1 Dendritic inclusion

In this work, we look at a multi-branching tree-like shaped, dendritic structure, whose fractal property determines a high interface density. A SEM image of the as-cast $\text{Ti}_{45}\text{Zr}_{25}\text{Nb}_6\text{Cu}_5\text{Be}_{17}\text{Sn}_2$ is shown in Fig.3.1[ZHA 16]. Intuitively, this high-interface-density composite is ideal material to enhance phonon-interface scattering compared to the simple geometry. But a deep understanding of its dynamic properties is still lack, a out-of-equilibrium acoustic wave propagation in such medium is needed. The dendrite phase distributes homogeneously in the glass matrix. In the following, we will firstly give a brief presentation of the preparation of the sample and its real materials properties. Then, instead of looking into the whole domain, we select one characteristic cluster of dendrites based on which we will reconstruct the mesh and study the shape-induced impact on the wave propagation using FE simulation. Parametric studies, similar to the work for the circular inclusion in the Chap.2, will be done for the matrix with the dendritic inclusion, tuning the rigidity contrast E_i/E_m and the frequency ω of the wave-packets. Two extreme cases of the rigidity contrast will be considered : $E_i/E_m = 0.2$ and 10.0 .

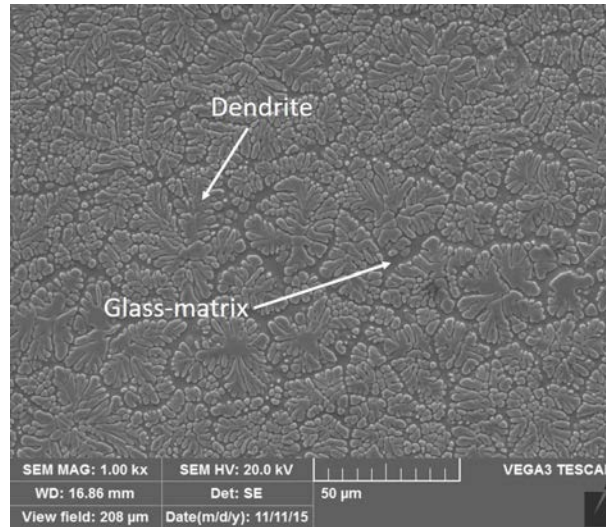


FIGURE 3.1: Cross sectional SEM images of the as-cast $\text{Ti}_{45}\text{Zr}_{25}\text{Nb}_6\text{Cu}_5\text{Be}_{17}\text{Sn}_2$, the dendrite-phase (light gray) distributes homogeneously in the glass-matrix (dark gray).

1.1 Dendrite phase in metallic glass

Bulk metallic glasses (BMGs) are promising structural materials because of their excellent properties such as high yield strength, excellent corrosion resistance and low stiffness[ZHA 16, JOH 99, QIA 16b, INO 11]. However, BMGs lack ductility and always fail in an apparently brittle manner, which seriously limits their applications

[QIA 17, SCH 07, SCH 09, QIA 16a]. The origin of this poor ductility is the strong spatial localization of plastic rearrangements, likely to line up along shear bands. Recently, in-situ introducing a second ductile phase into the glass-matrix, *i.e.*, metallic glass matrix composites (MGMCs), has been reported to inhibit the catastrophic failure due to the propagation of shear bands and thus improve the global plasticity. In-situ formed β -Ti dendrite-phase displays a plastic strain of 6% [HAY 00, GEN 20]. A larger dendrite-phase size offers higher ductility but decreases the yield strength of composites. In addition, the alloy compositional design could be used to modulate the mechanical properties of the BMG, indicating a possibility of tuning, for example, the stiffness ratio E_i/E_m as discussed in the last chapter. Besides the improvement of the ductility, the high density of interfaces in such composites has attracted our attention, which has potentially good sound attenuation performance due to the phonon-interface scattering. Our collaborator R. Yue from the Laboratory of Solidification Processing of NWPU has provided some SEM images of the Ti-based metallic glass containing dense dendrite phase [ZHA 16, XU 18]. The preparation and mechanical properties of these materials will be presented in the following. However, for our FE simulations we have chosen to use the same mechanical properties as in Chapter.2, referring thus to a well known system. This choice is motivated by the possibility to compare wave-packet propagation results on circular inclusions with the ones on dendritic inclusions and thus get a direct understanding of the impact of a fractal-like interface shape.

1.1.1 Material composition and preparing process

Ingots with nominal composition of $\text{Ti}_{45}\text{Zr}_{25}\text{Nb}_6\text{Cu}_5\text{Be}_{17}\text{Sn}_2$ are prepared by arc-melting the mixture of high purity elements (>99.9wt%) under a Ti-gettered argon atmosphere. The ingots were re-melted at least five times to ensure the homogeneity. Plate samples ($5 \times 20 \times 60$, mm) are prepared by casting into a water-cooled copper mold. The dendrite phase (light gray regions) was found to distribute uniformly within the featureless glass matrix (dark gray regions). Volume fractions and sizes of the dendrite phase are analyzed by the Image-Pro Plus software and resulting in a volume fraction 65.8 ± 2.0 .

1.1.2 Mechanical properties

Alloy	σ_y (MPa)	ϵ_y (%)	σ_u (MPa)
$\text{Ti}_{45}\text{Zr}_{25}\text{Nb}_6\text{Cu}_5\text{Be}_{17}\text{Sn}_2$	913	1.44	1521
ϵ_u (%)	E (GPa)	G (GPa)	ν
10.12	85.23 ± 0.22	31.23 ± 0.13	0.365 ± 0.005

TABLE 3.1: Mechanical and intrinsic properties of the $\text{Ti}_{45}\text{Zr}_{25}\text{Nb}_6\text{Cu}_5\text{Be}_{17}\text{Sn}_2$ BMG composites. Yielding strength (σ_y), yielding strain (ϵ_y), ultimate tensile strength (σ_u), tensile strain till necking (ϵ_u), Young's modulus (E), shear modulus (G) and Poisson's ratio (ν) [XU 18].

Phase component	E (GPa)	H (GPa)
Dendrite-phase	86.4 ± 4.1	3.78 ± 0.39
Glass-matrix	113.8 ± 2.5	6.13 ± 0.41

TABLE 3.2: Young’s modulus (E) and Hardness (H) of the dendrite-phase and glass-matrix in the $\text{Ti}_{45}\text{Zr}_{25}\text{Nb}_6\text{Cu}_5\text{Be}_{17}\text{Sn}_2$ BMG composites measured by the nanoindentation. [ZHA 16].

1.2 Reconstruction of the dendritic shape inclusion

1.2.1 SEM image to FEM mesh

In the present work, instead of looking at the whole dendrite domain, we focus on a cluster of dendritic structure as shown in Fig. 3.2(1) which is extracted from Fig. 3.1. It is interesting to investigate on this representative zone whose global shape seems to be comparable to a circular inclusion, while its internal tree-like structure may induce different acoustic features. To this aim, a non-dimensional analysis is expected to be carried out by scaling the above cluster of dendrite and the circular inclusion to a quasi-equivalent dimension. As shown in Fig. 3.2, this cluster of dendrite is encapsulated inside a square block. The square block containing a dendritic inclusion is then used as elementary brick

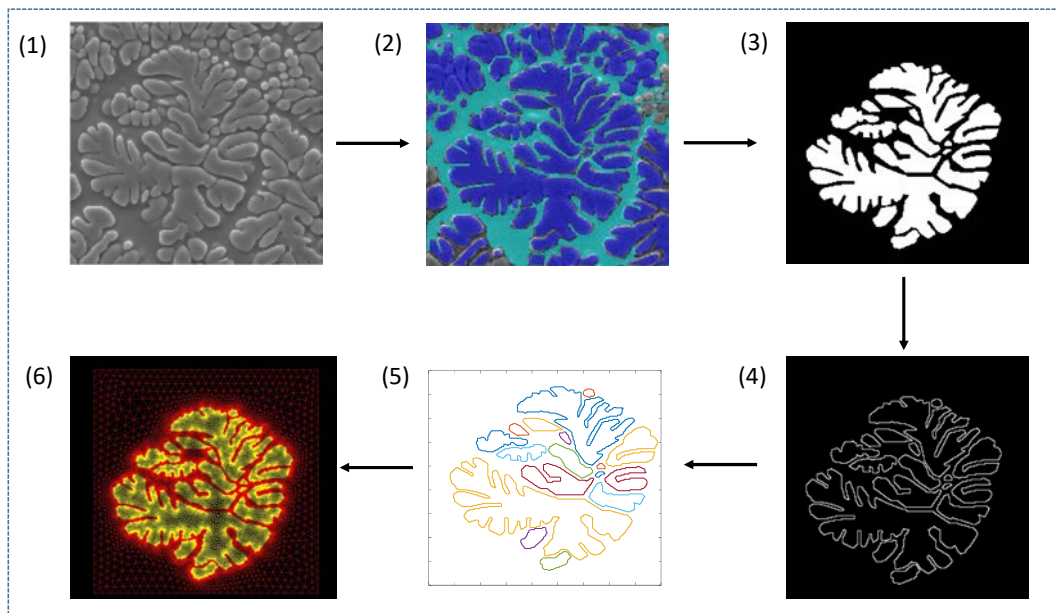


FIGURE 3.2: Flowchart from SEM to the finite element model : (1) Region of interest extracted from SEM image ; (2) Pixel-level labeling using Matlab toolbox Image Labeler ; (3) Binary image ; (4) Contour detection ; (5) Independent zone detection ; (6) Mesh generation.

The imaging procedure from the SEM image to a Finite Element mesh is : (1) The

region of interest (ROI) is selected and extracted from the original SEM image and is illustrated in Fig.3.2, as said previously, the ROI has a global shape comparable to a circular shape. (2) Using Matlab toolbox Image Laberler, a pixel-level labeling is manually done in which pixels belonging to either the dendritic inclusion or to the matrix are labeled accordingly. Of course there are human factors in the steps of determining the two areas, but it provides a better result than any other automatic imaging methods I have tried like Canny edge detector [CAN 86], level sets[RON 02], region growing [PAL 93], watershed[COU 09], etc. (3) The binary labeling information is then transformed into a binary image in which redundant parts are removed. The ROI is the white zone and the matrix is the black zone. (4) Contour detection gives accurate interfaces between the dendritic cluster and the matrix, and the width of the interfaces is one pixel. (5) The interfaces are segmented into separate zones, and each zone consists of a closed curve. Here, we have 17 independent zones. (6) To form the final geometry, we sequentially import pixels coordinates of the 17 zones into COMSOL Multiphysics to create interpolation curves. Each closed curve creates a part of the inclusion, and all those parts form the dendritic inclusion inside which mechanical properties are homogeneous. The surrounding zone forms the matrix whose mechanical properties are different from the inclusion. Finally, P-1 triangle elements are employed to generate the displayed elementary mesh including both the inclusion and the matrix. It is essential that the number of nodes on the four boundaries of the square are defined *a priori* as the same and the nodes are equally spaced, for the reason of compatibility given that we will copy and arrange this elementary mesh in the horizontal direction and implement the periodic boundary condition on the upper and lower boundaries as shown in Fig 3.3.

1.2.2 Volume fraction of the inclusion

Beside the dendritic inclusion, we also prepare another model with circular inclusion. In our previous work on the periodic circular inclusion, we have demonstrated the effect of the size of inclusion and contrast of rigidity on the energy transmission of wave-packets at different frequencies. In this work, since we are interested in the role of inclusion shape, we should ensure the best possible equivalence of the circular and dendritic inclusions, apart from the interface shape. To this aim, we chose equivalent geometries : Being the side length of the square defined as L , the diameter of the circular inclusion is $\frac{5}{6}L$, and its counterpart, the longest axis of the dendritic inclusion, is also about $\frac{5}{6}L$.

Therefore, the outer contour length is comparable between two types of inclusion which can be considered as primary interface. However, the volume fraction for the dendritic inclusion is measured as 28.35% and for the circular inclusion is 54.54%. The latter, which is close to twice the inclusion area of the former, intuitively allows for an efficient scattering according to the results in Chap.2. In the following, we will analyze the role of inclusion shape on acoustic attenuation in periodically arranged nanocomposites using finite element simulation.

1.3 Finite element simulation

We used Finite Element numerical calculations to study the vibrational properties of a 2D semi-infinite elastic system with dendritic and circular inclusions positioned along a cubic lattice. The computational model consists of 9 squares, aligned in the horizontal direction. There are no initial inclusion-free block in this model. The size of each square is defined as L , thus determining the distance between inclusions. The wave-packet with a coherence time $t = \frac{3t_0}{\omega}$ is generated imposing a displacement on the left side of the first square, while the right side of the last square allows for the implementation of the absorbing boundary conditions. As shown in Fig. 3.3, periodic boundary conditions (PBCs) are implemented along the vertical direction at the top and bottom of the sample. Perfect

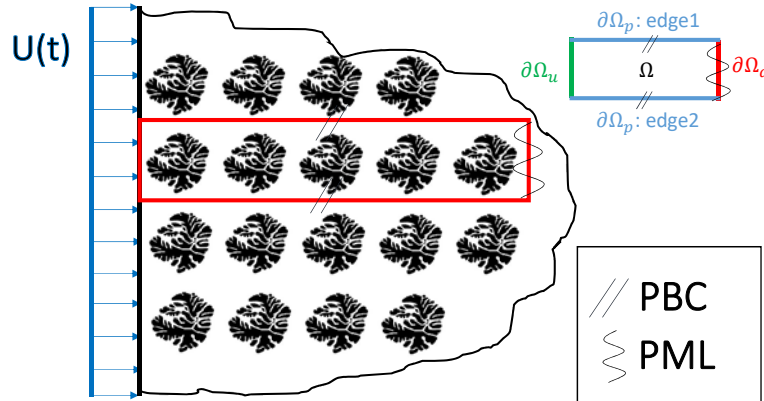


FIGURE 3.3: 2D simulation model of a solid with dendritic inclusion : this semi-infinite solid can be represented by only modeling only the part inside the red rectangle with Periodic Boundary Conditions (PBC) and Perfect Matched Layers (PML) as drawn; Black patterns represent the inclusions. (Ω represents simulation domain, $\partial\Omega$ indicates boundary conditions)

1.4 Acoustic transport in an isotropic homogeneous material with dendritic inclusions

A set of transient simulations of longitudinal wave-packet propagation is done using FEM for both the medium with dendritic and circular inclusions. From the results, we analyze the envelope of the kinetic energy from which we can find a clear transition of attenuation regime depending on the frequency. In addition, the penetration length and diffusivity are calculated to compare the attenuation ability for the two types of inclusions. In the following, the length is normalized by the inter-inclusion distance L , the kinetic energy E_k is normalized by the E_k at $x = 0$, and frequency ω is normalized by $\omega_0 = \frac{2\pi vL}{L}$

where v_L is longitudinal wave speed in the matrix material. Definition of the envelope is given in Eq.2.9. With the values used in Chap.2, $\omega_0=8.342$ THz.

1.4.1 Comparison of the envelopes

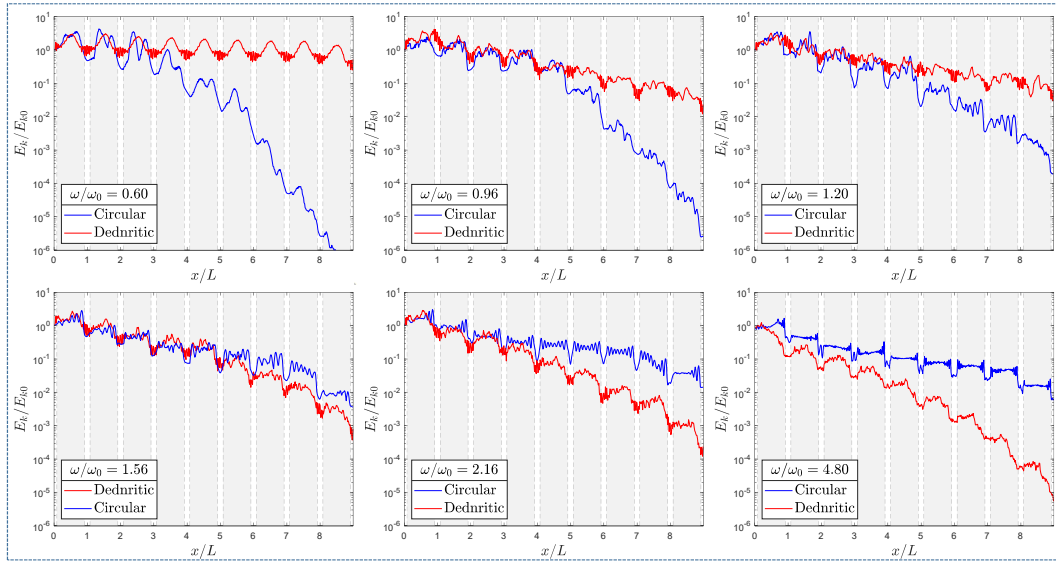


FIGURE 3.4: Comparisons of envelopes between circular and dendritic inclusions with $\frac{E_i}{E_m} = 0.2$ for different normalized frequencies ω/ω_0 (where $\omega_0 = 2\pi v_L/L$) : total simulation time steps 8400dt.

1.4.2 Comparison of the envelopes

In Fig.3.4, we present the envelopes of the kinetic energy as a function of position and for different normalized frequencies ω/ω_0 and for $\frac{E_i}{E_m} = 0.2$. Blue lines are for the circular inclusion and the red lines are for the dendritic inclusion. Surprisingly, for low frequencies, up to $\frac{\omega}{\omega_0} = 1.2$ included, the circular inclusions strongly attenuate the wave-packet, which is almost unaffected by the presence of the dendritic inclusions. The circular case corresponds actually to the studied case of $\omega = 5$ THz in Chap.2, where we identified a localization of the energy due to a resonance. The irregularly shaped dendritic inclusion does not lead to such resonance phenomena. As such, we can conclude that for low frequencies, long wavelengths, the high interface density of the dendritic inclusion is not dominant in determining the wave packet attenuation. The situation is reversed above $\frac{\omega}{\omega_0}=1.56$. Now the dendritic inclusions are more efficient in attenuating the wave-packet and such attenuation strongly increases with increasing frequency, *i.e.*, decreasing wavelength, while in the circular case the attenuation is almost constant for frequencies above $\frac{\omega}{\omega_0}=2.16$, suggesting a saturation of the attenuation effect of circular inclusions in the matrix. We can understand the change of attenuation efficiency regime as due to the major

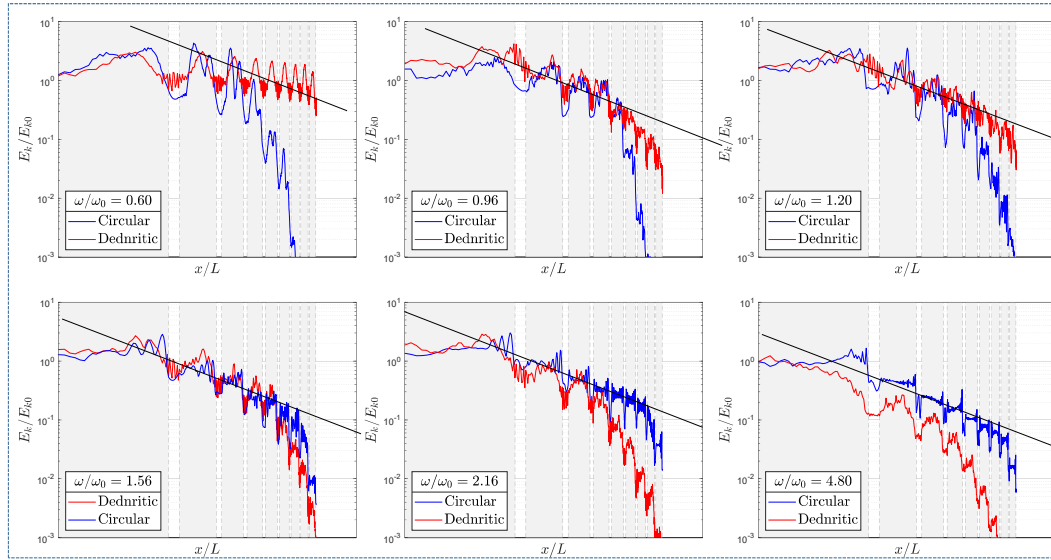


FIGURE 3.5: Fig.3.5 on a log-log scale. Black line indicates a $1/x$ decay.

importance of the tree-like interface in dendritic inclusions at wavelengths comparable with the dendritic structure lengthscale at the order of $\approx L/10$.

In Fig.3.6, snapshots of displacement field are shown for low frequency ($\frac{\omega}{\omega_0} = 0.6$), medium frequency ($\frac{\omega}{\omega_0} = 1.2$) and high frequency ($\frac{\omega}{\omega_0} = 4.8$) at half time (4200 dt) and at the end of time (8400 dt). For $\frac{\omega}{\omega_0} = 0.6$, the energy is localized and pinned to the first inclusions in the case of circular inclusion but spreads rapidly in the dendritic ones without huge dispersion meaning that the wavefront propagates ahead followed by a energy tail. At the medium frequency $\omega/\omega_0 = 1.2$, the energy is dispersed in space and their attenuation length is quite comparable. At the high frequency $\omega/\omega_0 = 4.8$, the energy is scattered violently at the inclusion-matrix interfaces. In the case of circular inclusion, energy is only scattered few times when crossing the circular interface. In addition, due the large curvature of the circular compared with the short wavelength, there is little but existing energy which keeps spreading ahead along the x direction. On the contrary, for dendritic inclusion, energy is totally broken and decomposed due to the random orientations of the normal at the surface and high interface density.

1.4.3 Comparison of the penetration length and diffusivity

In the previous section, by comparing the kinetic energy envelope, we have a first picture of the attenuation ability in the solids with two types of inclusions. Now, we will quantify this attenuation by calculating the penetration length and diffusivity defined in Eq.2.17 and Eq.2.16, respectively. Two groups of stiffness ratio are considered which are two extreme cases in the work in Chap.2 : $\frac{E_i}{E_m} = 0.2$ and 10.0.

The results of the normalized penetration length l_p/L is shown in Fig.3.7 where red triangles indicate the dendritic inclusion and the blue rounds represent the circular inclu-

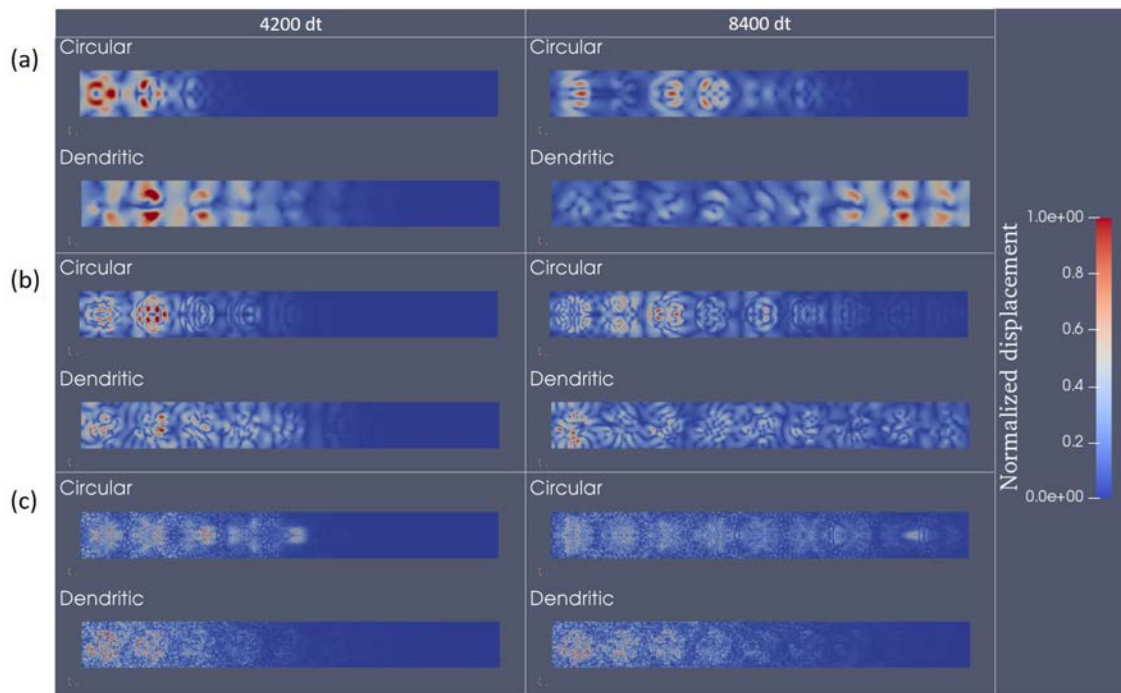


FIGURE 3.6: Snapshots of 3 case at $4200 \times dt$ and $8400 \times dt$ with $\frac{E_i}{E_m} = 0.2$ for circular and dendritic inclusion : (a) $\omega/\omega_0 = 0.6$ (b) $\omega/\omega_0 = 1.2$ (c) $\omega/\omega_0 = 4.8$. (see Supplementary Materials for the corresponding videos).

sion. In both cases of $\frac{E_i}{E_m}$, in the low frequencies, dendritic inclusion does not exhibit its high-interface-density advantage. Still, as wavelength decreases, dendrite begins showing a better performance to attenuate energy transfer with the reduced crossover frequency $\frac{\omega_c}{\omega_0}$ ranging between 1 and 1.5 depending on the stiffness ratio. Generally, for $\frac{\omega}{\omega_0} > \frac{\omega_c}{\omega_0}$, values of the penetration length is systematically shorter in the medium with dendritic inclusion, which highlights the possibility of low thermal conductance at least in the aspect of propagative contribution.

In order to investigate the effect on the diffusive contribution to thermal transport, we have calculated the diffusivity of a wave packet with randomly polarized amplitude, for the frequencies for which $\langle x \rangle \propto \sqrt{t}$. Results are shown in Fig.3.8. Generally, the transfer regime becomes diffusive due to the strong scattering when wavelength is smaller than the inter-inclusion distance, *i.e.*, $\frac{\omega}{\omega_0} > 1$ or $\frac{\lambda_m}{L} < 1$ where λ_m is the estimated wavelength in the matrix material. Similar to the penetration length, in the high frequencies, dendritic inclusion gives a smaller diffusivity than circular ones. While, the situation is more favorable in the case of $\frac{E_i}{E_m} = 10$ where dendritic inclusion always has a lower diffusivity for all wavelengths investigated. This is due to the concurrence of the effect of speed acceleration in rigid inclusion and the high volume fraction for circular inclusion.

Reduction of thermal conductivity can be directly ascribed to the reduction of wave propagation for ballistic phonons (propagons) and the reduction of diffusivity for the diffusive phonons (diffusons). In both case of stiffness ratio ($\frac{E_i}{E_m} = 0.2$ and 10.0), the dendritic inclusion indicates a generally better performance in reducing phonon transport than the circular inclusion with a comparable dimension. Summarizing the above four cases, the soft dendritic inclusion, which reduces both the attenuation length and diffusivity, provides insight into the complex interfaces that tune, hinder and reduce wave propagation.

Note however, that the waves dynamics in these nanocomposites is much more complex than a simple transition from ballistic to diffusive (strongly scattered) energy transfer. Indeed, when looking at the attenuation of kinetic energy (Fig. 3.5), it appears, that above ω_c , the nanocomposite with circular inclusions gives rise to a clear diffusive attenuation $P_\omega(x) \propto 1/x$ combined with a reduction of oscillations, while in the same frequency range the attenuation appears far stronger than diffusive for the dendritic inclusions, and displays intra-inclusions resonances.

1.5 Measurement of the sound speed

In our study, the wave propagation velocity will be mainly influenced by two factors : the effective rigidity of the medium and the properties of the interfaces. The effective rigidity of the composite will determine the wave speed at low frequency, when the wavelength is larger than the characteristic length of the scatterers. When the wavelength is comparable or even smaller than the characteristic length of the scatterers, strongly increasing scattering on the interfaces will become the key parameter determining the wave propagation inducing the redirection of the wave-vectors on the interfaces. In the following, we will investigate two types of wave speed : effective wave speeds at low frequencies and the instantaneous wave speed. The latter is especially useful when the

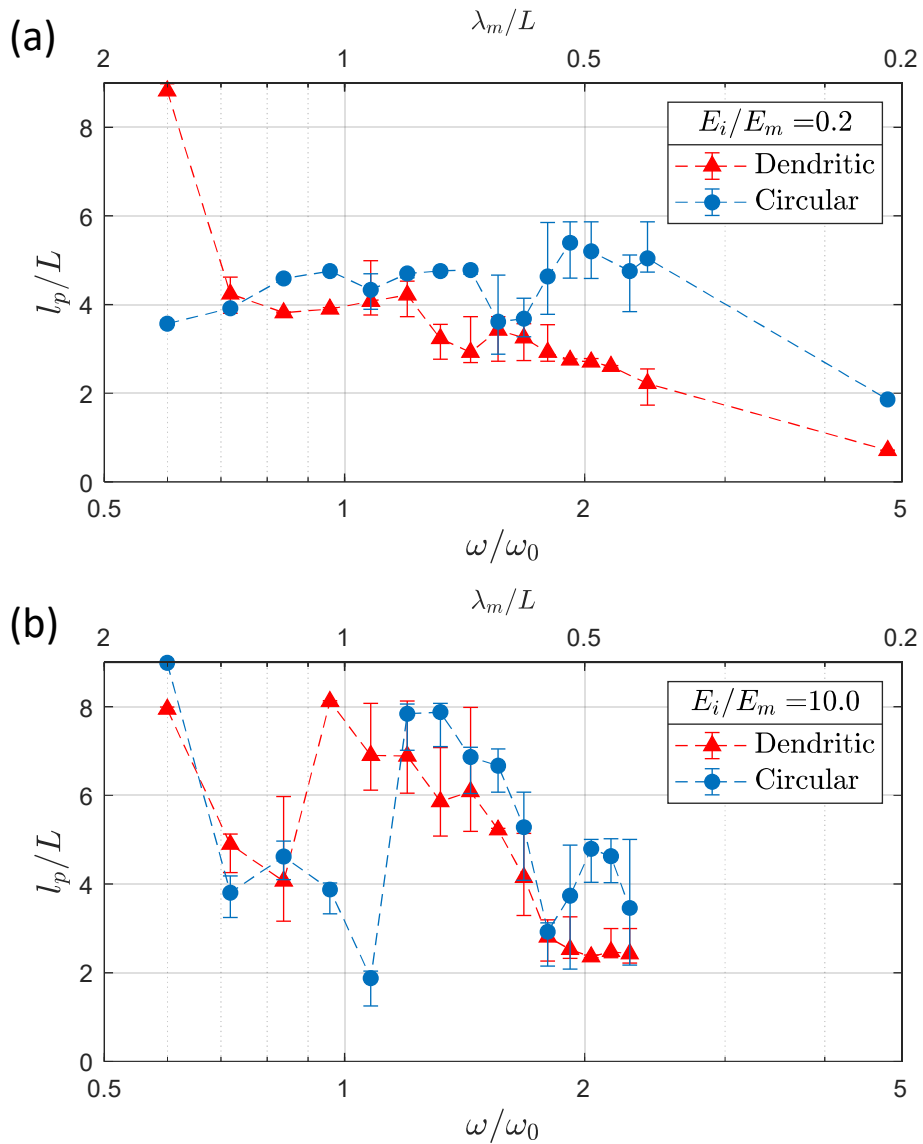


FIGURE 3.7: Comparisons of the penetration length between the circular and dendritic shape with $E_i/E_m = 0.2$ and 10.0 for longitudinal waves

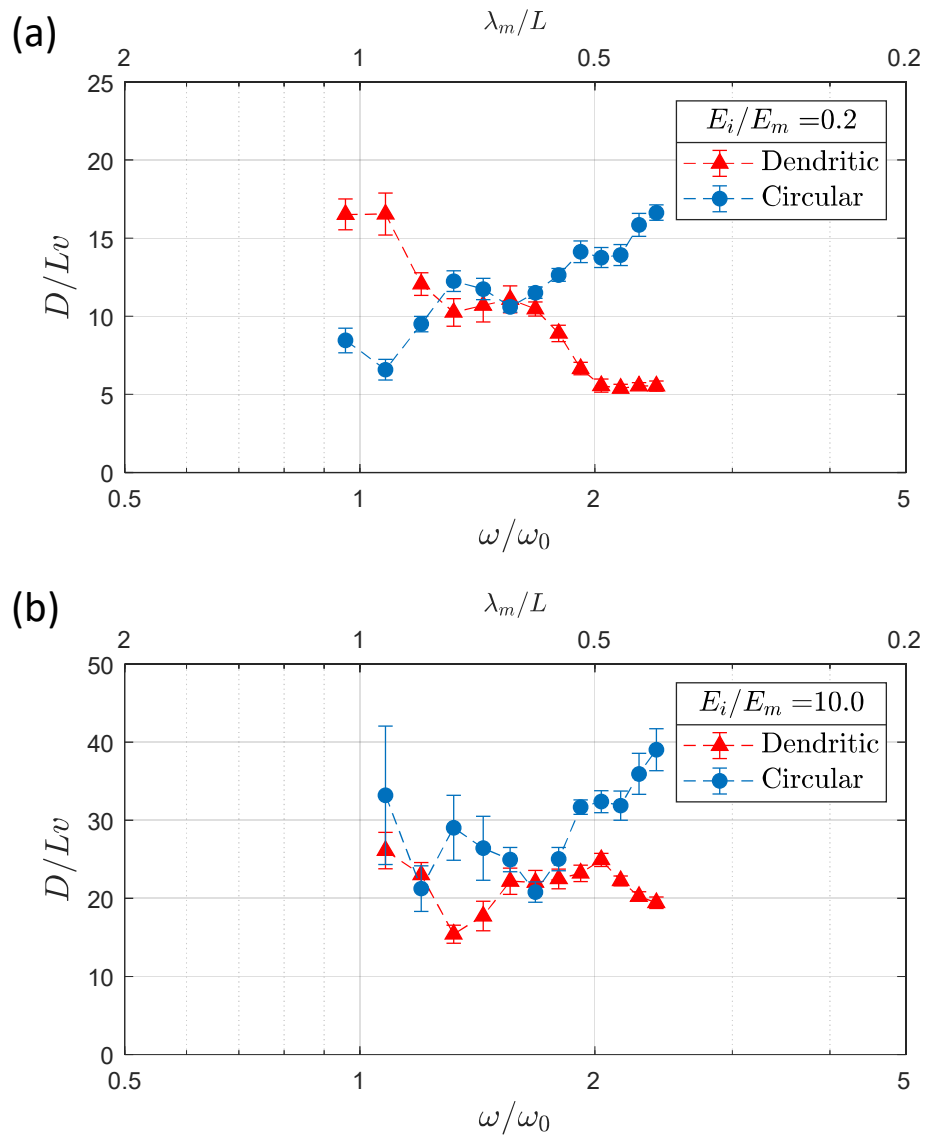


FIGURE 3.8: Comparisons of the diffusivity between the circular and dendritic shape with $E_i/E_m = 0.2$ and 10.0 for random longitudinal waves.

wave-vector can no longer be well-defined at high frequencies.

1.5.1 Long-wavelength speed

There exist two basic models for the stiffness of the two-materials composite : Voigt model and Reuss model. These two models allow to predict properties of a composite material made up of continuous and unidirectional fibers. As shown in Fig.1.5.1 (b), the Voigt model supposes the case of axial loading so **equal strain** for the matrix and the inclusion, which shows that the stiffness is given by a weighted average of the stiffness of the two components, also known as the "**Rule of Mixtures**". In Fig.1.5.1 (c), Reuss model supposes the case of transverse loading so **equal stress**, known as the **inverse Rule of Mixtures**, which states that the elastic modulus of a composite can be expressed as :

$$E_{eff} = \frac{1}{\Phi_i \times \frac{1}{E_i} + \Phi_m \times \frac{1}{E_m}} \quad (3.1)$$

where E_{eff} is the effective young's modulus of the composite, E_i (E_m) is the Young's modulus of the inclusion (matrix) and Φ_i (Φ_m) is the volume fraction of the inclusion (matrix). Interestingly, the Voigt model gives a upper-bound modulus and the Reuss model predicts the lower-bound modulus. Since we are in the plane strain state, our circular or dendritic surface is in fact an infinite long fiber in the third direction as shown in Fig.1.5.1 (a). Moreover, long-wavelength longitudinal wave can be considered as static transverse loading as the Fig.1.5.1 (c). Therefore, we can use the Reuss model (Eq.3.1) to make a prediction of the wave speeds for materials with circular and dendritic inclusion.

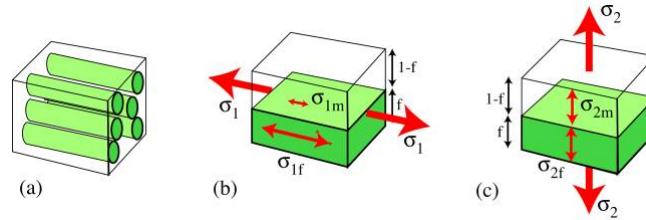


FIGURE 3.9: Stiffness of long fiber composites : (a) Matrix with cylinder fibers (b) Axial loading : Voigt model (c) Transverse loading : Reuss model. Subscript f and m indicate fiber and matrix respectively. σ_1 is the the load parallel to the fiber direction and σ_2 is the load perpendicular to the fiber direction. f is the volume fraction for the fiber and $1 - f$ the for the matrix.

We summarize the material properties, the effective Young's modulus and the estimated longitudinal wave speeds (Eq.1.51) in the Tab.3.3. From the estimated wave speeds, it is clear that the long-wavelength wave speed increases (compared to the homogeneous solid with $E_i/E_m = 1$) in the case $E_i/E_m > 1$ and decreases in the case $E_i/E_m < 1$ whatever the shape of inclusion is. We find that, both for a more rigid or a softer inclusion, the long wavelength speed is more strongly affected for a larger volume fraction, *i.e.*, in the

TABLE 3.3: Material properties, the effective Young's modulus and the effective longitudinal wave speed for composites with circular and dendritic inclusion with Poisson coefficient $\nu = 0.347$ and density $\rho = 2303 \text{ kg/m}^3$.

	Circular			Dendritic		
E_m (GPa)	92.25					
E_i/E_m	0.2	1.0	10	0.2	1.0	10
E_i (GPa)	18.45	92.25	922.5	18.45	92.25	922.5
Φ_m (%)	45.46			71.65		
Φ_i (%)	54.54			28.35		
E_{eff} (GPa)	28.99	92.25	181.19	43.23	92.25	123.85
$c_{L,eff}$ (m/s)	4466.1	7966.1	11164.3	5453.2	7966.1	9230.3

case of the circular inclusions. The speed at such wavelengths is thus essentially determined by the elastic moduli of the phases and the volume fraction of the secondary phase, independently on the inclusion shape.

This conclusion however does not hold when frequency increases, since the soft dendritic inclusion with lower volume fraction can give stronger attenuation. At high frequencies, diffusive transfer behavior can be found and there is no more well-defined wave-vector, for this reason, we turn now to measure the instantaneous speed.

1.5.2 Instantaneous wave speed at high frequencies

When wavelength approaches the size of the scatterer, the phonon-interface scattering becomes more important and wave speed begins to deviate from the long-wavelength speed. Due to the strong scattering by inclusions, its transport behavior may switch to diffusive or localized where phonons cannot be considered as propagative plane waves anymore. As such, wave-vector cannot be defined and definition of wave speed no longer makes sense. However, it is still interesting to look at the *instantaneous speed* changing with time.

Instantaneous wave speed is defined as the derivative of the average position

$$c_{ins} = \frac{\partial \langle x \rangle (t)}{\partial t} \quad (3.2)$$

Before calculating the instantaneous speed, we need to pre-treat the data of $\langle x \rangle$. Since when waves pass through a deeply heterogeneous medium, $\langle x \rangle (t)$ oscillates sharply, the calculated wave speed can be unreal and meaningless, as illustrated by the yellow dashed line shown in the right panel of Fig.3.10. Two smoothing methods are considered here: the first one is **Nearest neighbor smooth** (kernel smoother) defined as:

$$S_i = \frac{\sum_{j=i-n}^{i+n} P_j}{2n} \quad (3.3)$$

3. Mechanical response and acoustic attenuation for different types of interfaces

where P is the energy envelope and n is the number of the nearest neighbors. And the second method is Bezier interpolation smoothing. **Bezier curves** can be defined for any degree n :

$$B(t) = \sum_{i=0}^n C_n^i (1-t)^{n-i} t^i P_i, t \in [0, 1] \quad (3.4)$$

where C_n^i equals to the binomial coefficient and the degree n equals to the input number of the $\langle x \rangle (t)$. It is reported that Bezier based smooth curve gives smaller fluctuations and curvatures than other regular smoothing methods in Ref. [ZHO 11], meaning that it can effectively reduce the oscillation of the first derivative of the $\langle x \rangle$.

First of all, we used both methods for smoothing $\langle x \rangle (t)$ for dendritic inclusion with $\frac{E_i}{E_m} = 0.2$ and $\frac{\omega}{\omega_0} = 0.6$ in which case a wave front can still be identified as shown in Fig.3.6 thus a well-defined sound speed should be given by a quasi-constant instantaneous speed. The smoothed data of $\langle x \rangle (t)$ is shown in the left panel of Fig.3.10 by using the two smoothing methods. In the right panel, derivative of every $\langle x \rangle (t)$ shows that Bezier interpolation (red line) gives the most stable results of wave speed while the result from the unsmoothed data is useless with such a huge oscillation. In addition, a plateau is observed for $t \in [8, 13]$ in the case of Bezier curve, which gives a quasi-constant value of the wave speed (around 3500 m/s) confirming the prediction of the existence of a well-defined wave-vector. However, the very beginning and end of the Bezier curve should be ignored. Because the Bezier curve must begin and end at given points, *i.e.*, endpoint interpolation property, causing a much sharper oscillation than with Nearest neighbor smoother (blue line) at the two ends. Except for them, the beginning stage of acceleration before the plateau corresponds to the establishment step of the wave-packet whose duration depends inversely on the wave-packet frequency as shown in Fig.2.4. Compared to the Nearest neighbor smoother, Bezier interpolation gives a clearer presentation and interpretation of the instantaneous speed. Therefore, in the following work, we only use the Bezier curve to smooth $\langle x \rangle$ to and then get the instantaneous wave speed.

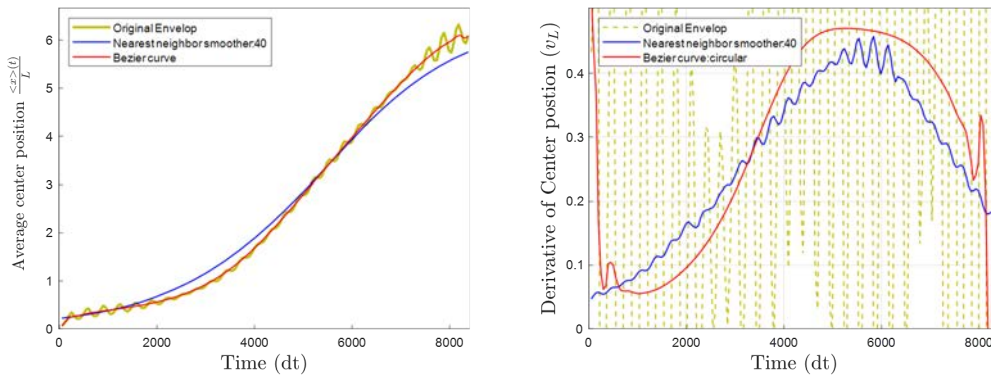


FIGURE 3.10: Average position (left) and instantaneous speed (right) for dendritic inclusion with $E_i/E_m = 0.2$ and $\frac{\omega}{\omega_0} = 0.6$ for longitudinal waves. Yellow lines : unsmoothed data ; Blue lines : Nearest neighbors smoother ; Red lines : Bezier interpolation.

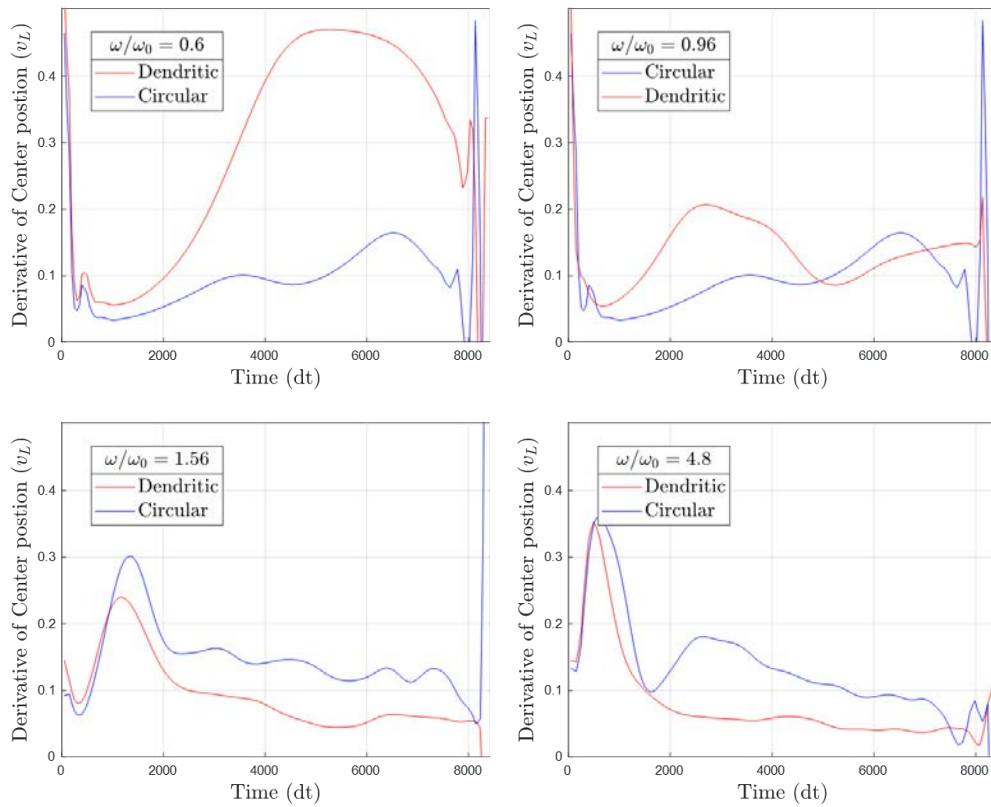


FIGURE 3.11: Instantaneous wave speed for dendritic and circular inclusion with $\frac{E_i}{E_m} = 0.2$ ($\langle x \rangle$ is smoothed by the Bezier interpolation). Red line indicates the dendritic inclusion and blue line indicates the circular inclusion.

We selected four frequencies from low to high : $\omega/\omega_0 = 0.6, 0.96, 1.56$ and 4.8 with $E_i/E_m = 0.2$. The corresponding instantaneous wave speeds are calculated and shown in Fig.3.11. Firstly, for $\omega/\omega_0 = 0.6$, the case of dendritic inclusion (red line), as previously shown, exhibits a plateau indicating a quasi-constant instantaneous speed. Oppositely, this plateau does not exist for the circular inclusion (blue line) because it is already in the diffusive-localized regime where energy is pinned in the first inclusions. The blue line is globally lower than the red line, meaning that energy moves slowly in the medium with circular inclusion at any time. Looking back to the penetration length, it is much smaller in the medium with circular inclusion at $\omega/\omega_0 = 0.6$ as shown in Fig.3.7(a). For $\omega/\omega_0 = 0.96$, the two lines are close to each other, indicating little difference between the two composites. This can be confirmed by looking at the envelope and the penetration length. $\omega/\omega_0 = 0.96$ can be considered as a separation point, because in the following two frequencies $\omega/\omega_0 = 1.56$ and 4.8 , the blue line is higher than the red line. Lower instantaneous speed at any times means that, at high frequencies, dendritic inclusion is more efficient to hinder and delay the energy transfer.

The analysis of the instantaneous speed gives a more obvious picture on the crossover of the attenuation performance from the circular inclusion at low frequencies to the dendritic inclusion at high frequencies for $E_i/E_m = 0.2$. We didn't investigate on the other frequencies nor the case of $E_i/E_m = 10.0$ since the above cases are enough to clarify the motivation for calculating the instantaneous speed to understand the wave propagation, especially when the wave-vector no longer exists.

1.6 Discussion

The impact of the interface on wave packet propagation depends on the materials properties, on the interface density and, of course, on the shape of the inclusion. As to the shape of the interface, dendritic shape inclusion is proved to have a good performance to hinder and redirect the wave propagation especially at higher frequencies. This is mainly due to the fractal shape (second characteristic length), the high interface density and the random orientation of the normal at the interface.

The case of dendritic inclusion for $E_i/E_m = 0.2$ gives a best performance in the sense of acoustic attenuation. The volume fraction of dendritic inclusion is much lower than that of circular inclusion. Based on the above discussion, we can imagine that a larger dendrite cluster with an equivalent volume fraction as the circular one would give a better attenuation effect. In the future, if we want to investigate the impact on the thermal conductivity, VDOS for different configurations will be needed.

In addition, this work can be further extended to the real materials (size, material properties, etc). Literature shows that rigidity of the dendrites phase is able to be tuned by tuning the elements composition ratio. This rigidity adjustment should be within a certain range to keep a excellent plasticity performance[XU 18]. Therefore, the present results and further research have instructive significance for material design.

1.7 Conclusion and perspectives

We have compare the sound attenuation performance between two shapes of inclusions : circular and dendritic inclusions. Our results show that the multi-branching tree like form of dendrite enhances phonon-interface scattering and phonon attenuation specifically for wavelengths comparable with the dendritic structure lengthscales. Unlike the circular inclusion which has only one characteristic length, the sub-interfaces inside the dendritic inclusion provide a continuous source for the increasing sound attenuation. This leads to a stronger reduction of both the penetration length and the apparent diffusivity in dendritic inclusion when the wavelength becomes smaller than the first characteristic length. The instantaneous wave speed is also globally affected, being much reduced at high frequencies by the dendritic fine structure.

2 Eshelby's inclusion

Named after J. D. Eshelby, Eshelby's inclusion is a useful tool in micromechanics and makes a deep contribution to many fields of modern science research. For example, Eshelby's inclusion model is widely used to the homogenization problem. It is also used to describe the quadrupolar stress map of the shear transformation zone (STZ) induced by plasticity in amorphous materials [BUL 94, BAR 02, MAL 04, ALB 16, NIC 18, BUL 94, MAL 04, ALB 16]

In this work, Eshelby's inclusion problem is numerically analyzed through Finite Element (FE) method. We will focus on an elastic field embedded with an elliptic inclusion induced by a "stress-free strain" (ϵ^*) in 2D plane strain case. This elliptic inclusion is placed in the center of a square matrix. The effects caused by geometry parameters will be investigated.

We will firstly give a brief description of the Eshelby's inclusion. Then, an elastic medium containing an Eshelby's inclusion is created using finite element method. Finally, by comparing to the analytic results, we show that the Eshelby's inclusion is correctly added into our FE model. Therefore, we can investigate other further research based on this model.

2.1 Ellipsoidal Eshelby's Inclusion

First of all, I will introduce the concept of Eshelby's inclusion and some important analytic results. The most remarkable finding given by Eshelby is that, for an ellipsoidal subdomain subjected to uniformly distributed "stress-free strain", the total strains and stresses inside the ellipsoidal inclusion are also uniform [WEI 05, FRA 12, ESH 57]. All these analytic results can be used to verify our FE simulations. Strains and stresses fields for an ellipsoidal inclusion inside an infinite medium are shown below :

"Stress-free strain" (or eigenstrain) :

ϵ^* is uniform inside the ellipsoidal inclusion.

Strain tensor inside the inclusion :

$$\epsilon^I = \mathbf{S} : \epsilon^* \quad (3.5)$$

where \mathbf{S} is a constant tensor called the Eshelby tensor.

Stress tensor inside the inclusion :

$$\sigma^I = \mathbf{C} : (\mathbf{S} - \mathbf{I}) : \epsilon^* \quad (3.6)$$

where \mathbf{C} is the elastic tensor and \mathbf{I} is a fourth order identity tensor. In our case, it is assumed the same \mathbf{C} inside and outside of the inclusion, meaning that there is no stiffness contrast between the matrix and the inclusion in opposition to the case discussed in Chap. 2. By using the method of the "fictitious equivalent inclusion" with eigenstrain ϵ^* , many other problems can be treated as application concerning ellipsoidal Eshelby's inclusion.

Particularly, an elastic inclusion and an Eshelby's inclusion with a proper eigenstrain is shown equivalent to each other [FRA 12].

Eshelby tensor inside the ellipsoidal inclusion (3D) :

See *Mechanical Behaviour of Materials*, Dominique François, et al., page 131 [FRA 12].

Eshelby tensor inside the elliptic cylinder inclusion (2D Plane strain) :

$$\mathbf{S} = \begin{bmatrix} \frac{1}{2(1-\nu)} \left[\frac{b^2+2ab}{(a+b)^2} + (1-\nu) \frac{b}{a+b} \right] & \frac{1}{2(1-\nu)} \left[\frac{b^2}{(a+b)^2} - (1-\nu) \frac{b}{a+b} \right] & 0 \\ \frac{1}{2(1-\nu)} \left[\frac{a^2}{(a+b)^2} - (1-\nu) \frac{a}{a+b} \right] & \frac{1}{2(1-\nu)} \left[\frac{a^2+2ab}{(a+b)^2} + (1-\nu) \frac{a}{a+b} \right] & 0 \\ 0 & 0 & \frac{1}{2(1-\nu)} \left[\frac{a^2+b^2}{(a+b)^2} + \frac{1-\nu}{2} \right] \end{bmatrix}$$

where a is semi-major axis of ellipse, b is semi-minor axis and ν is Poisson's coefficient.

2.2 Implementation in the FE code

2.2.1 Geometry

The computational model is shown in Fig.3.12. One ellipsoidal inclusion (I) is embedded into a square matrix (M). a and b are the semi-axes of ellipse with $a > b$. L is the length of the square matrix.

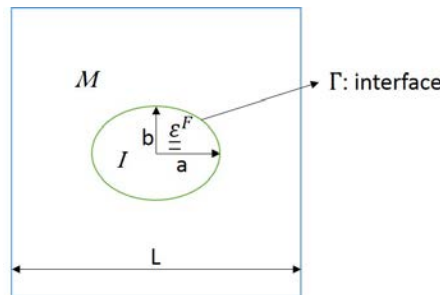


FIGURE 3.12: Model of a square matrix with an elliptic inclusion in the center.

2.2.2 Materials properties

Matrix and inclusion are assumed as the same material : Young's modulus is 92.25 GPa, Poisson's ratio is 0.347 and mass density is 2303 kg/m^3 . They are both considered as uniform and isotropic solid respectively.

2.2.3 Dynamical analysis

We investigate a dynamical analysis of the unfolding of the Eshelby's inclusion. At time $t = 0$, we impose a step pulse of eigenstrain ε^* inside the elliptic inclusion. The

inclusion will deform under this eigenstrain. Radiation is emitted and propagates in the form of waves in the surrounding medium. The dynamics is thus necessary to capture the transient process. Central difference integrator is applied for the time integration, and the time discretization is well selected to guarantee the stability of the simulation.

2.2.4 Spatial discretization

For $a = 5 \text{ \AA}$, two elliptic inclusions with $b/a = 1$ and $b/a = 0.25$ as shown in Fig.3.13 (a) and (b), respectively. The average edge length of a quadratic element is 1 \AA . Number of nodes on the elliptical curve is different, because the perimeter of the ellipse decreases with the decreasing ratio b/a for a given a . As the perimeter decreases, we need to decrease the number of nodes on the elliptical curve in order to create a pertinent mesh.

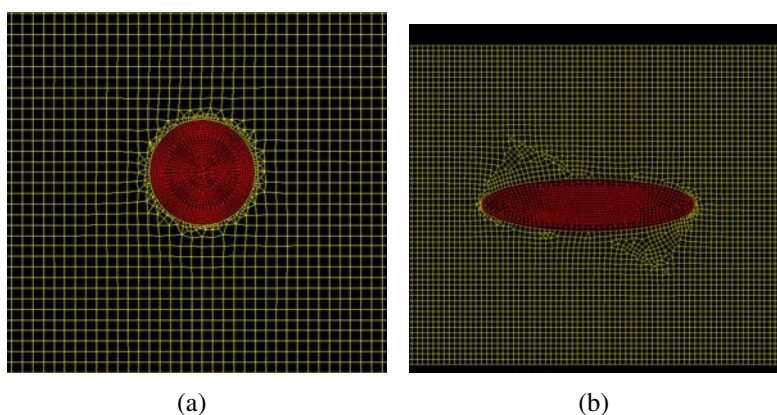


FIGURE 3.13: (a) Mesh for a circular inclusion. (b) Mesh for an elliptic inclusion with $b/a = 0.25$.

2.2.5 Boundary conditions

Before reaching the equilibrium state, there is a transient process for the establishment of Eshelby inclusion's elastic field. During this process, we can observe the emitted radiation in the form of wave which then propagates to the boundaries of the model. Therefore, PMLs are implanted on boundaries of the square matrix in order to avoid reflection.

2.2.6 Loading : eigenstrain

The eigenstrain in the Eshelby inclusion can be explained, for example, as a result of a phase change, plasticity, or thermal effects.

At $t = 0$, we impose a step pulse of eigenstrain ϵ^* inside the elliptic inclusion, which is uniform inside the inclusion. Eigenstrain, extracted for example from Ref.[ALB 16], is mapped from the MD results of model a-Si bulk sample. Therefore, this eigenstrain should reproduce the quadrupolar displacement field of a the plastic event in amorphous

materials. Since we consider a 2D problem, we only need three components of eigenstrain :

$$\boldsymbol{\epsilon}^* = \begin{bmatrix} 0.003 \\ -0.008 \\ 0.024 \end{bmatrix} \quad (3.7)$$

This uniform strain inside the inclusion results in a distributed force \boldsymbol{f} at the interface between the inclusion and the matrix :

$$\boldsymbol{f} = \nabla \cdot \boldsymbol{\sigma}^0 = \nabla \cdot (\mathbf{C} : \boldsymbol{\epsilon}^*) \quad (3.8)$$

where \mathbf{C} is the elastic constitutive tensor and $\boldsymbol{\sigma}^0$ is the equivalent initial stress due to the eigenstrain.

2.2.7 Numerical damping

When looking at the establishment of inclusion's elastic field, there are two reasons to add a numerical damping in the entire model :

Firstly, inside the inclusion, it takes a very long time to reach the equilibrium state. Every point oscillates with time, so the uniformity of the strain field inside the inclusion cannot be checked. By adding a numerical damping, residual waves inside are attenuated and finally we found a uniform strain field inside the inclusion. Secondly, outside of the inclusion : because the incident wave cannot be entirely absorbed by PMLs, there are still some reflected waves going back and passing through the Eshelby inclusion, thus influencing the elastic field near the inclusion. We could also set the model length very large to avoid this reflection, but a numerical damping is more efficient.

We select Rayleigh damping as it is efficient to attenuate both low and high frequency waves. Rayleigh damping is expressed as :

$$\mathbb{C} = \alpha \mathbb{M} + \beta \mathbb{K} \quad (3.9)$$

where \mathbb{M} and \mathbb{K} are respectively the mass and the stiffness matrix, α and β are damping coefficients and both will be set as $1e-16$. To explain this choice, in Fig.3.14, three groups of damping coefficients α and β are used. The shaded region shows strains data for all the points inside the inclusion and the middle line is the average. If this numerical damping is too small, it takes long time to attenuate the residual waves. $\alpha = \beta = 1e-16$ (the middle panel Fig.3.14) is efficient to reach equilibrium. It can be seen that the third group ($\alpha = 1e-16$ and $\beta = 1e-15$) gives a more efficient convergence and seems to be the upper limit of the values for damping. Beyond these limits, it is found that stronger damping would cause a computational instability of the Central difference integrator.

By adjusting the numerical damping, we can reduce the simulation time in transient process. In addition, this numerical damping has no physical meaning and should be removed once the establishment of elastic field is done.

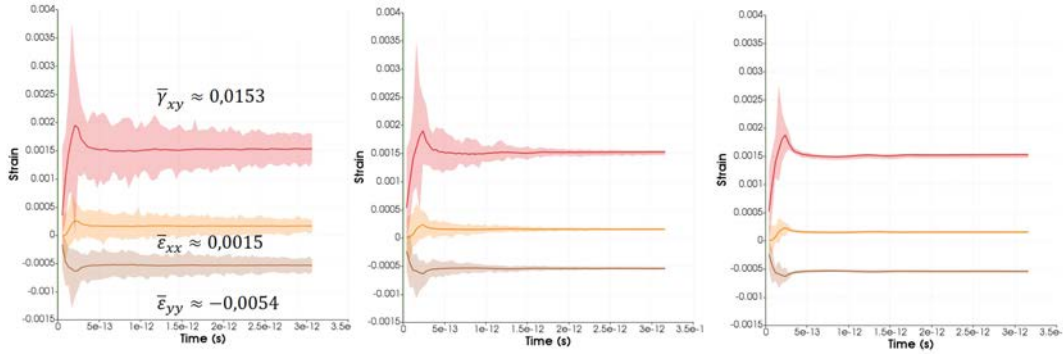


FIGURE 3.14: Average strain vs time $\bar{\epsilon}_{ij}^I(t)$ for different damping. The shadow region is ϵ_{ij}^n range, and the middle lines are average values $\bar{\epsilon}_{ij}^I$. In all three cases, the strains in equilibrium state are identical respectively with a negligible error (<1%). Left : $\alpha=1e-17$ and $\beta=1e-17$; Middle : $\alpha=1e-16$ and $\beta=1e-16$; Right : $\alpha=1e-16$ and $\beta=1e-15$.

2.3 FE simulation by varying the ratio b/a

A series of FE simulations have been done by varying not only the ratio b/a , but also others model parameters, such as model dimension and the mesh density on the border of the inclusions. The results of mechanical responses (strains, stresses and displacements) inside and outside the inclusion are compared to the analytic results. It shows that our FE simulation results are reliable. This section is structured as followed :

First of all, we concern about the strain field inside the inclusion. It shows that the ratio of model size to inclusion size $L/2a$ should be sufficiently large to ensure the uniformity of strains inside the inclusion. By way of indication, $L/2a > 5$. If $L/2a$ is enough, simulations results give uniform strains inside the inclusion and their values agree with the analytic results $\epsilon^I = \mathbf{S} : \epsilon^*$.

Secondly, the stresses and the displacements inside the inclusion are immediately checked if strain field is correct. The stress field is also uniform inside the inclusion which is express as $\sigma^I = \mathbf{C} : (\mathbf{S} - \mathbf{I}) : \epsilon^I$. And displacement field changes linearly inside the inclusion.

Finally, we go out of the inclusion. Displacement fields outside the inclusion will be compared to analytic results. Near the inclusion, numerical results are identical to what calculated Eshelby. Nevertheless, far away from the inclusion, an evident difference is observed. This difference decreases as the model size increases, and it is supposed to be disappeared if the model size is infinite as the analytic results are derived for an infinite large medium. This difference is still large even when $L/2a = 30$.

2.3.1 Strain inside the inclusion

Due to the eigenstrain, Eshelby inclusion will interact with the surrounding medium and end up with a final strain whose absolute values are smaller than eigenstrain's because of the constrains of the surrounding medium. This final strain inside the inclusion is given

by Eq.3.5. For an ellipsoidal inclusion, \mathcal{S} depends on the ratio b/a and Poisson's ratio ν . In this chapter, we have fixed $\nu = 0.347$, thus \mathcal{S} depends only on b/a .

Fig.3.14 shows the strain components for each points inside the inclusion (dashed region) and the average value (middle line) as a function of time defined as :

$$\bar{\varepsilon}_{ij}^I(t) = \sum_{n=1}^N \varepsilon_{ij}^n(t)/N \quad (3.10)$$

where N is the number of elements inside the inclusion, $i, j = x$ or y and ε^n is the n -th element's strain tensor.

We then compare the strains reached in equilibrium state to the analytic strains.

(1)Effect of spatial discretization : precision

Here we focus on the discretization of the ellipsoidal inclusion. Technically, we cut the circumference into n parts. Then, mesh will be created and optimized automatically by FE software *Cast3m* by keeping the n nodes on the circumference. In Tab.3.4, we show the *max* and *min* strains inside the inclusion by tuning the number of nodes n . n/C means number of nodes per unit length where C is the ellipse circumference. It shows that a finer mesh improves the uniformity of strains inside the inclusion from $n = 60$ to $n = 240$.

a (Å)	5						
L (Å)	60						15
n	60	80	120	140	180	240	120
n/C	1.91	2.55	3.82	4.46	5.73	7.64	3.82
$\varepsilon_{min}(\%)$	1.607	1.619	1.602	1.66	1.655	1.659	2.046
$\varepsilon_{max}(\%)$	1.677	1.689	1.678	1.672	1.668	1.671	2.588
dispersion (%)	4.17	4.14	4.53	0.72	0.78	0.72	20.94

TABLE 3.4: Effect of discretization on strains inside the inclusion : $b/a = 1$ and $a=5$ Å is the major-axis of ellipse. L is the model length, n is the number of nodes on the circumference, C is perimeter and ε is strain amplitude.

(2)Effect of system size : non-uniform strain

Non-uniform strains inside the inclusion after long-time transient process, can be due to finite size effects when model's length L is not large enough. For example, in Fig.3.15, $b/a = 0.25$, $a = 20$ Å, $L=60$ Å and ratio $L/2a = 3/2$. We show that, inside the inclusion, there is a 10% dispersion of the strains in equilibrium state due to the effect of the system size.

In Tab.3.5, we give a complete study of size effect. We adjust both discretization and model size to compare strain fields inside the inclusion. Given $L = 60$ Å, we found a dispersion about 20 % between *max* and *min* strains, which is far from an uniform strain field. It is noted that finer meshes ($n=240$ and 480) could not give a more uniform strain field but only give more confidence to us that our initial mesh is qualified. Then, we keep $n=240$ but change the value of L from 60 to 240 Å. As indicated by the dispersion,

3. Mechanical response and acoustic attenuation for different types of interfaces

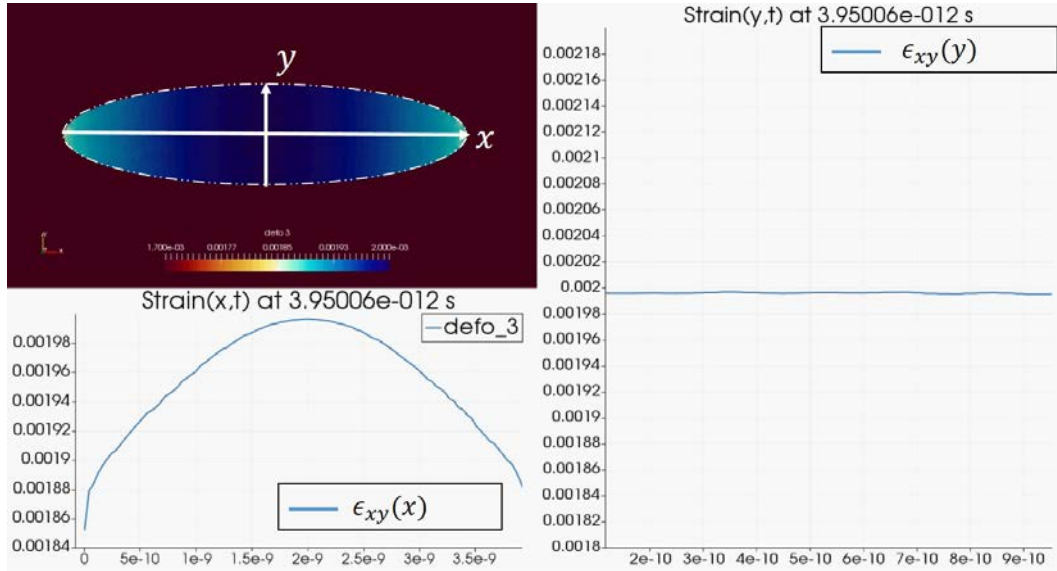


FIGURE 3.15: Strains field inside the inclusion : In stead of a uniform field, dispersion of the strains is attributed to the size effect for $L=60 \text{ \AA}$, $a= 20 \text{ \AA}$, $b/a = 0.25$. Along the x direction, a dispersion of the shear strains inside the inclusion up to 10% is found in equilibrium state (lower left plot).

$a \text{ (\AA)}$	20							
$L \text{ (\AA)}$	60			90	120	180	200	240
$L/2a$	1.5			2.25	3	4.5	5	6
n	120	240	480	240				
$\epsilon_{min}(\%)$	2.046	2.038	2.038	1.98	1.855	1.717	1.692	1.959
$\epsilon_{max}(\%)$	2.588	2.589	2.589	2.124	1.906	1.733	1.705	1.671
$\frac{\epsilon_{max}-\epsilon_{min}}{\epsilon_{max}}(\%)$	20.94	21.28	21.28	6.78	2.68	0.92	0.76	0.72

TABLE 3.5: Effect of model size on the strains inside the inclusion : $b/a = 1$ and $a=20 \text{ \AA}$. In the table, n is the number of nodes on the circumference, ϵ is the strain amplitude.

the strains inside the inclusion become more and more uniform with increasing L . When $L/2a = 4.5$, the dispersion of the strains is less than 1%.

(3) Verification

Thanks to the experience from previous tests, we finally investigated a series of FE simulations without the problem mentioned above.

For $a = 5 \text{ \AA}$ and $L = 60$ and 120 \AA , the results with different b/a (from 0.2 to 1) are also given in Tab.3.6 in which the analytic results are calculated according to b/a and ϵ^* . Both groups ($L = 60$ and 120 \AA) can give reliable strain field results.

b/a		1	0.9	0.8	0.6	0.5	0.3	0.2
$\epsilon_{xx}(\%)$	L=60	0.162	0.162	0.160	0.154	0.147	0.112	0.090
	L=120	0.165	0.166	0.165	0.159	0.153	0.127	0.099
	Analytic	0.164	0.165	0.164	0.158	0.151	0.123	0.097
$\epsilon_{yy}(\%)$	L=60	-0.557	-0.571	-0.585	-0.612	0.624	0.642	-0.644
	L=120	-0.543	-0.559	-0.574	-0.601	-0.622	-0.647	-0.651
	Analytic	-0.550	-0.550	-0.560	-0.600	-0.614	-0.640	-0.650
$\gamma_{xy}(\%)$	L=60	1.560	1.555	1.557	1.589	1.627	1.778	1.914
	L=120	1.497	1.498	1.503	1.544	1.584	1.741	1.872
	Analytic	1.480	1.480	1.490	1.540	1.580	1.750	1.890

TABLE 3.6: Verification of the strain components ϵ_{xx} , ϵ_{yy} and γ_{xy} in the equilibrium state. Numerical results are given by FE simulations with $L = 60$ and 120 \AA .

2.3.2 Stress inside the inclusion

Stress inside the inclusion is given by Eq.3.6. Considering that $\epsilon^I = \mathbf{S} : \epsilon^*$ has been verified in previous text, stress inside the inclusion is immediately checked.

2.3.3 Displacement inside the inclusion

For an elliptical inclusion, the Eshelby tensor is constant, leads to uniform strains and stresses inside the inclusion, so the displacement field is linear inside the inclusion. In Fig.3.19, we can clearly find a linear change of displacement inside the inclusion with the displacement being 0 in the center of the model.

2.3.4 Displacement outside of the inclusion

(1) Analytic results

In a 2D plane strain case, the displacement of an *elliptic* cylindrical inclusion is reported in Ref.[JIN 17] :

$$\begin{bmatrix} u_1 \\ u_2 \\ u_3 \end{bmatrix} = \begin{bmatrix} W_{111} & W_{122} & W_{133} & 0 & 0 & W_{112} \\ W_{211} & W_{222} & W_{233} & 0 & 0 & W_{212} \\ 0 & 0 & 0 & W_{323} & W_{313} & 0 \end{bmatrix} \begin{bmatrix} \varepsilon_{11}^* \\ \varepsilon_{22}^* \\ \varepsilon_{33}^* \\ 2\varepsilon_{23}^* \\ 2\varepsilon_{13}^* \\ 2\varepsilon_{12}^* \end{bmatrix} \quad (3.11)$$

where $[W]$ is the displacement Eshelby tensor

$$W_{111} = \frac{x_1}{2(1-\nu)} [(1-2\nu)J_1(\lambda) + 3a_1^2 J_{11}(\lambda) + \rho_1 \rho_2 (1-\rho_1^2) n_1^2] \quad (3.12)$$

$$W_{112} = \frac{1}{2(1-\nu)} \{ [(1-2\nu)J_2(\lambda) + a_1^2 J_{21}(\lambda)] x_2 + [\rho_1 \rho_2 (1-\rho_1^2) n_1 n_2] x_1 \} \quad (3.13)$$

$$W_{122} = \frac{x_1}{2(1-\nu)} [(2\nu-1)J_1(\lambda) + a_2^2 J_{12}(\lambda) + \rho_1 \rho_2 (1-\rho_2^2) n_2^2] \quad (3.14)$$

$$W_{133} = \frac{\nu x_1}{1-\nu} J_1(\lambda), W_{313} = x_1 J_1(\lambda), \quad (3.15)$$

All the other five non-zero entries of $[W]$ may be obtained by the permutation with respect to subindices (1,2), with following symmetry property :

$$W_{ikl} = W_{ilk} \quad (3.16)$$

λ is a parameter related to coordinates

$$\lambda = [x_1^2 + x_2^2 - a^2 - b^2 + \sqrt{(x_1^2 + x_2^2 - a^2 + b^2)^2 + 4(a^2 - b^2)x_2^2}] \quad (3.17)$$

where x_1 and x_2 are x and y coordinate respectively.

The corresponding results for the J -functions are as follow :

$$J_1(\lambda) = \frac{\rho_1^2 \rho_2 b}{a \rho_2 + b \rho_1}, J_2(\lambda) = \frac{\rho_2^2 \rho_1 a}{a \rho_2 + b \rho_1} \quad (3.18)$$

$$J_{12}(\lambda) = J_{21}(\lambda) = \frac{\rho_1^3 \rho_2^3}{(a \rho_2 + b \rho_1)^2} \quad (3.19)$$

$$J_{11}(\lambda) = \frac{\rho_1^4 \rho_2 a (2a \rho_2 + b \rho_1)}{3a^2 (a \rho_2 + b \rho_1)^2}, J_{22}(\lambda) = \frac{\rho_2^4 \rho_1 a (2b \rho_1 + a \rho_2)}{3b^2 (a \rho_2 + b \rho_1)^2} \quad (3.20)$$

$$J_3(\lambda) = J_{33}(\lambda) = J_{13}(\lambda) = J_{31}(\lambda) = J_{23}(\lambda) = J_{32}(\lambda) = 0 \quad (3.21)$$

the detailed expressions of ρ -functions and the outer unit vector n_i are

$$\rho_1 = \frac{a}{\sqrt{a^2 + \lambda}}, \rho_2 = \frac{b}{\sqrt{b^2 + \lambda}}, n_1 = \frac{m_1}{\sqrt{m_1^2 + m_2^2}}, n_2 = \frac{m_2}{\sqrt{m_1^2 + m_2^2}} \quad (3.22)$$

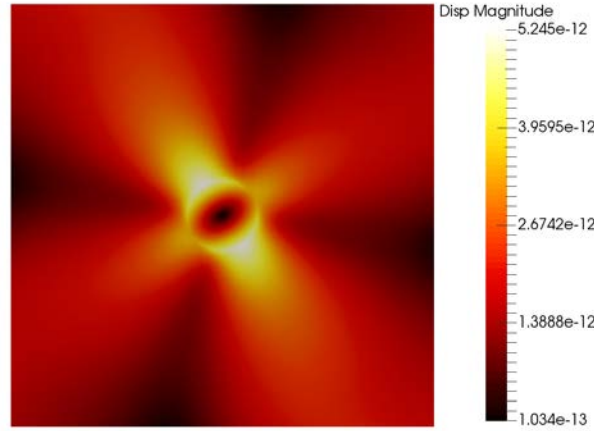


FIGURE 3.16: Contour of displacement inside and outside of the inclusion. Semi-major axis $a = 5 \text{ \AA}$, $b/a=1$ and $L = 240 \text{ \AA}$.

in which

$$m_1 = \frac{x_1}{a^2 + \lambda}, m_2 = \frac{x_2}{b^2 + \lambda} \quad (3.23)$$

(2) Verification

Here we analyze the displacement field outside the inclusion, especially at the boundaries of the system.

An example of displacement field is shown in Fig.3.16 where a quadrupolar shape can be seen. Semi-major axis $a = 5 \text{ \AA}$, $b/a=1$ and $L = 240 \text{ \AA}$. We saved the displacement data and then import them in Matlab in order to compare with the analytical solution as shown in the Fig.3.17(a). The red circles are the data from the simulation and the colored surface represents the analytic values, and z axis is the amplitude of the displacements $\|u\| = \sqrt{u_x^2 + u_y^2}$. Near the inclusion, the simulation results reproduce well the the analytic results. Nevertheless, evident difference can be observed far from the center, especially at the model's boundaries.

In addition, there are two peaks of displacement which are located on the interface between the inclusion and the matrix. This is because, when we reproduce analytic results through *matlab*, discrete points cannot give all the details about displacement-especially on the interface, as illustrated in Fig.3.17(b). Through the comparison between the red circles and the surface (part of analytic solution) near the inclusion, we can confirm that FE modeling gives a perfect result for displacement near the inclusion.

(3) Effect of system size at points far from the inclusion

We investigated a series of simulations by changing the model length $L = 120 \text{ \AA}$, 180 \AA and 300 \AA . Fig.3.18 shows the displacement amplitude, for an elliptic inclusion ($b/a = 0.9$) with different L . In Fig.3.19, we plot the amplitude of the displacements along the diagonal line. The difference mentioned above becomes smaller as L increases. And the analytic result (blue dash line) should thus be an asymptotic line when $L \rightarrow \infty$. Indeed, the analytic calculation assumes an inclusion immersed in an infinite medium.

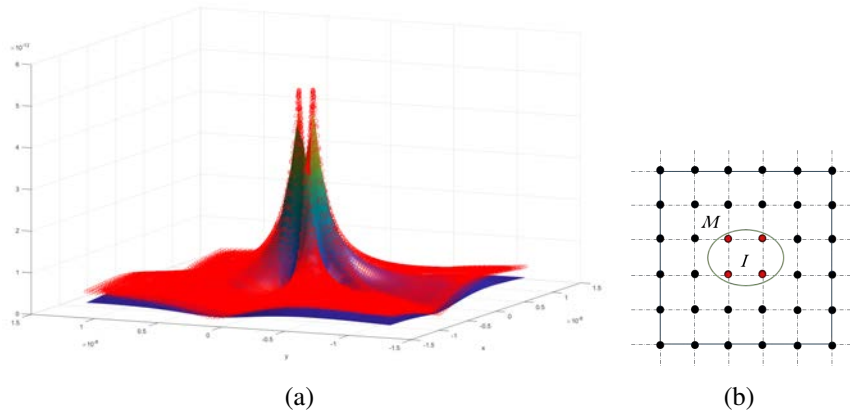


FIGURE 3.17: (a) Comparison between the numerical and the analytic results. Red circles are the numerical results and colored surface is the analytic results from Ref.[JIN 17]. $L=240 \text{ \AA}$, $a=5 \text{ \AA}$ and $b/a = 1$. (b) Only the points outside of the inclusion (black points) are used to reproduce analytic results outside of the inclusion. As such, the details on the interface (green line) cannot be given.

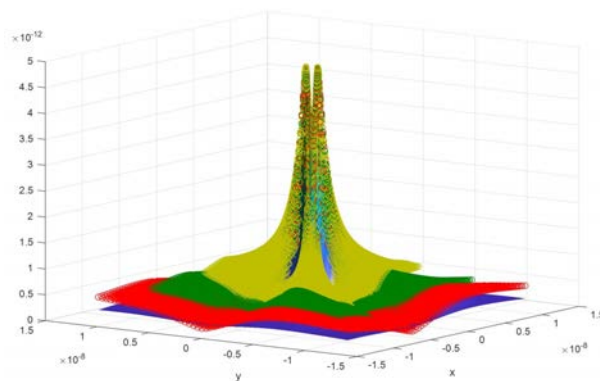


FIGURE 3.18: Effect of model length on the displacement field : $\|u\|(x,y)$ for $L=120$ (yellow circles), 180 (green circles) or 240 \AA (red circles). $a=5 \text{ \AA}$ and $b/a = 0.9$.

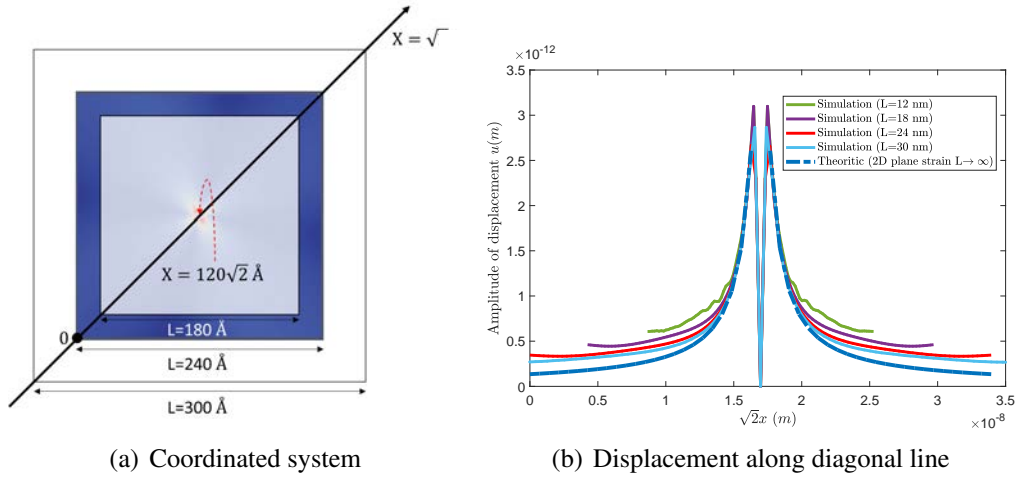


FIGURE 3.19: (a) Coordinated system : origin is in lower left corner of $L=240 \text{ \AA}$. $X = \sqrt{2}x$ with $x \in [0, L]$. (b) Displacement amplitude along the diagonal line $\|u\|(X)$ for $L=120, 180, 240$ or 300 \AA . $a=5 \text{ \AA}$ and $b/a = 0.9$.

2.4 Wave propagation in a medium with an Eshelby's inclusion

In the previous section, we demonstrated that the Eshelby's inclusion has been correctly placed in the elastic matrix, allowing us to continue the future research on the propagation of the wave packets in such a medium. Once the inclusion is well established, we will impose a wave packet at 5 THz from the left boundary. Two Eshelby's inclusions with different eigenstrains will be considered : one Eshelby's inclusion has an eigenstrain ϵ^* as given in Eq.3.7 , another has a smaller eigenstrain $= 0.1 \times \epsilon^*$. The displacement fields are shown in Figs. 3.20 and 3.21 when this wave packet is before and near the inclusion, respectively. Two Eshelby's inclusion cases are in the top and middle panels, and an elastic inclusion case with $E_i/E_m = 0.2$ studied in Chap.2 is also given to show the difference of the displacement fields caused by the eigenstrain.

In the top panel of Fig. 3.20, it is clear the Eshelby's inclusion with a stronger eigenstrain influences the displacement field over a longer distance compared with the other two cases. In Fig. 3.21, when the wave touches the inclusions, their displacement fields are very different. In the case of the elastic inclusion, the displacement field is vertically symmetric. However, it is not the case for the Eshelby's inclusions with a shear-strain dominant eigenstrain.

2.5 Conclusion and perspectives

In this work, we have extended the elastic inclusion to the Eshelby's inclusion featured with a "stress-free strain" (ϵ^*) in 2D plane strain case. One elliptic inclusion is placed in the center of a square matrix and the dynamic process of the inclusion establishment can be reproduced. At the equilibrium state, mechanical responses have been verified by

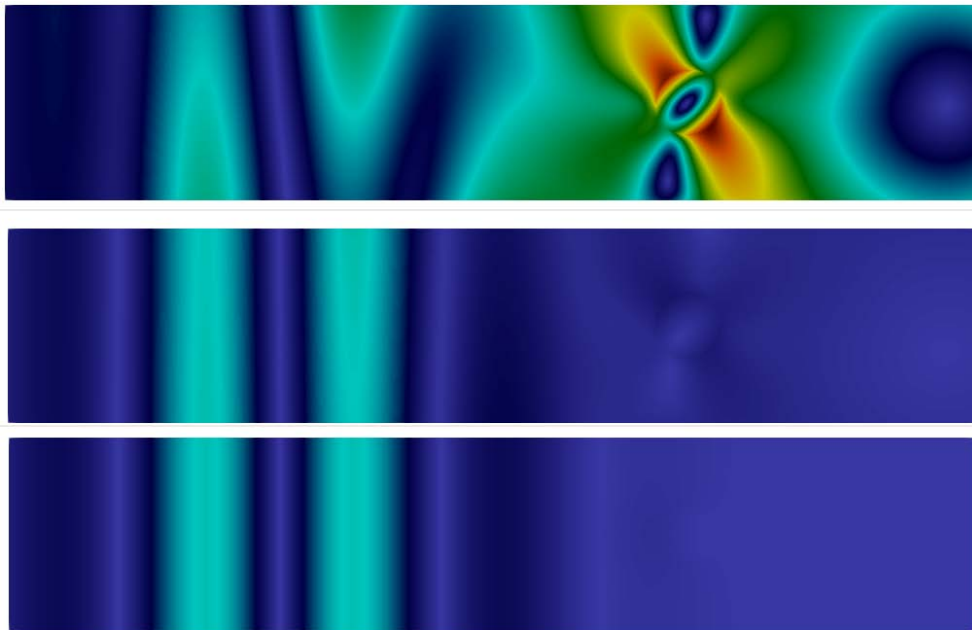


FIGURE 3.20: Before the wave packet touches the inclusion, comparison of displacement fields for three different inclusions with $R = 10 \text{ \AA}$ and $\omega = 5 \text{ THz}$: Top : an Eshelby's inclusion with an eigenstrain $= \epsilon^*$ (Eq.3.7). Middle : an Eshelby's inclusion with an eigenstrain $= 0.1 \times \epsilon^*$. Bottom : an elastic inclusion with $E_i/E_m = 0.2$.

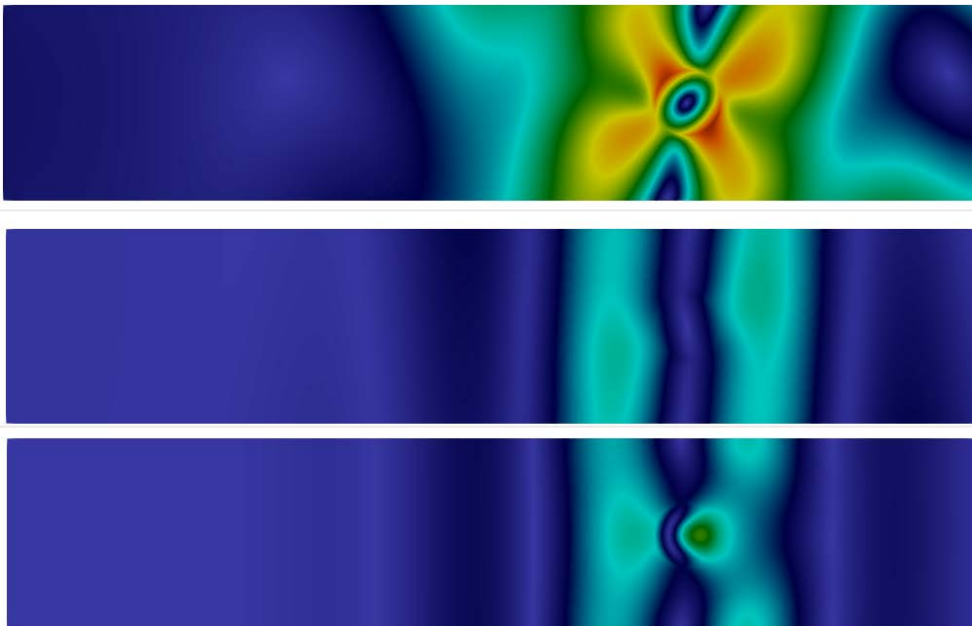


FIGURE 3.21: Idem. Near the inclusion.

the comparison with the analytic results. In addition, the effects caused by model size are presented. So far, a numerical tool to simulate a medium with Eshelby's inclusion is available. Several topics can be continued based on this model :

1) The work of T. Albaret et al. [ALB 16] has presented a possibility of extracting Eshelby inclusions associated with continuum mechanics from series of atomistic configurations, from which local plastic rearrangements are fitted through their displacement fields on collections of Eshelby spherical inclusions, allowing determination of their transformation strain tensors. Their results support the mesoscopic models that involve the Eshelby inclusion as the elementary brick of plasticity. Based on this point, our model should be extended to a larger size with collections of Eshelby inclusions.

2) The scattering of sound waves with Eshelby inclusion is an interesting topic. Based on his past work on dislocations[LUN 88], F. Lund has proposed an effective description of the role of Eshelby inclusions on scattering of sound waves in both static and dynamic cases. The derived equations link the eigenstrain and the spatial and temporal derivatives of the displacement field at the interface with the inclusion. The simulation based on the presented model can be used to verify this analytic description.

3) In the limit of the ratio $b/a \rightarrow 0$, an Eshelby's inclusion tends to be able to represent a dislocation dipole. The idea of mapping the Eshelby's inclusion and the dislocation loop and studying the response of stringlike dislocation loop to an external stress is another interesting point [LUN 88, ROD 09, MAU 05, CHU 16].

All these points encourage us to find an acoustic signature of plasticity in amorphous materials. This is very interesting since the structural signature of plasticity is still a subject of debate.

3 Nano-porous materials : from perfectly periodic to disordered holes arrangement

This is the special case where the second medium is the vacuum. The elastic contrast is zero and no vibration exists in the pores. As such, the interfaces play really the role of a boundary, with perfect matching, thus no roughness at this stage. This kind of system has been interpreted in the literature using the wave-behaviour of phonons and applying the optic laws of reflection to the propagating wave. Here we present such approaches, which, introduced for ultrasonic phononic media (microstructure on a millimeter scale), have been recently successfully applied to nanophononic membranes. Our purpose is to link such approaches to the microscopic understanding of the propagation of the wave-packet in the nanoporous medium, thanks to the insight that we can get with our FEM simulations.

3.1 Porous structure

In recent years, periodic nanoporous materials have arisen as very promising for heat transport control. The porous structure is composed of a host material from which periodic holes are removed to create a macroscopic array of nanoscale holes in two-dimensions (2D)[XIE 18] or three dimensions [MOO 16]. Such materials have been called nanophononic, as the nanometric counterpart of phononic materials, which, at their turn, are the acoustic counterpart of photonic materials for the control of electromagnetic waves propagation.

Phononic materials are materials structured with a periodicity, which is meant to affect phonon propagation. Because of the additional periodicity, two major effects arise : (1) the second periodicity defines a new Brillouin Zone much smaller than the atomistic one, causing the branch folding : as such, a large quantity of non-dispersive optic modes arise at very large wavelengths, and, when holes are replaced by other elements such as pillars or spheres, forbidden gaps can appear in the dispersion at the resonance frequency of those elements and (2) the multiple reflections of phonons by the periodic interfaces not only hinder their propagation but also give raise to constructive or destructive interference punctually localizing energy. Such interference only acts on waves keeping their phase after the multiple reflections, for which reason these waves are said coherent[TIG 06]. These phenomena can be observed on long-wavelength phonons, which do not see the atomic details of the interfaces, which are felt only like a boundary.

3.2 The optic-like approach to phonon scattering from periodic interfaces

When phonons have very long wavelengths, they cannot see the details of the atomic structure, they only feel the effective elastic properties of the medium and the interfaces are felt as boundary. In this limit, the elastic theory can describe their propagation and

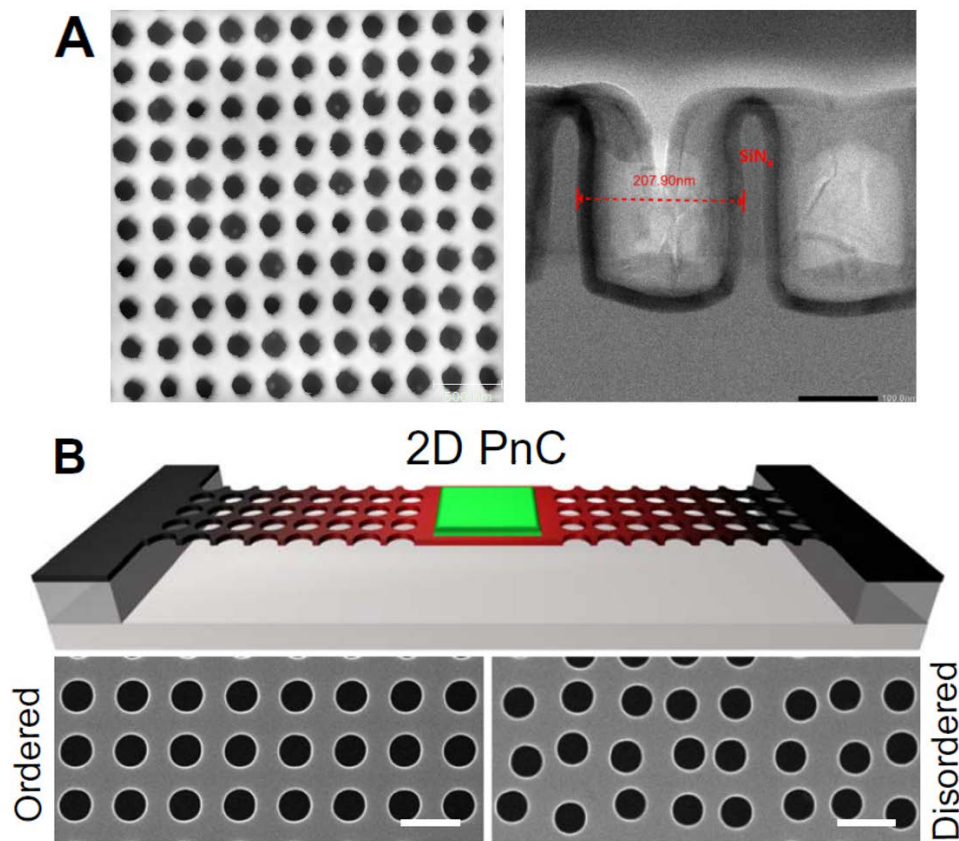


FIGURE 3.22: 2D porous material : SEM images of 2D porous phononic crystals (PnC) (A) Si_xN_y PnC with surface roughness $\eta_{wall} = 2.25$ nm, with position distribution $\eta_{eff,p} = 11.6$ nm and with size distribution $\eta_{eff,s} = 10.3$ nm. Left : top view ; Right : Side view of the profile of the holes. (B) Ordered and disordered in position PnC used to tune heat conduction at low temperature in the work of J. Maire[MAI 17].

give the right phonon dispersions. Such limit is obviously macroscopic. Its applicability is based on the assumption that the phonon can be treated as a wave and its reflection on the surface with the geometrical reflection laws.

It is clear that it exists a wavelength threshold below which the macroscopic continuum approach will fail, but even before that limit, another limit appears for coherent effects to take place : a wavelength threshold exists above which specular reflection allows for coherent wave interference, and below which this is not true anymore. For a perfectly planar boundary, this threshold will depend on the roughness of the interface : intuitively, as far as the phonon wavelength is much larger than the roughness, pure reflection will take place, but when they are comparable, the wave will be mostly diffusively scattered in all directions, losing the phase coherence needed for these phenomena to take place.

Traditionally, the coherent effects of a periodic structure have been essentially investigated in metamaterials for sound transmission guiding, filtering, hindering, which require a periodicity in the millimeter range, and a roughness not necessarily very small.

The technological advances allowing for a high quality of materials engineering, allowing for interfaces with a nm/sub-nm roughness, have opened the way to use coherent effects in nanostructured periodic metamaterials for impacting the propagation of smaller wavelength phonons, down to the nm-range, with the aim of affecting thermal transport at room temperature.

Indeed, very recently, the optic-like approach has been used to interpret some data collected on a phononic nano-porous membrane, showing an impressive agreement [MAI 17, WAG 16]. In those studies, it was shown that standing waves with wavelength in the micrometer range, due to coherent reflection from boundaries, could be observed down to the coherent threshold calculated with classical approaches. Moreover, the introduction of a slight disorder in the periodicity (holes size and position disorder) was shown to destroy the coherent effects, with consequences on thermal transport at very low temperature, where these long wavelength phonons dominate.

In this work we will present a FEM simulation of transient propagation of a wave-packet in a similar nano-porous membrane as the one investigated in Ref.[MAI 17] as shown in Fig.3.22 (b), at phonon wavelengths from larger to smaller than the periodicity, with the aim of identifying the microscopic features corresponding to the coherent effects. The first investigated system will have, by construction, no roughness, thus all phonons are supposed to be coherent. Then, similarly to Ref.[MAI 17], we will introduce some disorder in the pores position and size in order to disrupt the coherence.

Before introducing our model and simulations, we recall here the concept of wavelength threshold, based on the specularity parameter.

3.2.1 Roughness

As mentioned, coherent effects, as due to constructive interference between phonons, can arise only for wavelengths larger than a certain threshold, which depends on many geometrical parameters such as roughness, curvature, incidence angle at the interface.

Here we give a short introduction on the specularity parameter, which allows to calculate in a first approximation the threshold wavelength for coherent effects. We consider a rough surface on which a wave with wavelength λ with normal incidence is reflected. Referring to Fig. 3.23, the profile of the surface lies on the x, y plane. $y(x)$ indicates this profile as a function of the position x , measuring thus the asperities. A perfectly smooth surface would have $y=\text{constant}$ for all x . The deviation of height causes a shift in the plane wave phase along the surface :

$$\phi(x) = \frac{4\pi}{\lambda}y(x) \quad (3.24)$$

The variance of the phase will be

$$\langle \phi^2 \rangle = \frac{16\pi^2}{\lambda^2}\eta^2 \quad (3.25)$$

with η the root mean square deviation of the height of the surface with respect to a reference height.

If the incident wave comes with a non-zero incident angle (θ_1), we will have :

$$\langle \phi^2 \rangle = \frac{16\pi^2}{\lambda^2}\eta^2 \cos^2(\theta_1) \quad (3.26)$$

The phase autocorrelation function (*i.e.*, the probability to have the same phase, thus the same height y at a distance $x = \xi$) is

$$\rho_\phi(\xi) = e^{-\xi^2/L} \quad (3.27)$$

where L is a measure of the width of the bumps on the surface. The spectrum of the reflected way will depend on the reflected angle [ZIM 62] :

$$|F(s)| = e^{-\pi\langle\phi^2\rangle}\delta(s) + (1 - e^{-\pi\langle\phi^2\rangle})\frac{L}{\lambda\sqrt{\pi\langle\phi^2\rangle}}e^{-\frac{L^2}{\lambda^2\langle\phi^2\rangle}s^2} \quad (3.28)$$

with $s = \sin(\theta)$ and θ the angle of the reflected beam with respect to the surface normal. The first term is a perfectly specularly reflected beam, going back to the incident direction. While the second term represents waves reflected in all directions, thus diffused phonons.

The *specularity* parameter p is defined as the fraction of specularly back-reflected waves, so :

$$p(\lambda) = e^{-\pi\langle\phi^2\rangle} \quad (3.29)$$

Depending on the relation between the wavelength and the roughness, we may have three reflection regimes :

- if $\lambda \ll \eta$, $p(\lambda) \ll 1$, the incident wave is affected by the roughness, so the phase shift is very huge and the reflection is diffuse reflection.
- if $\lambda \gg \eta$, $p(\lambda) \approx 1$, the incident wave is not affected by the roughness, so the phase shift is small and the reflection is specular reflection.

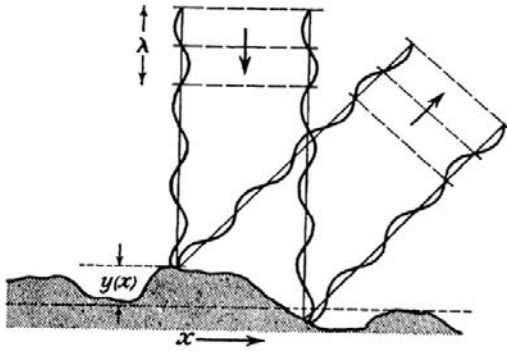


FIG. 142. Reflection from a rough surface.

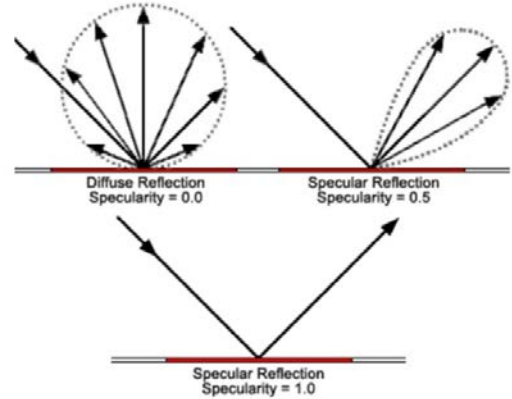


FIGURE 3.23: Reflection from a rough surface and three reflection regimes : diffuse, specular and intermediate regime [ZIM 62].

- for the intermediate regime $\lambda \approx \eta$, the reflected wave will be diffused but mainly concentrated in a cone around the specular direction.

Moreover, the roughness will have a distribution, so we can write p as the result of such a distribution :

$$p(\lambda) = \int P(\eta) e^{-\pi \langle \phi^2 \rangle} d\eta \quad (3.30)$$

It is generally assumed that for $p > 0.5$ the specularly reflected portion of the wave is important enough for giving visible coherent effects. This defines then the coherent wavelength threshold as the wavelength for which $p = 0.5$.

3.2.2 Real roughness and effective roughness

The amplitude of the profile roughness of a material surface is, as defined above, the standard deviation of the surface height. Besides the intrinsic surface roughness, other imperfections of nano-structure, like size and position disorder, will lead to the dephasing of the waves and the break down of coherence. If we consider a column of holes, they represent an interface which is met at the same time by a wavepacket ingoing onto it from the left. If holes have different size or slightly different positions, then they will be met at different times by the traveling wave-packet, inducing a phase shift and thus acting as an effective roughness

Let's first consider the hole **size disorder**. The incident wave fronts will touch the matter/holes interface and be reflected at different position as a function of the hole size, which will introduce new phase shift which will be added to the surface roughness. We note R_i the radius of the circular holes. If we note R_0 the reference size for which the phase shift is zero corresponding to the average of the size distribution and $\langle R_i \rangle = R_0$, for each hole the phase shift is $\phi = \frac{4\pi}{\lambda} (R_i - R_0) \cos(\theta_1)$. The standard deviation of the

phase shift due to the size is therefore :

$$\langle \phi^2 \rangle = \frac{16\pi^2}{\lambda^2} \eta_{eff,s}^2 \cos^2(\theta_1) \quad (3.31)$$

where $\eta_{eff,s}$ is the standard deviation of the radii of the holes.

Let's now consider the **positioning disorder**. Holes are translated along two directions with a translation length defined as D_x or D_y . Suppose a reference center position $\mathbf{x}_0 = (x_0, y_0)$, the phase shift due to the reflection on the interface for a given hole with center position $\mathbf{x}_i = (x_i, y_i)$ is related to the position difference $\Delta \mathbf{x} = |\mathbf{x}_i - \mathbf{x}_0|$. The standard deviation of phase shift due to the position is :

$$\langle \phi^2 \rangle = \frac{16\pi^2}{\lambda^2} \eta_{eff,p}^2 \cos^2(\theta_1) \quad (3.32)$$

where $\eta_{eff,p}$ is the standard deviation of the position difference of the holes belonging to the same column, *i.e.*, building up the same interface to the wavefront coming from the left. This standard deviation is linked to the "period" of the porous structure.

These effective roughness will be added to the real roughness from the walls of the holes (denoted as η_{wall}) to give a total roughness characterizing the material. This total roughness is given by :

$$\eta_{total}^2 = \eta_{wall}^2 + \eta_{eff,s}^2 + \eta_{eff,p}^2 \quad (3.33)$$

3.3 Model of nano-porous structure : ordered and disordered

In this section, I will give the details about the FE simulation, including the geometries of the model, materials properties as well as other information.

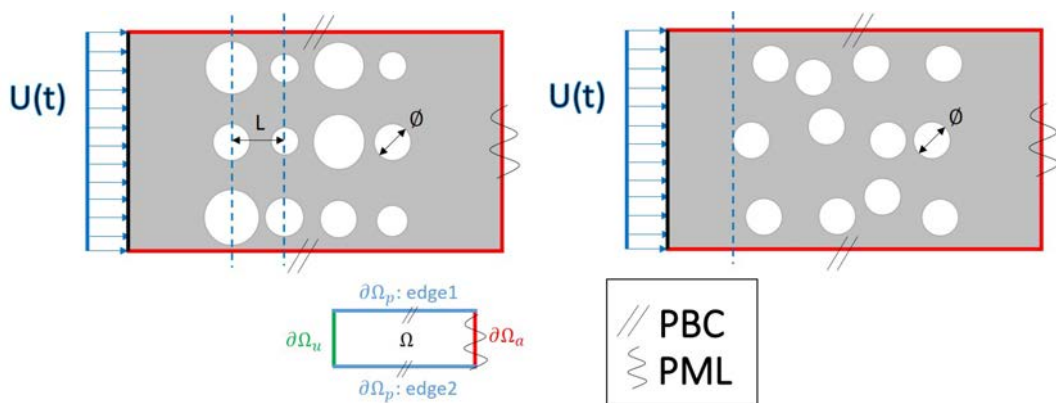


FIGURE 3.24: Illustration of effective roughness ascribed to the two types of disorder. The grey region is the material and the white regions are the holes. Left : center aligned circular with random radii ; Right : center non-aligned circular with identical radii.

3.3.1 Model geometry

Our aim is to model the nanoporous structure of Fig. 3.22, with periodicity $L=242$ nm and hole diameter $\phi =137.5$ nm, and gradually introduce size and position disorder. These geometrical values, of the same order of the ones in Ref.[MAI 17] have been chosen in order to investigate the same samples as the ones experimentally investigated within the PhD thesis of M. Hadi. For the same reason, as we will see later, the chosen material is amorphous SiNx. We thus establish a "pseudo-periodic" model based on the previous models in Chap.2 : equal square blocks are placed periodically along the x or y direction with period L being also the length of the square. Inside each block, only one hole can be placed at most. The computational model consists of 3×12 square blocks as illustrated in Fig.3.24 : the first 3×2 blocks without hole, then 3×9 blocks containing each a single circular hole, and finally another 1×3 blocks without hole. The large number of squares is necessary for establishing the wave-packet and studying the transient behavior, especially for the long-wavelength pulse *e.g.*, 402 nm. We will investigate the wave-packet propagation for wavelengths smaller, comparable and larger than the holes periodicity and size.

It is important that here we have created three alignments of holes instead of one. Here the reason of using an elementary cell with three holes rows can be appreciated. Disorder along x would not affect coherence as the wavefront coming from the left would always meet perfect interfaces, as reproduced by the periodic boundary conditions along y . Using three rows, with disorder of size and position in both x and y directions breaks the y -periodicity allowing to affect the coherence of the wave. However, if we use three alignments of holes with random radii or of non-aligned holes, wave front will touch earlier a certain hole among the three in the first column, thus breaking the vertical symmetry.

3.3.2 Model material properties

The nano-structure is a model amorphous SiNx, linearly elastic with isotropic homogeneous elastic behavior characterized by the Young's modulus $E = 130$ GPa, the mass density $\rho = 2650$ kg/m³ and the Poisson ratio $\nu = 0.27$. The above values are averaged values reported in Ref. [GAN 18]. For information, the speed of longitudinal wave in this bulk solid without holes is $c_L = 7829.4$ m/s.

3.3.3 Wavelength of the wave-packets

The expression of the wave-packet is the same as defined in Eq.2.1 with $t_0 = \frac{3\pi}{\omega}$. We have selected 5 representative frequencies ω given in Tab.3.7 as well as their corresponding wavelength λ . Experimental measurements of acoustic phonons have been done by our collaborators for 54 nm and 84 nm with X-ray Transient Grating techniques at the XFEL FERMI, so here we keep these two wavelengths. We study two wavelengths comparable with the nanostructure (inter-hole distance) : 104 nm and 163 nm, and finally a wavelength larger than the period (402 nm).

TABLE 3.7: Investigated frequencies and wavelengths in the model SiNx.

λ (nm)	54	84	104	163	402
ω ($\times 10^{12}$ rad/s)	0.9108	0.5855	0.472	0.3	0.1223

3.3.4 Implantation of the disorder

As mentioned before, two types of disorders will be introduced independently : random diameter Φ or random translation length D defined as the deviation of the hole position from the center of the block, and thus from perfect periodicity. Therefore, the only change we need to do is to set a random value, for each square, to specify the center translation or the scaling of the hole taking care that the resulting hole remains within its block.

• Random radius

We have defined a disorder parameter σ , as the standard deviation of a Gaussian distribution for the sample hole size. A routine randomly picks the hole diameter from such Gaussian distribution. We have investigated the case $\sigma=0$ (ordered), $\sigma=10.3$ and $\sigma=40$, which lead to a scaling of the diameter by a factor α , equal to 1 for $\sigma=0$ ($\Phi = \alpha\Phi_0$). The list of α factors for the different values of σ and for each hole in the elementary brick of the simulation is reported in Appendix.B, Tabs.B.1 and B.2.

• Random center position

In this case, we keep the same diameter for all holes and randomly modify their x and y position. We define then a translation factor d_x or d_y , such that the shift with respect to the center position is $D_x = d_x D_{max}$ and $D_y = d_y D_{max}$, with $D_{max} = 12$ nm and 45 nm. d_x , d_y are assumed to be uniformly distributed between -1 and 1. The d_x and d_y values are reported in Appendix.B, Tab.B.3.

In both disorder models, for each value of the disorder parameter, we have prepared three different samples and investigated the wavepacket propagation in each of them. Final results come from the average of the results of the three configurations. Such procedure allows us to get rid of effects due to the specific random configuration. More samples should be in the future prepared for each disorder configuration for improving this average procedure.

3.3.5 Other details about FE simulation

Central difference integrator is employed for the time integration with the time discretization $dt = 3.36 \times 10^{-14}$ s and the total simulation time is $40000 \times dt$. We measure the envelope of the kinetic energy induced in the system by the propagation of the wavepacket, summed over the y -direction. Energy is supported by the frame in x with width $\Delta x = 2.75$ nm in the x -direction.

3.4 Estimation of the coherence length

Here we will give an estimation of coherence length with respect to the disorder by

neglecting the roughness from the wall ($\eta_{wall} = 0$). This latter is characterized by the total roughness given by Eqs.3.31-3.33. Then, total roughness and wavelength of phonon determine the specular parameter $p(\lambda)$ (Eqs.3.29 and 3.29) which is between 0 and 1. p as a function of λ and η is shown in Fig.3.25 (a). It shows that, depending on the roughness, the critical wavelength increases with roughness. As mentioned, usually it is assumed that $p(\lambda_c) = 0.5$ is needed to see coherent effects. As such, one can get a critical wavelength λ_c , also called the coherence length.

A first estimation of the coherence length as a function of the disorder parameter σ is 135 nm for $\sigma = 10$ and 535 nm for $\sigma = 40$. The coherence length is linear with the disorder parameter, giving the red dashed line in Fig.3.25 (b). If the wavelength of initial coherent acoustic phonons is less than the coherence wavelength, phonons will lose their phase after successive scattering events. Therefore, wavepackets with wavelength larger than the coherence threshold are expected to show coherent effects, while wavepackets with smaller wavelengths are not. Thus, we use the red line to separate the coherent phonon regime ($p > 0.5$) or the incoherent regime ($p < 0.5$).

From the figure, we can observe that all investigated wavepackets in the perfectly periodic sample are in the coherent regime. However, if we assume an uncertainty on the position of the crossover between coherent and incoherent, all aperiodic cases should be incoherent at all disorder degrees, except for $\lambda=402$ nm. For $\lambda=402$ nm, only the large disorder should be incoherent.

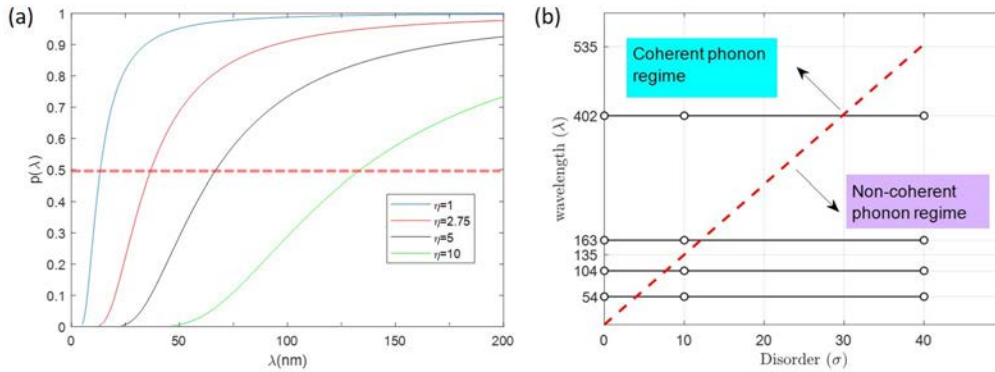


FIGURE 3.25: (a) Example of specular parameter as a function of wavelength λ for different values of the roughness η . (b) Phase diagram of the coherence regime as a function of the disorder parameter and of the wavelength. Coherent and non-coherent regime is identified. White circles are the data points for the FE simulations.

3.5 Results : Envelopes of the kinetic energy

There are two ways of comparing the results of the simulations, that we call longitudinal and transverse :

- Longitudinal : Observation of one disordered configuration over different wavelengths.

- Transverse : Observation of one wavelength over different disordered configurations.

Here, I only present a transverse survey for the envelope of the kinetic energy. For five different wavelengths $\lambda = 54, 84, 104, 163$ and 402 nm, we have five groups of comparison for the envelopes. As shown in Fig.3.26, in each group, the envelopes from different disordered configurations are superposed : one ordered structure (periodic) and four disordered structures. The yellow line (ordered structure) is observed always on the top of other lines (disordered structure). A special case is $\lambda = 402$ nm in which in the envelopes for weak disorder (size disorder with $\sigma = 10$ & position disorder with $D_{max} = 12$) the envelope is indistinguishable from the envelope in the ordered one.

Inside the figures, we use black straight lines to identify an exponential decay in the semi-log plot. The exponential decay of the energy envelope can be considered as a result of the acoustic attenuation in the *propagative* regime for acoustic phonon. In most cases, there exists a second regime after the first one, which is especially evident for the periodic structure. In the second regime, the attenuation of the energy envelope becomes weaker than that in the first regime. In the following, for each wavelength, we give our observations about the energy attenuation, which is inversely proportional to the mean-free path fitted by the Beer-Lambert law, in the first and second regimes, as well as the crossover positions between two regimes :

For $\lambda=54$ nm, the crossover for the periodic structure is at 1700 nm. Still, what we see is that the larger the disorder, the sooner the envelope detaches from the one of the periodic system and its energy remains smaller. There is almost one single regime for the disordered case since the crossover is not evident.

For $\lambda=84$ nm, the crossover is around 1500 nm and arrives slightly earlier in the disordered case. In the first regime, the envelopes for small disorder coincide with the envelopes for the periodic sample. However, the envelopes for large disorder have smaller mean-free paths, indicating stronger attenuation. In the second regime, the envelopes of small and large disorders join each other and their energy remains smaller than the one of the periodic sample.

For $\lambda=104$ nm, the crossover is around 1400 nm. We are here at the wavelength corresponding to inter-pores distance along the propagation direction (104.5 nm). Here disordered and periodic envelopes perfectly match until the crossover. Then all disordered structures are equivalent, they almost do not present a second regime, and their energy remains smaller than that in the periodic sample.

For $\lambda=163$ nm, the crossover is around 1600 nm for the periodic case. There is almost a single regime for disordered case. Compared to the periodic case, reduced mean-free path are remarked for the disordered and the reduction increases with the increasing disorder degree.

For $\lambda=402$ nm, the crossover position is around $x = 1500$ nm. Especially, small disorder and periodic are indistinguishable which is different from the small disordered cases for any other investigated wavelengths.

Three main observations can be summarized : (1) The envelopes for the periodic case are always at equal or higher energy than the ones for the disordered cases. In some cases,

3. Mechanical response and acoustic attenuation for different types of interfaces

the more the disorder, the smaller the energy of the envelope. This means that at a given position x the stronger the disorder the smaller the kinetic energy which is transported through x . (2) A crossover separating two regimes can be found in almost all the cases, (3)

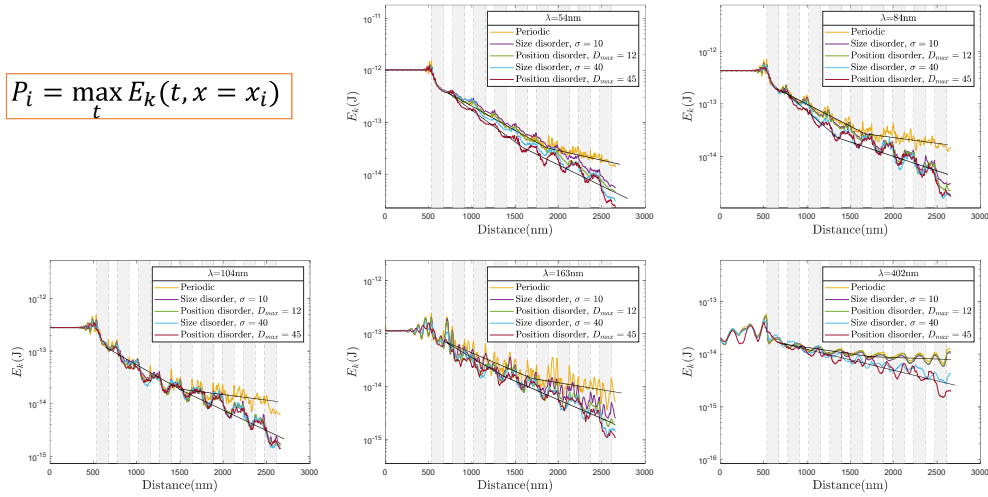


FIGURE 3.26: Envelope of the kinetic energy $P(x)$ for the ordered and the disordered PnC with wavelength $\lambda = 54, 84, 104, 163$ and 402 nm. Exponential decay is illustrated as the black lines. Crossover from the first exponential decay regime to the second exponential regime is clearly shown for the periodic cases and the envelope in fact turns to a $1/x$ decay.

3.6 Discussion

Let's go back to the classical optic-like concept of coherence [ZIM 62] : a wave will be said *coherent* if at the interface it reflects almost specularly at a single reflection angle. If the interface is rough, a dephasing is introduced and the wave is diffused in a solid angle whose width depends on the roughness. In a periodic system, this coherence allows to see the pores as a diffraction grating, and intensity peaks can appear, similarly to the Bragg diffraction. If coherence is lost, the grating is lost. The question is : if we look at the propagation of a wave packet, and more specifically at the propagation of the vibrational energy, how this concept of coherence translates? We have seen that, following the classical optic-like treatment, we should be always in a coherent case for the periodic sample, and always in incoherent conditions for the disordered ones, except for $\lambda=402$ nm. At this wavelength, the large disordered cases lie in the incoherent regime, while the small disordered ones in the coherent one. Indeed we see here that the energy envelope for small disorder at 402 nm is indistinguishable from the periodic case. For those which are incoherent, the reduction of the mean free path with respect to that in periodic structure could be thus associated to the incoherently scattered wave. Moreover, their second

regime is not as obvious as in the periodic case.

The second regime introduces a sort of slow down of the normal dissipation found in the first regime. Here energy remains longer in the system at large traveled distances. Indeed, one can verify that in the periodic sample, in the first regime the Beer-Lambert law is followed, while in the second the envelope follows a $1/x$ dependence. As such, this crossover marks the change from a propagative to a diffusive regime, similarly to Refs.[[BEL 18](#), [TLI 19](#)]. The x position of this crossover marks the traveled distance after which the wave-packet loses its propagative character and turns to a diffusive motion. Thus, the diffusive character is built up during the path, and at the end it gives a crossover when diffusion dominates on propagation. Interestingly, such crossover is always present in the periodic case, while it is only weakly present in disordered systems, so that we can assume almost a single propagative regime.

On the basis of all of this, we can apparently relate the presence of a diffusive regime as an effect of coherence (coherent trapping of the energy due to multiple coherent reflections, which then diffusively spreads). Due to this trapping, the total envelope energy decreases more slowly, and energy is not straight propagated anymore, but moves on in a diffusive way. The coherence degree will thus correspond to the amount of total energy which diffusively spreads in the second regime. By comparing the envelopes in the second regime, it is seen that coherence decreases with disorder as expected. The reduction of the mean free path proportional to disorder degree in the first regime is likely related again to this trapping : in the periodic case the trapping increases the local energy because of the back-reflection, thus it increases the mean free path. In the disordered case the mean free path is thus reduced with respect to the ordered one because of the lack of coherent back-reflected waves and trapping.

To summarize, we observe a first regime marked by disorder with mean free path decreasing with disorder, and a the second regime, which comes from the constructive interference of waves multiply reflected. This second regime is purely diffusive for a perfectly periodic nanoporous sample while in a disordered sample there appears a mixed regime, where, if the slope decreases, the $1/x$ behavior is actually not followed. This is likely due to the coexistence of localization between pores (see maxima more pronounced with disorder) and diffusion or anomalous diffusion. It is tempting to associate the change of regime with an effective Ioffe-Regel crossover, induced by the nanostructure. If its position along the traveled distance does not depend on disorder, it is clear that the regime beyond it will be different, as we move from a pure diffusive regime for a periodic system to a mixed one for a disordered one.

Finally, it is worth reminding that in the first approximation we neglect here the possible existence and role of surface waves on the pore surface. Also note that the dynamics remains indeed far more complex, for example it keeps spatial oscillations in the kinetic energy that are located between the inclusions in the aperiodic case.

3.7 Conclusion and perspectives

To conclude, we investigated a series of simulations of wave propagation in a phononic crystal with ordered/disordered circular holes. Two types of disorder are independently introduced into the model, *i.e.*, the size of the holes and of the position of the holes. Our results demonstrate that periodic porous structures promote the presence of a diffusive regime as an apparent effect of coherence at sufficiently small wavelength or large distance. Increasing the disorder degree has two effects : the reduction of the mean free path in the first propagative regime, and the weakening of the crossover to the second regime, with a second regime where the behavior is not fully diffusive, but has a mixed and more complex character. Both effects can be brought back to results of a reduction of the coherent multiple reflections of the wave with increasing disorder.

Wave interference effects are at the origin of new approaches for manipulating heat flow. However, application of the coherence of phonon to manipulate phonon transport is a challenging work. To maintain the phase of coherent phonons at room temperature, phonons must scatter specularly inside the nanostructures. Therefore, nanoscale periodicity and atomically smooth surfaces are required. Our results allow to identify the effect of coherence and lack of coherence on the wave-packet propagation, and thus energy transport. Interestingly, we have shown that, since the coherence is also found in the weakly disordered structure, there is a frequency-dependent tolerance range of disorder inside which coherent effects are preserved as in a perfectly periodic structure.

Work can be extended in many ways. Firstly, further temporal and spectrum analysis can be done to complete the work by obtaining other propagation and vibration properties, such as effective group velocity, the DOS, etc. The experimental work in Ref.[MAI 17] can be numerically studied to verify the reduction of the thermal conductivity due to the coherence effect, since their Fourier-transport-equation-based FEM simulation can not show the impact of disorder. Secondly, the shape of the holes can be easily changed to other shapes. It is clear that our nano-porous model with disorder opens the way to a large variety of studies.

Finally, the strong oscillations in the kinetic energy induced by disorder in our results cannot be described within a classical optic-like approach. Mechanisms are much more complex if the nanostructures are aperiodic and it's not a simple wave scattering mechanism. A more comprehensive understanding is therefore necessary.

4 Acoustic attenuation in a medium with heterogeneous elasticity

In this section, based on the concept of the heterogeneous-elasticity theory, acoustic attenuation in disordered solids containing random elasticity in space will be analyzed using FEM simulations. No dissipation is introduced in this frame, the attenuation is only ascribed to the disorder-induced scattering of plane waves, still in the harmonic approximation. The results of the frequency-dependent acoustic attenuation is measured and compared with the results from the MD and the predictions of the theory.

4.1 Introduction of the vibrational anomalies in glasses in the terahertz range

Numerous anomalies show up in atomistically disordered materials, like glasses, in the terahertz frequency range : the most renowned is an enhancement of DOS with respect to the Debye prediction $g(\omega) \propto \omega^2$ [ALL 99, FEL 99] which gives rise to a maximum of the reduced DOS $g(\omega)/\omega^2$ (3D) called "boson peak" (BP). From inelastic scattering experiments (IXS) and MD simulations [MON 09b, MON 09a, BAL 11, MAR 13, SCH 15b], it was reported that the BP is associated with a dip of the group velocity (negative dispersion of the sound velocities) and a strong increase of the Brillouin line width $\Gamma(\omega) \propto \omega^4$, which has been explained as disorder-induced Rayleigh-like scattering. Such a sudden decay in the group velocity is responsible for the peak of the function $C(T)/T^3$, where C is the specific heat, while the anomalous dissipative behaviour is responsible for the unusual temperature dependence of the thermal conductivity, a plateau in the glassy thermal conductivity occurring at $T \approx 10K$ that is for a thermal energy comparable to the vibrational energy of the Boson peak [TLI 19, POH 01, ZEL 71].

Recently, the results of IXS [MON 09b, MON 09a, BOV 05, CAP 09] and MD simulations [TAN 02, MON 09b, LEO 05, HOR 01, LÉO 06b, MAY 09, PIL 04, SCH 04, RUO 08, DER 12] have shown that the disorder-affected local transverse elasticity play a key role for producing the anomalies. In addition, in many materials (glassy or crystalline) there exist localized vibrations in addition to plane wave contribution to the low-frequency vibrations. Therefore, models in which glasses are assumed to have quasi-local disorders induced oscillators have been proposed. These oscillator are assumed to be created by glass-specific soft bistable potentials, similar to those in the two level system (TLS) model. Regardless of the associated issue of energy barriers, all these models lead to a spatially fluctuating elastic constants, as it could also have been inferred simply from the disordered nature of the atomic structure [TSA 09]. Starting from these points, field-theoretical derivations of a mean-field theory of heterogeneous elasticity have been given by W. Schirmacher, including two versions : the coherent-potential approximation (CPA) and the self-consistent Born approximation (SCBA) [MAR 13, SCH 15b]. In heterogeneous elasticity theory the shear modulus G is assumed to spatially fluctuate according to a given probability distribution. In such a spatial disorder medium, the effective

frequency-dependent elastic moduli have a real and imaginary part [SCH 13, SCH 15a], the imaginary part of the effective shear modulus being responsible for the acoustic attenuation induced by disorder.

The frequency-dependent attenuation coefficient Γ predicted by the heterogeneous-elasticity theory is compared to the MD simulation results in Ref.[MAR 13, SCH 15b] in which a good agreement is reported. Based on the previous works, by means of the FEM simulation, we prepared disordered computational models containing random elasticity in space. Dynamic attenuation of the wave-packet as it goes through the samples will be investigated. No dissipation is introduced in this frame, the attenuation is only due to the disorder-induced scattering of the harmonic motion. The purpose is to measure the attenuation from a transient process of wave-propagation and compare with the result from the MD and the predictions of the theory.

This chapter is organized as follows : In Section.4.2 the basic definition and two versions of a mean-field theory for solving the stochastic equations of motion are presented. In Section.4.3, FE simulation of wave propagation in disordered media with random elasticity will be investigated and the attenuation from FE simulation is then compared to that from MD simulation and predictions of the heterogeneous-elasticity theory. Discussion and conclusion will be given in Sec.4.4 and Sec.4.5.

4.2 Introduction of the theory of heterogeneous elasticity

4.2.1 Basic definition

(a) Frequency-dependent elastic moduli and attenuation

By analogy with magnetic systems, but replacing the magnetic field by the volumic forces, the longitudinal dynamic susceptibility in a glass $\chi_L(k, z) = \chi'_L(k, \omega) + i\chi''_L(k, \omega)$ (k is the wave number and $z = \omega + i\varepsilon$, $\varepsilon \rightarrow +0$) can be expressed as [SCH 06] :

$$\chi_L(k, z) = \frac{k^2}{-z^2 + k^2 v_L^2(z)} = k^2 G_L(k, z) \quad (3.34)$$

where the longitudinal frequency-dependent sound velocity $v_L(z)$ is associated to the frequency-dependent longitudinal modulus $M(z)$ by

$$M(z) = \rho_m v_L(z)^2 = M'(\omega) - iM''(\omega) \quad (3.35)$$

$G_L(k, z)$ is the longitudinal (disorder-averaged) Green's function which determines the response of displacement to a perturbation of the force per unit mass.. The sound attenuation coefficient (inversely proportional to the relaxation time) can be defined as

$$\Gamma_L(\omega) = \omega M''(\omega) / M'(\omega) \quad (3.36)$$

The correlation function in the displacements is the one-phonon dynamical structure factor $S(k, \omega)$ which is related to the longitudinal dynamical susceptibility by the

fluctuation-dissipation theorem [KUB 57, SCH 15b]. Defining the resonance frequency $\Omega_L(\omega) = v_L(\omega)k$, we obtain the dynamical structure factor

$$S(k, \omega) = \frac{k_B T}{\pi m \omega} \chi_L''(k, \omega) \quad (3.37)$$

$$= \frac{k_B T}{m \omega} \frac{1}{\pi} k^2 \frac{\Omega_L^2 \Gamma_L(\omega) / \omega}{(\Omega_L^2 - \omega^2)^2 + (\Omega_L^2 \Gamma_L(\omega) / \omega)^2} \quad (3.38)$$

where m is the ratio of the mass density ρ_m and the number density N/V of the material, V is the total volume of the sample and N is the total number of atoms or molecular units.

Near resonance $\omega = \Omega_L$ we get the "damped-harmonic-oscillator" (DHO) function, with which many Brillouin-scattering spectra have been fitted :

$$S(k, \omega) = \frac{k_B T}{\pi m \omega} k^2 \frac{\omega \Gamma_L(\omega)}{(\Omega_L^2 - \omega^2)^2 + \omega^2 \Gamma_L(\omega)^2} \quad (3.39)$$

In a disordered harmonic system (heterogeneous-elasticity), there is no anharmonic damping as due to phonon-phonon interactions. A finite Γ is explained due to the disorder and describes static scattering. Γ is inversely proportional to the mean-free path, divided by the wave velocity, which involves no dissipation.

Transverse properties (T) can be defined in a similar way.

(b) Wavenumber-independent spectra

Within a generalized Debye model, which is described by the Green's function $G_{L,T}$, the vibrational density of states (VDOS) is given by [SCH 15b]

$$g(\omega) = \frac{2\omega}{3\pi} \frac{3}{k_D^3} \int_0^{k_D} dk k^2 (G_L''(k, \omega) + 2G_T''(k, \omega)) \quad (3.40)$$

where $k_D = \sqrt[3]{6\pi^2 N/V}$ is the Debye cutoff wavenumber.

It is useful to define longitudinal and transverse susceptibility integrated up to a certain wavenumber cutoff k_ξ

$$\chi_{L,T}^\xi(z) = \frac{3}{k_\xi^3} \int_0^{k_\xi} dk k^2 \chi_{L,T}(k, z) \quad (3.41)$$

k_ξ can be related to the correlation length ξ of the spatially fluctuating parameter, for example the shear modulus G , denoted as ξ_G . More details can be found in Ref. [SCH 15b].

4.2.2 Heterogeneous-elasticity theory

(a) Model

Heterogeneous-elasticity theory is formulated in terms of standard elasticity theory [LAN 86]. For a linear and isotropic medium as in Eq. 1.43, we can write the Hooke's law as

$$\sigma_{ij} = 3K \epsilon_{ij}^{sph} + 2G(\mathbf{r}) \epsilon_{ij}^{dev} \quad (3.42)$$

where ε_{ij}^{sph} and ε_{ij}^{dev} are defined in Eq.1.32 and \mathbf{r} is the position.

Next, we introduce the spatial fluctuations of the shear modulus G as first step for establishing the heterogeneous-elastic theory.

(b) SCBA & CPA

Now, the above theory of elasticity is generalized for allowing the elastic constants to fluctuate in space. W. Schirmacher has given two versions of a mean-field theory for solving the stochastic equations of motion [MAR 13, SCH 15b] : the self-consistent Born approximation (SCBA) and the coherent-potential approximation (CPA) . I will compare briefly the results of both. Before that, two common assumptions : (1) the breakdown of the homogeneity is more important than that of the isotropy and (2) the fluctuations of the shear modulus G are stronger than those of the bulk modulus.

SCBA assumes that the spatial statistic fluctuations of the shear modulus G follow a *Gaussian* distribution

$$P(G) = \frac{1}{\sqrt{2\pi \langle \Delta G^2 \rangle}} e^{-(G-G_0)^2/2\langle \Delta G^2 \rangle} \quad (3.43)$$

where G_0 is the mean and $\langle \Delta G^2 \rangle$ is the variance and G are decorrelated. The mean-field theory for heterogeneous shear elasticity gives the following self-consistent equations for the macroscopic moduli [MAR 13]

$$\tilde{G}(\omega) = \tilde{G}_0 - \Sigma(\omega) = v_T^2(\omega) \quad (3.44)$$

$$\tilde{M}(\omega) = \tilde{K} + \frac{4}{3}\tilde{G}(\omega) = v_L^2(\omega) \quad (3.45)$$

$$\Sigma(\omega) = \gamma \tilde{G}_0^2 \frac{1}{N} \sum_{|k| < k_D} \left[\frac{2}{3} \chi_L(k, \omega) + \chi_T(\mathbf{k}, \omega) \right] \quad (3.46)$$

\tilde{x} means the quantity x normalized by the the mass density ρ , for example, $\tilde{G}(\omega) = G(\omega)/\rho = G'(\omega)/\rho - iG''(\omega)/\rho$. The influence of the disorder is given by the complex self-energy function $\Sigma(\omega)$. The \mathbf{k} summation $\frac{1}{N} \sum_{|k| < k_D} k^2 dk$ is restricted to values smaller than the Debye wavenumber $k_D = \sqrt[3]{6\pi^2 N/V}$ where N is the number of atoms and V is the volume of the sample. γ is the disorder parameter :

$$\gamma = (N/V)V_c \langle \Delta G^2 \rangle / G_0^2 \quad (3.47)$$

where V_c is the coarse-graining volume. The second parameter of the theory is the ratio K/G_0 . It is noticed that there exists a critical value of the disorder parameter γ_c beyond which shear modulus becomes negative and the system is unstable. SCBA is limited in small disorder case.

CPA version allows the use of any distribution of the shear elasticity G and the presence of the negative modulus [SCH 15b]. In CPA theory, the microscopic fluctuations of G are averaged over a coarse-graining volume of diameter ξ_G , where ξ_G is the correlation length of the G fluctuations, meaning that the values of G_i corresponding to the volume

TABLE 3.8: Comparison between the SCBA and CPA (SCBA can be included in CPA in the weak-disorder limit)

	SCBA	CPA
Distribution of G	Gaussian distribution	Arbitrary distributions
Disorder level	Weak disorder	Weak & strong disorder
Can G be negative ?	$G > 0$	G can be negative
Parameter	γ and K/G_0	$\langle \Delta G^2 \rangle$, G_{min} and $\tilde{\nu}$.

with center r_i are assumed to be statistically uncorrelated. The self-consistent equation for $G(\omega)$ are :

$$G(z) = \left\langle \frac{G_i}{1 + \frac{\tilde{\nu}}{3}(G_i - G(z))\Lambda(z)} \right\rangle_i \quad (3.48)$$

$$\Lambda(z) = \frac{4}{3}\chi_L^{\xi G}(z) + 2\chi_T^{\xi G}(z) \quad (3.49)$$

where $\tilde{\nu}$ is an inverse effective density restricted to the correlation volume ξ^3 . $\chi_{L,T}^{\xi G}$ is defined in Eq.3.41. $\langle \dots \rangle_i$ denotes an average over the space. In SCBA, the shear modulus G depends on the Σ thus the γ which is determined by the parameters of the Gaussian distribution. However, in CPA, the fluctuations of $G(\mathbf{r})$ can be any distribution.

A most studied case is when the fluctuations of the shear modulus are assumed to follow a *truncated Gaussian* distribution [SCH 15b]

$$P(G) = P_0 \theta(G - G_{min}) e^{-(G-G_0)^2/2\langle \Delta G^2 \rangle} \quad (3.50)$$

where P_0 is a normalizing constant, $\theta(x)$ is the Heaviside step function and G_{min} is the lower cutoff which can be negative. It was shown that the CPA theory with Gaussian distribution of G reduces to the SCBA in the weak-disorder limit, *i.e.*, $\Delta G/G_0 \ll 1$. We compare the two versions in Tab.3.8.

4.2.3 Explanation of the vibrational anomalies in glasses in terms of the heterogeneous-elasticity theory

Frequency-dependent vibrational properties in glassy materials are not only predicted by the heterogeneous-elasticity theory but also investigated by MD simulation. some interesting results from literature are reported in Fig.3.27 which show that the BP associated anomalies can be qualitatively and quantitatively explained and reproduced in terms of this theory by comparing to the MD simulation.

We first show the results from MD simulation, for example, the results of DOS and attenuation are shown in Fig.3.27 (a), the Ioffe-Regel (IR) frequency is marked by the intersection of $\Gamma\pi$ (symbols) and frequency Ω (solid lines) where Γ and Ω are obtained by the DHO fit as presented in Eq.3.39. In the inset figure, the boson peak frequency is

given by the maximum of the reduced DOS ($g(\omega)/\omega^2$) around $\omega = 1$. The BP frequency is near the transverse IR frequency.

In (c), the results of G' and G'' from the theory (SCBA) and from the above mentioned MD simulation are compared. It can be seen that the SCBA results agree with the simulations. It is said that the frequency of the dip of G' and the strong increase of G'' coincide with the BP frequency. However, this range of the BP is relatively large since the location of the dip is in fact around 0.5.

In (b), from the prediction of CPA theory, it is shown that the frequency of the BP can be modified by tuning the disorder parameter, *e.g.*, G_{min}/G_0 .

As explained in Ref.[SCH 15b], within both theories (CPA & SCBA) the disorder-induced fluctuations of the shear modulus are transformed into a frequency dependence of the complex macroscopic shear modulus $G(\omega) = G'(\omega) + iG''(\omega)$ and G'' is proportional to the sound attenuation Γ and to the inverse mean-free path. When the mean-free path becomes comparable to the wavelength of the vibrational excitations (phonons), the concept of waves breaks down, and the excitations are random-matrix-type states. The boson peak and the related anomalies appear as the consequence of such a transition from wave-like to random-matrix-like behavior in glasses.

4.3 Wave propagation in a medium with heterogeneous elasticity

In this section, I will firstly present the computational model with random elasticity. By spatially perturbing the Young's modulus E thus the shear modulus G , we define a random-elastic medium and then look at wave-packet passing through this sample. As usual, from the envelope of the kinetic energy, frequency-dependent acoustic attenuation is found. To quantify the attenuation length, we measure the mean-free path by fitting the average energy envelopes with the Beer-Lambert law, then compare it to the results reported in the MD simulations and heterogeneous-elasticity theory. This work is inspired by the work of W. Schirmacher et al[MAR 13, SCH 15b].

4.3.1 Computational model

(a) Geometry

The computational model, as illustrated in Fig.3.28, consists of one big square block and many small square blocks connecting to each other with perfect connection. Each square is assumed as linear elastic, homogeneous and isotropic. The height of the model is $L = 60$ nm and the length of the model is $9L$. The side length of the first big square is L and the side length of the small square is ξ . In the figure, the gray level represents the different elasticities. The first big homogeneous square is used for the establishment of the wave-packet, followed by the heterogeneous-elasticity sample. Just like the previous works in the Chap.2, wave-packet is imposed at the left side, PMLs and PBCs are applied on the other boundaries. In addition, the correlation length is set as $\xi = L/3$ in this work.

(b) Materials properties

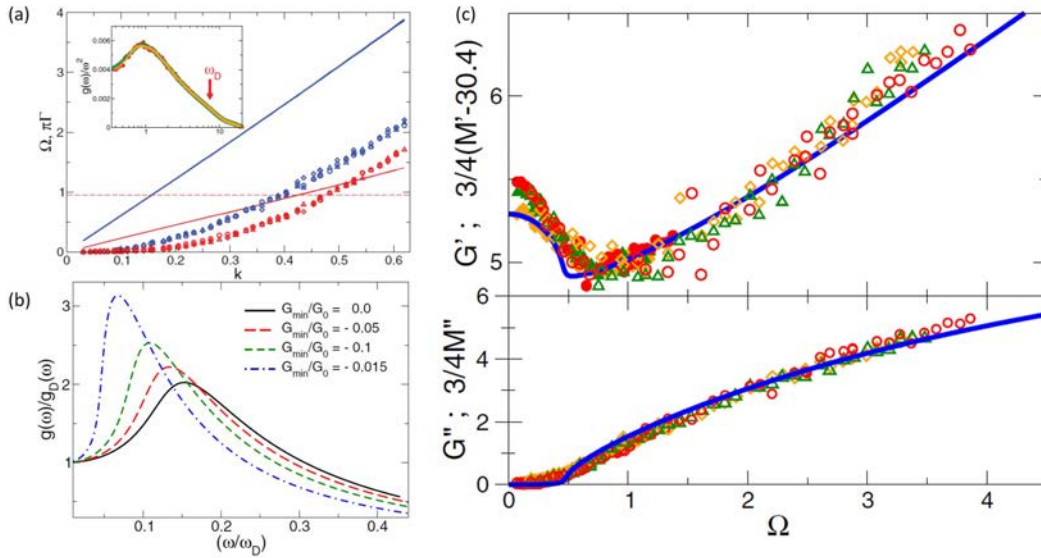


FIGURE 3.27: Some results based on the heterogeneous shear modulus in the literature (a) From MD simulation : Resonance frequencies $\Omega_{L,T}(k)$ (straight lines) and Brillouin line widths $\Gamma_{L,T}(k)$, multiplied with π . The dashed line indicates the BP position, which is near the transverse Ioffe-Regel crossing. (Insert : Reduced density of states $g(\omega)/\omega^2$ as obtained from the velocity autocorrelation function) [MAR 13] (b) From the CPA : Reduced density of states $g(\omega)/g_D(\omega)$ as a function of reduced frequency ω/ω_D for different values of the parameter G_{min}/G_0 . (c) Comparison of results of MD simulations (symbols) with the predictions of heterogeneous-elasticity theory in SCBA. Real (imaginary) part of G is shown in upper (lower) panel as a function of frequency. The SCBA parameters are $\gamma - \gamma_c = 0.08$ and $K/G_0 = 3.166$ [MAR 13, SCH 15b].

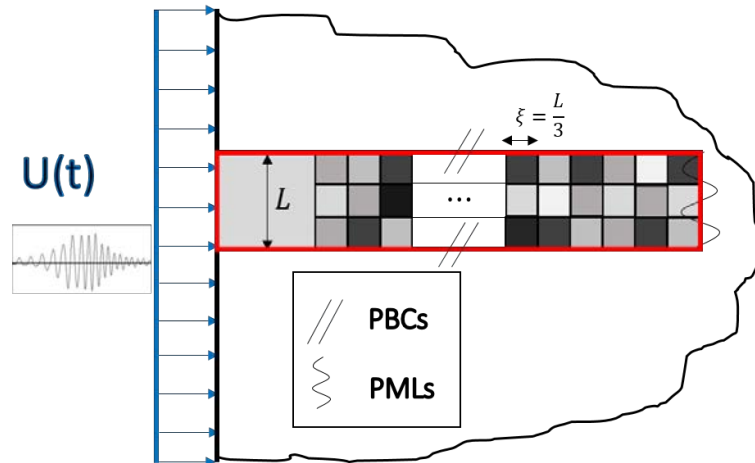


FIGURE 3.28: Illustration of the disordered elasticity model with height L and correlation length ξ . The gray level indicates the random elasticity. Wave-packets are imposed at the left side boundary. PBCs are applied on the top and bottom boundaries. PMLs are applied on the right side boundary.

To be consistent with the works of W. Schirmacher et al [MAR 13, SCH 15b], we use the macroscopic elastic moduli $K = 30.4$ GPa and $G_0/K = 3.166$. From the extracted data of $G(\omega)$ and $c_T(\omega)$ in Fig.3.27 (c), we can get the mass density $\rho \approx 0.985$ which is independent on ω , thus we assume a constant mass density $\rho = 1$ kg/m³. Material properties are summarized in Tab. 3.9 in which other properties have been derived from the known values. The Poisson's ratio $\nu = \frac{3K-2G}{2(3K+G)} = 0.357$. ν and ρ are homogeneous over the entire sample.

In addition, being a material with mass density $\rho = n$ kg/m³, that material is equivalent to the present material in terms of wave properties, *e.g.*, $c_{L,T}$ and $\lambda(\omega)$, if its elastic moduli are scaled by a factor $n/1000$. For example, for $\rho = 2303$ kg/m³ as in Chap. 2, the equivalent $K_{eq} = 2.303 \times K = 70.011$ GPa.

TABLE 3.9: Material properties for the computational model

ρ (kg/m ³)	K (GPa)	G_0 (GPa)	E_0 (GPa)	ν	$c_{T,0}$ (km/s)
1	30.4	9.602	26.062	0.357	3.099

Inside every correlation zone (small square with edge length ξ in Fig.3.28), a constant G_i is assigned which follows the Gaussian distribution with a mean being the G_0 and the variance being $\frac{\Delta G^2}{G_0^2}$ which is chosen as 0.19. It has been checked that no negative value exists for the G_i .

(c) Wave-packets

We only consider here the transverse polarization. As presented in the SCBA and CPA, the fluctuation of the bulk modulus is much smaller than the one of the shear modulus G . However, this condition can not be satisfied due to the fact that $K_i \propto G_i$ (ν is a constant) for a linear-elastic solid. Therefore, it is the same fluctuation for G and K . This fact will have an impact on the longitudinal waves because their wave speed ($c_L = \sqrt{\frac{M}{\rho}}$) depends on M , and $M = K + \frac{4}{3}G$. But it will change nothing for the transverse waves ($c_T = \sqrt{\frac{G}{\rho}}$). As such, we could only study the acoustic attenuation for the wave propagation with the transverse polarization.

As before, the wave-packet (Eq.2.1) with $t_0 = 3\pi/\omega$ is generated by imposing a displacement on the left side of the model, and it is established in the first homogeneous square before touching the heterogeneous-elasticity medium. A series of ω is investigated from 0.15 to 1.2 THz.

(d) Correlation length ξ

In the SCBA and CPA theory, ξ is the correlation length of the coarse-graining volume over which the microscopic fluctuations of G are averaged. It means that the resulting values of G_i corresponding to the volume with center \mathbf{r}_i can be assumed to be statistically uncorrelated. In our simulation, G_i is supposed constant inside a square zone with center \mathbf{r}_i and edge length ξ . The value of ξ will certainly influence the k -dependent properties.

According to the heterogeneous-elasticity theory, Boson-peak related anomalies are ascribed to the spatially disordered shear elasticity. The boson peak frequency is given roughly by the sound velocity, divided by the correlation length of the spatial fluctuations, in our case the box size, *i.e.*, $\omega_{BP} = 2\pi \times c_T / \xi$ where c_T is given in Tab.3.9. Assuming ω_{BP} is located at 1 THz, we estimate $\xi = 19.45$ nm. Considering the model height is 60 nm, we thus choose the correlation length $\xi = 20$ nm = $L/3$ to simplify the problem.

4.3.2 Measurement of the mean-free path

We prepared nine samples with random elasticity to have results which won't depend on the actual elasticity map in one single configuration. All values of the G_i are generated according to the Gaussian distribution with a mean being $G_0 = 9.602$ GPa and a variance being 0.19 as detailed in the previous section.

The transverse wave-packet created on the left side of the sample, advances along the sample. Due to the presence of the spatial inhomogeneity, the wave-packet is scattered by the interfaces. We measure the envelope of the kinetic energy induced in the system by the propagation of the wave-packet, averaged over the y-direction. The definition of the energy envelope is given in Eq.2.9. As we have 9 samples, we average the nine envelopes obtained from the samples at each frequency. An example is demonstrated in Fig.3.29.

The averaged envelopes for transverse wave-packets propagating in a heterogeneous-elasticity medium with correlation length $\xi = 20$ and different frequencies are plotted in Fig.3.30. To be visually clear, the envelopes are vertically shifted with respect to each other. The perturbations induced by the disorder can still be seen despite we have averaged from nine configurations, which is mainly ascribed to the extremely soft local elasticity ($G_i \rightarrow 0$). In addition, we also prepared a sample with the height $L = 90$ nm for $\omega = 0.3$ THz without modifying the correlation length. It is noticed that a significant attenuation is found at $\omega = 0.3$ THz which is supposed to be due to the resonance effect as the wavelength of the transverse wave at such frequency ($\lambda = 64$ nm) is close to the height of the model $L = 60$ nm. When we enlarge the height of the model $L = 90$ nm, the strange attenuation disappears and we get the energy envelope shown in Fig.3.30. To verify the resonance effect, we let a wave-packet with $\omega = 0.2$ THz ($\lambda = 97$ nm) propagate in the large model with $L = 90$ nm, we find again a significant attenuation not present in the model with $L = 60$ nm for $\omega = 0.2$ THz.

Attenuation begins after the first homogeneous block around $x = L = 60$ nm, from which point we measure the it. Wave attenuation is quantified by means of the Beer-Lambert law, as described in Eq.2.11, from which the mean-free path is fitted. The results of the mean-free path as a function of the position x and the frequency ω is presented in Fig.3.30. Moreover, we also give the results of mean-free path derived from MD simulations [MAR 13] and the prediction of the heterogeneous-elasticity theory [SCH 15b, MAR 13]. It should be mentioned that the strange behavior of SCBA mean-free path values at low frequency is only due to the poor data extraction from literature, as these data were reported in a linear - non logarithmic - scale, contrary to the MD results. The two groups of results remain anyway consistent with each other at low frequency.

From the comparison between the results from the FE simulation and the literature, we have the following observations : Firstly, an impressive agreement is found in the low-frequency range below $\omega = 0.4$ THz. Then, a difference appears for $\omega > 0.4$ THz and the mean-free path from FEM is longer than that from the literature, meaning that the attenuation measured from the energy envelope varies only weakly with frequency. In fact, the results from MD simulations are fitted from the dynamical structure factor using the DHO model. As reported in Ref.[BEL 16], in the low-frequency range below the Ioffe-Regel frequency, the mean-free path fitted from Beer-Lambert law and that from the dynamical structure factor coincide with each other for transverse waves. However, near the Ioffe-Regel frequency the mean-free path from Beer-Lambert law remains longer than that from dynamical structure factor. In our work, the under-estimation of the attenuation above $\omega = 0.4$ THz is also supposed to be related to the transition of the transport regimes. And Beer-Lambert law should not still be valid above the Ioffe-Regel frequency.

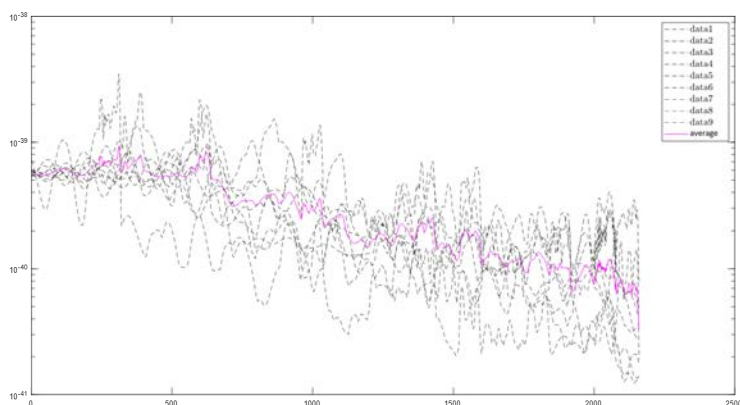


FIGURE 3.29: Demonstration of the average envelope of the kinetic energy. The black dots are the envelopes from nine different configurations with random elasticity and the red line is the average.

4.4 Discussion

Our results demonstrate the presence of a frequency-dependent acoustic attenuation due to the disordered elasticity and the attenuation length or fitted mean-free path, they agree impressively well with the simulations and the prediction of the SCBA below $\omega < 0.4$ THz. When $\omega > 0.5$ THz, the measured mean-free path is only weakly dependent on the frequency. As a consequence, we cannot reproduce the predicted attenuation behavior in the high frequency range in the present work.

One possibility for explaining why we did not observe the increasing attenuation for $\omega > 0.5$ THz is that the strong increase of G'' above $\omega = 0.5$ THz (as shown in Fig.3.27 (c)) marks the approach of the crossover from ballistic to diffusive transport regimes, indicating a gradual failure of the Beer-Lambert model for estimating the mean-free path.

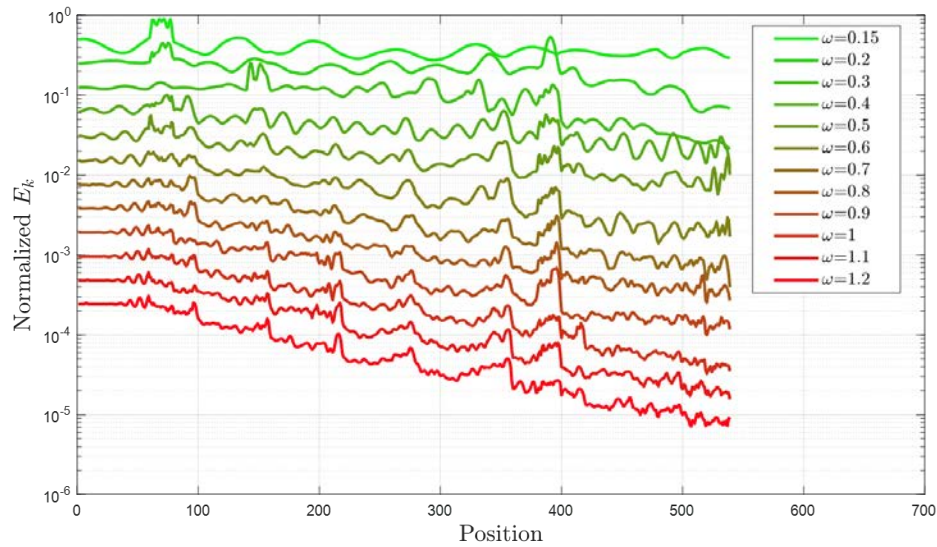


FIGURE 3.30: Average envelopes of the kinetic energy as a function a position x and frequency ω . $L = 90$ nm for $\omega = 0.3$ THz and $L = 60$ nm for other frequencies. (The envelopes are vertically shifted with respect to each other to be visually clear)

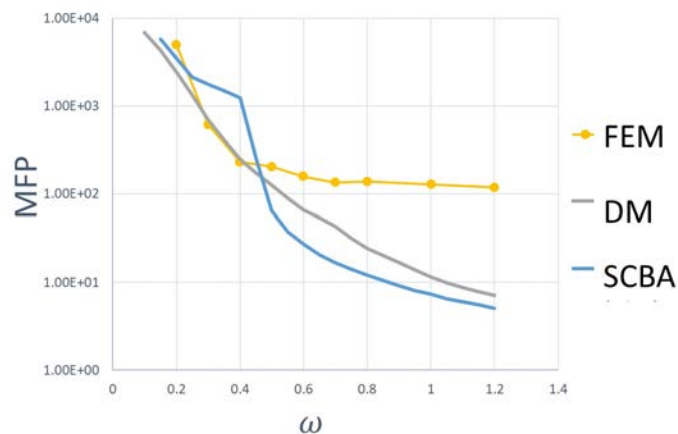


FIGURE 3.31: Comparison of the mean-free path (nm) as a function of frequency ω (THz) from our FE simulations (yellow), MD simulations (blue) and the prediction of the SCBA theory (gray). Data from Refs. [SCH 15b, MAR 13].

The same situation is reported in Ref.[[BEL 18](#)] in which the fitted values of mean-free path from the energy envelopes are longer than those fitted from the dynamic structure factors.

It is also possible that we did not compare the "correct" results, since the results from the MD simulations and theory are obtained in 3D and our FEM simulations are in 2D although the plane strain state is assumed.

In addition, the average angle of the interfaces is another factor whose impact is not clear. In the present model, the small squared boxes which are considered as correlation areas are arranged as shown in Fig.3.28, generating two privileged angles for the interfaces of random elasticity : 0° and 90° . Its impact on the results can be studied in the future work.

4.5 Conclusion

Unlike the crystalline solid, a glass features properties is intimately shaped by the intrinsic structural disorder. In this work, we built a inhomogeneous solid with random elasticity to model glassy material. By means of FEM simulation, we have investigated a series of transient process of the propagation of wave-packets in such disordered medium with a weak Gaussian distribution of the shear modulus. A frequency-dependent acoustic attenuation is found and the attenuation length is then quantified in terms of the mean-free path which is obtained by exponential fit from the energy envelopes. Agreement with the results in the literature is observed below a critical frequency ($\omega \approx 0.4$ THz), while above it the measured attenuation length varies only weakly with frequency and remains larger than the literature results. This critical frequency is lower than the estimated Ioffe-Regel frequency ($\omega_{IR} = 1$ THz) while it is at the same location as the strong increase of the attenuation and the dip of the sound velocities in the SCBA theory likely indicating the existence of another key frequency marking the approach to the diffusive regime.

The current work is mainly focused on the frequency-dependent attenuation length. More vibrational properties are expected to be studied in the future works, such as the group velocity and the vibrational density of states.

In terms of the computational time/storage cost, it is clear that the inhomogeneous model costs significantly more than a homogeneous model with the same size. Therefore, to reproduce such type of acoustic attenuation which has microscopic origin in FEM simulations, useful for modeling large samples for engineering applications, we need to develop a strategy to homogenize the microscopic properties and get a macroscopic effective constitutive law to describe the frequency-dependent acoustic attenuation. This is exactly the objective of the next Chapter.

Chapter 4

Effective constitutive laws for an amorphous material (with acoustic attenuation)

We connect atomistic and macroscopic description of acoustic attenuation in glasses. Two versions of a continuum visco-elastic mechanical model are proposed to encode their specific frequency dependent phononic attenuation.

Contents

1	Acoustic attenuation and apparent visco-elasticity	111
1.1	Introduction on acoustic attenuation in amorphous materials	111
1.2	Three regimes of acoustic attenuation vs frequency	112
1.3	Acoustic attenuation in a viscous medium	112
2	A simple Constitutive model for longitudinal and transverse attenuation in glasses	115
2.1	Description of the model	115
2.2	Calibration of the model	118
2.3	Finite element simulation	119
2.4	Results compared to MD simulation	121
3	Taking into account the different attenuation regimes (ω^2 & ω^4)	124
3.1	Description of the new model	125
3.2	Calibration of the model	126
3.3	Influence of the parameters on the Q^{-1}	127
3.4	Crossover frequencies	129
3.5	Discussion	130
4	Conclusion	132

1 Acoustic attenuation and apparent visco-elasticity

Acoustic attenuation, phonon attenuation, or sound damping, is a measure of the decay of sound propagation in media. It can be related to thermal consumption of mechanical energy in viscous medium due to an anharmonic mechanism, or it can result from acoustic scattering in disordered harmonic systems. It can be temperature-dependent, or not. Most interestingly, it is frequency-dependent. Numerous experiments and numerical works (atomistic simulations) have investigated this issue [BAL 10, RUF 03, RUF 06, MON 09a, VAC 97, MON 09b, RUO 99, MAS 04, BEN 05, MAS 06, DEV 08, DIE 79, BUC 14, MIZ 19, WAN 19, GEL 16, SCO 03, FIO 99, BEN 96]. Nevertheless, little consideration has been given so far to the use of those results on acoustic attenuation at the macroscale due to the lack of adapted continuum constitutive laws. However, this could allow macroscale dynamical simulations of acoustic properties for large structures or composites including glasses in agreement with experimental measurements.

In this chapter, we connect atomistic and macroscopic scales, keeping the information on the intrinsic attenuation in glasses and the frequency dependence of the phonon attenuation. Two versions of continuum mechanical models for a viscoelastic medium are proposed to encode this frequency-dependent property. The first version exhibits an ω^2 dependence attenuation. Using finite element method, a series of transient simulations of quasi-monochromatic wave-packets at different frequencies has been done, which shows that a well-calibrated macroscopic linear viscoelastic constitutive law can reproduce the microscopic frequency-dependent sound attenuation. Based on that, the second version is proposed which gives a more complete ω^2 - ω^4 - ω^2 dependence attenuation where the different power laws are found in different frequency ranges.

1.1 Introduction on acoustic attenuation in amorphous materials

In glasses, many attenuation channels are present, whose importance depends on phonon frequency and temperature : tunneling due to two level systems [GIL 81], soft modes [JI 19], thermally activated relaxation processes [AYR 11], anharmonicity [BUC 92], and scattering induced by structural disorder [BEL 16, GEL 16, BEL 18]. This last contribution is temperature independent, and dominates acoustic attenuation at frequencies in the GHz-THz range [DAM 17]. For lower frequencies, anharmonicity gives rise to a phonon attenuation, or damping, Γ , inversely proportional to phonon lifetime, which changes with frequency as ω^2 . Approaching the THz range, corresponding to phonon wavelengths in the nanometer scale, scattering on disorder starts to dominate, characterized by a Rayleigh-like dependence $\Gamma \propto \omega^4$, with a progressive transition to a strong scattering regime, finally leading to a new high frequency $\Gamma \propto \omega^2$ regime, as reported in a number of experimental and theoretical studies [RUF 03, RUF 06, RUF 08, LEV 06, MON 09a, BAL 10, DUV 98, AYR 11, MIZ 14]. This strong scattering takes place at frequencies comparable with the Boson Peak, i.e. the excess of modes in the phonon density of states with respect to the Debye prediction at low frequency, and has been explained as due to phonon scattering by nanometric elastic heterogenei-

ties [TAN 02, LEO 06a, TAN 10, DUV 98, MIZ 14, MAR 13, SCH 15b]. At low temperature, molecular-dynamics simulations have been able to reproduce this attenuation crossover, with some different scaling rules [MON 09b, MAR 13, BEL 16, GEL 16, WAN 19]. The addition of anharmonicity at finite temperatures has finally provided a complete picture of combination of the different attenuation channels [RUF 08, MIZ 19].

1.2 Three regimes of acoustic attenuation vs frequency

On the whole, three regimes of acoustic attenuation versus frequency can be classified : (1) $\Gamma \propto \omega^2$ due to the anharmonicity at low frequencies, with a temperature dependent strength and quadratic power law ; (2) $\Gamma \propto \omega^4$ due to Rayleigh-like scattering induced by disorder and leading to a dramatic phonon lifetime reduction, so that the collective vibrational modes loose progressively their plane wave character ; (3) $\Gamma \propto \omega^2$ above Ioffe-Regel frequency ($\omega_{IR} = \pi\Gamma$), where phonons cannot be considered as propagative plane waves anymore. As such, they do not propagate anymore but are diffusive, and, at higher frequency, even localized [ALL 99, BEL 16, BEL 18]. In Tabs. 4.1 and 4.2, we summarized the experimental and numerical results on acoustic attenuation in the literature.

1.3 Acoustic attenuation in a viscous medium

In this work we propose to develop a model to homogenize the effective attenuation triggered by multiple mechanisms, and characterized by a defined frequency dependence. To this aim, we start from the viscous attenuation of acoustic waves in compressible Newtonian fluids, as formulated within Stoke's theory [STO 80] : the amplitude of a plane wave decreases exponentially with the propagation distance, with a decay rate given, in the low frequency limit $\omega\tau \ll 1$, by $\alpha = \frac{\omega^2\tau}{2c}$, with $\tau = \frac{4\eta}{3\rho c^2}$ where η is the dynamic viscosity coefficient, ρ is the fluid density and c is the speed of sound in the absence of viscosity. This behavior leads to a typical attenuation distance $l = 1/\alpha$ scaling as $\propto \omega^{-2}$. A similar exponential attenuation of acoustic wave packets was also evidenced in amorphous materials below the Ioffe-Regel frequency [BEL 18], allowing defining a mean-free path from the corresponding Beer-Lambert law for acoustic transport attenuation. This behavior is thus similar in amorphous materials and in Newtonian liquids. Glasses could be then characterized by an effective viscoelastic behaviour for their acoustic properties, even below the glass transition temperature (that is, in the solid state). This corresponds also to the requirement that the internal friction in the material can be characterized by the quality factor $Q^{-1} = G''/G'$ where $G = G' + iG''$ is the complex elastic modulus in the linear regime [GIL 81]. This is indeed the case in a glass [DAM 17] for frequencies below the Ioffe-Regel crossover, where acoustic phonons (named propagons [ALL 99]) still maintain well-defined wave vectors and exhibit an exponential decay. A relation can be found between the microscopic quantity (phonon attenuation) and the macroscopic one (quality factor) : $\Gamma/\omega = Q^{-1}$ [POH 02, DAM 17, SCH 13, SCH 15b, PAR 66, CAR 98].

TABLE 4.1: Sound attenuation of glasses in the literature - Part I : Experimental results. (TJ : tunneling junction; BLS : Brillouin light scattering; BUVS : Brillouin ultraviolet light scattering; POT : picosecond optical technique.)

Materials	Method	T (K)	Power	Frequency range and/or v_c	LA velocity (m/s)	Ref
v-SiO ₂	TJ	1	4	0.1-0.4 THz		[DIE 79]
	IXS	16 167	2	1-6 nm ⁻¹		[RUO 99]
	IUVS	300	2	0.08-0.1nm ⁻¹		[MAS 04]
	BUVS	300	2	0.005-0.075nm ⁻¹		[BEN 05]
	IUVS	300	2-4	75-150 GHz $v_c = 100 \pm 10$ GHz	5950	[MAS 06]
	POT	300	2	near 250 GHz	5940	[DEV 08]
	IXS	1050	2	1-3 THz	5800	[BEN 96]
	IXS	1620	4-2	1- 4THz $v_c = 1.5$ THz	6500	[BAL 10]
d-SiO ₂	IXS	565	4.21	1.2-1.9 THz		[RUF 03]
Li ₂ O- 2B ₂ O ₃	BLS	300 573	1	20-40 GHz	7600	[RUF 06]
	IXS	573	4	1.2-2.4 THz		[RUF 06]
Glycerol	IXS	150.1	4-2	1-2.5 THz $v_c = 1.2$ THz	3630	[MON 09a]
BeF ₂	IXS	297	2	0.6-6 THz	5500	[SCO 03] [BUC 14]
Poly- butadiene	IXS	140	2	0.6-3.6 THz	2770	[FIO 99] [BUC 14]

4. Effective constitutive laws for an amorphous material (with acoustic attenuation)

TABLE 4.2: Sound attenuation of glasses in the literature - Part II : Numerical results (Molecular Dynamic simulation). Symbol \searrow (or \nearrow) means a power law with a positive (or negative) exponent.

Materials	T	Polarization	Power	v_c	LA velocity (m/s)	Ref
L-J glass	0.001	TA	4-2	$v_c = 1$	3.72	[MON 09b]
		LA	4-2	$v_c = 1$	8.75	
	0.001	TA	4-2	$v_c = 1$	3.65	[MIZ 19]
			1.5-4 4-2	$v_{c1} = 0.6$ $v_{c2} = 1$		
			1.5-2	$v_c = 0.9$		
			1.5-2	$v_c = 0.45$		
	0	TA	4-2	depends on T_p	≈ 2	[WAN 19]
		LA	4-2	depends on T_p		
	0.32	LA	$-k^4 \ln k$	breaks down for $k > 0.3$	8.04	[GEL 16]
		TA			3.17	
a-Si		LA	$\nearrow - \searrow - \nearrow$	$v_{IR,T} \text{ \& } v_{IR,L}$	depends on Λ	[BEL 16]
		TA	$f(\Lambda) - 2$	$v_{IR,T}$		

2 A simple Constitutive model for longitudinal and transverse attenuation in glasses

We therefore develop here a new continuum mechanical model for a viscoelastic medium, where no disorder is introduced. We will show that this model is able to bridge atomic and macroscopic scales in amorphous materials and describe phonon attenuation in a prototype material, amorphous silicon, at wavelengths where its origin is atomistic. As such our model proves to be able to give a continuum description of atomistic processes, valid for out-of-equilibrium transient transport of energy (acoustic attenuation), as well as for a general description of the effective mechanical behavior of disordered heterogeneous materials.

We will derive the mechanical response both in frequency and time domain. The frequency-dependent response allows to obtain the analytic expression for the figure of merit Q^{-1} , which is related to the phonon attenuation below the Ioffe-Regel crossover, as $Q^{-1} = \Gamma/\omega$. The time-domain one corresponds to the so-called stress-strain constitutive law, that we need for running Finite Element simulations (FEM) for investigating the wave-packets propagation at large scale.

2.1 Description of the model

Let's assume an isotropic, homogeneous and viscous solid : we can express the elastic constitutive laws describing the stress-strain relation using the Hooke's law and separating the hydrostatic from the deviatoric components as reminded in Chap.3 Sec.4.2.2

$$\sigma_{ij} = 3K\epsilon_{ij}^{sph} + 2G\epsilon_{ij}^{dev} \quad (4.1)$$

where K is the bulk modulus and G is the shear modulus. The hydrostatic (or spherical) part and the deviatoric part of strain are given by Eq.1.32. Stress respects the same separation rule, and can be written as :

$$\begin{cases} \sigma_{ij}^{sph} &= \frac{1}{3}\delta_{ij}\sigma_{kk} = 3K\epsilon_{ij}^{sph} \\ \sigma_{ij}^{dev} &= \sigma_{ij} - \frac{1}{3}\delta_{ij}\sigma_{kk} = 2G\epsilon_{ij}^{dev} \end{cases} \quad (4.2)$$

The interest of such separation is that in the following we will use different rheological models : a Kelvin-Voigt (K-V) approach for the hydrostatic part and a Maxwell-like model for the deviatoric one, as illustrated in Fig.4.1.

Here, we use the simplest version of the generalized Maxwell model called the standard linear model [ROY 01] as shown in Fig. 4.1 (right panel). The idea behind this model is that the deviatoric part will generate a viscous flow still limited by the elasticity of the solid. The time-dependent stress-strain relation following the Standard linear model reads :

$$\sigma_{ij}^{dev}(t) + \tau_a \dot{\sigma}_{ij}^{dev}(t) = E_a \epsilon_{ij}^{dev}(t) + 2E_a \tau_a \dot{\epsilon}_{ij}^{dev}(t) \quad (4.3)$$

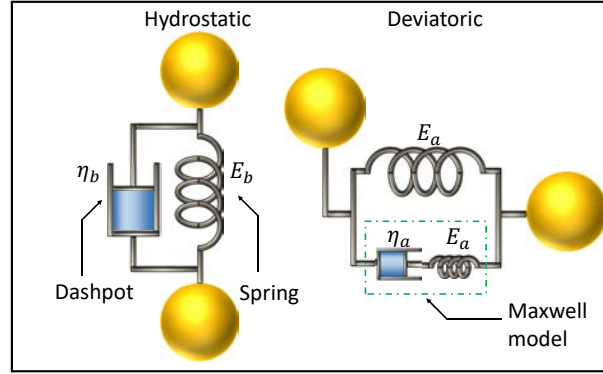


FIGURE 4.1: Illustration of the viscoelastic models : the Kelvin-Voigt model for the hydrostatic part and the standard linear model (one type of the generalized Maxwell model with $N=1$) for the deviatoric part

where $\tau_a = \eta_a/E_a$ is the relaxation time, η_a is the viscosity and E_a is the shear modulus. Supposing that nothing happens before $t = 0$, Eq.4.3 can be written on a complex plane by means of a Laplace transform :

$$(1 + \tau_a s) \mathcal{L}[\sigma_{ij}^{dev}(t)](s) = (E_a + 2E_a \tau_a s) \mathcal{L}[\epsilon_{ij}^{dev}(t)](s) \quad (4.4)$$

with $s = i\omega + \xi$ the Laplace frequency parameter (with $\xi \rightarrow 0$). We can then define the transfer function between strain and stress :

$$\frac{\mathcal{L}[\sigma_{ij}^{dev}(t)](s)}{\mathcal{L}[\epsilon_{ij}^{dev}(t)](s)} = E_a \left(1 + \frac{\tau_a s}{1 + \tau_a s}\right) \quad (4.5)$$

Replacing s , we obtain the expression of the complex elastic modulus $E_A^*(\omega) = E'_A(\omega) + iE''_A(\omega)$ for the Standard linear model :

$$\begin{aligned} E_A^*(\omega) &= \left. \frac{\mathcal{L}[\sigma_{ij}^{dev}(t)](s)}{\mathcal{L}[\epsilon_{ij}^{dev}(t)](s)} \right|_{s=i\omega+\xi} \\ &= E_a \left(1 + \frac{i\omega\tau_a}{1 + i\omega\tau_a}\right) \end{aligned} \quad (4.6)$$

For the hydrostatic part, we use the Kelvin-Voigt model (left panel in Fig.4.1). This is motivated by the fact that the hydrostatic part will mainly give rise to a delayed response, without inducing a macroscopic flow. For this reason, the rheological contribution from the hydrostatic part is often neglected [KAL 97], the deviatoric contribution being much more significant at large times. Still, a more precise description of the attenuation can be obtained if it is taken into account [FEN 13]. K-V stress-strain relation can be expressed as :

$$\sigma_{ij}^{sph}(t) = E_b(\epsilon_{ij}^{sph}(t) + \tau_b \dot{\epsilon}_{ij}^{sph}(t)) \quad (4.7)$$

where $\tau_b = \eta_b/E_b$ with E_b the bulk modulus.

Similar to the Standard linear model, the transfer function of K-V model is given by

$$\frac{\mathcal{L}[\sigma_{ij}^{sph}(t)](s)}{\mathcal{L}[\varepsilon_{ij}^{sph}(t)](s)} = E_b(1 + \tau_b s) \quad (4.8)$$

which allows us to define the complex modulus :

$$E_B^*(\omega) = E_b(1 + i\omega\tau_b) \quad (4.9)$$

It is straightforward to link such expressions to Eq. 4.2 by simply replacing the elastic moduli $3K$ and $2G$ by their viscoelastic analogues of the trace part, *i.e.*, E_B^* , and the deviatoric part, *i.e.*, E_A^* , respectively [ROY 01]. In the low-frequency limit ($\omega \rightarrow 0$), it should be :

$$\begin{cases} E_A^*(\omega \rightarrow 0) = E_a(1 + \frac{i\omega\tau_a}{1+i\omega\tau_a})|_{\omega \rightarrow 0} = 2G \\ E_B^*(\omega \rightarrow 0) = E_b(1 + i\omega\tau_b)|_{\omega \rightarrow 0} = 3K \end{cases} \quad (4.10)$$

which leads to the following identities :

$$\begin{cases} E_a = 2G = \frac{E}{1+\nu} \\ E_b = 3K = \frac{E}{1-2\nu} \end{cases} \quad (4.11)$$

where E is the Young modulus and ν is the Poisson ratio.

We can now write down the full complex constitutive elastic tensor \mathbb{G}^* , including hydrostatic and deviatoric components. This tensor links the strain tensor and stress tensor as represented in Appendix. 1. Due to the assumption of isotropy, this tensor is reduced to a 6×6 symmetric matrix, imposing the conditions $G_{11}^* = G_{22}^* = G_{33}^*$ and $G_{44}^* = G_{55}^* = G_{66}^*$, where G_{ij}^* is the i -th row and j -th column. These 6 elements can thus be expressed in terms of only four parameters (E, ν, τ_a and τ_b), as detailed in the Appendix. 1 :

$$\mathbb{G}^* = \begin{bmatrix} \frac{E_B^*+2E_A^*}{3} & \frac{E_B^*-E_A^*}{3} & \frac{E_B^*-E_A^*}{3} & 0 & 0 & 0 \\ \frac{E_B^*-E_A^*}{3} & \frac{E_B^*+2E_A^*}{3} & \frac{E_B^*-E_A^*}{3} & 0 & 0 & 0 \\ \frac{E_B^*-E_A^*}{3} & \frac{E_B^*-E_A^*}{3} & \frac{E_B^*+2E_A^*}{3} & 0 & 0 & 0 \\ 0 & 0 & 0 & \frac{1}{2}E_A^* & 0 & 0 \\ 0 & 0 & 0 & 0 & \frac{1}{2}E_A^* & 0 \\ 0 & 0 & 0 & 0 & 0 & \frac{1}{2}E_A^* \end{bmatrix} \quad (4.12)$$

with E_A^* and E_B^* given in Eq. 4.6, Eq. 4.9 and Eq. 4.11.

In order to obtain the stress-strain constitutive law we need to solve the time-domain expressions given in Eq.4.3 and Eq.4.7, reminding that the total stress is $\sigma_{ij} = \sigma_{ij}^{sph} + \sigma_{ij}^{dev}$. For the deviatoric part, solution of Eq.4.3 is :

$$\sigma_{ij}^{dev}(t) = E_a[\varepsilon_{ij}^{dev} + \int_0^t \exp(-\frac{t-t'}{\tau_a}) \frac{\partial \varepsilon_{ij}^{dev}}{\partial t'} dt'] \quad (4.13)$$

Combining Eq. 4.7, Eq. 4.13 and Eq. 4.11, the stress-strain constitutive law then reads :

$$\begin{aligned} \sigma_{ij}(t) = & \frac{E}{1-2\nu}(\epsilon_{ij}^{sph} + \tau_b \frac{\partial \epsilon_{ij}^{sph}}{\partial t}) + \\ & \frac{E}{1+\nu}[\epsilon_{ij}^{dev} + \int_0^t \exp(-\frac{t-t'}{\tau_a}) \frac{\partial \epsilon_{ij}^{dev}}{\partial t'} dt'] \end{aligned} \quad (4.14)$$

Our approach for solving the convolution integral in Eq. 4.14 is to introduce an internal variable tensor h_{ij} [KAL 97, KAL 00] whose evolution indirectly includes the mechanical history of a material. We re-formulate the Eq. 4.14 as :

$$\begin{aligned} \sigma_{ij}(t) = & \frac{E}{1-2\nu}(\epsilon_{ij}^{sph} + \tau_b \frac{\partial \epsilon_{ij}^{sph}}{\partial t}) \\ & + \frac{E}{1+\nu} \epsilon_{ij}^{dev} + h_{ij} \end{aligned} \quad (4.15)$$

where $h_{ij}(t)$ is defined by a recurrence relation :

$$\begin{aligned} h_{ij}(t) = & \exp(-\frac{t-t_n}{\tau_a}) h_{ij}(t_n) \\ & + \frac{E}{1+\nu} \int_{t_n}^t \exp(-\frac{t-t'}{\tau_a}) \frac{\partial \epsilon_{ij}^{dev}}{\partial t'} dt' \end{aligned} \quad (4.16)$$

where t_n is any moment before t . As such, instead of computing the convolution integral from 0, we only need to integrate from t_n to t if $h_{ij}(t_n)$ is known.

2.2 Calibration of the model

Eq.4.14 only depends on 4 material parameters, two of them related to elasticity (E and ν), and two to viscoelasticity (τ_a and τ_b). In order to use it for running a finite element simulation on a given material, these quantities need to be fixed to the ones of the material under investigation. To this aim, we derive from the elastic tensor the longitudinal and transverse quality factors and acoustic waves velocities, to be compared with the same quantities extracted from experiments or atomistic numerical simulations, to fix the four parameters.

By definition, isotropic longitudinal (L) and transverse (T) sound speeds are defined as

$$\begin{cases} v_L(\omega)^2 & = \frac{G'_{11}(\omega)}{\rho} \\ v_T(\omega)^2 & = \frac{G'_{44}(\omega)}{\rho} \end{cases} \quad (4.17)$$

similarly, the inverse quality factors are obtained as :

$$Q_L^{-1}(\omega) = \frac{G''_{11}(\omega)}{G'_{11}(\omega)} \text{ and } Q_T^{-1}(\omega) = \frac{G''_{44}(\omega)}{G'_{44}(\omega)} \quad (4.18)$$

where $G'_{ij} = \text{Re}(G_{ij}^*)$ and $G''_{ij} = \text{Im}(G_{ij}^*)$.

It is worth noticing that by construction this model describes $\Gamma \propto \omega^2$ energy-dependent attenuation, as can be verified by substituting G'' and G' in the $Q_{L,T}^{-1}$ expression. This behavior is in agreement with the energy dependence of acoustic attenuation in glasses as observed in experiments and numerical simulations at THz energies just above the Ioffe-Regel crossover. However, here the quality factor does not describe correctly the attenuation anymore, since the model is well adapted only below the Ioffe-Regel criterion [DAM 17]. In the low scattering regime where phonon attenuation and quality factor can be related to each other, the former should go as ω^4 . Still, this Rayleigh scattering regime is very short, and it makes the transition between two ω^2 dependencies, as described in the introduction. For this reason, as a first step for assessing the validity of our viscoelastic model, we propose to use a ω^2 dependence as a good empirical description even in this intermediate regime [BEL 16].

In the following, we will use this model for simulating wave packet propagation in amorphous silicon, and compare the results with atomistic molecular dynamics simulations [FUS 10, BEL 16, BEL 18]. In those works, amorphous silicon is described by the Stillinger-Weber potential [STI 85], where the three body parameter Λ is tuned for modifying the rigidity of the system. We compare here with the case $\Lambda = 21$, which gives a good description of real amorphous silicon, with mass density $\rho = 2303 \text{ kg/m}^3$ [FUS 10].

E and ν are the macroscopic elastic properties, that we fix to the ones reported in Ref. [FUS 10]. τ_a and τ_b are found by fitting the frequency dependent quality factor $Q^{-1} = \Gamma(\tau_a, \tau_b, \omega)/\omega$ against the one reported in Ref. [BEL 16] for longitudinal and transverse modes. Our best fits are reported in Fig. 4.2, together with the Γ/ω values from [BEL 16]. Optimal values for the relaxation times, together with the static values for the elastic parameters are reported in Table 4.3.

As anticipated, the quality of the fit is limited by the approximation that we do in using a ω^2 law for representing the Rayleigh ω^4 dependence of acoustic attenuation, as clearly demonstrated by the departure of the model from the numerical data in the deviatoric part in Fig. 4.2 (a). Moreover, in the trace part (Fig. 4.2 (b)), a marked hollow is visible in the molecular dynamics measurements, which is not reproduced by our model, being due to the attenuation of the transverse waves above the Ioffe-Regel crossover.

It is worth stressing here that by calibrating our model onto the cited molecular dynamics simulations, we will investigate exactly the same system but representing it as a continuum medium, with no need of describing the inter-atomic interactions.

2.3 Finite element simulation

Once we have defined the constitutive equation (Eq. 4.14) and we have calibrated our model on amorphous silicon, we can run finite element simulations, for investigating the

TABLE 4.3: Parameters of the viscoelastic continuum model, fixed on atomistic molecular dynamics simulations.

E	ν	$\tau_a(10^{-15}s)$	$\tau_b(10^{-15}s)$
92.25 GPa [FUS 10]	0.347 [FUS 10]	9.3(± 0.4)	3.3(± 0.1)

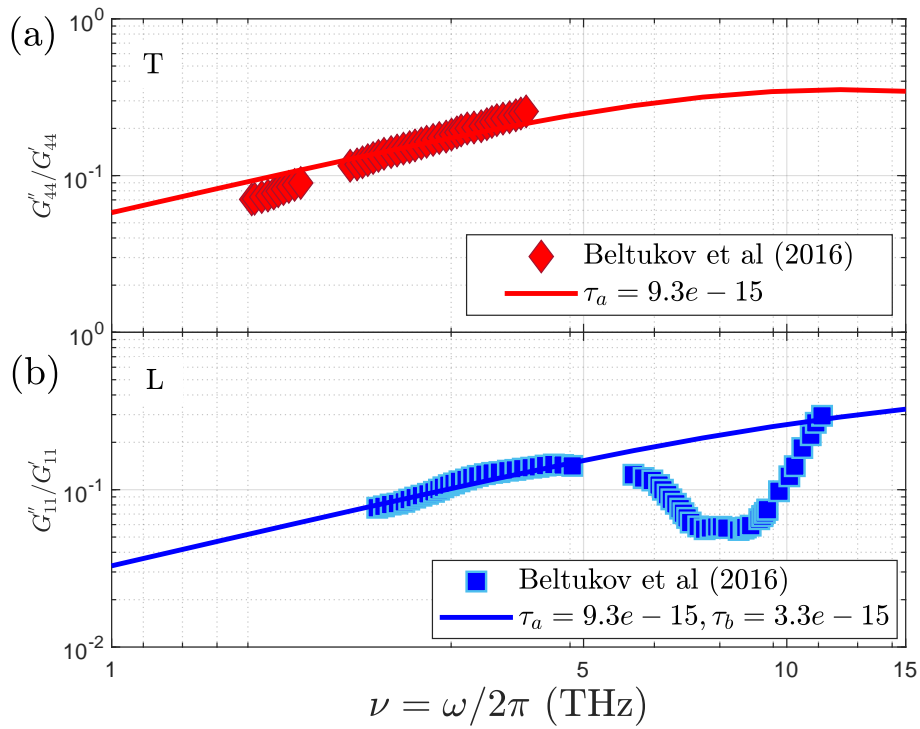


FIGURE 4.2: Identification of parameters τ_a and τ_b by fitting $Q_{L,T}^{-1}$ against Γ/ω (data from Beltukov et al, 2016) [BEL 16] : (a) Evolution of $Q_T^{-1}(\omega)$ for transverse modes with $\tau_a = 9.3e-15$. (b) Evolution of $Q_L^{-1}(\omega)$ for longitudinal modes with $\tau_a = 9.3e-15$ s and $\tau_b = 3.3e-15$ s.

propagation of wavepackets in large-scale materials, and compare their out-of-equilibrium attenuation with the one dictated by atomistic mechanisms. This method is the general approach we will follow whatever the choice of the constitutive law.

To this aim, we prepare a system made of an horizontal line of 9 squares with a side length of 60 \AA , and a total length of 540 \AA , as illustrated in Fig. 4.3. Such dimension is larger than the largest phonon mean free path at THz frequencies as reported in Ref. [BEL 18], assuring that we will be able to observe it. The size is also larger than 20 times the interatomic distance ($2\sim 4 \text{ \AA}$ reported in Ref. [VAZ 13, UKP 09]), thus the system can be considered homogeneous and isotropic, as demonstrated in Ref.

acot
rect
con:

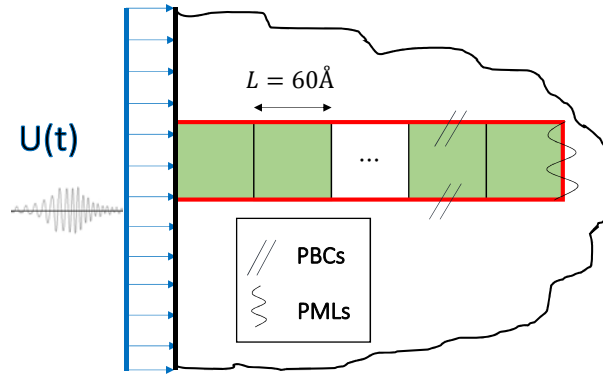


FIGURE 4.3: 2D simulation model of solid : A semi-infinite solid can be represented by only modeling a single layer (green zone) with Periodic Boundary Conditions (PBCs) on the top and bottom and Perfectly Matched Layers (PMLs) on the right edge.

In order to investigate the propagation of the vibrational energy, we excite a quasi monochromatic wave packet on the left side of the sample at position $x = 0$ in a small time interval around $t = 0$ as given by Eq.2.1 with $t_0 = \frac{3\pi}{\omega}$.

A semi-infinite solid is represented by only modeling a single layer as shown in Fig.4.3, periodic boundary conditions (PBCs) are applied at the top and the bottom by means of Lagrange multipliers $U_{\eta}^{top} = U_{\eta}^{bottom}$. On the right side of the model, the perfectly matched layers (PMLs) are implemented to avoid wave reflection [LYS 69, CLA 77, KIM 14]. Details about these two boundary conditions are presented in Ref. [LUO 19] and in Chap.2. Moreover, plane strain state achieves the infinite length in the third direction (perpendicular to the illustrated model).

2.4 Results compared to MD simulation

We have run a series of transient simulations, following the propagation of wavepackets with energies in the THz range through a model amorphous silicon sample. As

said before, the wave-packet is created by imposing a displacement on the left side of the sample. Its propagation is then followed along the sample, in the x direction, which is the initial direction of propagation of the exciting wave. In order to investigate the acoustic attenuation due to the viscoelasticity of the medium, we measure the envelope of the kinetic energy induced in the system by the propagation of the wave-packet along the x direction, and averaged over the y -direction. The energy envelope is defined as Eq.2.9 for each excitation frequency ω .

where $E_k(x, t)$ is the instantaneous kinetic energy supported by the frame located in x with width $\Delta x = 1 \text{ \AA}$. We report in Fig. 4.4 the normalized kinetic energy envelopes

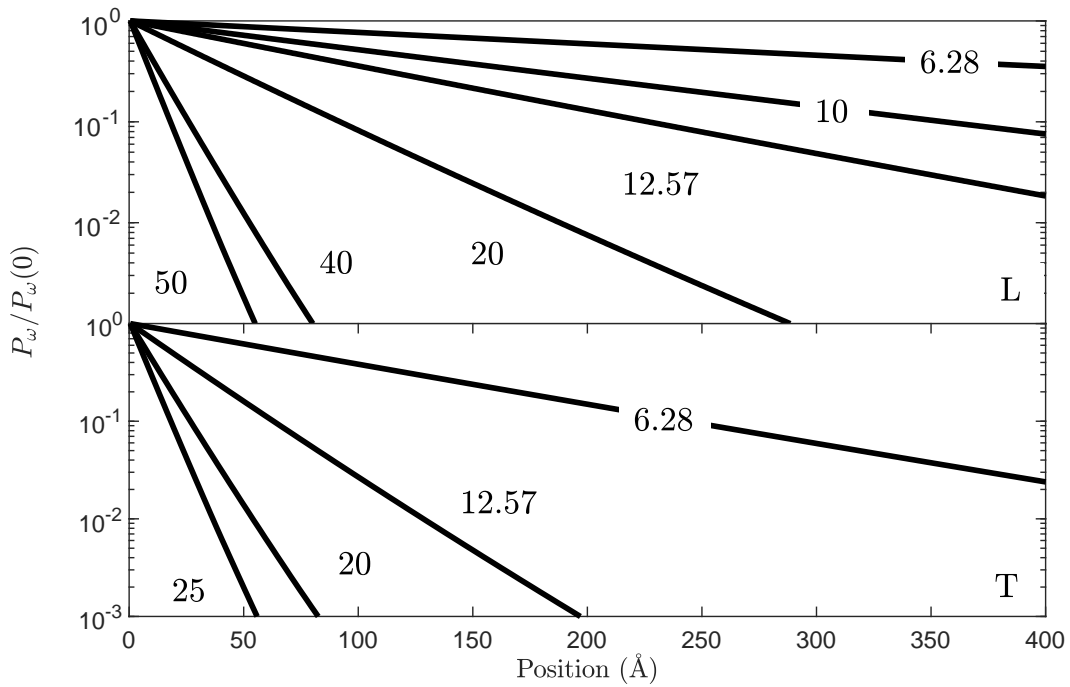


FIGURE 4.4: Envelope of the normalized kinetic energy $P_\omega(x)/P_\omega(0)$ for different frequencies in a semi-log graph. Top : longitudinal polarization ; bottom : transverse polarization. Numbers near curves represent angular frequencies ω in THz.

Far below the Ioffe-Regel limit, a global exponential attenuation similar to a Beer-Lambert law is observed [SWI 62, BEL 18], leading to a linear behavior in the semi-log representation :

$$P_\omega(x) \propto \exp(-x/\Lambda(\omega)) \quad (4.19)$$

By fitting the kinetic energy envelope with this law, one can get the value of the mean-free path Λ_{FE} (FE standing for FE simulations), which is expected to be inversely proportional to the acoustic attenuation via the wave-packet velocity thus to follow the prediction

of Q^{-1} of the viscoelastic model. Our results for the mean free path of propagating longitudinal and transverse wave-packets in amorphous silicon are compared with results from molecular dynamics simulations. [BEL 18] in Fig 4.5. Here we compare with two different estimations from the atomistic calculations : Λ_{DSF} is obtained from the Dynamical Structure Factor as detailed in Ref. [BEL 16], while Λ_{BL} has been calculated from the Beer-Lambert fit of the attenuation of propagating wave-packets as in our case. It is reported that the results of Λ_{DSF} and Λ_{BL} begin to deviate near the Ioffe-Regel frequency, which indicates a crossover from weak scattering to strong scattering. As a consequence, Beer-Lambert law gradually fails when approaching the Ioffe-Regel limit. In our case, this model do not take into account the Ioffe-Regel limit, and no source of scattering exists in this continuum law. As such, deviation above Ioffe-Regel frequency is only a consequence of a saturation in frequency, but not representative of atomistic scale scattering. The agreement between the mean free path from continuum Finite Element Simulations with the ones obtained in atomistic molecular dynamics simulations is quite satisfying, in the low frequency regime, and holds as far as we remain below the Ioffe-Regel crossover, our constitutive equation having been derived in such regime, as said before. The deviation at the highest frequencies investigated is indeed due to the approaching of the diffusive regime.

We also observe that our FE mean-free paths are closer to Λ_{DSF} rather than Λ_{BL} despite both Λ_{FE} and Λ_{BL} are fitted by the Beer-Lambert law. This is due to the fact that our model has been calibrated against the attenuation obtained from the dynamical structure factor, thus related to Λ_{DSF} . That is to say, proper calibration of the parameters for the input attenuation data will result in accurate reproduction of this attenuation when following the transient wave packet propagation.

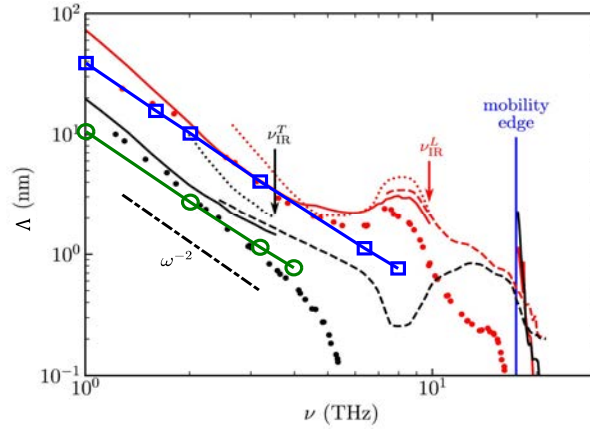


FIGURE 4.5: Result obtained from finite element (FE) simulation compared to atomistic analysis for longitudinal waves (blue or red) and transverse waves (green or black). For FE simulation, solid lines with open symbols (blue or green) show the mean free path Λ_{FE} obtained by the exponential fit of the envelope. For DM simulation (Y. Beltukov [BEL 18]), points show the results from the DHO fit of the DSF, Λ_{DSF} ; Solid lines show the mean free path Λ_{BL} ; Dashed lines show the penetration length l_{pen} . (The Ioffe-Regel frequencies for longitudinal and transverse waves are shown by red and black arrow respectively.)

3 Taking into account the different attenuation regimes (ω^2 & ω^4)

In the previous work, we have developed a law for describing acoustic attenuation in an amorphous material at THz frequencies, in a limited range below the Ioffe-Regel criterium. We have assumed a constant viscosity, thus leading to a ω^2 behaviour in the acoustic attenuation. However, at such energies, the dominant scattering source is the structural disorder at the atomic scale [MIZ 14, DAM 17] thus leading to a ω^4 behaviour, as found in [RUF 06, MON 09a, BAL 10, AYR 11, MIZ 14, MIZ 19]. The corresponding low scattering is potentially responsible for the unusual temperature dependence $\kappa \propto T$ observed in the low temperature regime [TLI 19], while this low temperature sensitivity was also related to anharmonic effects in the 2-level model [GIL 81, BUC 92]. The progressive transition to a stronger scattering and to the resulting diffusive motion of initially plane waves will be responsible for the progressive saturation which may be observed as a plateau in the glassy thermal conductivity at around 10 K followed by an increase of κ with the temperature, and is responsible for the peak in the specific heat at the same temperature [ZEL 71, POH 01, TLI 19]. Modeling amorphous materials for thermal applications clearly needs including different frequency dependences, with at least three successive regimes including $\Gamma \propto \omega^\alpha$ with $\alpha \approx 2$ to take account of possible anharmonic effects in the low frequency range (low temperatures [MIZ 19]), $\Gamma \propto \omega^4$ in the low scattering regime and then $\Gamma \propto \omega^2$ again at very high frequencies in the strong scattering (diffusive) regime.

In order to extend the model to larger frequency ranges, we thus need to describe two successive $\omega^2 - \omega^4$ crossovers. This is the purpose of a second version of viscoelastic model, which will allow to reproduce at a macroscopic level, through a single continuum model, the combined effect of parallel sources of acoustic attenuation and their crossovers. As shown in Fig. 4.6, two Maxwell-like models are in parallel, with μ_1 and μ_2 the rigidity and $\eta_1\omega^{-4}$ and $\eta_2\omega^{-2}$ the frequency-dependent viscosity, respectively. The physical idea behind this model is the asynchronous activation of the ω^4 and the ω^2 dependence, resulting from two processes contributing additionally to the global stress in the system.

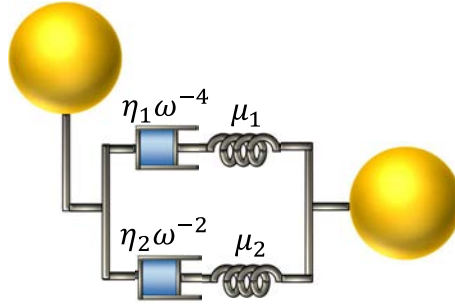


FIGURE 4.6: Illustration of the viscoelastic model : two Maxwell-like models are in parallel.

3.1 Description of the new model

Similar to what we did in the first version, we will derive the complex elastic modulus in order to obtain the analytic expression of the quality factor $Q^{-1} = G''/G'$. Holding the relation $Q^{-1} = \Gamma/\omega$, ideally, we expect to get a $\omega^3 - \omega^1 - \omega^3$ behavior from Q^{-1} . At the same time, the amplitude of Γ/ω and the crossover position should be clearly reproduced.

For simplicity, we directly give out the frequency-dependent elastic modulus $G^*(\omega) = G'(\omega) + iG''(\omega)$ for the new model illustrated in Fig. 4.6 :

$$\begin{aligned}
 G^*(\omega) &= \frac{\mu_1\eta_1\omega^{-4}s}{\eta_1\omega^{-4}s + \mu_1} + \frac{\mu_2\eta_2\omega^{-2}s}{\eta_2\omega^{-2}s + \mu_2} \\
 &= \frac{\mu_1\eta_1\omega^{-4}i\omega}{\eta_1\omega^{-4}i\omega + \mu_1} + \frac{\mu_2\eta_2\omega^{-2}i\omega}{\eta_2\omega^{-2}i\omega + \mu_2} \\
 &= \frac{\mu_1\eta_1\omega^{-3}i}{\eta_1\omega^{-3}i + \mu_1} + \frac{\mu_2\eta_2\omega^{-1}i}{\eta_2\omega^{-1}i + \mu_2}
 \end{aligned} \tag{4.20}$$

from which G' and G'' can be extracted :

$$\begin{aligned}
 G'(\omega) &= \frac{\mu_1\eta_1^2}{\mu_1^2\omega^6 + \eta_1^2} + \frac{\mu_2\eta_2^2}{\mu_2^2\omega^2 + \eta_2^2} \\
 &= \mu_1\left(\frac{\tau_1^2}{\omega^6 + \tau_1^2} + \alpha\frac{\tau_2^2}{\omega^2 + \tau_2^2}\right)
 \end{aligned} \tag{4.21}$$

$$\begin{aligned}
 G''(\omega) &= \frac{\mu_1^2 \eta_1 \omega^3}{\mu_1^2 \omega^6 + \eta_1^2} + \frac{\mu_2^2 \eta_2 \omega}{\mu_2^2 \omega^2 + \eta_2^2} \\
 &= \mu_1 \left(\frac{\tau_1 \omega^3}{\omega^6 + \tau_1^2} + \alpha \frac{\tau_2 \omega}{\omega^2 + \tau_2^2} \right)
 \end{aligned} \tag{4.22}$$

where $\tau_1 = \frac{\eta_1}{\mu_1}$, $\tau_2 = \frac{\eta_2}{\mu_2}$ and $\alpha = \frac{\mu_2}{\mu_1}$. As such, there are only three parameters left to characterize the attenuation. Finally, the quality factor $Q^{-1} = G''/G'$ is given by :

$$\begin{aligned}
 Q^{-1}(\omega) &= \frac{\frac{\tau_1 \omega^3}{\omega^6 + \tau_1^2} + \alpha \frac{\tau_2 \omega}{\omega^2 + \tau_2^2}}{\frac{\tau_1^2}{\omega^6 + \tau_1^2} + \alpha \frac{\tau_2^2}{\omega^2 + \tau_2^2}} \\
 &= \frac{\alpha \tau_2 \omega^7 + \tau_1 \omega^5 + \tau_1 \tau_2^2 \omega^3 + \alpha \tau_1^2 \tau_2 \omega}{\alpha \tau_2^2 \omega^6 + \tau_1^2 \omega^2 + (1 + \alpha) \tau_1^2 \tau_2^2}
 \end{aligned} \tag{4.23}$$

3.2 Calibration of the model

In the following, we will calibrate the new model against silica glasses. The attenuation Γ is extract from the experimental results in the literature as shown in Fig. 4.7.

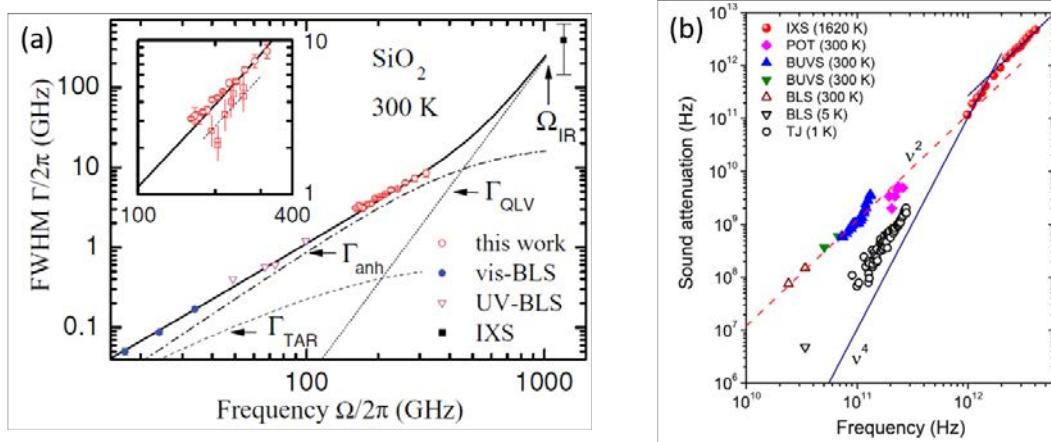


FIGURE 4.7: (a) Extracted from Ref. [AYR 11] : acoustic linewidth $\Gamma/2\pi$ of the sample in Ref. [AYR 11] (named "this work" in the figure) at 300K compared to visible BLS result (Ref. [MAS 97]) and UV-BLS ones (Refs. [MAS 04] and [BEN 05]). The point above the Ioffe-Regel frequency is from Ref. [MAS 97]. (b) Extracted from [BAL 10] : sound attenuation, $\Gamma/2\pi$, of v-SiO₂ as a function of frequency in log-log scale. The points at high frequency (red circles) are from the work in Ref. [BAL 10] at T=1620K. Lower frequencies data are from : picosecond optical technique (POT)[DEV 08], BUVS[MAS 06, BEN 05], BLS [VAC 80], and a tunneling junction (TJ) technique [DIE 79].

Fig. 4.7(a) is extracted from Ref. [AYR 11]. In this figure, sound attenuation is measured at 300K in the subterahertz range (from 0.01 to 0.3 THz) with different experimental

methods : picosecond optical techniques (POT), Brillouin light scattering (BLS) and UV-BLS (ultraviolet Brillouin scattering). Fig. 4.7 (b) is extracted from Ref. [BAL 10]. In this figure, sound attenuation is measured at 1620K at terahertz frequencies (> 1 THz), with inelastic x-ray scattering (IXS). From these two figures, we can now easily get a global image of acoustic attenuation from GHz to THz frequencies range at different temperatures. The three regimes mentioned before can be clearly found in the figures. At high frequency, a ω^4 - ω^2 crossover appears around $\nu = 1.5$ THz as shown in Fig. 4.7 (b). In addition, in the subterahertz range, there should be another ω^2 - ω^4 crossover which is not explicitly given by the experimental data but shown as the intersection of the auxiliary lines (ω^2 and ω^4).

Next, we will calibrate our model on silica glasses, starting from those literature data. By adjusting the parameters of the model (τ_1 , τ_2 and α), we give our best fit in Fig. 4.8 and values are summarized in Tab. 4.4. Experimental attenuation data are also reported and analytic $Q(\omega)$ is indicated by the red line. In the next sections, we will detail how this fit was obtained.

TABLE 4.4: Parameters of the new viscoelastic continuum model. Calibration on silica glass [AYR 11, BAL 10].

$\tau_1(s^{-3})$	$\tau_2(s^{-1})$	α
3e39	2.7e13	1.4

3.3 Influence of the parameters on the Q^{-1}

A good fit should give a Q^{-1} reproducing not only the amplitude of the acoustic attenuation, but also at least the crossover from ω^4 to ω^2 around 1.5 THz. It is not easy to reach these two conditions through a simple minimization algorithm, because most of the time it only meets the amplitude condition but the crossover condition is ignored. To meet the two conditions simultaneously, let's start with a know-how to illustrate the evolution of the amplitude and the crossover frequencies versus the three parameters τ_1 , τ_2 and α . This approach is necessary as the first step of the parameters identification before finding an alternative optimization algorithm in future work.

The roles of the three parameters are displayed one by one Fig. 4.9. By default, we set $\tau_1 = 1e30 s^{-3}$, $\tau_2 = 1e10 s^{-1}$ and $\alpha = 1$. The chosen order of magnitude for different parameters can be estimated based on the crossover positions presented in Appendix. D.

Let's first consider τ_2 , as shown in the top panel of Fig. 4.9. We can find that the global amplitude of the Q^{-1} decreases with τ_2 . Therefore, in the first step, we change τ_2 in order to get the same order of magnitude for Q^{-1} obtained in the numerical model, and the experimental values of Γ/ω . During this process, one peak appears at $\omega = 1e10 \text{ rad} \cdot s^{-1}$ whose position and amplitude are determined by two other parameters. This peak corresponds to a transition between two different dominant frequency powers in the constitutive model. This transition depends on the relation among three parameters of the model. In

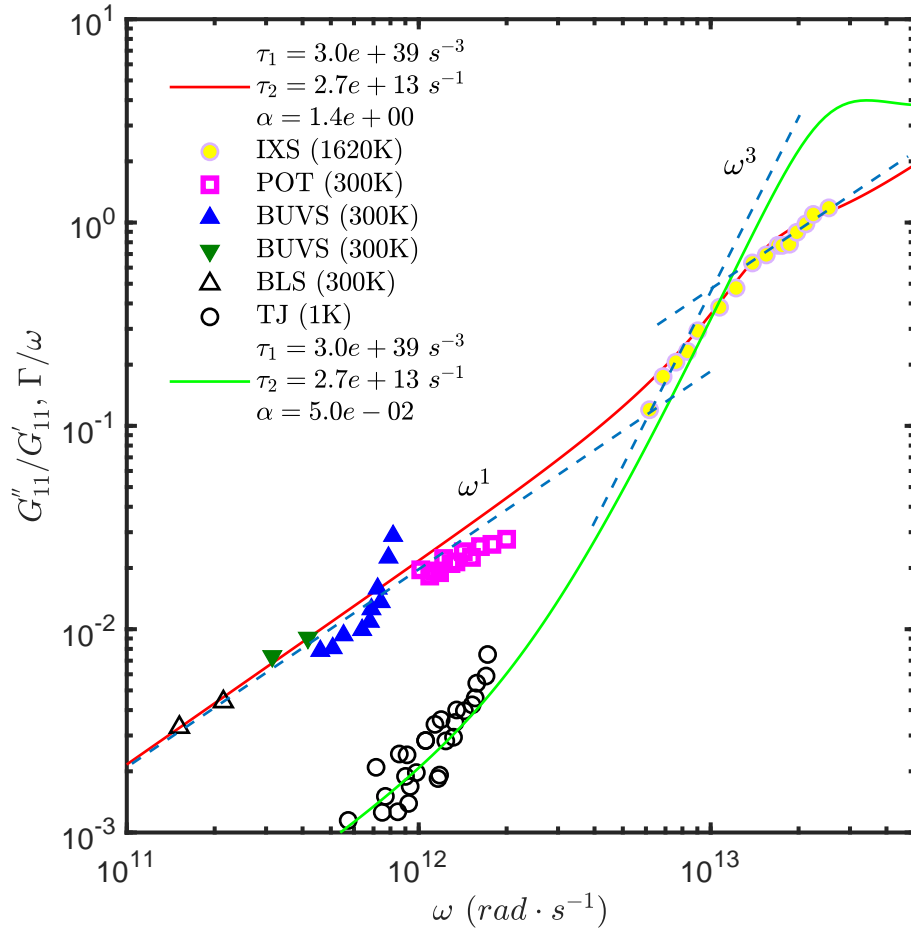


FIGURE 4.8: Comparison between Γ/ω and Q^{-1} with $\tau_1 = 3e39s^{-3}$, $\tau_2 = 2.7e13s^{-1}$ and $\alpha = 1.4$ (red line) or $\alpha = 0.05$ (green line). The red (green) line is the Q^{-1} of the present viscoelastic model. Experimental data are from : IXS [BAL 10], POT [AYR 11], BUVS [MAS 06, BEN 05], BLS [VAC 80] and TJ [DIE 79]. The blue dashed lines are two power law fits representing $\Gamma/\omega \propto \omega$ and $\Gamma/\omega \propto \omega^3$, respectively.

the current configuration, (that is for $\tau_1 = 1e30 s^{-3}$ and $\alpha = 1$, it shows a $\omega^3 - \omega^{-3}$ cross-over.

Let's now consider the variations of τ_1 , given the last value of τ_2 considered previously. The influence of τ_1 is shown in the middle panel of Fig. 4.9. Increasing τ_1 pushes to the right the above $\omega^3 - \omega^{-3}$ peak horizontally. When this peak moves to the right, it becomes small and the ω^{-3} part disappears first due to the collapse with the increasing ω background. In this step, only the peak moves and the amplitude of left or right wing is unchanged.

Finally, let's consider the role played by the ratio $\alpha = \mu_1/\mu_2$, which characterizes the rigidity difference between the two parallel processes of dissipation contributing additionally to the stress state. As shown in the bottom panel of Fig. 4.9, changing α will raise or lower the left wing and modify the power law near the crossover between left and

TABLE 4.5: Estimation of the relaxation time for $\tau_1 = 3e39 \text{ s}^{-3}$ and $\tau_2 = 2.7e13 \text{ s}^{-1}$.

ω (Hz)	$\tau_1 \omega^{-4}$ (s)	$\tau_2 \omega^{-2}$ (s)
1e11	3e-5	2.7e-9
1e12	3e-9	2.7e-11
1e13	3e-13	2.7e-13
3e13	3.7e-15	3e-14

right wing. When $\alpha \ll 1$, the left wing will drop significantly. However, when $\alpha \gg 1$, the crossover $\omega^3 - \omega^{-3}$ will progressively disappear and the whole line, especially the part $\propto \omega^3$, tends to a single ω power law. Between them, the ω^3 tends to ω . Therefore, an appropriate α should raise the left wing to fit the experiments data, while keeping the ω^3 apparent power law as much as possible.

In addition, the relaxation times $\tau_1 \omega^{-4}$ and $\tau_2 \omega^{-2}$ should make sense physically, which requires them being longer than $1e - 14 \sim 1e - 15 \text{ s}$. Using the orders of magnitude of τ_1 and τ_2 , we estimate the corresponding relaxation time in Tab.4.5. Relaxation times shorten as the frequency increases, indicating that upper limit of the frequency ω can reach 3e13 Hz.

The $\omega - \omega^3 - \omega$ behaviour observed experimentally for Γ/ω thus corresponds to one possibility offered by our model, as a function of the relative values of the three parameters of our model. We will now discuss the related values of the cross-over frequencies.

3.4 Crossover frequencies

In Appendix.D, we discuss in more details the conditions giving rise to a $\omega - \omega^3 - \omega$ behavior. If these conditions are strictly met, then the crossover frequencies can be expressed in terms of α , τ_1 and τ_2 . We recall the two crossover frequencies evidenced in Appendix.D :

- Position of the crossover $\omega - \omega^3$:

$$\omega_{1-3} = \frac{1}{\alpha + 1} \tau_2$$

- Position of the crossover $\omega^3 - \omega$:

$$\omega_{3-1} = \left(\frac{1}{\alpha}\right)^{1/2} \left(\frac{1}{\alpha + 1}\right)^{1/2} \tau_2$$

Note that in the present model, the ratio $\omega_{1-3}/\omega_{3-1}$ depends only on α . It is limited by :

$$\frac{\omega_{3-1}}{\omega_{1-3}} = \sqrt{\frac{\alpha + 1}{\alpha}}, \text{ with } \alpha > 0.76 \quad (4.24)$$

This gives an upper limit of the ratio $\omega_{1-3}/\omega_{3-1}$ less than 1.52. In practice, these conditions may not be strictly met. However, the results about the crossover frequencies are still very useful because they determine the magnitude of the parameters. For example, knowing that $\omega_{3-1} \approx 2\pi * 1.5 \approx 9.4e12 \text{ rad} \cdot \text{s}^{-1}$ and α is normally supposed as 1 at first, then we have $\tau_2 = \omega_{3-1}/\sqrt{0.5} \approx 1.3e13 \text{ s}^{-1}$ and $\tau_1 = \frac{\tau_2^3}{4} \approx 5e38 \text{ s}^{-3}$.

3.5 Discussion

Provided the parameters τ_1 , τ_2 and α in Tab.4.4, the interesting case with three principal frequency dependencies ω - ω^3 - ω is only a special case offered by the visco-elastic model. As discussed in the Appendix.D, the expression Q^{-1} (Eq.4.23) of the new model has 4 different powers in the numerator (ω^{-1} , ω^{-3} , ω^{-5} and ω^{-7}) and 3 terms in the denominator (ω^{-2} , ω^{-6} and ω^{-8}), which could reproduce more power laws than three.

For this special case, we can write down the asymptotic approximation for the three frequency dependencies : (1) Low frequency : $Q_{(1)}^{-1} \sim \frac{\alpha}{1+\alpha} \frac{1}{\tau_2} \omega$; (2) Intermediate frequency : $Q_{(2)}^{-1} \sim \frac{1}{1+\alpha} \frac{1}{\tau_1} \omega^3$; (3) High frequency : $Q_{(3)}^{-1} \sim \frac{1}{\tau_2} \omega$. It is noticed that the process with viscosity $\eta_2 \omega^{-2}$ dominates the low and high frequency regimes, while the $\eta_1 \omega^{-4}$ process activates mainly in the intermediate frequencies corresponding to the Rayleigh-like damping below the Ioffe-Regel frequency. Especially, it can be seen that, when $\alpha \gg 1$, $Q_{(1)}^{-1}$ tends to $\frac{1}{\tau_2} \omega$, thus $Q_{(3)}^{-1}$, and the intermediate regime disappears $Q_{(2)}^{-1} \sim 0$ as illustrated in Fig.4.9. In contrast, when $\alpha \ll 1$, low-frequency ω process gives a smaller value of the quality factor compared to the high-frequency ones. This α -dependent ω process is impressively adapted to describe the temperature-dependent acoustic attenuation $\Gamma/\omega \propto \omega$ in the low frequencies due to anharmonicity, thermal activation, two level system, which is also shown in the MD simulation[MIZ 19]. As such, small α corresponds to low temperature and large α corresponds to a relatively high temperature.

Finally, as shown in the Tab.4.5, the frequency-dependent relaxation times given by the fitted values of three parameters are reasonable up to $\omega = 30 \text{ THz}$ which covers all spectrum range of experimental data. Therefore, we can conclude that the values of this model are all physically meaningful.

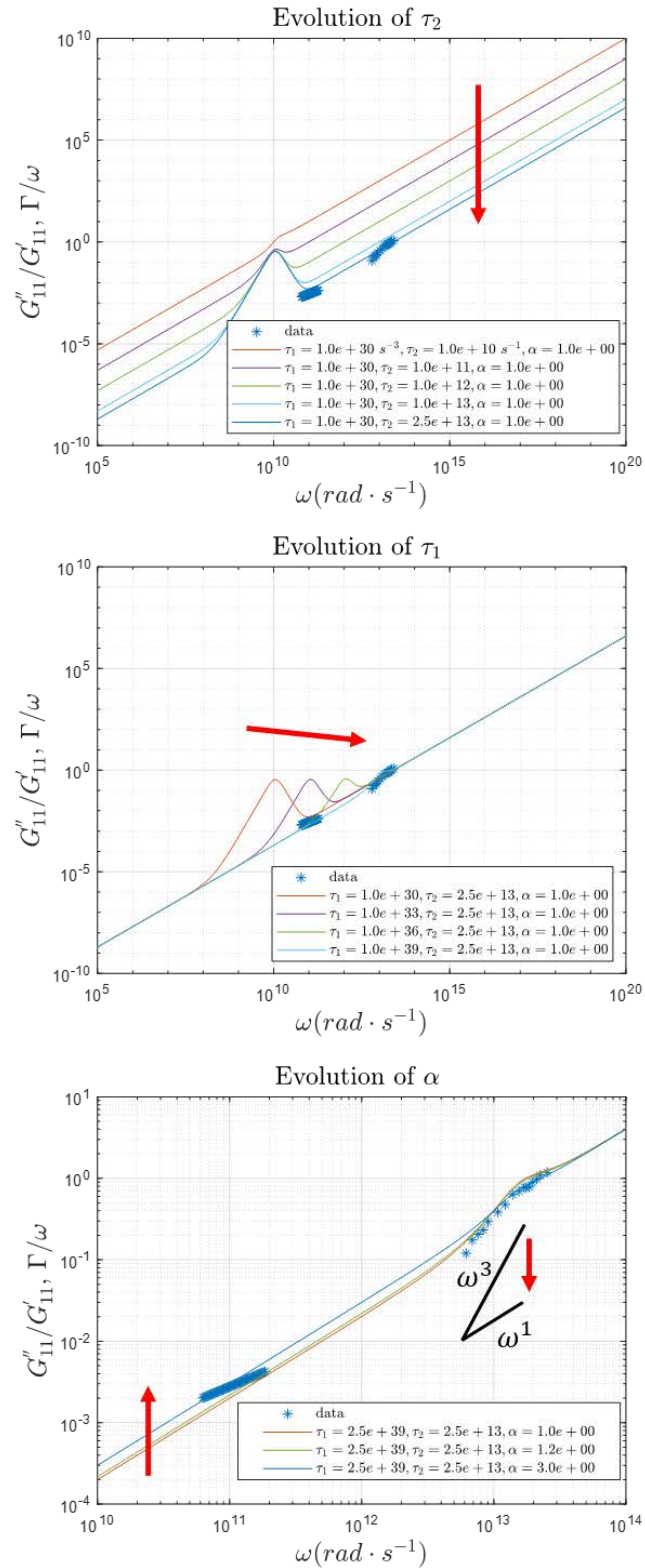


FIGURE 4.9: Evolution of Q^{-1} as a function of τ_2 , τ_1 and α , respectively. The red arrow indicates the growth direction of the parameter.

4 Conclusion

In this chapter, we proposed two versions of a continuum visco-elastic model, able to bridge the atomic and macroscopic scales in amorphous materials and describe phonon attenuation due to atomistic mechanisms, with specific frequency dependencies.

For the first simple model, our finite element results demonstrate that the effective sound attenuation in a continuum model may strictly follow the atomistic quality factor Q^{-1} for a well-calibrated macroscopic linear viscoelastic constitutive law. We are here interested to phonons with energies in the THz range and wavelengths in the nm range, which dominate thermal transport at room temperature. The limitation of this model consists in the assumption of a quasi-constant speed of sound (Eq. 4.17), while this is expected to be modified due to the atomic discretization and structural disorder. This part can be improved in the future. In addition, by choice, this model imposes a $\Gamma \propto \omega^2$ behavior that does not hold at all frequencies.

This is the reason why we proposed the second version of viscoelastic model which involves two parallel sources of dissipation with a frequency dependent viscosity able to reproduce these successive regimes $\omega^2 - \omega^4 - \omega^2$. In practice, we investigated a calibration of the model on a-SiO₂ which gives a quality factor Q^{-1} that fits well the experimental attenuation data Γ/ω [BAL 10, RUF 03, RUO 99, MAS 04, BEN 05, MAS 06, DEV 08, DIE 79, BEN 96]. Interestingly, the frequency dependence of the viscosities involves two mechanisms : one is related to an attenuation time $\tau_1 \propto 1/\eta_1 \propto \omega^4$ (maybe related to low acoustic scattering at the atomic scale as discussed before [GEL 16]), while the other involves a relaxation time $\tau_2 \propto 1/\eta \propto \omega^2$ (maybe related to anharmonicity or to strong acoustic scattering at small scale, as already discussed in the introduction). The combination of these two well-known processes could be responsible for the two experimentally observed crossovers. The comparison of our model with experimental data leads to the determination of the 3 parameters involved in the model, that is : $\tau_1 = 3e39 \text{ s}^{-3}$, $\tau_2 = 2.7e13 \text{ s}^{-1}$ and $\alpha = 1.4$. These numerical values are reasonable for $\omega < 1e14 \text{ rad} \cdot \text{s}^{-1}$ that is the largest frequency that can be reached at the atomic scale.

To conclude, our work has the merit to be a proof of concept : by developing the appropriate viscoelastic law, and calibrating it against atomistic quantities thanks to experimental data, we are able to reproduce the correct acoustic attenuation. As such, our work is of evident interest in view of the current technological interests and needs for large scale simulations in a number of different applications ranging from acoustics, to mechanical and to thermal management, where complex nanostructured heterogeneous materials have arisen as the most promising. Such metamaterials are made of the ordered or disordered intertwining of different materials with different properties, with a heterogeneity lengthscale (the nano/micro structure lengthscale) which can range from macroscopic to nanometric depending on the applications. Such large scale systems can be realistically modeled only through Finite Element Simulations, to catch the effect of the interfaces and elastic heterogeneities on acoustic properties and thermal transport. Our model proposes a way to identify a continuum constitutive law able to reproduce faithfully the full dynamical response of our system, including the apparent frequency dependent dissipative

processes resulting from atomic scale acoustic scattering processes. This represents a first decisive step for investigating the effect of a complex nano or micro structure on acoustic attenuation, while including the atomistic contribution as well. From this first step, further work can focus on the ability to reproduce other power laws for phonon attenuation, as well as introducing anisotropy, and the effect of temperature, finally allowing to describe thermal transport as well as sound propagation in metamaterials of arbitrary complexity.

General conclusions and prospects

Conclusions

In this thesis, using the FEM based numerical simulation, we studied the thermo-mechanical properties in the heterogeneous solids, mainly focusing on two parts : (1) the propagation and attenuation of the wave packets in the heterogeneous elastic media with different types of interfaces showing an energy conversion from mechanical to thermal ; (2) the acoustic attenuation in the homogeneous viscous media where the microscopic frequency-dependent phonon attenuation in glasses can be described by effective viscoelastic models.

For the first part, we have seen in detail the effect of mechanical (rigidity contrast) and geometrical (volume fraction, shape, disorder) parameters on the properties of vibrational energy transfer in a nanocomposite material. Our numerous finite element calculations have revealed that the dependence of the attenuation length as well as the diffusivity on the different parameters is far from simple, and exhibits the following non monotonous behaviors : (1) with respect to the rigidity contrast. Softer inclusions clearly appear as more efficient for energy attenuation, but the rigid inclusions are also able to decrease strongly the attenuation length at specific frequencies in the case of periodic circular inclusion ; (2) with respect to the volume fraction. The results from the circular inclusion suggest the existence of optimal inclusions radius and interface area, sufficiently large to allow for an efficient scattering but sufficiently small to prevent any energy percolation between the inclusions ; (3) with respect to the shape. The dendritic inclusion shows appealing performance to prevent wave propagation compared to the simple circular shape when looking at the high frequency attenuation length and the diffusivity due to the high interface density which can enhance the interface scattering. (4) with respect to the disorder. From the results of the ordered/disordered porous materials, it can be seen that the ordered structures promote the transition of transport behavior from propagative to diffusive, thanks to the multiple reflections, the local resonances and the localization of mechanical energy, phenomena which are disrupted when disorder is introduced.

For the second part, we have developed two continuum mechanical models based on viscoelastic descriptions of amorphous materials, where the frequency dependence of the microscopic phonon attenuation can be reliably reproduced once the model has been properly calibrated on atomistic data. To do so, we have derived the analytic expression of the speed of sound and the quality factor Q^{-1} , which can be calibrated against sound

velocity and attenuation as experimentally reported or calculated in atomistic numerical simulations. We have proved the validity of our approach by investigating the acoustic attenuation in amorphous silicon/silica at THz frequencies, *i.e.*, at the frequency of the phonons which are the most responsible for thermal transport at room temperature.

We have also explored the continuum simulation of nanostructured materials in different ways : (1) different heterogeneous nanostructures have been set up. They can be as simple as periodic circular elastic inclusions or holes, or as complex as the dendrite and random spatial arrangements ; (2) viscoelastic model can be used to describe the intrinsic acoustic attenuation in the amorphous component. (3) Eshelby's inclusion, that can be used as the elementary brick of plasticity for amorphous materials, are shown to scatter acoustic waves, thus opening the way to new structural health monitoring of glasses. As such, our work has laid a solid foundation for understanding amorphous-based acoustic/thermal transport in heterogeneous architected materials, most promising for energy management applications.

Prospects

For the determination of the phonon contribution to the thermal conductivity, it is now needed to take into account the atomic scale dispersive contribution to the vibrational density of states, together with atomic scale scattering processes controlling the diffusivities above the Ioffe-Regel frequency. In addition, we also aim at finding a stable and efficient method to obtain the vibrational density of states of the nanostructure. Indeed, as for now, Castem fails due to the calculation singularity problem in calculating the eigenfrequencies.

For the role of Eshelby's inclusion on scattering of sound waves, the equations derived by F. Lund et al. link the eigenstrain and the spatial and temporal derivatives of the displacement field at the interface with the inclusion. Future work will thus deal with the investigation of the scattering of sound waves with Eshelby inclusion to verify this analytic description.

For the random elasticity, despite the agreement at low frequency compared to the coherent approximation method found in the literature, much needs to be understood. Specifically, the investigation of wavepacket propagation in a very large wavelength range, going from coherent to incoherent waves, will allow to get a microscopic understanding of the coherent concept in the case of atomic vibrational waves, marking the difference with the optic treatment.

For the viscoelastic constitutive law, further work can focus on the ability to reproduce other power laws for phonon attenuation and successive cross-over frequencies, as well as introducing mechanical anisotropy, and the effect of temperature, finally allowing to describe thermal transport as well as sound propagation in metamaterials of arbitrary complexity.

Appendix A

Supplementary materials for the Chap.2

1 Contribution of phonons to thermal conductivity

In the propagative regime, the thermal conductivity results from the product of the attenuation length characteristic of scattering processes (Fig. 2.13) with the heat capacity C_v and the group velocity v_g , integrated over all frequencies as in the following formula [KIT 04] :

$$\kappa_T^{prop}(T) = \frac{1}{3} \int_0^{\omega_{IR}} d\omega g(\omega) C_v(\omega, T) v_g(\omega) l_p(\omega)$$

while in the diffusive regime [LAR 14], it is given by the diffusivity (Fig. 2.9) as

$$\kappa_T^{diff}(T) = \int_{\omega_{IR}}^{\omega_{max}} d\omega g(\omega) C_v(\omega, T) D(\omega)$$

2 1 alignment vs 10 alignments : verification of the periodic boundary condition

Since we applied periodic boundary conditions on the top and bottom of the model as shown in Fig.2.2, we only modeled one single line of inclusions to represent an infinite number of parallel lines in the vertical direction. This idea can be easily verified through modeling a much larger system and comparing the results. In Figs.A.1, A.2 and A.3, we show the snapshots of displacement field for three sets of simulation with different parameters. For each set, one can easily find that the displacement fields are equivalent between one line of inclusions and ten lines of inclusions thus confirm the successful implementation of the PBCs.

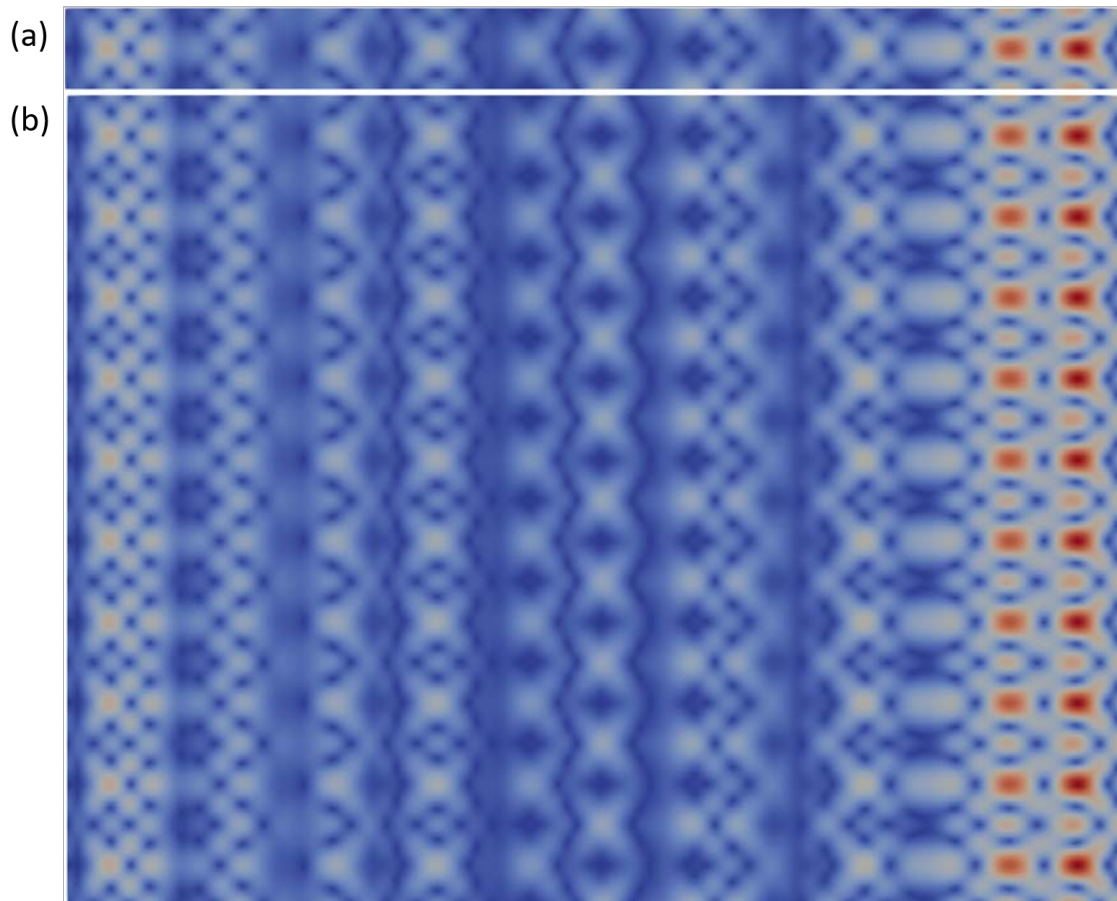


FIGURE A.1: Snapshots of displacement field at the same time with $\omega = 5$ THz, $\frac{E_i}{E_m} = 1.2$ and $R = 25$ Å (a) 1 alignment with PBCs on the top and bottom (b) 10 parallel alignments of inclusions on the top and bottom

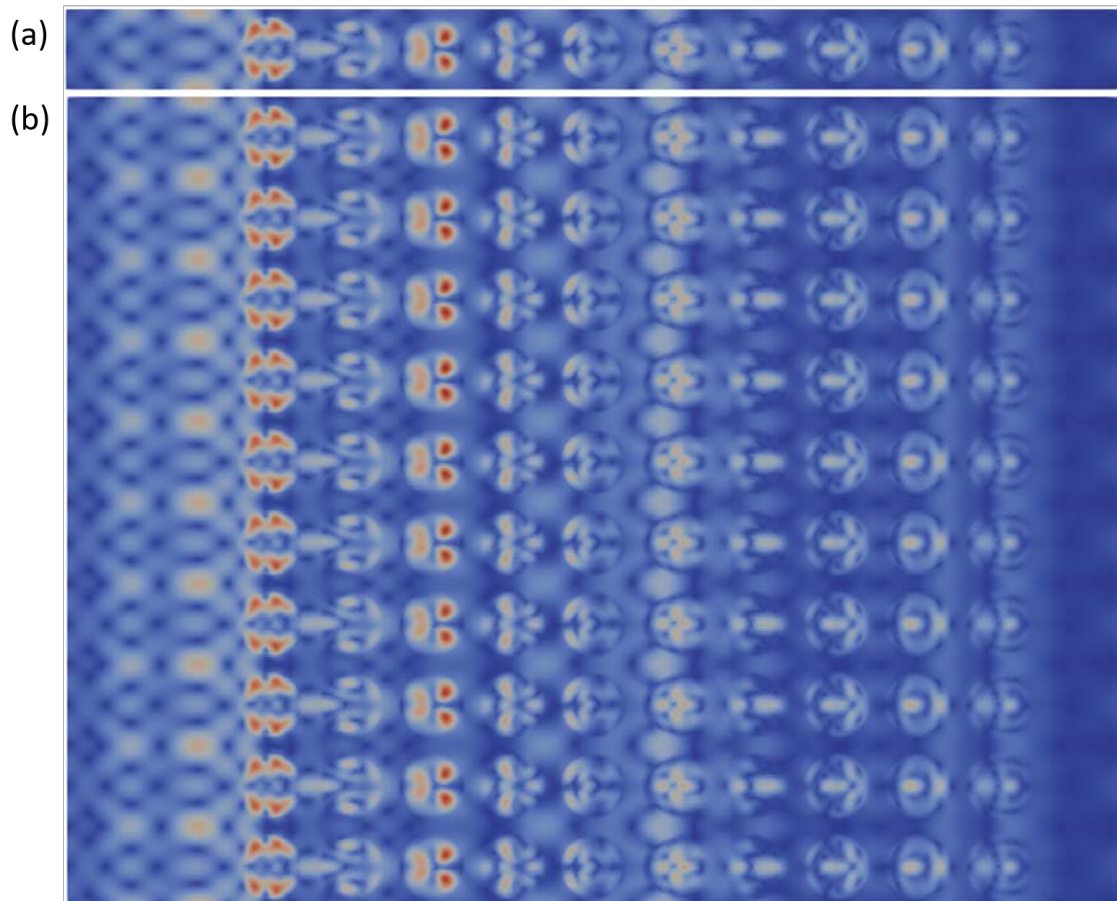


FIGURE A.2: Snapshots of displacement field at the same time with $\omega = 5$ THz, $\frac{E_i}{E_m} = 0.2$ and $R = 25 \text{ \AA}$ (a) 1 alignment on the top and bottom (b) 10 parallel alignments of inclusions on the top and bottom

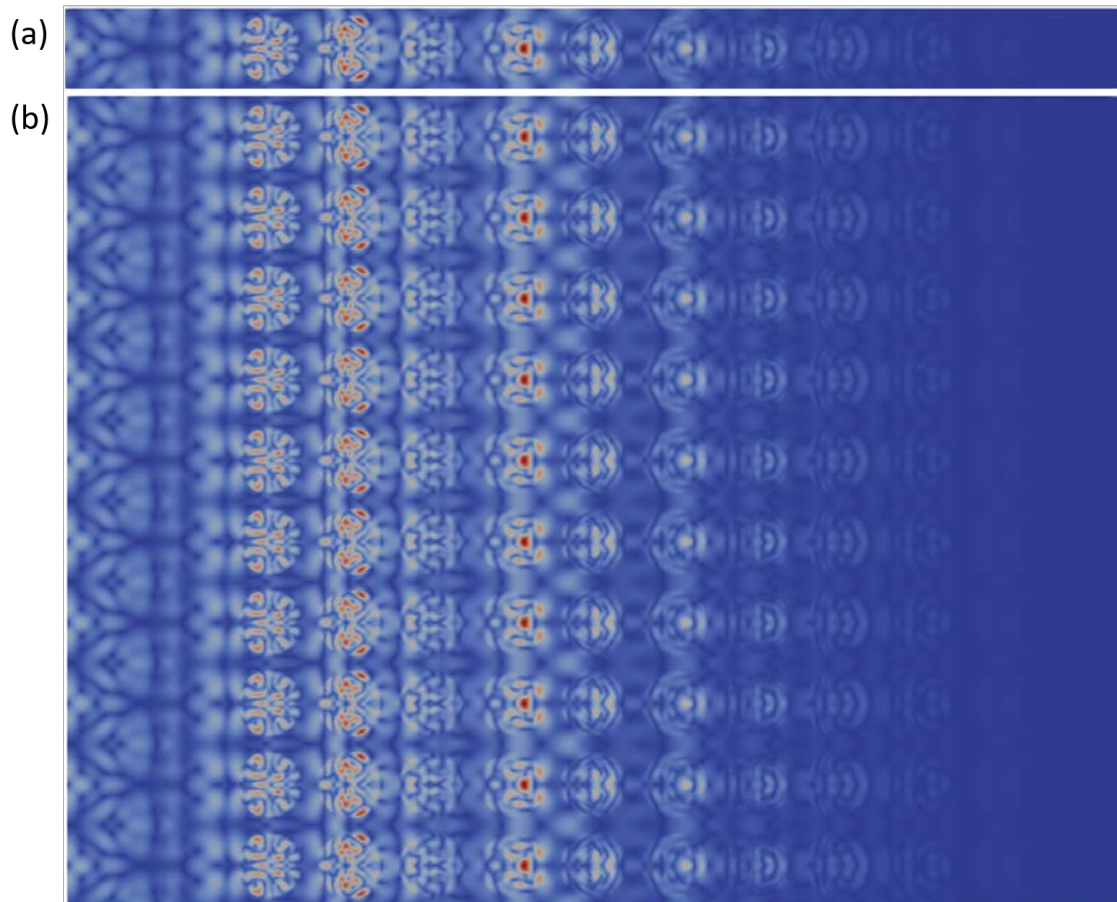


FIGURE A.3: Snapshots of displacement field at the same time with $\omega = 9$ THz, $\frac{E_i}{E_m} = 0.2$ and $R = 25$ Å (a) 1 alignment on the top and bottom (b) 10 parallel alignments of inclusions on the top and bottom

Appendix B

Data of disorder holes

• Random radius

For the case of random size. We prepared different values of disorder parameter σ : $\sigma = 0$ (ordered periodic holes) or $\sigma > 0$ (disordered holes). We used **Gaussian** distribution and σ is the standard deviation with $\sigma = 0, 10.3$ and 40 . For each σ , three configuration are prepared for each σ to increase the number of samples. Average of three configurations results will be the final result. Defining the amplifier α , thus the diameter of each hole is $\alpha\Phi_0$. The values of the amplifiers α for $\sigma = 10.3$ and 40 are listed in Tabs.B.1 and B.2.

• Random center position

For the case of random center position. We keep the same radius for all the holes but translate the holes along x and y direction with distance D_x and D_y . The maximum of translation distance D_{max} is defined as 12 nm and 45 nm. We suppose **uniform** distribution for the translation distance D_x and D_y . Defining a translation amplifier d_x (or d_y) with $D_x = d_x D_{max}$ (or $D_y = d_y D_{max}$) and $d_x, d_y \in [-1, 1]$ are both uniformly distributed. The values of the amplifiers d_x and d_y are listed in Tab.B.3.

TABLE B.1: Distribution of the amplifier for $\sigma = 10$ with 3 configurations.

	Amplifier								
1	1.2075	0.8989	1.2273	1.0543	0.9953	1.0535	0.9846	0.9907	1.1116
	0.8463	1.0262	0.96	0.9464	1.023	1.0293	0.9749	0.9772	0.9228
	0.9734	0.9775	0.8499	1.1012	0.9058	1.0338	1.0414	1.0017	1.0711
2	0.9383	1.0017	1.0722	0.9831	0.9351	0.9902	1.0778	1.0038	1.023
	0.8818	0.9803	1.0389	0.9558	0.9867	1.0137	0.9162	1.0618	1.0101
	1.038	0.8688	0.9984	0.9779	1.0592	0.9643	1.0944	1.1143	1.0385
3	1.0211	0.9786	0.9973	0.9364	0.9002	1.0645	1.0494	1.0349	1.0195
	1.0025	0.9377	0.9402	0.916	0.8254	0.8979	0.9949	0.9842	0.9294
	0.9	0.9266	1.0763	1.1892	0.8914	1.034	0.9853	1.0468	0.9878

TABLE B.2: Distribution of the amplifier for $\sigma = 40$ with 3 configurations.

		Amplifier								
1		0.8639	0.5725	1.7052	0.8375	1.0784	1.3415	0.8565	1.1531	1.2363
		0.9636	1.0559	1.279	0.9094	1.1437	1.0369	0.9474	0.9242	1.1587
		1.4302	0.7607	0.9081	0.8341	0.5685	0.8089	1.0133	1.1745	0.694
2		0.7495	0.9725	1.1246	0.7016	0.7031	0.569	0.9814	1.1727	1.1156
		1.2282	1.0978	0.6986	0.7356	0.8699	1.0452	1.1778	0.364	0.7812
		1.0897	0.7368	1.5462	0.9389	1.0319	1.2381	1.0318	0.6139	1.441
3		0.9319	0.9161	1.2736	0.5057	1.3283	0.9148	1.5277	0.5807	0.9905
		0.6925	1.1018	1.229	1.1767	0.9156	0.8426	1.0907	1.1169	1.4759
		0.9173	0.4659	0.7452	0.9657	1.3669	0.9102	1.5249	1.4276	0.8763

TABLE B.3: Distribution of the amplifier for d_x and d_y with 3 configurations.

		Amplifier								
1	d_x	-0.123	-0.109	0.310	0.171	0.782	0.681	-0.607	0.171	-0.239
		0.531	0.419	-0.762	0.503	0.094	0.629	0.232	0.834	-0.848
		-0.626	-0.448	0.920	0.0120	-0.701	0.859	-0.297	0.514	0.062
	d_y	-0.237	0.293	-0.675	-0.552	0.919	-0.491	-0.498	0.099	0.136
		0.590	0.509	-0.003	-0.490	-0.723	-0.513	-0.053	-0.428	-0.892
		-0.021	0.359	-0.319	0.398	-0.485	-0.300	0.662	0.508	0.558
2	d_x	0.378	-0.695	-0.787	-0.831	-0.636	0.100	-0.196	-0.166	-0.325
		-0.100	0.077	-0.991	-0.480	-0.709	0.706	-0.520	0.805	-0.262
		-0.542	-0.844	0.635	-0.137	0.739	-0.298	-0.632	-0.018	0.561
	d_y	0.496	0.652	0.924	-0.200	-0.472	-0.710	-0.848	-0.900	0.800
		-0.832	0.992	0.550	0.600	-0.728	0.244	-0.753	0.890	-0.778
		0.827	-0.115	0.737	0.821	0.159	0.027	-0.520	-0.022	-0.221
3	d_x	-0.517	0.150	-0.914	0.094	-0.263	-0.026	0.635	-0.299	-0.585
		-0.807	-0.530	0.298	0.489	0.561	-0.106	0.289	0.752	-0.058
		0.884	0.642	0.296	0.374	0.859	0.017	0.623	0.245	0.689
	d_y	-0.192	-0.880	-0.662	-0.407	0.251	-0.128	0.590	0.878	-0.398
		-0.736	-0.291	0.463	-0.622	-0.838	-0.387	-0.243	0.100	-0.539
		0.912	-0.969	-0.098	-0.633	0.551	0.022	0.066	0.174	-0.611

Appendix C

Complex constitutive tensor & implementation of the viscoelastic constitutive law in FE code

1 3D complex constitutive tensor

The stress-strain constitutive law describes the relation between those two quantities. Tensor can be expressed in matrix form, strain and stress are $n \times 1$ vectors, constitutive tensor is $n \times n$ matrix, where $n = d^2$, and d is dimension of space. In 3-D case, there should have been 9 terms but thanks to the symmetry of shear strain $\varepsilon_{ij} = \varepsilon_{ji}$ and shear stress $\sigma_{ij} = \sigma_{ji}$. In Voigt notation, strain and stress vector are reduced to 6 terms and read respectively :

$$\varepsilon_{ij} = \begin{bmatrix} \varepsilon_{11} \\ \varepsilon_{22} \\ \varepsilon_{33} \\ 2\varepsilon_{12} \\ 2\varepsilon_{13} \\ 2\varepsilon_{23} \end{bmatrix} \text{ and } \sigma_{ij} = \begin{bmatrix} \sigma_{11} \\ \sigma_{22} \\ \sigma_{33} \\ \sigma_{12} \\ \sigma_{13} \\ \sigma_{23} \end{bmatrix}$$

It is conventional to express the shear strain as $2\varepsilon_{ij} = \gamma_{ij}$ which is called engineering shear strain.

The symmetric constitutive tensor \mathbb{G} ($G_{ij} = G_{ji}$) can be developed as :

$$\mathbb{G} = \begin{bmatrix} G_{11} & G_{12} & G_{13} & G_{14} & G_{15} & G_{16} \\ G_{21} & G_{22} & G_{23} & G_{24} & G_{25} & G_{26} \\ G_{31} & G_{32} & G_{33} & G_{34} & G_{35} & G_{36} \\ G_{41} & G_{42} & G_{43} & G_{44} & G_{45} & G_{46} \\ G_{51} & G_{52} & G_{53} & G_{54} & G_{55} & G_{56} \\ G_{61} & G_{62} & G_{63} & G_{64} & G_{65} & G_{66} \end{bmatrix} \quad (\text{C.1})$$

We recall that the complex constitutive law of our model (which has a form similar to Hooke's law) reads : $\sigma_{ij} = E_B^* \epsilon_{ij}^{sph} + E_A^* \epsilon_{ij}^{dev}$ from which we can find each term of tensor \mathbb{G} , where $\epsilon_{ij}^{sph} = \frac{1}{3} \delta_{ij} (\epsilon_{11} + \epsilon_{22} + \epsilon_{33})$ and $\epsilon_{ij}^{dev} = \epsilon_{ij} - \epsilon_{ij}^{sph}$.

For example, for σ_{11} :

$$\sigma_{11} = E_B^* \frac{\epsilon_{11} + \epsilon_{22} + \epsilon_{33}}{3} + E_A^* (\epsilon_{11} - \frac{\epsilon_{11} + \epsilon_{22} + \epsilon_{33}}{3}) \quad (C.2)$$

$$= \frac{E_B^* + 2E_A^*}{3} \epsilon_{11} + \frac{E_B^* - E_A^*}{3} \epsilon_{22} + \frac{E_B^* - E_A^*}{3} \epsilon_{33} \quad (C.3)$$

It is easy to find that $G_{11} = \frac{E_B^* + 2E_A^*}{3}$, $G_{12} = \frac{E_B^* - E_A^*}{3}$, $G_{13} = \frac{E_B^* - E_A^*}{3}$ and $G_{14} = G_{15} = G_{16} = 0$

Similarly, for σ_{12} :

$$\sigma_{12} = E_A^* \epsilon_{12} \quad (C.4)$$

$$= \frac{E_A^*}{2} \times (2\epsilon_{12}) \quad (C.5)$$

So except $G_{44} = \frac{E_A^*}{2}$, other terms equal to 0.

Therefore, one can get the expression for all terms of the tensor \mathbb{G} as given by Eq. 4.12. In addition, notice that G_{ij} is all complex number, so we use \mathbb{G}^* to represent the complex constitutive tensor.

2 Finite Elements Simulations details

In this work, we developed an explicit dynamic algorithm based on the finite element code Cast3m from CEA [VER 89, SCH 18, LUO 19]. To simplify the subscripts, we use bold symbols to represent vectors, *i.g.* $\boldsymbol{\sigma} = \sigma_{ij}$. The finite element semi-discrete in space of a transient dynamic motion equation can be described as :

$$\boldsymbol{f}^{int}(t) + \mathbb{M}\ddot{\boldsymbol{u}}(t) = \boldsymbol{f}^{ext}(t) \quad (C.6)$$

where \boldsymbol{f}^{int} is internal force vector, \mathbb{M} is mass matrix, \boldsymbol{u} is displacement vector and \boldsymbol{f}^{ext} is exciting force vector. Among them, \boldsymbol{f}^{int} can be obtained from

$$\boldsymbol{f}^{int}(t) = \int_{\Omega} \mathbb{B}^T \boldsymbol{\sigma}(\boldsymbol{\epsilon}, \dot{\boldsymbol{\epsilon}}, \boldsymbol{h}) d\Omega \quad (C.7)$$

with

$$\boldsymbol{\epsilon}(t) = \mathbb{B}\boldsymbol{u}(t) \quad (C.8)$$

where \mathbb{B} is the strain-displacement matrix derived from the shape function of the element used and Ω is the model domain. The calculation of $\boldsymbol{\sigma}(\boldsymbol{\epsilon}, \dot{\boldsymbol{\epsilon}}, \boldsymbol{h})$ obeys the viscoelastic constitutive law described as Eq.4.14. In practice, the convolution operation in Eq. 4.14 is replaced by a recurrence formula based on the internal variable \boldsymbol{h} which has a "memory

effect” [KAL 97, KAL 00, REE 98, LIN 03, ROU 17], yielding Eq. 4.15. One linearization method dedicated for the generalized Maxwell viscosity derived by Kaliske *et al.* [KAL 97, KAL 00] has been implemented in this FEM code.

In the next step, we need to discretize the motion equation (Eq. C.6) in time. We assume a uniform partition in time and choose a time step size Δt . Combined with the central-difference time integrator, the space-time discretized form can be obtained :

$$\mathbb{M}\ddot{\mathbf{u}}_{n+1} = \mathbf{f}_{n+1}^{ext} - \int_{\Omega} \mathbb{B}^T \boldsymbol{\sigma}_{n+1}(\boldsymbol{\epsilon}_{n+1}, \dot{\boldsymbol{\epsilon}}_{n+\frac{1}{2}}, \mathbf{h}_{n+1}) d\Omega \quad (\text{C.9})$$

where indices n and $n + 1$ are successive time steps. And the derivative of strain at time $n + \frac{1}{2}$ is :

$$\dot{\boldsymbol{\epsilon}}_{n+\frac{1}{2}} = \frac{1}{\Delta t}(\boldsymbol{\epsilon}_{n+1} - \boldsymbol{\epsilon}_n) \quad (\text{C.10})$$

Reference to Eq.4.15, the temporally discretized constitutive law $\boldsymbol{\sigma}_{n+1}(\boldsymbol{\epsilon}_{n+1}, \dot{\boldsymbol{\epsilon}}_{n+\frac{1}{2}}, \mathbf{h}_{n+1})$ can be expressed as a recursive equation :

$$\boldsymbol{\sigma}_{n+1} = \frac{E}{1-2\nu}(\boldsymbol{\epsilon}_{n+1}^{sph} + \dot{\boldsymbol{\epsilon}}_{n+\frac{1}{2}}^{sph}) + \frac{E}{1+\nu}\boldsymbol{\epsilon}_{n+1}^{dev} + \mathbf{h}_{n+1} \quad (\text{C.11})$$

where \mathbf{h}_{n+1} is the updated internal variable tensor [KAL 97] :

$$\mathbf{h}_{n+1} = \exp\left(-\frac{\Delta t}{\tau_a}\right)\mathbf{h}_n + \frac{E}{1+\nu}\tau_a[1 - \exp\left(-\frac{\Delta t}{\tau_a}\right)]\dot{\boldsymbol{\epsilon}}_{n+\frac{1}{2}}^{dev} \quad (\text{C.12})$$

To resume, the RHS of Eq. C.11 shows that the updated stress consists of three part : (1) $\boldsymbol{\epsilon}$ gives the purely elastic stress (2) $\dot{\boldsymbol{\epsilon}}$ gives the viscous stress at the current time step (3) \mathbf{h} records the time-dependent relaxation process. For more details about the implemented central-difference time integrator algorithm see Ref. [LUO 19].

Appendix D

Existence of $\omega - \omega^3 - \omega$ behavior

In this section, we will prove the existence of the objective power law ($\omega - \omega^3 - \omega$) given by the quality factor Q^{-1} of the proposed viscoelastic model in the Chap. 4 Sec. 3.

As given by the Eq. 4.23, the quality factor $Q^{-1} = G''/G'$ is :

$$Q(\omega)^{-1} = \frac{\alpha\tau_2\omega^{-1} + \tau_1\omega^{-3} + \tau_1\tau_2^2\omega^{-5} + \alpha\tau_1^2\tau_2\omega^{-7}}{\alpha\tau_2^2\omega^{-2} + \tau_1^2\omega^{-6} + (1 + \alpha)\tau_1^2\tau_2^2\omega^{-8}} \quad (\text{D.1})$$

where $\tau_1 = \frac{\eta_1}{\mu_1}$, $\tau_2 = \frac{\eta_2}{\mu_2}$ and $\alpha = \frac{\mu_2}{\mu_1}$.

There are 4 different powers in the numerator (ω^{-1} , ω^{-3} , ω^{-5} and ω^{-7}) and 3 terms in the denominator (ω^{-2} , ω^{-6} and ω^{-8}). So, a total of $A_7^7 = 5040$ permutation provides sufficient possibilities to seek the power law that we want. However, such large numbers of possibilities cannot be listed out all together in this appendix. As a results, a goal-oriented investigation is done to check the existence of the $\omega - \omega^3 - \omega$ behavior. To this aim, we will first deal with the numerator and denominator separately to determine the how the parameters affect the permutation of the powers. Then, we will look for the candidate permutation of the powers by considering the $\omega - \omega^3 - \omega$ condition, and those permutation that cannot meet the condition will be rejected, thus reducing the total workload. Finally, we will combine the candidates of numerator and of denominator to confirm the existence of the wanted power laws as well as to determine the crossover positions as a function of the parameters.

1 $\alpha < 1$

1.1 Numerator

There are 4 terms in the numerator, a pairwise comparison gives $C_4^2 = 6$ cases listed below :

- ① $\tau_1\omega^{-3} > \tau_1\tau_2^2\omega^{-5} \rightarrow \omega > \tau_2$
- ② $\alpha\tau_2\omega^{-1} > \tau_1\omega^{-3} \rightarrow \omega > \sqrt{\frac{1}{\alpha}}\sqrt{\frac{\tau_1}{\tau_2}}$

- ③ $\tau_1 \omega^{-3} > \alpha \tau_1^2 \tau_2 \omega^{-7} \rightarrow \omega > \alpha^{1/4} (\tau_1 \tau_2)^{1/4}$
- ④ $\alpha \tau_2 \omega^{-1} > \tau_1 \tau_2^2 \omega^{-5} \rightarrow \omega > \frac{1}{\alpha}^{1/4} (\tau_1 \tau_2)^{1/4}$
- ⑤ $\tau_1 \tau_2^2 \omega^{-5} > \alpha \tau_1^2 \tau_2 \omega^{-7} \rightarrow \omega > \sqrt{\alpha} \sqrt{\frac{\tau_1}{\tau_2}}$
- ⑥ $\alpha \tau_2 \omega^{-1} > \alpha \tau_1^2 \tau_2 \omega^{-7} \rightarrow \omega > \tau_1^{1/3}$

Cases ①-⑥ indicate, in fact, the permutation of the four terms which depends on the position of the six crossovers. As such, 6 conditions give 6 separators which are the expression on the right side of " $\omega >$ ". Each separator judges the dominant power between the pairwise terms as frequency sweeps. For example, case ① means that $\tau_1 \omega^{-3} < \tau_1 \tau_2^2 \omega^{-5}$ if $\omega < \alpha^{1/4} (\tau_1 \tau_2)^{1/4}$ and $\tau_1 \omega^{-3} > \tau_1 \tau_2^2 \omega^{-5}$ if $\omega > \alpha^{1/4} (\tau_1 \tau_2)^{1/4}$. In the following, we use ① to represent the corresponding separator instead of the inequality. For example, ① directly means τ_2 .

It is noticed that the permutation of $\sqrt{\frac{1}{\alpha}} \sqrt{\frac{\tau_1}{\tau_2}}$ and $\sqrt{\alpha} \sqrt{\frac{\tau_1}{\tau_2}}$ in ② and ⑤ or $\alpha^{1/4} (\tau_1 \tau_2)^{1/4}$ and $\frac{1}{\alpha}^{1/4} (\tau_1 \tau_2)^{1/4}$ in ③ and ④ only depends on α . In this section, we discuss the case of $\alpha < 1$, and the case of $\alpha > 1$ will be discussed in the next section.

In the following, we will judge the permutation of the separators ① -⑥ as a function of τ_1 and τ_2 . In order to simplify the formula, we note $A = \tau_2$, $B = \sqrt{\frac{\tau_1}{\tau_2}}$, $C = (\tau_1 \tau_2)^{1/4}$ and $D = \tau_1^{1/3}$.

Because $\alpha < 1$, thus $\alpha^n < \frac{1}{\alpha}^n$, ② $>$ ⑤ and ④ $>$ ③.

- ① $<$ ② : $A < \sqrt{\frac{1}{\alpha}} B \rightarrow \tau_2^3 < \frac{1}{\alpha} \tau_1$
- ① $<$ ③ : $A < \alpha^{1/4} C \rightarrow \tau_2^3 < \alpha \tau_1$
- ① $<$ ④ : $A < \frac{1}{\alpha}^{1/4} C \rightarrow \tau_2^3 < \frac{1}{\alpha} \tau_1$
- ① $<$ ⑤ : $A < \sqrt{\alpha} B \rightarrow \tau_2^3 < \alpha \tau_1$
- ① $<$ ⑥ : $A < D \rightarrow \tau_2^3 < \tau_1$
- ② $<$ ③ : $\sqrt{\frac{1}{\alpha}} B < \alpha^{1/4} C \rightarrow \tau_2^3 > (\frac{1}{\alpha})^3 \tau_1$
- ② $<$ ④ : $\sqrt{\frac{1}{\alpha}} B < \frac{1}{\alpha}^{1/4} C \rightarrow \tau_2^3 > \frac{1}{\alpha} \tau_1$
- ② $<$ ⑤ : $\sqrt{\frac{1}{\alpha}} B < \sqrt{\alpha} B \rightarrow$ not possible, it should be ② $>$ ⑤
- ② $<$ ⑥ : $\sqrt{\frac{1}{\alpha}} B < D \rightarrow \tau_2^3 < (\frac{1}{\alpha})^3 \tau_1$
- ③ $<$ ④ : $\alpha^{1/4} C < \frac{1}{\alpha}^{1/4} C \rightarrow$ without condition
- ③ $<$ ⑤ : $\alpha^{1/4} C < \sqrt{\alpha} B \rightarrow \tau_2^3 < \alpha^3 \tau_1$
- ③ $<$ ⑥ : $\alpha^{1/4} C < D \rightarrow \tau_2^3 < \alpha^3 \tau_1$
- ④ $<$ ⑤ : $\frac{1}{\alpha}^{1/4} C < \sqrt{\alpha} B \rightarrow \tau_2^3 < \alpha^3 \tau_1$
- ④ $<$ ⑥ : $\frac{1}{\alpha}^{1/4} C < D \rightarrow \tau_2^3 < \alpha^3 \tau_1$
- ⑤ $<$ ⑥ : $\sqrt{\alpha} B < D \rightarrow \tau_2^3 > \alpha^3 \tau_1$

Each pairwise comparison gives a new conditions about τ_1 , τ_2 and α . Once the relation among three parameters are given, we will get the permutation of the six separators ①-⑥ thus the permutation of the powers in the numerator. We arrange all the new conditions and easily find some conditions are reputed. Considering when τ_2 sweeps on the parametric space related to τ_1 and α , we list below all the possibilities of permutation of the powers in the numerator for $\alpha < 1$:

$$N\textcircled{a} : \tau_2^3 < \alpha^3 \tau_1$$

Separator	①	③	④	⑥	⑤	②	
Power	ω^{-7}	ω^{-7}	ω^{-3}	ω^{-3}	ω^{-3}	ω^{-3}	ω^{-1}

$$N\textcircled{b} : \alpha^3 \tau_1 < \tau_2^3 < \alpha \tau_1$$

Separator	①	⑤	⑥	③	④	②	
Power	ω^{-7}	ω^{-7}	ω^{-5}	ω^{-5}	ω^{-3}	ω^{-3}	ω^{-1}

$$N\textcircled{c} : \alpha \tau_1 < \tau_2^3 < \tau_1$$

Separator	⑤	①	③	⑥	④	②	
Power	ω^{-7}	ω^{-5}	ω^{-5}	ω^{-3}	ω^{-3}	ω^{-3}	ω^{-1}

$$N\textcircled{d} : \tau_1 < \tau_2^3 < \frac{1}{\alpha} \tau_1$$

Separator	⑤	⑥	③	①	④	②	
Power	ω^{-7}	ω^{-5}	ω^{-5}	ω^{-3}	ω^{-3}	ω^{-3}	ω^{-1}

$$N\textcircled{e} : \frac{1}{\alpha} \tau_1 < \tau_2^3 < \frac{1}{\alpha^3} \tau_1$$

Separator	⑤	⑥	③	②	④	①	
Power	ω^{-7}	ω^{-5}	ω^{-5}	ω^{-5}	ω^{-5}	ω^{-1}	ω^{-1}

$$N\textcircled{f} : \tau_2^3 > \frac{1}{\alpha} \tau_1$$

Separator	⑤	②	⑥	③	④	①	
Power	ω^{-7}	ω^{-5}	ω^{-5}	ω^{-5}	ω^{-5}	ω^{-1}	ω^{-1}

1.2 Denominator

Similar to the numerator, we will go through the same procedure to get the permutation of the powers. There are three terms in the denominator, which gives only $C_3^2 = 3$ pairwise comparisons as listed below :

$$\begin{aligned} \textcircled{7} \quad \tau_1^2 \omega^{-6} &> (\alpha + 1) \tau_1^2 \tau_2^2 \omega^{-8} \rightarrow \omega > \sqrt{\alpha + 1} \tau_2 \\ \textcircled{8} \quad \alpha \tau_2^2 \omega^{-2} &> \tau_1^2 \omega^{-6} \rightarrow \omega > \left(\frac{1}{\alpha}\right)^{1/4} \sqrt{\frac{\tau_1}{\tau_2}} \\ \textcircled{9} \quad \alpha \tau_2^2 \omega^{-2} &> (\alpha + 1) \tau_1^2 \tau_2^2 \omega^{-8} \rightarrow \omega > \left(\frac{\alpha + 1}{\alpha}\right)^{1/6} \tau_1^{1/3} \end{aligned}$$

Then, we compare the three separators ⑦, ⑧ and ⑨ :

$$\begin{aligned} \textcircled{7} < \textcircled{8} : \sqrt{\alpha + 1} A &< \left(\frac{1}{\alpha}\right)^{1/4} B \rightarrow \tau_2^3 < \frac{(1/\alpha)^{1/2}}{\alpha + 1} \tau_1 \\ \textcircled{7} < \textcircled{9} : \sqrt{\alpha + 1} A &< \left(\frac{\alpha + 1}{\alpha}\right)^{1/6} D \rightarrow \tau_2^3 < \frac{(1/\alpha)^{1/2}}{\alpha + 1} \tau_1 \\ \textcircled{8} < \textcircled{9} : \left(\frac{1}{\alpha}\right)^{1/4} B &< \left(\frac{\alpha + 1}{\alpha}\right)^{1/6} D \rightarrow \tau_2^3 > \frac{(1/\alpha)^{1/2}}{\alpha + 1} \tau_1 \end{aligned}$$

Considering when τ_2 sweeps on the parametric space related to τ_1 and α , we list below all the possibilities of permutation of the powers in the denominator for $\alpha < 1$:

$$D\textcircled{a} : \tau_2^3 < \frac{(1/\alpha)^{1/2}}{\alpha + 1} \tau_1$$

Separator	⑦	⑨	⑧	
Power	ω^{-8}	ω^{-6}	ω^{-6}	ω^{-2}

$$D\textcircled{b} : \tau_2^3 > \frac{(1/\alpha)^{1/2}}{\alpha + 1} \tau_1$$

Separator	⑧	⑨	⑦	
Power	ω^{-8}	ω^{-8}	ω^{-2}	ω^{-2}

1.3 Combination of the numerator and the denominator

The powers in the numerator are : ω^{-7} , ω^{-5} , ω^{-3} and ω^{-1} .

The powers in the denominator are : ω^{-8} , ω^{-6} and ω^{-2} .

As said in the beginning, the idea is to conduct goal-oriented searches instead of listing all possibilities. As such, we will concentrate on those combination of the numerator and the denominator which can provide $\omega - \omega^3 - \omega$ behavior.

Power	ω	ω^3	ω
Combination	ω^{-7}/ω^{-8}	ω^{-3}/ω^{-6}	ω^{-7}/ω^{-8}
	ω^{-5}/ω^{-6}	ω^{-5}/ω^{-8}	ω^{-5}/ω^{-6}
	ω^{-1}/ω^{-2}		ω^{-1}/ω^{-2}

In order to obtain a $\omega - \omega^3 - \omega$ behavior, we observe the different ω behavior given by the different permutation of the separator. For example, NⒻ gives a $\omega^{-7} - \omega^{-5} - \omega^{-1}$ power law, and DⒼ gives a $\omega^{-8} - \omega^{-9} - \omega^{-7}$ power law. Therefore, a proper combination of these numerator and denominator makes it possible to get the objective power law.

Note : 9 separators ① - ⑨ need $C_9^2 = 36$ pairwise comparisons among which $C_6^2 = 15$ has been reported in the section of the numerator and the rest pairwise comparisons will not be elaborated here due to space limitations. In short, once the relation between τ_1 , τ_2 and α is known, the permutation of the 9 separators is known, vice versa. The detail can be found in the corresponding manuscript (if possible).

1.4 Existence of $\omega - \omega^3 - \omega$ behavior

NⒻ + DⒼ :

Separator	⑤	⑧	②	⑥	③	④=⑨	①	⑦
Num. power	ω^{-7}	ω^{-5}	ω^{-5}	ω^{-5}	ω^{-5}	ω^{-5}	ω^{-1}	ω^{-1}
Deno. power	ω^{-8}	ω^{-8}	ω^{-8}	ω^{-8}	ω^{-8}	ω^{-8}	ω^{-2}	ω^{-2}
Power	ω^1	ω^3	ω^3	ω^3	ω^3	ω^3	ω^1	ω^1

Conditions :

$$\left\{ \begin{array}{l} 0 < \alpha < 1 \\ N\text{Ⓕ} + D\text{Ⓖ} \rightarrow \tau_2^3 > \frac{1}{\alpha^3} \tau_1 \\ \text{④} = \text{⑨} \rightarrow \tau_2^3 = (\alpha + 1)^2 \alpha \tau_1 \end{array} \right.$$

As a result, $0.76 < \alpha < 1$.

Properties :

Position of the crossover $\omega - \omega^3$:

$$\omega_{1-3} = \frac{1}{\alpha + 1} \tau_2$$

Position of the crossover $\omega^3 - \omega$:

$$\omega_{3-1} = \left(\frac{1}{\alpha}\right)^{1/2} \left(\frac{1}{\alpha + 1}\right)^{1/2} \tau_2$$

2 $\alpha > 1$

For $\alpha > 1$, we also find that at least one case gives a $\omega - \omega^3 - \omega$ behavior.

Conditions :

$$\left\{ \begin{array}{l} \alpha > 1 \\ \tau_2^3 > \alpha^3 \tau_1 \\ \tau_2^3 = (\alpha + 1)^2 \alpha \tau_1 \end{array} \right.$$

Properties :

Position of the crossover $\omega - \omega^3$:

$$\omega_{1-3} = \frac{1}{\alpha + 1} \tau_2$$

Position of the crossover $\omega^3 - \omega$:

$$\omega_{3-1} = \left(\frac{1}{\alpha}\right)^{1/2} \left(\frac{1}{\alpha + 1}\right)^{1/2} \tau_2$$

3 Conclusion

To conclude, we discuss the existence of $\omega - \omega^3 - \omega$ in our viscoelastic model when some conditions are met. We give two possibilities as well as the corresponding conditions. In addition, the position of crossovers are determined which can be used as a reference to get the approximate magnitude of the parameter. In practice, we have slightly relaxed the conditions when calibrating the model on A-SiO₂.

Bibliography

- [ACH 12] ACHENBACH J.
Wave propagation in elastic solids, vol. 16. Elsevier, 2012.
- [ALB 13] ALBE K., RITTER Y., ŞOPU D.
Enhancing the plasticity of metallic glasses : Shear band formation, nanocomposites and nanoglasses investigated by molecular dynamics simulations. *Mechanics of Materials*, vol. 67, 2013, p. 94–103, Elsevier BV.
- [ALB 16] ALBARET T., TANGUY A., BOIOLI F., RODNEY D.
Mapping between atomistic simulations and Eshelby inclusions in the shear deformation of an amorphous silicon model. *Physical Review E*, vol. 93, n° 5, 2016, American Physical Society (APS).
- [ALL 90] ALLEN P. B., FELDMAN J. L.
Thermal Conductivity of Glasses : Theory and Application to Amorphous Si. *Physical Review Letters*, vol. 64, n° 20, 1990, p. 2466–2466, American Physical Society (APS).
- [ALL 93] ALLEN P. B., FELDMAN J. L.
Thermal conductivity of disordered harmonic solids. *Physical Review B*, vol. 48, n° 17, 1993, p. 12581–12588, American Physical Society (APS).
- [ALL 99] ALLEN P. B., FELDMAN J. L., FABIAN J., WOOTEN F.
Diffusons, locons and propagons : Character of atomic vibrations in amorphous Si. *Philosophical Magazine B*, vol. 79, n° 11-12, 1999, p. 1715–1731, Informa UK Limited.
- [ANU 16] ANUFRIEV R., NOMURA M.
Reduction of thermal conductance by coherent phonon scattering in two-dimensional phononic crystals of different lattice types. *Physical Review B*, vol. 93, n° 4, 2016, American Physical Society (APS).
- [AYR 11] AYRINHAC S., FORET M., DEVOS A., RUFLÁL' B., COURTENS E., VACHER R.
Subterahertz hypersound attenuation in silica glass studied via picosecond acoustics. *Physical Review B*, vol. 83, 2011, page 014204.

- [BAL 10] BALDI G., GIORDANO V. M., MONACO G., RUTA B.
Sound Attenuation at Terahertz Frequencies and the Boson Peak of Vitreous Silica. *Physical Review Letters*, vol. 104, n° 19, 2010, American Physical Society (APS).
- [BAL 11] BALDI G., GIORDANO V. M., MONACO G.
Elastic anomalies at terahertz frequencies and excess density of vibrational states in silica glass. *Physical Review B*, vol. 83, n° 17, 2011, American Physical Society (APS).
- [BAR 02] BARET J.-C., VANDEMBROUCQ D., ROUX S.
Extremal Model for Amorphous Media Plasticity. *Physical Review Letters*, vol. 89, n° 19, 2002, American Physical Society (APS).
- [BEL 13] BELYTSCHKO T., LIU W. K., MORAN B., ELKHODARY K.
Nonlinear Finite Elements for Continua and Structures. Wiley John + Sons, 2013.
- [BEL 16] BELTUKOV Y. M., FUSCO C., PARSHIN D. A., TANGUY A.
Boson peak and Ioffe-Regel criterion in amorphous siliconlike materials : The effect of bond directionality. *Physical Review E*, vol. 93, n° 2, 2016, American Physical Society (APS).
- [BEL 18] BELTUKOV Y., PARSHIN D., GIORDANO V., TANGUY A.
Propagative and diffusive regimes of acoustic damping in bulk amorphous material. *Physical Review E*, vol. 98, n° 2, 2018, page 023005, APS.
- [BEN 96] BENASSI P., KRISCH M., MASCIOVECCHIO C., MAZZACURATI V., MONACO G., RUOCCO G., SETTE F., VERBENI R.
Evidence of High Frequency Propagating Modes in Vitreous Silica. *Physical Review Letters*, vol. 77, n° 18, 1996, p. 3835–3838, American Physical Society (APS).
- [BEN 05] BENASSI P., CAPONI S., ERAMO R., FONTANA A., GIUGNI A., NARDONE M., SAMPOLI M., VILIANI G.
Sound attenuation in a unexplored frequency region : Brillouin ultraviolet light scattering measurements in ν -SiO₂. *Physical Review B*, vol. 71, n° 17, 2005, American Physical Society (APS).
- [BET 77] BETTESS P.
Infinite elements. *International Journal for Numerical Methods in Engineering*, vol. 11, n° 1, 1977, p. 53–64, Wiley.
- [BON 14] BONNET M., FRANGI A., REY C.
The finite element method in solid mechanics. McGraw Hill Education, 2014.
- [BOV 05] BOVE L. E., FABIANI E., FONTANA A., PAOLETTI F., PETRILLO C., PILLA O., BENTO I. C. V.
Brillouin neutron scattering of ν -GeO₂. *Europhysics Letters (EPL)*, vol. 71, n° 4, 2005, p. 563–569, IOP Publishing.

- [BRI 08] BRINSON H. F., BRINSON L. C. et al.
Polymer engineering science and viscoelasticity. Springer, 2008.
- [BUC 92] BUCHENAU U., GALPERIN Y., GUREVICH V., PARSHIN D., RAMOS M., SCHOBER H.
Interaction of soft modes and sound waves in glasses. *Physical Review B*, vol. 46, n° 5, 1992, page 2798.
- [BUC 14] BUCHENAU U.
Evaluation of x-ray Brillouin scattering data. *Physical Review E*, vol. 90, n° 6, 2014, American Physical Society (APS).
- [BUL 94] BULATOV V., ARGON A.
A stochastic model for continuum elasto-plastic behavior. I. Numerical approach and strain localization. *Modelling and Simulation in Materials Science and Engineering*, vol. 2, n° 2, 1994, page 167, IOP Publishing.
- [CAN 86] CANNY J.
A Computational Approach to Edge Detection. *IEEE Transactions on Pattern Analysis and Machine Intelligence*, vol. PAMI-8, n° 6, 1986, p. 679–698, Institute of Electrical and Electronics Engineers (IEEE).
- [CAP 09] CAPONI S., COREZZI S., FIORETTO D., FONTANA A., MONACO G., ROSSI F.
Raman-Scattering Measurements of the Vibrational Density of States of a Reactive Mixture During Polymerization : Effect on the Boson Peak. *Physical Review Letters*, vol. 102, n° 2, 2009, American Physical Society (APS).
- [CAR 98] CARFAGNI M., LENZI E., PIERINI M.
The loss factor as a measure of mechanical damping. *Proceedings-spie the international society for optical engineering*, vol. 1 SPIE INTERNATIONAL SOCIETY FOR OPTICAL, 1998, p. 580–284.
- [CHR 12] CHRISTENSEN R.
Theory of viscoelasticity : an introduction. Elsevier, 2012.
- [CHU 16] CHUROCHKIN D., BARRA F., LUND F., MAUREL A., PAGNEUX V.
Multiple scattering of elastic waves by pinned dislocation segments in a continuum. *Wave Motion*, vol. 60, 2016, p. 220–230, Elsevier BV.
- [CLA 77] CLAYTON R., ENGQUIST B.
Absorbing boundary conditions for acoustic and elastic wave equations. *Bulletin of the Seismological Society of America*, vol. 67, n° 6, 1977, page 1529.
- [COU 09] COUSTY J., BERTRAND G., NAJMAN L., COUPRIE M.
Watershed cuts : Thinnings, shortest path forests, and topological watersheds. *IEEE*

- Transactions on Pattern Analysis and Machine Intelligence*, vol. 32, n° 5, 2009, p. 925–939, IEEE.
- [CUM 16] CUMMER S. A., CHRISTENSEN J., ALÙ A.
Controlling sound with acoustic metamaterials. *Nature Reviews Materials*, vol. 1, n° 3, 2016, Springer Science and Business Media LLC.
- [DAM 15] DAMART T., GIORDANO V. M., TANGUY A.
Nanocrystalline inclusions as a low-pass filter for thermal transport in a-Si. *Physical Review B*, vol. 92, n° 9, 2015, American Physical Society (APS).
- [DAM 17] DAMART T., TANGUY A., RODNEY D.
Theory of harmonic dissipation in disordered solids. *Physical Review B*, vol. 95, n° 5, 2017, American Physical Society (APS).
- [DER 12] DERLET P., MAASS R., LÄUFFLER J.
The Boson peak of model glass systems and its relation to atomic structure. *The European Physical Journal B*, vol. 85, n° 5, 2012, Springer Science and Business Media LLC.
- [DEV 08] DEVOS A., FORET M., AYRINHAC S., EMERY P., RUFFLÉ B.
Hypersound damping in vitreous silica measured by picosecond acoustics. *Physical Review B*, vol. 77, n° 10, 2008, American Physical Society (APS).
- [DEY 17] DEYMIER P. A., GOLE V., LUCAS P., VASSEUR J. O., RUNGE K.
Tailoring phonon band structures with broken symmetry by shaping spatiotemporal modulations of stiffness in a one-dimensional elastic waveguide. *Physical Review B*, vol. 96, n° 6, 2017, American Physical Society (APS).
- [DIE 79] DIETSCH W., KINDER H.
Spectroscopy of Phonon Scattering in Glass. *Physical Review Letters*, vol. 43, n° 19, 1979, p. 1413–1417, American Physical Society (APS).
- [DUV 98] DUVAL E., MERMET A.
Inelastic x-ray scattering from nonpropagating vibrational modes in glasses. *Physical Review B*, vol. 58, n° 13, 1998, p. 8159–8162, American Physical Society (APS).
- [ESH 57] ESHELBY J. D.
The determination of the elastic field of an ellipsoidal inclusion, and related problems. *Proceedings of the royal society of London. Series A. Mathematical and physical sciences*, vol. 241, n° 1226, 1957, p. 376–396, The Royal Society London.
- [FEL 99] FELDMAN J. L., ALLEN P. B., BICKHAM S. R.
Numerical study of low-frequency vibrations in amorphous silicon. *Physical Review B*, vol. 59, n° 5, 1999, p. 3551–3559, American Physical Society (APS).

- [FEN 13] FENG Y., GOREE J., LIU B.
Longitudinal viscosity of two-dimensional Yukawa liquids. *Physical Review E*, vol. 87, n° 1, 2013, American Physical Society (APS).
- [FIO 99] FIORETTO D., BUCHENAU U., COMEZ L., SOKOLOV A., MASCIOVECCHIO C., MERMET A., RUOCCO G., SETTE F., WILLNER L., FRICK B., RICHTER D., VERDINI L.
High-frequency dynamics of glass-forming polybutadiene. *Physical Review E*, vol. 59, n° 4, 1999, p. 4470–4475, American Physical Society (APS).
- [FRA 12] FRANÇOIS D., PINEAU A., ZAOUI A.
Mechanical Behaviour of Materials : Volume 1 : Micro-and Macroscopic Constitutive Behaviour, vol. 180. Springer Science & Business Media, 2012.
- [FRA 14] FRANCE-LANORD A., MERABIA S., ALBARET T., LACROIX D., TERMENT-ZIDIS K.
Thermal properties of amorphous/crystalline silicon superlattices. *Journal of Physics : Condensed Matter*, vol. 26, n° 35, 2014, page 355801, IOP Publishing.
- [FUS 10] FUSCO C., ALBARET T., TANGUY A.
Role of local order in the small-scale plasticity of model amorphous materials. *Physical Review E*, vol. 82, n° 6, 2010, American Physical Society (APS).
- [GAN 18] GAN Z., WANG C., CHEN Z.
Material Structure and Mechanical Properties of Silicon Nitride and Silicon Oxynitride Thin Films Deposited by Plasma Enhanced Chemical Vapor Deposition. *Surfaces*, vol. 1, n° 1, 2018, p. 59–72, MDPI AG.
- [GEL 16] GELIN S., TANAKA H., LEMAÎTRE A.
Anomalous phonon scattering and elastic correlations in amorphous solids. *Nature Materials*, vol. 15, n° 11, 2016, p. 1177–1181, Springer Science and Business Media LLC.
- [GEN 20] GENTILE J. M., STAUFFER D. D., HOFMANN D. C., TRELEWICZ J. R.
Shear localization and its dependence on microstructural length scales in metallic glass composites. *Materialia*, vol. 9, 2020, page 100598, Elsevier BV.
- [GER 14] GERADIN D. J. R.
Mechanical Vibrations : Theory and Application to Structural Dynamics, 3rd Edition. John Wiley & Sons, 2014.
- [GIL 81] GILROY K. S., PHILLIPS W. A.
An asymmetric double-well potential model for structural relaxation processes in amorphous materials. *Philosophical Magazine B*, vol. 43, n° 5, 1981, p. 735–746, Informa UK Limited.

- [HAY 00] HAYS C. C., KIM C. P., JOHNSON W. L.
Microstructure Controlled Shear Band Pattern Formation and Enhanced Plasticity of Bulk Metallic Glasses Containing in situ Formed Ductile Phase Dendrite Dispersions. *Physical Review Letters*, vol. 84, n° 13, 2000, p. 2901–2904, American Physical Society (APS).
- [HOR 01] HORBACH J., KOB W., BINDER K.
High frequency sound and the boson peak in amorphous silica. *The European Physical Journal B*, vol. 19, n° 4, 2001, p. 531–543, Springer Science and Business Media LLC.
- [HUG 12] HUGHES T. J.
The finite element method : linear static and dynamic finite element analysis. Courier Corporation, 2012.
- [INO 11] INOUE A., TAKEUCHI A.
Recent development and application products of bulk glassy alloys☆. *Acta Materialia*, vol. 59, n° 6, 2011, p. 2243–2267, Elsevier BV.
- [JI 19] JI W., POPOVIÄĀ M., DE GEUS T. W. J., LERNER E., WYART M.
Theory for the density of interacting quasilocalized modes in amorphous solids. *Physical Review E*, vol. 99, 2019, page 023003.
- [JIN 17] JIN X., ZHANG X., LI P., XU Z., HU Y., KEER L. M.
On the Displacement of a Two-Dimensional Eshelby Inclusion of Elliptic Cylindrical Shape. *Journal of Applied Mechanics*, vol. 84, n° 7, 2017, ASME International.
- [JOH 99] JOHNSON W. L.
Bulk Glass-Forming Metallic Alloys : Science and Technology. *MRS Bulletin*, vol. 24, n° 10, 1999, p. 42–56, Cambridge University Press (CUP).
- [KAL 97] KALISKE M., ROTHERT H.
Formulation and implementation of three-dimensional viscoelasticity at small and finite strains. *Computational Mechanics*, vol. 19, n° 3, 1997, p. 228–239, Springer Nature.
- [KAL 00] KALISKE M.
A formulation of elasticity and viscoelasticity for fibre reinforced material at small and finite strains. *Computer Methods in Applied Mechanics and Engineering*, vol. 185, n° 2-4, 2000, p. 225–243, Elsevier BV.
- [KHE 06] KHELIF A., AOUBIZA B., MOHAMMADI S., ADIBI A., LAUDE V.
Complete band gaps in two-dimensional phononic crystal slabs. *Physical Review E*, vol. 74, n° 4, 2006, American Physical Society (APS).

- [KIM 14] KIM H. S.
A Study on the Performance of Absorbing Boundaries Using Dashpot. *Engineering*, vol. 06, n° 10, 2014, p. 593–600, Scientific Research Publishing, Inc.,
- [KIT 04] KITTEL C.
Introduction to Solid State Physics. John Wiley & Sons Inc, 2004.
- [KUB 57] KUBO R.
Statistical-Mechanical Theory of Irreversible Processes. I. General Theory and Simple Applications to Magnetic and Conduction Problems. *Journal of the Physical Society of Japan*, vol. 12, n° 6, 1957, p. 570–586, Physical Society of Japan.
- [LAN 86] LANDAU L., LIFSHITZ E.
Theory of elasticity. 1986.
- [LAR 14] LARKIN J. M., MCGAUGHEY A. J. H.
Thermal conductivity accumulation in amorphous silica and amorphous silicon. *Physical Review B*, vol. 89, n° 14, 2014, American Physical Society (APS).
- [LEE 16] LEE S., KANG B., KEUM H., AHMED N., ROGERS J. A., FERREIRA P. M., KIM S., MIN B.
Heterogeneously Assembled Metamaterials and Metadevices via 3D Modular Transfer Printing. *Scientific Reports*, vol. 6, n° 1, 2016, Springer Science and Business Media LLC.
- [LEO 05] LEONFORTE F., BOISSIÈRE R., TANGUY A., WITTMER J. P., BARRAT J.-L.
Continuum limit of amorphous elastic bodies. III. Three-dimensional systems. *Physical Review B*, vol. 72, n° 22, 2005, American Physical Society (APS).
- [LEO 06a] LEONFORTE F., TANGUY A., BARRAT J.-L.
Inhomogeneous elastic response of silica glass. *Physical Review Letters*, vol. 97, n° 5, 2006, page 055501.
- [LEO 06b] LÉONFORTE F., TANGUY A., WITTMER J. P., BARRAT J.-L.
Inhomogeneous Elastic Response of Silica Glass. *Physical Review Letters*, vol. 97, n° 5, 2006, American Physical Society (APS).
- [LEV 06] LEVELUT C., PARC R. L., PELOUS J.
Dynamic sound attenuation at hypersonic frequencies in silica glass. *Physical Review B*, vol. 73, n° 5, 2006, American Physical Society (APS).
- [LIN 03] LIN R., SCHOMBURG U.
A finite elastic–viscoelastic–elastoplastic material law with damage : theoretical and numerical aspects. *Computer Methods in Applied Mechanics and Engineering*, vol. 192, n° 13-14, 2003, p. 1591–1627, Elsevier BV.

- [LIU 00] LIU Z.
Locally Resonant Sonic Materials. *Science*, vol. 289, n° 5485, 2000, p. 1734–1736, American Association for the Advancement of Science (AAAS).
- [LU 18a] LU Y., BLAL N., GRAVOUIL A.
Datadriven HOPGD based computational vademecum for welding parameter identification. *Computational Mechanics*, vol. 64, n° 1, 2018, p. 47–62, Springer Science and Business Media LLC.
- [LU 18b] LU Y., BLAL N., GRAVOUIL A.
Multi-parametric space-time computational vademecum for parametric studies : Application to real time welding simulations. *Finite Elements in Analysis and Design*, vol. 139, 2018, p. 62–72, Elsevier BV.
- [LUN 88] LUND F.
Response of a stringlike dislocation loop to an external stress. *Journal of Materials Research*, vol. 3, n° 2, 1988, p. 280–297, Cambridge University Press.
- [LUO 19] LUO H., GRAVOUIL A., GIORDANO V., TANGUY A.
Thermal Transport in a 2D Nanophononic Solid : Role of bi-Phasic Materials Properties on Acoustic Attenuation and Thermal Diffusivity. *Nanomaterials*, vol. 9, n° 10, 2019, page 1471, MDPI AG.
- [LUO 20] LUO H., GRAVOUIL A., GIORDANO V. M., SCHIRMACHER W., TANGUY A.
Continuum constitutive laws to describe acoustic attenuation in glasses. *Physical Review E*, vol. 102, n° 3, 2020, American Physical Society (APS).
- [LYS 69] LYSMER J., KUHLEMEYER R. L.
Finite dynamic model for infinite media. *Journal of the Engineering Mechanics Division*, vol. 95, n° 4, 1969, p. 859–878, ASCE.
- [MAI 17] MAIRE J., ANUFRIEV R., YANAGISAWA R., RAMIERE A., VOLZ S., NOMURA M.
Heat conduction tuning by wave nature of phonons. *Science Advances*, vol. 3, n° 8, 2017, page e1700027, American Association for the Advancement of Science (AAAS).
- [MAL 04] MALONEY C., LEMAÎTRE A.
Universal Breakdown of Elasticity at the Onset of Material Failure. *Physical Review Letters*, vol. 93, n° 19, 2004, American Physical Society (APS).
- [MAR 08] MARBURG S., NOLTE B., Eds. *Computational Acoustics of Noise Propagation in Fluids - Finite and Boundary Element Methods*. Springer Berlin Heidelberg, 2008.
- [MAR 13] MARRUZZO A., SCHIRMACHER W., FRATALOCCHI A., RUOCCO G.
Heterogeneous shear elasticity of glasses : the origin of the boson peak. *Scientific Reports*, vol. 3, n° 1, 2013, Springer Science and Business Media LLC.

- [MAR 14] MARC ANDRE MEYERS K. K. C.
Mechanical Behavior of Materials. Cambridge University Press, 2014.
- [MAS 97] MASCIOVECCHIO C., RUOCCO G., SETTE F., BENASSI P., CUNSOLO A., KRISCH M., MAZZACURATI V., MERMET A., MONACO G., VERBENI R.
High-frequency propagating modes in vitreous silica at 295 K. *Physical Review B*, vol. 55, n° 13, 1997, p. 8049–8051, American Physical Society (APS).
- [MAS 04] MASCIOVECCHIO C., GESSINI A., FONZO S. D., COMEZ L., SANTUCCI S. C., FIORETTO D.
Inelastic Ultraviolet Scattering from High Frequency Acoustic Modes in Glasses. *Physical Review Letters*, vol. 92, n° 24, 2004, American Physical Society (APS).
- [MAS 06] MASCIOVECCHIO C., BALDI G., CAPONI S., COMEZ L., FONZO S. D., FIORETTO D., FONTANA A., GESSINI A., SANTUCCI S. C., SETTE F., VILIANI G., VILMERCATI P., RUOCCO G.
Evidence for a Crossover in the Frequency Dependence of the Acoustic Attenuation in Vitreous Silica. *Physical Review Letters*, vol. 97, n° 3, 2006, American Physical Society (APS).
- [MAU 05] MAUREL A., PAGNEUX V., BARRA F., LUND F.
Interaction between an elastic wave and a single pinned dislocation. *Physical Review B*, vol. 72, n° 17, 2005, American Physical Society (APS).
- [MAY 09] MAYR S. G.
Relaxation kinetics and mechanical stability of metallic glasses and supercooled melts. *Physical Review B*, vol. 79, n° 6, 2009, American Physical Society (APS).
- [MCC 92] MCCALL S. L., LEVI A. F. J., SLUSHER R. E., PEARTON S. J., LOGAN R. A.
Whispering-gallery mode microdisk lasers. *Applied Physics Letters*, vol. 60, n° 3, 1992, p. 289–291, AIP Publishing.
- [MER 12] MERABIA S., TERMENTZIDIS K.
Thermal conductance at the interface between crystals using equilibrium and nonequilibrium molecular dynamics. *Physical Review B*, vol. 86, n° 9, 2012, American Physical Society (APS).
- [MIC 15] MICHEL GERADIN D. J. R.
Mechanical Vibrations. John Wiley & Sons Inc, 2015.
- [MIZ 14] MIZUNO H., MOSSA S., BARRAT J.-L.
Acoustic excitations and elastic heterogeneities in disordered solids. *Proceedings of the National Academy of Sciences*, vol. 111, n° 33, 2014, p. 11949–11954, Proceedings of the National Academy of Sciences.

- [MIZ 19] MIZUNO H., RUOCCO G., MOSSA S.
Sound damping in glasses : interplay between anharmonicities and elastic heterogeneities. *arXiv preprint arXiv :1905.10235*, , 2019.
- [MOL 16] MOLNÁR G., GANSTER P., TÁŔŔÁŔK J., TANGUY A.
Sodium effect on static mechanical behavior of MD-modeled sodium silicate glasses. *Journal of Non-Crystalline Solids*, vol. 440, 2016, p. 12–25, Elsevier BV.
- [MON 09a] MONACO G., GIORDANO V. M.
Breakdown of the Debye approximation for the acoustic modes with nanometric wavelengths in glasses. *Proceedings of the National Academy of Sciences*, vol. 106, n^o 10, 2009, p. 3659–3663, Proceedings of the National Academy of Sciences.
- [MON 09b] MONACO G., MOSSA S.
Anomalous properties of the acoustic excitations in glasses on the mesoscopic length scale. *Proceedings of the National Academy of Sciences*, vol. 106, n^o 40, 2009, p. 16907–16912, Proceedings of the National Academy of Sciences.
- [MOO 16] MOON J., MINNICH A. J.
Sub-amorphous thermal conductivity in amorphous heterogeneous nanocomposites. *RSC Advances*, vol. 6, n^o 107, 2016, p. 105154–105160, Royal Society of Chemistry (RSC).
- [NEW 59] NEWMARK N. M.
A method of computation for structural dynamics. *Journal of the engineering mechanics division*, vol. 85, n^o 3, 1959, p. 67–94, ASCE.
- [NIC 18] NICOLAS A., FERRERO E. E., MARTENS K., BARRAT J.-L.
Deformation and flow of amorphous solids : Insights from elastoplastic models. *Reviews of Modern Physics*, vol. 90, n^o 4, 2018, American Physical Society (APS).
- [PAL 93] PAL N. R., PAL S. K.
A review on image segmentation techniques. *Pattern Recognition*, vol. 26, n^o 9, 1993, p. 1277–1294, Elsevier BV.
- [PAR 66] PARKE S.
Logarithmic decrements at high damping. *British Journal of Applied Physics*, vol. 17, n^o 2, 1966, page 271, IOP Publishing.
- [PAR 17] PARK G., KANG S., LEE H., CHOI W.
Tunable Multifunctional Thermal Metamaterials : Manipulation of Local Heat Flux via Assembly of Unit-Cell Thermal Shifters. *Scientific Reports*, vol. 7, n^o 1, 2017, Springer Science and Business Media LLC.
- [PEN 08] PENNEC Y., DJAFARI-ROUHANI B., LARABI H., VASSEUR J. O., HLADKY-HENNION A. C.

- Low-frequency gaps in a phononic crystal constituted of cylindrical dots deposited on a thin homogeneous plate. *Physical Review B*, vol. 78, n° 10, 2008, American Physical Society (APS).
- [PIL 04] PILLA O., CAPONI S., FONTANA A., GONÇALVES J. R., MONTAGNA M., ROSSI F., VILIANI G., ANGELANI L., RUOCCO G., MONACO G., SETTE F.
The low energy excess of vibrational states in v-SiO₂ : the role of transverse dynamics. *Journal of Physics : Condensed Matter*, vol. 16, n° 47, 2004, p. 8519–8530, IOP Publishing.
- [POH 01] POHL R.
Amorphous Materials : Thermal Conductivity. *Encyclopedia of Materials : Science and Technology*, p. 232–237 Elsevier, 2001.
- [POH 02] POHL R. O., LIU X., THOMPSON E.
Low-temperature thermal conductivity and acoustic attenuation in amorphous solids. *Reviews of Modern Physics*, vol. 74, n° 4, 2002, p. 991–1013, American Physical Society (APS).
- [PRA 09] PRASHER R. S., HU X. J., CHALOPIN Y., MINGO N., LOFGREEN K., VOLZ S., CLERI F., KEBLINSKI P.
Turning Carbon Nanotubes from Exceptional Heat Conductors into Insulators. *Physical Review Letters*, vol. 102, n° 10, 2009, American Physical Society (APS).
- [QIA 16a] QIAO J., YAO Y., PELLETIER J., KEER L.
Understanding of micro-alloying on plasticity in Cu₄₆Zr_{47-x}Al₇Dy_x ($0 \leq x \leq 8$) bulk metallic glasses under compression : Based on mechanical relaxations and theoretical analysis. *International Journal of Plasticity*, vol. 82, 2016, p. 62–75, Elsevier BV.
- [QIA 16b] QIAO J., JIA H., LIAW P. K.
Metallic glass matrix composites. *Materials Science and Engineering : R : Reports*, vol. 100, 2016, p. 1–69, Elsevier BV.
- [QIA 17] QIAO J., SUN B., GU J., SONG M., PELLETIER J., QIAO J., YAO Y., YANG Y.
Abnormal internal friction in the in-situ Ti₆₀Zr₁₅V₁₀Cu₅Be₁₀ metallic glass matrix composite. *Journal of Alloys and Compounds*, vol. 724, 2017, p. 921–931, Elsevier BV.
- [REE 98] REESE S., GOVINDJEE S.
A theory of finite viscoelasticity and numerical aspects. *International Journal of Solids and Structures*, vol. 35, n° 26-27, 1998, p. 3455–3482, Elsevier BV.
- [ROD 09] RODRÍGUEZ N., MAUREL A., PAGNEUX V., BARRA F., LUND F.
Interaction between elastic waves and prismatic dislocation loops. *Journal of Applied Physics*, vol. 106, n° 5, 2009, page 054910, AIP Publishing.

- [RON 02] RONALD FEDKIW S. O.
Level Set Methods and Dynamic Implicit Surfaces. Springer New York, 2002.
- [ROU 17] ROULEAU L., DEÑIJ J.-F.
Time-domain analysis of viscoelastic systems. *Procedia Engineering*, vol. 199, 2017, p. 384–390, Elsevier BV.
- [ROY 01] ROYLANCE D.
Engineering viscoelasticity. *Department of Materials Science and Engineering—Massachusetts Institute of Technology, Cambridge MA*, vol. 2139, 2001, p. 1–37.
- [RUF 03] RUFFLÉ B., FORET M., COURTENS E., VACHER R., MONACO G.
Observation of the Onset of Strong Scattering on High Frequency Acoustic Phonons in Densified Silica Glass. *Physical Review Letters*, vol. 90, n° 9, 2003, American Physical Society (APS).
- [RUF 06] RUFFLÉ B., GUIMBRETIERE G., COURTENS E., VACHER R., MONACO G.
Glass-Specific Behavior in the Damping of Acousticlike Vibrations. *Physical Review Letters*, vol. 96, n° 4, 2006, American Physical Society (APS).
- [RUF 08] RUFFLÉ B., PARSHIN D. A., COURTENS E., VACHER R.
Boson Peak and its Relation to Acoustic Attenuation in Glasses. *Physical Review Letters*, vol. 100, n° 1, 2008, American Physical Society (APS).
- [RUO 99] RUOCCO G., SETTE F., LEONARDO R. D., FIORETTO D., KRISCH M., LORENZEN M., MASCIOVECCHIO C., MONACO G., PIGNON F., SCOPIGNO T.
Nondynamic Origin of the High-Frequency Acoustic Attenuation in Glasses. *Physical Review Letters*, vol. 83, n° 26, 1999, p. 5583–5586, American Physical Society (APS).
- [RUO 08] RUOCCO G.
When disorder helps. *Nature Materials*, vol. 7, n° 11, 2008, p. 842–843, Springer Science and Business Media LLC.
- [SAL 12] SALENÇON J.
Handbook of continuum mechanics : General concepts thermoelasticity. Springer Science & Business Media, 2012.
- [SCH 98] SCHIRMACHER W., EICHENGRÜN M., BREYMAN W.
Quantum chaotic scattering and resistance fluctuations in mesoscopic junctions. *physica status solidi (b)*, vol. 205, n° 1, 1998, p. 219–222, Wiley Online Library.
- [SCH 02] SCHELLING P. K., PHILLPOT S. R., KEBLINSKI P.
Phonon wave-packet dynamics at semiconductor interfaces by molecular-dynamics simulation. *Applied Physics Letters*, vol. 80, n° 14, 2002, p. 2484–2486, AIP Publishing.

- [SCH 04] SCHOBER H. R.
Vibrations and relaxations in a soft sphere glass : boson peak and structure factors. *Journal of Physics : Condensed Matter*, vol. 16, n° 27, 2004, p. S2659–S2670, IOP Publishing.
- [SCH 06] SCHIRMACHER W.
Thermal conductivity of glassy materials and the “boson peak”. *Europhysics Letters (EPL)*, vol. 73, n° 6, 2006, p. 892–898, IOP Publishing.
- [SCH 07] SCHUH C. A., HUFNAGEL T. C., RAMAMURTY U.
Mechanical behavior of amorphous alloys. *Acta Materialia*, vol. 55, n° 12, 2007, p. 4067–4109, Elsevier.
- [SCH 09] SCHROERS J.
Processing of Bulk Metallic Glass. *Advanced Materials*, vol. 22, n° 14, 2009, p. 1566–1597, Wiley.
- [SCH 13] SCHIRMACHER W.
The boson peak. *physica status solidi (b)*, vol. 250, n° 5, 2013, p. 937–943, Wiley.
- [SCH 15a] SCHIRMACHER W., RUOCCO G., MAZZONE V.
Theory of heterogeneous viscoelasticity. *Philosophical Magazine*, vol. 96, n° 7-9, 2015, p. 620–635, Informa UK Limited.
- [SCH 15b] SCHIRMACHER W., SCOPIGNO T., RUOCCO G.
Theory of vibrational anomalies in glasses. *Journal of Non-Crystalline Solids*, vol. 407, 2015, p. 133–140, Elsevier BV.
- [SCH 18] SCHWAAB M.-É., BIBEN T., SANTUCCI S., GRAVOUIL A., VANEL L.
Interacting Cracks Obey a Multiscale Attractive to Repulsive Transition. *Physical Review Letters*, vol. 120, n° 25, 2018, American Physical Society (APS).
- [SCO 03] SCOPIGNO T., YANNOPOULOS S. N., KASTRISSIOS D. T., MONACO G., PONTECORVO E., RUOCCO G., SETTE F.
High frequency acoustic modes in vitreous beryllium fluoride probed by inelastic x-ray scattering. *The Journal of Chemical Physics*, vol. 118, n° 1, 2003, p. 311–316, AIP Publishing.
- [SKL 18] SKLAN S. R., LI B.
Thermal metamaterials : functions and prospects. *National Science Review*, vol. 5, n° 2, 2018, p. 138–141, Oxford University Press (OUP).
- [STA 19] STASIO J. D., DUREISSEIX D., GRAVOUIL A., GEORGES G., HOMOLLE T.
Benchmark cases for robust explicit time integrators in non-smooth transient dynamics. *Advanced Modeling and Simulation in Engineering Sciences*, vol. 6, n° 1, 2019, Springer Nature.

- [STI 85] STILLINGER F. H., WEBER T. A.
Computer simulation of local order in condensed phases of silicon. *Physical Review B*, vol. 31, n° 8, 1985, p. 5262–5271, American Physical Society (APS).
- [STO 80] STOKES G. G.
On the Theories of the Internal Friction of Fluids in Motion, and of the Equilibrium and Motion of Elastic Solids. *Mathematical and Physical Papers vol.1*, p. 75–129 Cambridge University Press, 1880.
- [SWI 62] SWINEHART D. F.
The Beer-Lambert Law. *Journal of Chemical Education*, vol. 39, n° 7, 1962, page 333, American Chemical Society (ACS).
- [TAN 02] TANGUY A., WITTMER J., LEONFORTE F., BARRAT J.-L.
Continuum limit of amorphous elastic bodies : A finite-size study of low-frequency harmonic vibrations. *Physical Review B*, vol. 66, 2002, page 174205.
- [TAN 10] TANGUY A., MANTISI B., TSAMADOS M.
Vibrational modes as a predictor for plasticity in a model glass. *Europhysics Letters*, vol. 90, n° 1, 2010, page 16004.
- [TER 09] TERMENTZIDIS K., CHANTRENNE P., KEBLINSKI P.
Nonequilibrium molecular dynamics simulation of the in-plane thermal conductivity of superlattices with rough interfaces. *Physical Review B*, vol. 79, n° 21, 2009, American Physical Society (APS).
- [TIA 10] TIAN Z. T., WHITE B. E., SUN Y.
Phonon wave-packet interference and phonon tunneling based energy transport across nanostructured thin films. *Applied Physics Letters*, vol. 96, n° 26, 2010, page 263113, AIP Publishing.
- [TIG 06] VAN TIGGELEN B.
Ondes et Acoustique I, vol. 2. 2004-2006.
- [TLI 17] TLILI A., PAILHÈS S., DEBORD R., RUTA B., GRAVIER S., BLANDIN J.-J., BLANCHARD N., GOMÈS S., ASSY A., TANGUY A., GIORDANO V.
Thermal transport properties in amorphous/nanocrystalline metallic composites : A microscopic insight. *Acta Materialia*, vol. 136, 2017, p. 425–435, Elsevier BV.
- [TLI 19] TLILI A., GIORDANO V. M., BELTUKOV Y. M., DESMARCHELIER P., MERABIA S., TANGUY A.
Enhancement and anticipation of the Ioffe–Regel crossover in amorphous/nanocrystalline composites. *Nanoscale*, vol. 11, n° 44, 2019, p. 21502–21512, Royal Society of Chemistry (RSC).

- [TSA 09] TSAMADOS M., TANGUY A., GOLDENBERG C., BARRAT J.-L.
Local elasticity map and plasticity in a model Lennard-Jones glass. *Physical Review E*, vol. 80, n° 2, 2009, American Physical Society (APS).
- [UKP 09] UKPONG A. M.
Studies of the electronic and vibrational signatures of the unusual bonding geometries in melt-quenched amorphous silicon. *Molecular Physics*, vol. 107, n° 23-24, 2009, p. 2521–2530, Informa UK Limited.
- [VAC 80] VACHER R., SUSSNER H., HUNKLINGER S.
Brillouin scattering in vitreous silica below 1 K. *Physical Review B*, vol. 21, n° 12, 1980, p. 5850–5853, American Physical Society (APS).
- [VAC 97] VACHER R., PELOUS J., COURTENS E.
Mean free path of high-frequency acoustic excitations in glasses with application to vitreous silica. *Physical Review B*, vol. 56, n° 2, 1997, p. R481–R484, American Physical Society (APS).
- [VAS 08] VASSEUR J., HLADKY-HENNION A.-C., DUBUS B., DJAFARI-ROUHANI B., MORVAN B.
Design and characterization of stop-band filters using PZT layer on silicon substrate phononic crystals. *The Journal of the Acoustical Society of America*, vol. 123, n° 5, 2008, p. 3039–3039, Acoustical Society of America (ASA).
- [VAZ 13] VAZHAPPILLY T., MICHA D. A.
Atomic modeling of structural and optical properties of amorphous silicon. *Chemical Physics Letters*, vol. 570, 2013, p. 95–99, Elsevier BV.
- [VER 89] VERPEAUX P., MILLARD A., CHARRAS T., COMBESURE A.
A modern approach of large computer codes for structural analysis. , 1989, IASMiRT.
- [VER 06] VERBERT J.
Réalisation et étude optique de microcavités à modes de galerie intégrées sur silicium. Thèse de doctorat, 2006.
- [VER 18] VERDIER M., LACROIX D., DIDENKO S., ROBILLARD J.-F., LAMPIN E., BAH T.-M., TERMENTZIDIS K.
Influence of amorphous layers on the thermal conductivity of phononic crystals. *Physical Review B*, vol. 97, n° 11, 2018, American Physical Society (APS).
- [WAG 16] WAGNER M. R., GRACZYKOWSKI B., REPARAZ J. S., SACHAT A. E., SLEDZINSKA M., ALZINA F., TORRES C. M. S.
Two-Dimensional Phononic Crystals : Disorder Matters. *Nano Letters*, vol. 16, n° 9, 2016, p. 5661–5668, American Chemical Society (ACS).

- [WAL 16] WALDROP M. M.
The chips are down for Moore's law. *Nature News*, vol. 530, n° 7589, 2016, page 144.
- [WAN 12] WANG W. H.
The elastic properties, elastic models and elastic perspectives of metallic glasses. *Progress in Materials Science*, vol. 57, n° 3, 2012, p. 487–656, Elsevier BV.
- [WAN 19] WANG L., BERTHIER L., FLENNER E., GUAN P., SZAMEL G.
Sound attenuation in stable glasses. *Soft Matter*, vol. 15, n° 35, 2019, p. 7018–7025, Royal Society of Chemistry (RSC).
- [WEI 05] WEINBERGER C., CAI W., BARNETT D.
Lecture notes—elasticity of microscopic structures. Citeseer, 2005.
- [XIE 18] XIE G., DING D., ZHANG G.
Phonon coherence and its effect on thermal conductivity of nanostructures. *Advances in Physics : X*, vol. 3, n° 1, 2018, page 1480417, Informa UK Limited.
- [XU 18] XU Y., ZHOU Q., DU Y., REN Y., ZHAI H., LI Q., CHEN J., WANG H.
Modulating mechanical properties of Ti-based bulk metallic glass composites by tailoring dendrite composition with Sn addition. *Journal of Alloys and Compounds*, vol. 745, 2018, p. 16–25, Elsevier BV.
- [YAN 17] YANG L., MINNICH A. J.
Thermal transport in nanocrystalline Si and SiGe by ab initio based Monte Carlo simulation. *Scientific Reports*, vol. 7, n° 1, 2017, Springer Science and Business Media LLC.
- [ZEL 71] ZELLER R., POHL R.
Thermal Conductivity and Specific Heat of Noncrystalline Solids. *Physical Review B*, vol. 4, n° 6, 1971, American Physical Society (APS).
- [ZEN 14] ZEN N., PUURTINEN T. A., ISOTALO T. J., CHAUDHURI S., MAASILTA I. J.
Engineering thermal conductance using a two-dimensional phononic crystal. *Nature Communications*, vol. 5, n° 1, 2014, Springer Science and Business Media LLC.
- [ZHA 09] ZHANG S., YIN L., FANG N.
Focusing Ultrasound with an Acoustic Metamaterial Network. *Physical Review Letters*, vol. 102, n° 19, 2009, American Physical Society (APS).
- [ZHA 16] ZHAI H., WANG H., LIU F.
A strategy for designing bulk metallic glass composites with excellent work-hardening and large tensile ductility. *Journal of Alloys and Compounds*, vol. 685, 2016, p. 322–330, Elsevier BV.

- [ZHO 11] ZHOU F., SONG B., TIAN G.
Bezier Curve Based Smooth Path Planning for Mobile Robot. *Journal of Information & Computational Science*, vol. 8, n° 12, 2011, p. 2441–2450.
- [ZIE 00a] ZIENKIEWICZ O. C., TAYLOR R. L., TAYLOR R. L., TAYLOR R. L.
The finite element method : solid mechanics, vol. 2. Butterworth-heinemann, 2000.
- [ZIE 00b] ZIENKIEWICZ O. C., TAYLOR R. L., TAYLOR R. L., TAYLOR R. L.
The finite element method : solid mechanics, vol. 2. Butterworth-heinemann, 2000.
- [ZIM 62] ZIMAN J. M.
Electrons and Phonons : Theory of Transport Phenomena in Solids. Clarendon Press, 1962.



FOLIO ADMINISTRATIF

THESE DE L'UNIVERSITE DE LYON OPEREE AU SEIN DE L'INSA LYON

NOM : LUO

DATE de SOUTENANCE : 18/12/2020

Prénoms : Luo

TITRE : High frequency thermomechanical study of heterogeneous materials with interfaces

NATURE : Doctorat

Numéro d'ordre : 2020LYSEI130

Ecole doctorale : MECANIQUE, ENERGETIQUE, GENIE CIVIL, ACOUSTIQUE

Spécialité : Génie Mécanique

RESUME : Heat transfer is actually intimately related to the sound propagation (acoustic transfer) in materials, as in insulators and semi-conductors the main heat carriers are acoustic phonons. The concept of the presence of interfaces has been largely exploited for efficiently manipulating phonons from long-wavelength to nanometric wavelengths, *i.e.*, frequencies in THz regime. In this thesis, the finite element method is used to perform transient analysis of wave-packet propagation in different mediums. I started with a parametric study of attenuation of acoustic wave-packets in a 2D semi-infinite elastic system with periodic circular interfaces. Three key parameters are investigated, including rigidity contrast, interface density and phonon wavelength. Different transfer regimes (propagative, diffusive, and localized) are identified thus relating the phonon contribution to thermal conductivity. Besides the circular interfaces, mechanical response and acoustic attenuation for different types of interfaces are also investigated, such as Eshelby's inclusion, dendritic shape inclusion and porous materials with ordered/disordered holes. In order to extend the study to amorphous materials, I also considered a heterogeneous medium with random rigidities distributed in space according to Gaussian distribution based on the theory of heterogeneous shear elasticity of glasses. Finally yet importantly, viscoelastic constitutive laws are proposed to take into account the frequency-dependent intrinsic phonon attenuation in glasses, with the aim that a homogeneous viscous medium can reproduce this intrinsic attenuation. Finite element simulation confirms that a continuum model may strictly follow the atomistic attenuation (Γ) for a well-calibrated macroscopic linear viscoelastic constitutive law. Compared with the experimental data in A-SiO₂, our constitutive law reproduces qualitatively and quantitatively the three regimes of acoustic attenuation versus frequency: successively $\Gamma \propto \omega^2, \omega^4, \omega^2$.

MOTS-CLÉS : Nanocomposite material; Nanophononic material; Amorphous material; Acoustic and thermal transfer; Acoustic attenuation; Numerical simulations.

Laboratoire (s) de recherche : Laboratoire de Mécanique des Contacts et des Structures
UMR CNRS 5259 - INSA de Lyon
20, avenue Albert Einstein
69621 Villeurbanne Cedex FRANCE

Directeur de thèse: Anne TANGUY
Valentina GIORDANO

Président de jury :

Composition du jury : Benoît RUFFLE	Jérôme VASSEUR
Haozhe LIU	Georges JACQUET-RICHARDET
Fernando LUND	Anthony GRAVOUIL

